University of Strathclyde

Department of Chemical and Process Engineering

Influence of Controlled Fluid Shear on Glycine Crystal Nucleation from Solution

Carol Forsyth

A thesis submitted to the Department of Chemical and Process Engineering in fulfilment of the requirements for the degree of Doctor of Philosophy.

2015

Declarations

This thesis is the result of the author's original research. It has been composed by the author and has not been previously submitted for examination which has led to the award of a degree.

The copyright of this thesis belongs to the author under the terms of the United Kingdom Copyright Acts as qualified by University of Strathclyde Regulation 3.50.

Due acknowledgement must always be made of the use of any material contained in, or derived from, this thesis.

Signed:

Date:

Acknowledgements

I would like to thank Jan Sefcik for supervising my PhD project, buying equipment and coming up with useful ideas. Thanks to Iain Burns for useful discussions about laser based measurements. I'd particularly like to thank Paul Mulheran for providing valuable help and advice on statistical analyses of results.

I would like to thank Jim Murphy for his great help in the lab and good banter. I'm also very grateful to Linda for her friendly chat and keeping the lab clean, despite the mess that I made. Thanks to the admin and IT staff, particularly Laura for helping with orders. Thanks to the other PhD students for any good chat. Thanks to the Carnegie Trust for funding my PhD project.

Thank you to my sister Claire for help with various aspects of my project. Thanks to my mum and dad for providing me with food and shelter. Finally I would like to thank my beautiful cat Cindy for being entertaining, kind, inspirational and truly wonderful.

Abstract

This thesis describes work done to investigate the influence of controlled fluid shear on the primary nucleation of glycine from aqueous solution. Crystallisation from solution is vital to many natural and industrial processes. It is widely used for separation and purification in industries such as chemicals, food and pharmaceuticals. Nucleation, which is the first step in the formation of a new crystalline solid phase from solution, is of fundamental importance in determining product crystal quality, however, at present it is poorly understood mechanistically. An improved understanding of nucleation and the effects of relevant industrial process parameters on nucleation pathways and resulting kinetics is therefore necessary to better design and optimise industrial applications of crystallisation.

In industrial processes, fluid shear is widely encountered, for example through agitation in a vessel, or transport through pipes. The role of fluid shear on the primary nucleation of small organic compounds from solution has not been well studied to date so in this work, the influence of fluid shear on the primary nucleation of glycine, the smallest amino acid, is studied. Couette and capillary flow setups were used to obtain flow conditions which were well understood and quantifiable. Supersaturated aqueous glycine solutions were exposed to flow in these setups under isothermal conditions and induction times (time between the creation of supersaturation and the formation of a new crystalline phase) were measured. Efforts were taken to ensure that the first crystals formed through primary nucleation and the measured induction times were related to the rates of primary nucleation in the solutions. Dynamic light scattering measurements were also carried out to study the mesoscale clusters which exist in aqueous glycine solutions.

The work carried out showed that fluid shear had a profound effect on the primary nucleation of glycine from aqueous solution, with exposure to fluid shear resulting in higher rates of primary nucleation. The onset of nucleation was associated with an increase in average mesoscale cluster size. It is proposed that exposure to fluid shear resulted in the coalescence of mesoscale clusters, with the larger coalesced clusters leading to a more rapid nucleation pathway.

Conferences and Publications

<u>Conferences</u>

IChemE Chemical Engineering Day 2013, Imperial College
Influence of Controlled Fluid Shear on Crystal Nucleation from Solution
25th-26th March 2013

Direct Assembly of Functionalised Nanomaterials 2013, Strathclyde
Effect of Controlled Fluid Shear on Glycine Nucleation from Solution
12th-13th June 2013

North West Chemical Engineering Conference 2013, Newcastle
Effect of Controlled Fluid Shear on Glycine Nucleation from Solution
8th-9th August 2013

British Association for Crystal Growth 2014, Leeds
Influence of Controlled Fluid Shear on the Nucleation of Glycine Solutions
13th-15th July 2014

AIChE Annual Meeting 2014, Atlanta
Influence of Controlled Fluid Shear on Nucleation Kinetics in Glycine Aqueous Solutions
16th-21st November 2014

Nucleation Faraday Discussions 2015, Leeds
Influence of Controlled Fluid Shear on Nucleation Kinetics in Glycine Aqueous Solutions
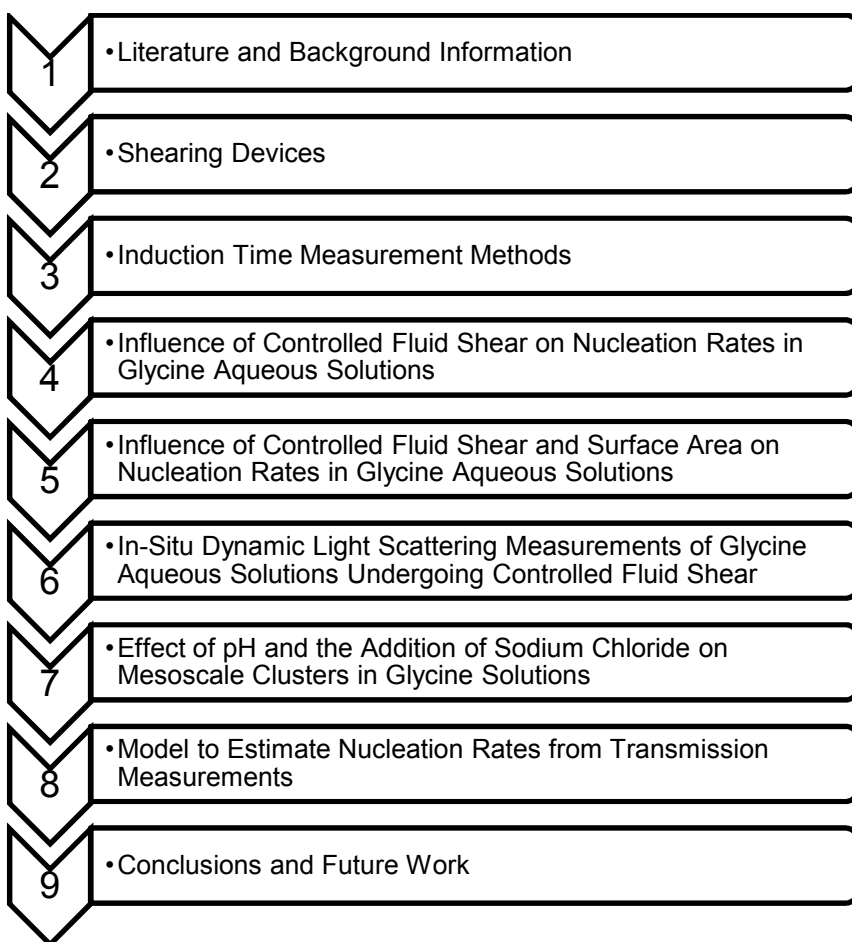30th March-1st April 2015

Papers

1. Forsyth, C., et al., *Influence of Controlled Fluid Shear on Nucleation Rates in Glycine Aqueous Solutions.* Crystal Growth and Design, 2015. **15**(1): p. 94-102.

2. Forsyth, C., et al., *Influence of Controlled Fluid Shear and Surface Area on Glycine Nucleation Rates from Solution.* In preparation, 2015.

3. Forsyth, C., et al., *Effect of pH and Sodium Chloride on Mesoscale Clustering in Glycine Solutions.* In preparation, 2015.

4. Forsyth, C., et al., *Clustering Behaviour in β-Lactoglobulin Solutions at Low Protein Concentrations.* In preparation, 2015.

5. Forsyth, C., et al., *Method of Estimating Nucleation Rates from Transmission Measurements.* In preparation, 2015.

6. Trap, D., et al., *Influence of Controlled Fluid Shear on Urea Nucleation from Aqueous Solution.* In preparation, 2015.

Thesis Layout

This thesis is split into 9 chapters. Chapter 1 provides background theory and literature information relevant to the work done for this thesis. Chapter 2 covers the theory and setup of the flow cells used in the experiments, Chapter 3 describes the methods used to measure induction times, Chapters 4-7 cover the main experimental and data analysis work, Chapter 8 details a basic model that was developed to obtain nucleation rates from transmission measurements and Chapter 9 details the main conclusions that can be drawn from this work, as well as suggestions for future work.

1 • Literature and Background Information

2 • Shearing Devices

3 • Induction Time Measurement Methods

4 • Influence of Controlled Fluid Shear on Nucleation Rates in Glycine Aqueous Solutions

5 • Influence of Controlled Fluid Shear and Surface Area on Nucleation Rates in Glycine Aqueous Solutions

6 • In-Situ Dynamic Light Scattering Measurements of Glycine Aqueous Solutions Undergoing Controlled Fluid Shear

7 • Effect of pH and the Addition of Sodium Chloride on Mesoscale Clusters in Glycine Solutions

8 • Model to Estimate Nucleation Rates from Transmission Measurements

9 • Conclusions and Future Work

1. Literature and Background Information

Chapter 1 contains background theory on crystallisation (with a focus on nucleation), information from literature on the influence fluid shear may have on primary nucleation, examples of methods that can be used to measure nucleation rates and background information on glycine.

2. Shearing Devices

Chapter 2 contains basic theory on Couette and capillary flow, as well as details of the Couette and capillary flow cell setups that were used in the experiments detailed in Chapters 4, 5 and 6 to achieve well controlled flow conditions.

3. Induction Time Measurement Methods

Chapter 3 begins by describing the principles of induction time measurements and different methods that can be used to measure induction times. This is followed by information on the methods used to measure induction times in this thesis (visual monitoring, transmission and scattering measurements and imaging).

4. Influence of Controlled Fluid Shear on Nucleation Rates in Glycine Aqueous Solutions

Chapter 4 details the procedure and results for experiments that were carried out using the capillary and Couette flow cells (detailed in Chapter 2) and induction time measurement methods (detailed in Chapter 3) to investigate the influence of controlled fluid shear on nucleation rates in glycine aqueous solutions. A method of obtaining primary nucleation rates from induction time measurements is described and a detailed statistical analysis, which was done to ensure that the number of repetitions was sufficient for trends to be valid, is outlined.

5. Influence of Controlled Fluid Shear and Surface Area on Nucleation Rates in Glycine Aqueous Solutions

Advancing the work detailed in Chapter 4, Chapter 5 describes work done to investigate the influence that the surface area that solutions were exposed to had on nucleation rates in glycine aqueous solutions. This was achieved by using a range of Couette cell geometries which exposed solutions to different surface to volume ratios (outlined in Chapter 2). The experimental procedure is described and a robust analysis of the results obtained is given. The concept of induction times scaling with

shear rate and surface area is analysed. The chapter ends with a discussion on possible reasoning behind the behaviour seen.

6. In-Situ Dynamic Light Scattering Measurements of Glycine Aqueous Solutions Undergoing Controlled Fluid Shear

Leading on from Chapter 5's possible explanations for the behaviour seen when glycine solutions were exposed to increased shear rates and surface areas, Chapter 6 aims to improve understanding of mesoscale clustering in glycine solutions through in-situ dynamic light scattering measurements of solutions that had been sheared in the Couette cells. The setup and layout of the dynamic light scattering hardware which was used to take in-situ measurements from solution in the Couette cells is described. The dynamic light scattering results and statistical analyses of the results are given. The chapter ends with a consideration of the nucleation pathway and possibility of the coalescence of mesoscale clusters.

7. Effect of pH and the Addition of Sodium Chloride on Mesoscale Clusters in Glycine Solutions

To gain further knowledge of the mesoscale clusters detailed in Chapter 6, Chapter 7 describes dynamic light scattering work that was done to study the influence of pH and the addition of sodium chloride on mesoscale clustering in unsheared solutions. The experimental procedures and results obtained are given and possible explanations are then discussed.

8. Model to Estimate Nucleation Rates from Transmission Measurements

Chapter 8 describes a basic model that was developed to allow nucleation rates to be estimated from transmission measurements.

9. Conclusions and Future Work

In Chapter 9, overall conclusions from the work done in this thesis are given. This is followed by a range of suggestions for future work.

Main Conclusions

The nucleation of glycine in supersaturated aqueous solution was investigated under well-controlled flow conditions at constant temperature using bespoke experimental setups.

Increased shear rates and surface areas led to shorter induction times and hence higher rates of primary nucleation.

Results suggested that shearing can cause the coalescence of mesoscale clusters and the coalesced clusters can lead to a more rapid nucleation pathway.

The concentration of mesoscale clusters was strongly influenced by the pH of the solutions and the presence of sodium chloride.

Contents

1. Literature and Background Information

Chapter Outline and Contents

Crystallisation from solution is vital to many natural and industrial processes. It is widely used for separation and purification in industries such as chemicals, food and pharmaceutical. Nucleation, which is the first step in the formation of a new crystalline solid phase from solution, is of fundamental importance in determining product crystal quality, however, at present it is poorly understood mechanistically. In this chapter, classical nucleation theory is described and the possibility of nucleation taking place through non-classical mechanisms is discussed. Several methods of calculating nucleation rates are described.

In industrial processes, fluid shear is widely encountered, for example through agitation in a vessel, or transport through pipes. The role of fluid shear on the nucleation of compounds from solution is not well understood and the current literature on the area is reviewed.

This chapter also contains information on glycine, the compound studied for all work in this thesis. Areas such as glycine polymorphism and speciation are described.

This chapter covers:

- General theory on crystallisation and classical nucleation theory.
- Information on non-classical nucleation theories.
- A review of previous studies on the influence of fluid shear on nucleation.
- Examples of methods that can be used to estimate nucleation rates.
- Information on glycine behaviour in solution e.g. influence of pH and addition of sodium chloride.

1.1 Introduction

Crystallisation is a purification and separation technique. It is a complex process based on the nucleation and subsequent growth of crystalline substances[1-4]. It is a supramolecular process in which an ensemble of randomly organised molecules, ions or atoms in a fluid come together to form an ordered three-dimensional array (precipitate), known as a crystal[1-4]. The process is non-equilibrium and is driven by differences in chemical potential between the solute in the solution and the solute at equilibrium. A material is said to be crystalline if its constituent molecules, ions or atoms form an infinite three-dimensional array with regular packing i.e. long range order[1-4].

Crystallisation is vital to many natural and industrial processes. It is widely used as a method of product formation and purification in industries such as chemicals, food and pharmaceutical. More than 90% of pharmaceutical products make use of crystalline solids as part of their synthesis[5]. It is generally considered to be the best and least costly method for the production of pure solids from impure solutions and it produces an end product with highly desirable properties. Crystals have good flow and handling characteristics, and they are often aesthetically pleasing. The quality of crystals is typically based on size distribution, purity, morphology and crystal structure[5].

Controlling crystallisation processes to allow manufacturers to produce quality products in a reproducible manner is therefore crucial. In solution crystallisation (solid crystals precipitated from supersaturated solution), nucleation plays an important role in determining crystal quality, particularly with regards to crystal structure and size distribution[5]. Nucleation is the first step in the formation of a new crystalline solid phase from solution. Nuclei are particles of a given solid phase with a sufficient size to be thermodynamically stable in a solution and can grow by incorporating solute molecules from the surrounding solution. Gaining an improved understanding of nucleation is crucial to better design and optimise industrial applications of crystallisation, hence the purpose of the work in this thesis.

1.2 Terminology

1.2.1 Supersaturation

If a solution contains a higher concentration of solute (c) than its equilibrium concentration (solubility) at a given temperature (c_{sat}), the solution is supersaturated and supersaturation is the driving force for crystallisation processes[3].

Supersaturation can be expressed in several ways. The most common are outlined below.

- The concentration driving force (Δc) can be defined as:

$$\Delta c = c - c_{sat} \tag{1.1}$$

- The supersaturation ratio (S) can be defined as:

$$S = \frac{c}{c_{sat}} \tag{1.2}$$

- The relative supersaturation (σ) can be defined as:

$$\sigma = \frac{\Delta c}{c_{sat}} = S - 1 \tag{1.3}$$

It should be noted that these definitions of supersaturation are based on ideal solutions with activity coefficients equal to 1.

1.2.2 Generation of Supersaturation

There are four main methods to generate supersaturation: (1) temperature change, (2) evaporation of the solvent, (3) changing the solvent composition and (4) chemical reaction.

The solubility of most solid materials decreases as the temperature decreases; cooling is therefore often used to generate supersaturation and is the most common method. In some cases, however, the solubility of a material is still high at low temperatures, so this method of generating supersaturation would not be economical. Another issue can be that the solubility changes only very slightly over

the temperature range of interest. In such cases, other methods for the generation of supersaturation can be used[1, 3].

Evaporation is the second most commonly used method for generating supersaturation. For this, solvent is evaporated from the system, therefore increasing the system's concentration (evaporation also causes the system to cool). The method is often used when the solvent is non-aqueous and has a relatively high vapour pressure (high volatility), and if the product is heat sensitive. Evaporation can be done at a constant temperature but in practice, a combination of cooling and evaporation are usually carried out[1, 3].

The mixing of solvents (one of which is a poor solvent for the solute) can lead to a substantial decrease in the solubility of a solute in a solution. This is often known as 'anti-solvent' crystallisation or 'drowning out'[1, 3]. The solute should be soluble in the solvent. The anti-solvent must be miscible with the solute-solvent system, and the solute should be poorly soluble in it[1, 3]. The solubility of the solute is decreased by increasing the fraction of anti-solvent. This method is widely used with organic materials[3]. Mixing is important to avoid local regions of extreme supersaturation[1, 3].

Precipitation is the creation of a solid in a solution during a chemical reaction. Chemical reaction can therefore lead to the generation of supersaturation. Two soluble substances can be added together in a solution and react to form a product with low solubility. Due to the low solubility of the reaction product, its solubility is soon surpassed and the solution becomes supersaturated, with material crystallising (precipitating) out[1, 3]. This method is commonly used in the production of inorganic materials[1, 3]. Again, mixing is crucial and the control of supersaturation is difficult since it involves the control of the mixing of the reactants and/ or the control of the reaction rate[3].

1.2.3 Basic Thermodynamics

The crystallisation process is driven by the difference in chemical potential ($\Delta\mu$) between the solute in the solution (μ_s) and the solute at equilibrium (μ_{sat}), which is in turn related to the difference in supersaturation. The chemical potential at equilibrium is equal to the chemical potential of the crystallising material in crystal form ($\mu_{crystal}$)[6].

$$\Delta\mu = \mu_s - \mu_{crystal} \qquad \text{(1. 4)}$$

If $\Delta\mu > 0$, the solution is supersaturated and crystal nucleation and growth can occur. If $\Delta\mu < 0$, the solution is undersaturated and crystal nucleation and growth cannot occur.

When a solution is in equilibrium, $\Delta\mu = 0$: the chemical potential of the solute in solution is equal to the chemical potential of the solute at equilibrium (and the solid (crystalline) phase).

$$\mu_s = \mu_{crystal} \qquad \text{(1. 5)}$$

For crystal formation, solutions have to be non-equilibrium and supersaturated, where the concentration of solute (c) is greater than the solubility (c_{sat}). Crystallisation occurs to bring the system to equilibrium. Crystal formation results in a drop in the solute's concentration in solution, and crystallisation can occur until the solute's concentration in solution is equal to the solute's solubility[1] .

Chemical potential (μ) can be expressed in terms of a standard chemical potential (μ^o) and an activity (a):

$$\mu = \mu^o + kTln(a) \qquad \text{(1. 6)}$$

Here k is the Boltzmann constant and T is the absolute temperature.

The driving force for crystallisation can therefore be expressed as:

$$\Delta\mu = kTln\left(\frac{a_s}{a_{sat}}\right) \qquad \text{(1. 7)}$$

This can then be expressed in terms of activity coefficients (γ) and concentrations:

$$\Delta\mu = kTln\left(\frac{\gamma_s c}{\gamma_{sat} c_{sat}}\right) \qquad \text{(1. 8)}$$

Assuming that the activity coefficients of the solute in solution and the solute at equilibrium are equal (i.e. they are a weak function of concentration), the driving force for crystallisation can be expressed as:

$$\Delta\mu = kTln\left(\frac{c}{c_{sat}}\right) = kTln(S) \qquad \textbf{(1. 9)}$$

Therefore if $S > 1$, $\Delta\mu > 0$ and crystals may form.

Although it is often assumed that $\frac{\gamma}{\gamma_{sat}} = 1$, in non-ideal solutions (or very precise studies), activity coefficients are often used.

1.2.4 Solution Stability
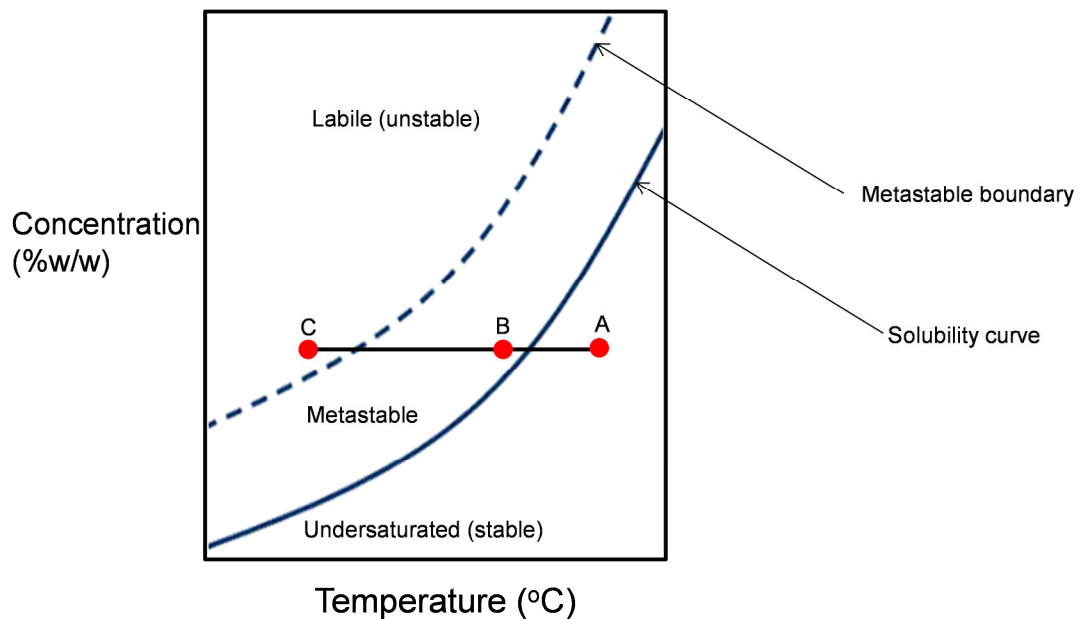
Figure 1. 1
Example solubility curve for 2 phase system with a positive relationship between temperature and solubility.

Figure 1. 1 is an example of a solubility diagram. If a solution is at the concentration and temperature represented by point A, the solution is stable (undersaturated) and crystals will not form. If the solution is cooled to point B, the solution is

supersaturated but in the metastable zone; this means that it is improbable that crystallisation will occur spontaneously due to a barrier that must be overcome. If the solution is cooled further to point C, the solution is supersaturated in the labile region; this means that spontaneous crystallisation is probable, but not inevitable[1]. In the labile region, crystals would typically form quickly without a notable induction time. The metastability of a solution decreases as the supersaturation increases[3]. The reason that metastability occurs is because, according to classical nucleation theory, a critical sized cluster (nucleus) must form before crystal growth will take place. This is explained in more detail in Section 1.3.1.

1.3 Crystal Nucleation from Solution

Crystallisation is a complex process based on the nucleation and subsequent growth of crystalline substances[1-4]. Nucleation is the first step of crystallisation and can be considered as the birth of nuclei. A nucleus is the minimum amount of a new phase capable of independent existence[1-4]. Nucleation involves the formation of clusters, formed when dissolved molecules begin to coagulate (e.g. through concentration fluctuations). Once clusters reach a certain size, they become nuclei and these can act as 'centres' of crystallisation[1-4]. Nucleation is followed by a growth stage which is governed by the diffusion of molecules to the surface of nuclei and the incorporation of these into the structure of the crystal lattice[1-4].

At present, no accurate description of nucleation exists and the design of crystallisation processes is fairly empirical[1-4]. Due to its simplicity, classical nucleation theory (explained in Section 1.3.1) has commonly been applied to solution crystallisation, however, experimental results have shown marked differences to theoretical predictions, suggesting that the application of classical nucleation theory is not always valid[5]. Various other proposals for nucleation mechanisms therefore exist, including a two-step model, which is often thought to be more appropriate for crystallisation processes from solution (see Section 1.3.2)[5].

Nucleation can be affected by many factors such as supersaturation, pH and temperature and it can occur spontaneously or be artificially induced[1]. It can be affected by many external factors such as agitation[7-10], mechanical shock and friction[11-14], electric and magnetic fields[15, 16], electromagnetic radiation (e.g. UV, x-

rays)[17], gravity[18] and ultrasound[1, 19]. The influence of fluid shear on nucleation is discussed in Section 1.4.

Primary and Secondary Nucleation

Nucleation can be classed as primary (Section 1.3.1) or secondary (Section 1.3.3), and primary nucleation can be classed as either homogeneous (Section 1.3.1.1) or heterogeneous (Section 1.3.1.2) [1-4]. Primary nucleation occurs in systems that do not contain any crystals, or when there are crystals present but they do not have any influence on the process[1-4]. On the other hand, secondary nucleation occurs in, and is attributable to, the presence of existing crystals[1-4]. A system nucleates much more readily (at a lower supersaturation) if solute crystals are already present[1].

Homogeneous and Heterogeneous Nucleation

Homogeneous nucleation occurs spontaneously and occurs when there is no influence from an additional material or phase[1-4]. On the other hand, heterogeneous nucleation occurs when foreign particles e.g. surfaces are present. The presence of the foreign particles can greatly affect nucleation[1-4]. The presence of a surface typically reduces the free energy barrier to nucleation (ΔG_{crit}) and critical cluster sizes for nucleation, resulting in enhanced nucleation and allowing it to occur more readily at a lower supersaturation[1-4].

1.3.1 Primary Nucleation- Classical Nucleation Theory

Classical nucleation theory is the simplest and most widely used theory to describe nucleation[5]. The thermodynamic description of the process was developed by Gibbs at the end of the 19th century[5]. It was derived for the condensation of a vapour into a liquid but has been applied elsewhere.

When applied to solution crystallisation, the theory is based on the idea that for a nucleus to form, constituent molecules must coagulate, resisting the tendency to redissolve, until they reach a critical, stable size forming a nucleus that can then undergo crystal growth[1-4].

The transfer of solute from the solution to crystals is driven by the change in Gibbs free energy. The free energy change for creating a cluster can be thought of as a

trade-off between the system forming stable solid (volume) and the penalty of producing extra solid-liquid interface (surface) [1-4]. Therefore, the free energy change for creating a cluster (ΔG) can be summarised written as follows:

$$\Delta G = \Delta G_V + \Delta G_S \qquad \textbf{(1. 10)}$$

ΔG_V is the volume free energy change required for the phase transformation and describes the spontaneous tendency of a saturated solution to produce a solid state. Since the solid state is more stable than the liquid, the term is negative and decreases the free energy of the system.

ΔG_S is the surface free energy change and describes the effect of introducing a solid-liquid interface. The term is positive since free energy increases in an amount proportional to the surface area of the clusters [5].

The free energy change ($\Delta G(n)$ (joules)) to form a cluster of n molecules can be found from thermodynamics [1-4]. It is defined as the difference between the free energy of the system in its final and initial states (before and after cluster formation) [1-4]. If n molecules are assembled into an n-sized cluster, the free energy change if the cluster was part of the bulk crystal would be $-n\Delta\mu$. The free energy decreases since molecules are more stable in the cluster than in solution (negative sign).

An additional term that accounts for the presence of the crystal surface (interface between cluster and solution) must be accounted for as the molecules at the interface have different properties from the bulk crystal [20]. The term for this is positive since it leads to an increase in free energy.

Therefore,

$$\Delta G(n) = -n\Delta\mu + \phi(n) \qquad \textbf{(1. 11)}$$

Here, $\phi(n)$ is the total surface energy of the cluster.

9

1.3.1.1 Homogenous Nucleation

For homogenous nucleation, it is assumed that nucleation takes place in the volume of ideally pure solutions (solutions contain solvent and solute molecules only). Since $\phi(n)$ is equal to the total surface energy of the cluster, it can be expressed in terms of the cluster's surface area ($A_c(n)$) and the interfacial tension/ surface energy (γ) [1-4]:

$$\phi(n) = A_c(n)\gamma$$
(1. 12)

The surface area can be expressed in terms of a shape coefficient (β) and the number of molecules in the cluster n [4]:

$$A_c(n) = \beta n^{2/3}$$
(1. 13)

For spheres:

$$\beta = (36\pi v^2)^{1/3}$$
(1. 14)

Here v is the molecular volume.

For cubes:

$$\beta = 6v^{2/3}$$
(1. 15)

Using Eqn. (1. 9), Eqn. (1. 12) and Eqn. (1. 13), the free energy change required for cluster formation (Eqn. (1. 11)) can therefore be expressed as:

$$\Delta G(n) = -nkT\ln(S) + \beta\gamma n^{2/3}$$
(1. 16)

Since the volume and surface terms have opposite signs, the free energy change required for cluster formation goes through a maximum, as shown in Figure 1. 2.

The maximum can be found from $\frac{d\Delta G(n)}{dn} = 0$ and represents the free energy barrier that must be overcome for nucleation to occur.

$$\frac{d\Delta G(n)}{dn} = -kT\ln(S) + \frac{2}{3}\beta\gamma n^{-\frac{1}{3}} = 0 \qquad \textbf{(1. 17)}$$

Rearranging for n:

$$n = n^* = \left(\frac{2\beta\gamma}{3kT\ln(S)}\right)^3 \qquad \textbf{(1. 18)}$$

Here, n is equal to the critical nucleus size, n^*.

For spheres:

$$n^* = \frac{32\pi}{3}v^2\left(\frac{\gamma}{kT\ln(S)}\right)^3 \qquad \textbf{(1. 19)}$$
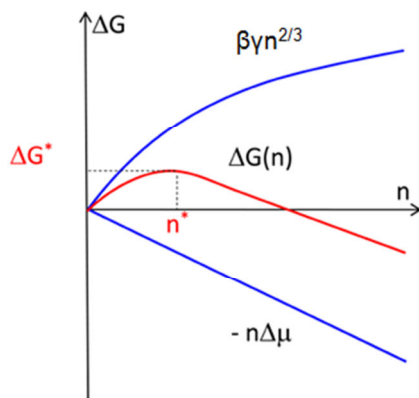
Figure 1. 2
Free energy diagram for nucleation[21]. Here n is the number of molecules per cluster.

These terms for n^* can be substitued into Eqn. (1. 16) to obtain terms for the critical free energy change (ΔG_{crit}) .

$$\Delta G_{crit} = \frac{4}{27}\left(\frac{\beta^3\gamma^3}{k^2T^2\ln^2(S)}\right) \qquad \textbf{(1. 20)}$$

For spheres:

$$\Delta G_{crit} = \frac{16\pi}{3}\left(\frac{v^2\gamma^3}{k^2T^2\ln^2(S)}\right) \qquad \textbf{(1. 21)}$$

The behaviour of a cluster therefore depends on its size. It can either grow or dissolve but whichever process takes place should result in a decrease in free energy. From Figure 1. 2, the surface free energy dominates at small cluster sizes and the total free energy increases initially with cluster growth. Small clusters in the solutions therefore typically dissolve. As the cluster size increases, the volume free energy term becomes more influential and the total free energy change goes through a maximum at a critical cluster size (n^*). As the cluster size increases beyond its critical size, the total free energy continuously decreases. This means cluster growth becomes energetically favourable and particles larger than the critical size will continue to grow.

From Eqn. (1. 18) and Eqn. (1. 20), it can be seen that as the supersaturation increases, the nucleation barrier (ΔG_{crit}) and the critical cluster size (n^*) decrease, reducing metastability.

1.3.1.2 Heterogeneous Nucleation

It is widely accepted that true homogenous nucleation is uncommon and heterogeneous nucleation is the most likely[1]. With heterogeneous nucleation, nucleation takes place in solutions that contain impurity molecules and/ or foreign microparticles or substrates where crystallising material can adsorb[4]. These essentially catalyse the nucleation and the overall free energy change for heterogeneous nucleation is therefore less than the corresponding free energy change for homogeneous nucleation, meaning that nucleation can occur more

readily at supersaturations lower than those required for homogeneous nucleation, as mentioned in Section 1.3.1[1]. The extent of the reduction in free energy depends on how well the catalysing body mimics the structure of the crystallising material[2].

The shape of a cluster that has formed through heterogeneous nucleation on a solid surface is usually approximated to be that of a spherical cap with wetting angle, θ. For spherical caps, the nucleation is 3D- the cluster changes size in all directions, as with homogeneous nucleation[20].

As shown before, the surface tension (γ) is important in controlling nucleation. For heterogeneous nucleation, γ is replaced by an effective surface tension , γ_{ef}.

$$\gamma_{ef} = \psi^3(\theta)\gamma$$

(1. 22)

Here, ψ is a factor that depends on the wetting angle.

$$\psi(\theta) = \frac{(2 + \cos(\theta))\,(1 - \cos(\theta))^2}{4}$$

(1. 23)

The wetting angle is defined from $0°$ to $180°$. When $\theta = 0^o$, complete wetting is said to have occurred and $\psi = 0$. When $\theta = 180^o$, complete non-wetting is said to have occurred and $\psi = 1$ (i.e. homogeneous nucleation).

When $0^o < \theta < 180^o$, incomplete wetting is said to have occurred and $0 < \psi < 1$.

Therefore, for homogeneous nucleation $\gamma_{ef} = \gamma$ and for heterogeneous nucleation, $\gamma_{ef} < \gamma$.

The better the wetting, the smaller the θ and the smaller the γ_{ef}; therefore the critical nucleus sizes and free energy changes required for nucleation are smaller. The case of compete wetting with $\gamma_{ef} = 0$ corresponds to the case of a saturated solution being seeded with crystals (see Section 1.3.3) i.e. the formation of nuclei is not required, as $\Delta G_{crit} = 0$ (see Eqn. (1. 20)).

Eqn. (1. 16) can be adapted to express the free energy change for heterogeneous nucleation:

$$\Delta G(n) = -nkT\ln(S) + \beta\gamma_{\text{ef}}n^{2/3}$$ **(1. 24)**

1.3.1.3 Nucleation Rates

The primary nucleation rate (J) is the number of crystals created per unit volume per unit time. From related kinetic theory for thermally activated processes, the steady state rate of nucleation can be deduced through an Arrhenius reaction rate equation[1, 4]:

$$J = Ae^{-\frac{\Delta G_{crit}}{kT}}$$ **(1. 25)**

Here, A is a pre-exponential factor, which is difficult to measure[1, 4]. It is related to the rate of attachment of molecules to the critical nucleus. It therefore depends on molecular mobility[22] and since this is strongly affected by temperature, the pre-exponential factor can be highly temperature dependent.

Terms for the Gibbs free energy change corresponding to the critical nucleus size e.g. Eqn. (1. 20) can be substituted in:

$$J = AS \exp\left(-\frac{4}{27}\left(\frac{\beta^3\gamma^3}{k^3T^3\ln^2(S)}\right)\right)$$ **(1. 26)**

This suggests that temperature, supersaturation and interfacial tension are the main factors that govern nucleation rates. Since the temperature affects supersaturation, it is particularly important. If experiments to determine nucleation rates are carried out for a range of supersaturations or temperatures, Eqn. (1. 26) can be linearised and values for the pre-exponential and interfacial tension can be estimated from nucleation rates[1, 23]. Nucleation rates can be approximated from induction time measurements, as detailed in Chapter 3.

The effect of supersaturation on the nucleation rate is shown in Figure 1. 3. It indicates that a rapid increase in nucleation rate occurs once a critical supersaturation level has been reached[1, 4]. As mentioned, increasing the supersaturation reduces the size of the critical nucleus and therefore free energy barrier. Increasing the temperature results in smaller critical nuclei and lower free energy barriers as shown in Figure 1. 4.
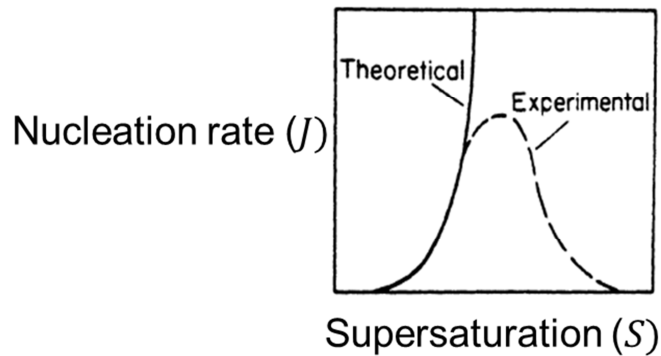
Figure 1. 3
Effect of supersaturation on nucleation rates. Often experimental results do not match theoretical predications, as shown[1].
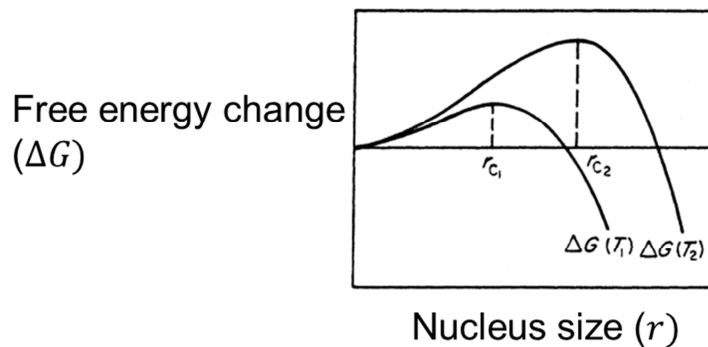
Figure 1. 4
Effect of temperature (T) on the critical nucleus size and free energy change required for a critical nucleus (T$_1$>T$_2$)[1].

Nucleation rates are often written in the following form (Becker-Doering relation[1, 3]), where k_n and b are values based on experimental results. b is typically between 5 and 10 for organic systems.

$$J = k_n \Delta c^b$$

(1. 27)

1.3.1.4 Classical Nucleation Assumptions and Shortcomings

Classical nucleation theory is based on several assumptions[5]. These simplify the theory but restrict its applications. Some of the major assumptions are given below.

- Clusters are assumed to be spherical with uniform densities/ compositions and sharp interfaces. Droplet density is assumed independent of droplet size and is taken as equal to the macroscopic density of the bulk condensed phase. From a crystallisation from solution viewpoint, these assumptions mean that the arrangement of a crystal's nucleus is identical to that of a large crystal.
- The surface tension is assumed to be unaffected by the size/ curvature of a cluster. Surface tension is assumed to be temperature independent, which is not the case.
- Clusters are assumed to grow by the addition of one monomer at a time. Collisions between more than two particles or two clusters are ignored. Fragmentation of pre-existing clusters into more numerous, smaller clusters is ignored. Therefore clusters are assumed to be at rest and do not undergo motion.
- The stationary size distribution of clusters is assumed to be established instantly after the solution becomes supersaturated.
- The nucleation rate is assumed constant i.e. steady-state kinetics.
- Clusters are assumed incompressible and surrounded by an ideal gas at constant pressure. Cluster formation therefore does not change the vapour state.

Shortcomings

Due to the assumptions made, there are several problems with classical nucleation theory. Here, various major problems are summarised[5]:

- In the case of condensation experiments, all of the inputs to classical nucleation theory should be known with high accuracy, so discrepancies found between experimental and theoretical values suggest inadequacy of classical nucleation theory.

- The assumption of uniform composition in clusters is inaccurate since enrichment effects have been found to occur at the surface of droplets e.g. ethanol-water clusters[24].

- The steady-state nucleation rate is based on an unchanging size distribution of clusters with time, leading to a constant rate which would imply the number of nuclei would increase linearly with time.[25] This, however, fails at the start of the process since a transition time is required to establish a steady-state cluster distribution[26]. In some instances, a steady-state nucleation rate is never reached.

- The assumption of clusters growing only through the addition of monomers is unlikely and cluster-cluster interactions (e.g. collisions between two clusters) have been found to play an important role[27].

- The pre-exponential factor cannot be accurately predicted. It is related to molecular mobility but classical nucleation theory assumes no movement of clusters occurs.

- The macroscopic description of a liquid drop is not valid for small nuclei (<50 molecules) [28, 29].

- Clusters with fewer than 100 molecules cannot be accurately described by the classical nucleation theory surface tension concept, and they also cannot be approximated as spheres[30, 31] .

- For small clusters, the assumption of the molecular arrangement being identical to that of crystals cannot be accurate since e.g. with lysozyme, small clusters of 1-10 molecules cannot take the shape of a tetragonal lysozyme crystal[32].

- Size is taken as the only criterion on whether clusters become nuclei or not, which is not the case. It does not distinguish between organised clusters or clusters where the constituent molecules are not organised into their orientation in a crystal.

- Classical nucleation theory often overestimates the nucleation rates by several orders of magnitiude[6].

1.3.2 Non Classical Primary Nucleation Hypotheses

Due to inadequacies with classical nucleation theory, alternative nucleation theories have been proposed. These often involve the role of clusters of molecules in a two-step mechanism[6, 32].

The two-step mechanism suggests that solute molecules first assemble to form dense, liquid-like mesoscale clusters[33]. A second step then involves the reorganisation of these clusters (once they reach a critical size) into ordered crystalline nuclei arrangements [5, 17, 34-38]. The crystal nuclei therefore form inside the clusters. These steps are shown diagrammatically in Figure 1. 5.

This pathway is thought to consist of at least two energy barriers: the first is associated with cluster formation, while the second is for the transformation of the disorganised clusters into crystalline nuclei. The rate determining step is thought to vary due to the role of viscosity within the liquid droplet affecting the kinetics of forming the ordered solid phase[39]. Generally studies have found that the second stage is rate determining[40].
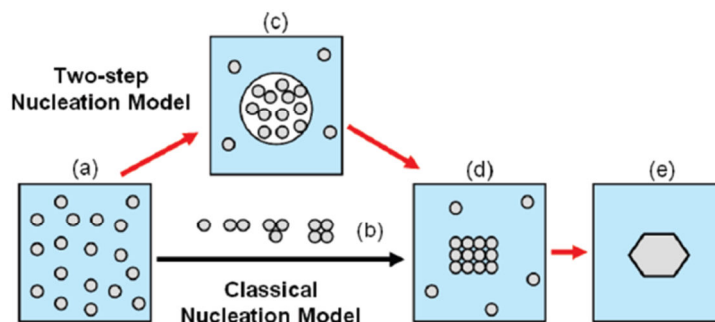
Figure 1. 5
Possible mechanisms (two-step mechanism and classical nucleation) that lead to solid crystal from solution [5].
a= supersaturated solution; b= ordered subcritical cluster of solute molecules; c= liquid-like cluster of solute molecules; d= ordered crystalline nuclei; e= solid crystal

Evidence for the two-step mechanism has been found for a wide range of crystallisation processes. For example:

- Mesoscale clusters of dense liquid were found to exist in lysozyme solutions and crystal nuclei then formed within these clusters[6, 41].

- The two step-mechanism was found to occur in the nucleation of amyloid fibrils of various proteins and peptide fragments, for example with the amyloid beta peptide associated with Alzheimer's disease and the yeast prion protein[42, 43].

- Metastable dense liquid clusters were found to act as precursors to ordered nuclei of haemoglobin polymers[44-46].

- Particularly strong evidence for the two-step mechanism comes from studying colloids. Scanning confocal microscopy of nucleation of crystals in colloidal solutions showed that the formation of crystal nuclei occurred within dense, ordered fluid regions of the solutions[47, 48].

- Amorphous or liquid clusters of calcium and carbonate ions were found to be present in calcium carbonate solutions and facilitate the nucleation of calcite crystals in a manner similar to the mechanism found for lysozyme solutions[49-52].

- Strong evidence for a two-step mechanism comes from non-photochemical laser induced nucleation of glycine and urea. Exposure to laser light caused these small organic molecules to nucleate faster than control solutions[17, 53-55]. This was thought to be due to the electric field of the light aligning pre-nucleation clusters, therefore reducing the barrier for crystal lattice formation. If classical nucleation was true, the alignment of molecules would not have had a significant effect on results since the clusters would already be accordingly ordered.

- Laser light was found to induce different polymorphs of glycine, depending on the laser's polarisation (circular polarisation produced the α form, while linear polarisation produced the γ form)[54]. This emphasised the stage of alignment within the clusters.

- Small angle x-ray studies on glycine solutions have indicated that glycine dimers form mass fractal aggregates in supersaturated solutions, which are then transformed into surface fractal structures, prior to nucleation. The transformation was attributed to the organisation of disordered liquid-like

structures into more ordered lattice structures. This therefore supported the two-stage model[38].

It is worth noting that experimental results are supportive through various techniques including dynamic light scattering, static light scattering, small angle x-ray scattering, differential scanning calorimetry, electrodynamic levitation and non-photochemical laser induced nucleation[17, 26, 32, 38, 53, 54, 56-58]. The two-step mechanism has also been supported by several computer simulations [35, 36, 59-61], as well as theoretical studies[59, 62-65].

For the two-step mechanism to be valid, disordered liquid or amorphous metastable clusters must be present in solutions prior to nucleation. Clustering behaviour has been found to occur in a wide range of solutions as mentioned above, from proteins such as lysozyme[6, 41] to smaller molecules such as urea and glycine[17, 53, 54, 66]. There is therefore a lot of evidence that mesoscale clustering and associative behaviour is widespread so many solutions cannot be considered as homogenous, random mixtures of solute and solvent. This adds further support for the two-step nucleation pathway, however, it is likely that not all solutions will support the existence of clusters so other nucleation mechanisms may also occur[6].

1.3.3 Secondary Nucleation

Unlike primary nucleation which occurs in systems that do not contain any crystals (or the crystals have no influence on the process), secondary nucleation occurs in, and is attributable to, the presence of existing crystals. For secondary nucleation, new crystals are induced only due to the prior presence of the material being crystallised. When seed crystals are present, nucleation can generally occur readily at much lower supersaturations than primary nucleation and even heterogeneous nucleation (the presence of seed crystals effectively corresponds to the case of heterogeneous nucleation with complete wetting, see Section 1.3.1.2)[2, 4].

A number of mechanisms can cause secondary nucleation. Often if dry seed crystals are placed in a supersaturated solution, they will shed particles of crystalline dust that has been adhering to their surfaces. These shed crystalline particles are considered to be secondary nuclei and can become centres of growth. Crystals with

needle or dendrite structures can be fragile and secondary nuclei may form from small parts breaking off of these[1]. It is also known that shear forces can cause secondary nucleation. Shear forces imposed on a crystal face can be sufficient to produce secondary nuclei from the crystal surface[1, 2]. Secondary nucleation occurs most commonly by contact nucleation. This occurs due to contact between the crystals and objects such as the walls of the container, stirrers, pumps or even other crystals[2].

1.3.4 Nucleation in Polymorphic Systems

A system is said to exhibit polymorphism if it is capable of crystallising into different, but chemically identical, crystalline forms[1]. It is widely accepted that most substances can exist in two or more solid phases, provided experimental conditions are suitable. Each polymorph will have a unique combination of physical, thermal and mechanical properties, so being able to control polymorphism is desirable in chemical manufacturing[1, 2].

Ostwald's Rule of Stages is a generalised rule based on observing the nucleation of many systems and it postulates that a crystallising system progresses from the supersaturated state to equilibrium in stages. Each stage represents the smallest possible free energy change. This means that for a polymorphic system, each possible polymorphic structure would form before the most stable phase would appear. This generally means that the least stable polymorph would crystallise first. This is not a universal law and polymorphism is still not fully understood[1, 2].

1.3.5 Crystal Growth

When a crystal surface is exposed to a supersaturated environment, the flux of growth units (solute atoms, molecules or ions) will exceed the equilibrium flux. This means that there will be a net increase in the number of growth units joining the crystal and the surface will grow. Crystal growth is influenced by the mass transfer of solute from the bulk of the solution to the crystal-solution interface of the growing crystal and the incorporation of the solute into the crystal lattice. Due to mass transfer resistance, the concentration at the crystal-solution interface is less than in bulk solution.

1.4 Influence of Fluid Shear on Primary Nucleation

As mentioned in Section 1.3, primary nucleation can be affected by many factors such as supersaturation, pH and temperature. It can also be affected by many external factors such as agitation[7-10], mechanical shock and friction[11-14], electric and magnetic fields[15, 16], electromagnetic radiation[17], gravity[18] and ultrasound[1, 19]. In industrial processes, fluid shear is widely encountered, for example through agitation in a vessel, or transport through pipes. Fluid shear is known to have an effect on secondary nucleation, but the effect that fluid shear can have on primary nucleation from solution is not well understood to date, particularly for small organic molecules. More progress has been made on the influence shear can have on the crystallisation of larger protein molecules or polymers, but the effects are still unclear. The research done in this thesis is therefore of value as the nucleation of glycine, a widely investigated molecule, is studied using well characterised flow systems (Couette and capillary flow) over a wide range of conditions.

The use of mechanical stimuli to influence nucleation dates back to the early 20th century when experiments were carried out that showed the critical supercooling could be reduced by striking an anvil placed in a supersaturated solution[11-14]. During the 1960s, systematic studies of the influence of mechanical agitation on nucleation were carried out on aqueous salt solutions[7-9]. It was found that increased agitation rates increased the rate of nucleation up to a point, where it then started to decrease again. This was thought to be due to a trade-off between agitation enhancing mass transfer and therefore nucleation, and agitation enhancing the attrition of clusters and hampering nucleation.

Shear has been found to have a strong influence on the crystallisation of synthetic polymers, such as polyethylene and polypropylene. Shear was found to affect not only nucleation and growth kinetics, but morphology as well[67, 68]. The enhanced nucleation observed suggested that shear may have induced some form of ordering in the system, therefore facilitating crystal nucleation [69-72].

There have been a small number of studies on the effect that fluid shear can have on the nucleation of protein molecules, and the impact of shear on nucleation is not always clear cut in literature and depends strongly on the nature of the crystallising system and method of applying shear. The effect of controlled shear rates between 10^{-3} s^{-1} and 10^{-1} s^{-1} on the nucleation of a various proteins (ferritin, apoferritin and lysozyme) was investigated. Rotational flow, induced by applying an electric field to a droplet, was found to influence the nucleation process[73]. Lysozyme nucleation was enhanced by all shear rates studied, while the nucleation of ferritin and apoferritin was found to be suppressed or enhanced depending on shear rate. These results were thought to be due to flow helping or suppressing the formation of ordered nuclei within the dense liquid clusters[74] thought to exist according the two-step nucleation model[32]. Oscillatory flow in capillary tubes, resulting in maximum shear rates between 0.23 s^{-1} and 0.62 s^{-1}, was shown to affect the nucleation of insulin[75]. A large increase in nucleation was seen with increased flow rates compared to stationary conditions and the yield for flow conditions could reach twice that of stationary. Flow therefore affected the number and size of crystals formed. Capillary flow (shear rates up to 14 s^{-1}) was found to enhance the growth of lysozyme crystals resulting in improved yield compared with stationary conditions, however, the flow conditions did not appear to affect the rate of nucleation[76].

The impact of shear on protein nucleation is therefore not clear, for example, although shear was found to promote nucleation of lysozyme in the rotational flow experiment system[73], lysozyme nucleation was not enhanced by capillary flow[76]. Lysozyme nucleation was also not enhanced for the case for anti-solvent induced lysozyme crystallisation undergoing oscillatory shear in a Linkam Cambridge Shear System with a maximum shear rate of 47 s^{-1}. In such systems interfacial (protein-precipitant) instabilities, with regions of elevated supersaturation, appeared to play an important role in nucleation[77]. Shear was found to reduce the formation of these interfacial instabilities, and nucleation was reduced. Similar conclusions regarding the detrimental effect shear can have on interfaces have been made in other work[78], where it was found that thaumatin nucleation in microcapillaries was reduced at increased flow rates due to the reduction of the interface's lifetime. Literature on the crystallisation of colloids also often shows conflicting results. Several reports suggest that shearing can enhance the crystallisation of colloids[79-81], while others

report that it can significantly suppress it[82-84]. Studies have found that shear can induce crystallisation in oscillatory flow, but not steady flow[79].

Literature on the nucleation of low to medium molecular weight organic compounds under flow conditions is very limited, as mentioned. Agitation by a magnetic stirring bar has been reported to enhance the primary nucleation of various small organic compounds under certain conditions, including glycine[85] (see Section 1.5), L-glutamic acid[86], butyl paraben[87], m-hydroxybenzoic acid[88] and carbamazepine[89], however, shear rates are difficult to quantify in such an arrangement due to irregular motions and interactions of the stirring bar with the bottom of the vial. In some cases, for example butyl paraben[87], once a certain rotational rate was reached, nucleation rates were no longer enhanced so significantly. Shear imposed by mixing has been found to enhance nucleation in some systems of small organic molecules, for example with the anti-solvent nucleation of DL-valine[66]. Fluid shear can also influence the polymorphic outcome, for example with carbamazepine[89] and m-hydroxybenzoic acid[88].

In order to study effects of fluid flow on nucleation in a more systematic and quantitative way, well-controlled and ideally uniform flow fields are clearly advantageous. An example of a well-controlled and quantifiable shear flow is cylindrical Couette flow. Nucleation studies using such a flow have shown that increased shear rates (up to to 190 s^{-1}) led to higher nucleation rates of butyl paraben[87] and m-hydroxybenzoic acid[88].

Reasons behind the role that fluid shear has on nucleation are unclear. Fluid shear could potentially enhance molecular alignment[6, 67, 73], cluster aggregation[49, 85, 87] or mass transfer[7-9], resulting in higher nucleation rates[85, 87]. This is discussed in more detail in Chapter 5 and Chapter 6. Fluid shear can also have a large impact on interfaces in some systems[77, 78].

1.5 Glycine Solution Behaviour

Glycine is the simplest and smallest amino acid (NH_2CH_2COOH) and has been widely studied due to its molecular simplicity. This section summarises some main characteristics of glycine, such as its polymorphs, behaviour under acid or basic conditions, behaviour in solutions with sodium chloride, possible molecular clustering in glycine solutions and the effect of fluid shear on glycine crystallisation.

1.5.1 Glycine Speciation

Glycine contains both a carboxylic acid and an amine (base) group as shown in Figure 1. 6. It is amphoteric, meaning it can react as an acid (proton donator) or as a base (proton acceptor). The pKa values for the acid and amine groups are given in Table 1.1. The isoelectric point (pH at which a molecule carries no net electrical charge) is 5.97[90].
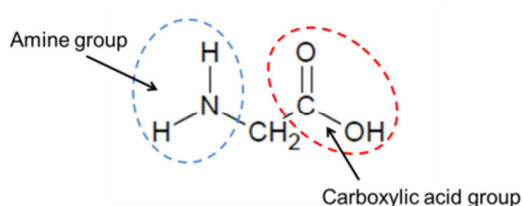
Figure 1. 6
Glycine structure showing the carboxylic acid and amine groups.

Table 1.1

pKa value of acid and amine groups

Group	pKa[91]
Carboxylic acid	$pK_{a1} = 2.34$
Amine	$pK_{a2} = 9.60$

In aqueous solution, glycine can generally exist in three forms (anion, cation or zwitterion), as shown in Figure 1. 7. The relative amounts of each of these that form depends on the pH of the solution, as show in Figure 1. 8, and this is thought to influence polymorph formation, which is outlined in Section 1.5.2. The pH also has

an effect on solubility, with the solubility increasing significantly at high and low pH[92-94].
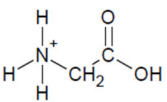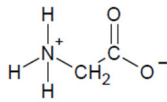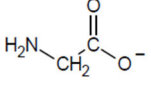
Cation	Zwitterion (neutral molecule with positive and negative electrical charge)	Anion

Figure 1. 7

Glycine structure in cation, zwitterion and anion forms.
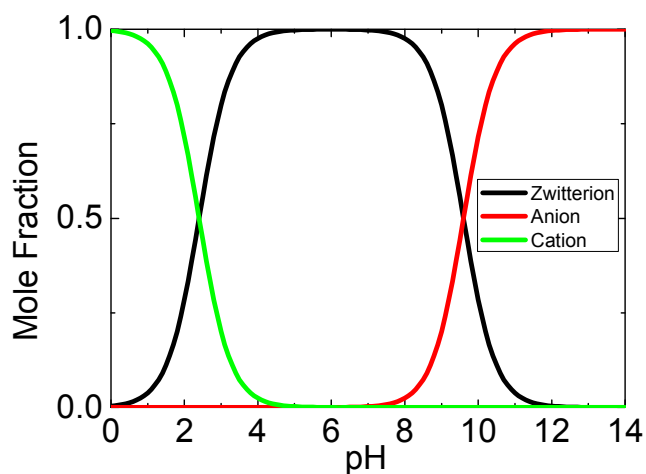
Figure 1. 8

Effect of pH on mole fractions of glycine anions, cations and zwitterions. More information on glycine speciation and how Figure 1. 8 was calculated is given in Chapter 7 Section 7.1.2

Close to its isoelectric point, glycine exists in zwitterionic form. At low pH, glycine zwitterions can be protonated and form cations (Eqn. (1. 28)), while at high pH, glycine can be deprotonated and form anions (Eqn.(1. 29)). The acid dissociation constants for each equation are given in Eqn. (1. 30) and Eqn. (1. 31).

$$H_3N^+CH_2COOH(aq) \leftrightarrow H_3N^+CH_2COO^-(aq) + H^+(aq)$$ **(1. 28)**

$$H_3N^+CH_2COO^-(aq) \leftrightarrow H_2NCH_2COO^-(aq) + H^+(aq)$$ **(1. 29)**
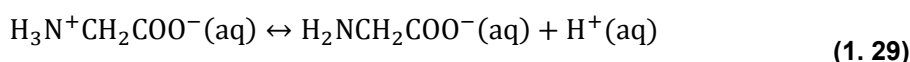
$$K_{a1} = \frac{[H_3N^+CH_2COO^-][H^+]}{[H_3N^+CH_2COOH]}$$ **(1. 30)**

$$K_{a2} = \frac{[H_2NCH_2COO^-][H^+]}{[H_3N^+CH_2COO^-]}$$ **(1. 31)**

1.5.2 Glycine Polymorphs

Under ambient conditions, glycine has three polymorphic forms- α, β and γ [90, 95-98]. The thermodynamic stability under ambient conditions in neutral solutions is γ > α > β [95]. α-glycine is centrosymmetric (non-polar) and is made from sheets of hydrogen-bonded cyclic zwitterion dimers [17, 90, 95, 99] (see Figure 1. 9). Despite not being the most stable form, α-glycine crystallises out of aqueous glycine solutions at its natural isoelectric pH (5.97). γ-glycine never appears under these conditions, despite its thermodynamic stability[90]. γ-glycine is polar and is made from open polar chains of glycine zwitterions that are connected head-to-tail by hydrogen bonds[95, 99] (see Figure 1. 9). γ-glycine , can be crystallised by several methods, for example, changing the pH of the system[90], using additives such as sodium chloride [95, 96, 98, 100-102] or through non-photochemical laser induced nucleation[17, 37]. These are mentioned in more detail below. The γ-glycine polymorph has been shown to convert to the α-glycine polymorph by heating to temperatures well above ambient (~165°C), suggesting the order of stability may change with temperature[96].
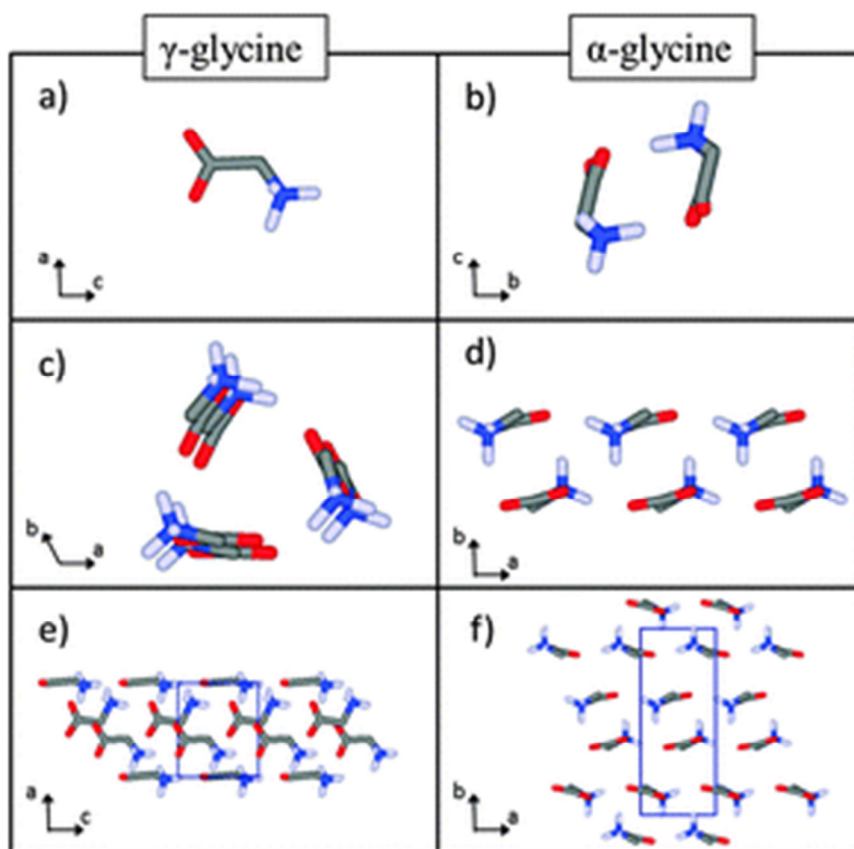
Figure 1. 9
Details of the crystal structures of γ-glycine and α-glycine[103].

(a) zwitterionic monomers: the building block of γ-glycine, (b) hydrogen-bonded cyclic dimers: the building block of α-glycine, (c) helical chain around the 3-fold screw axes, parallel to the *c*-axis: packing of γ-glycine and (d) hydrogen-bonded molecular bilayers of centrosymmetric dimers: packing of α-glycine. (e) and (f) show the packing of α-glycine and γ-glycine.

β-glycine is the least stable form of glycine and is unstable under ambient conditions[96]. Structurally it is similar to α-glycine (hydrogen bonded layers) but is polar, rather than centrosymmetric[90, 95 99, 104]. It can be made to crystallise through various methods that result in high supersaturation, for example through antisolvent crystallisation from ethanol-water and methanol-water mixtures or freeze drying[17, 38, 96, 104-107]. It has been found to transform rapidly into α-glycine in air or water, but the crystals remained unchanged if kept in a dry environment[104]. Since the work carried out here is based on ambient conditions, β-glycine is not considered further.

28

Influence of pH on Glycine Solution Behaviour

γ-glycine can be crystallised by changing the pH of the system to <3.8 or >8.9[90]. From literature, it remains unclear as to why pH affects the polymorphic outcome of glycine, particularly why the less stable α-glycine forms in conditions close to neutral. As mentioned, α-glycine is centrosymmetric and is thought to be made from sheets of hydrogen-bonded cyclic zwitterion dimers [17, 90, 95, 99]. It had been thought that cyclic zwitterion dimer units, like those which make up α-glycine, were the most prevalent structures in close to neutral aqueous glycine solutions, so the prevalence of these cyclic dimers in solution was thought to lead to facile nucleation of α-glycine (these cyclic dimer structures are not found in β- or γ-glycine)[108].

Speciation shows that when the pH is moved away from the region of the isoelectric point, charged glycine anions and cations form and these charged glycine molecules would not form cyclic dimers, therefore reducing the population of the suspected α-glycine growth units. This could be thought of as a reason why α-glycine does not form preferentially under certain pH conditions. It, however, is unlikely to be the main reason as the transition to γ-glycine occurs when the fraction of anions/ cations is fairly small- the decrease in number of dimers would likely to be very modest (~7%)[90].

A 'self-poisoning' mechanism is currently associated with the influence of pH on glycine polymorph formation[90, 93]. For this, the cations that occur at low pH, and anions that occur at high pH, act as foreign species and join onto faces of α-glycine. In doing so, they inhibit α-glycine growth and result in γ-glycine forming preferentially.

Another study[93] suggests that in acid/ basic conditions, glycine organises itself differently than in the more neutral conditions where it form cyclic dimers. In acid/ basic conditions, the glycine cations or anions induce glycine to form head-to-tail open chains, and they undermine the formation of cyclic dimers. The open head-to-tail chains structurally match the head-to-tail linear chains in γ-glycine's crystal structure and may act as nucleation precursors and building blocks for γ-glycine.

Influence of Sodium Chloride on Glycine Solution Behaviour

Additives can be used to induce γ-glycine crystallisation, for example sodium chloride[99, 102]. γ-glycine can also be crystallised using racemic hexafluorovaline, deuterium, acetic acid or ammonia solutions. They are generally thought to act as inhibitors to α-glycine formation[95, 96, 98, 100-102].

The role of sodium chloride in promoting the formation of γ-glycine over α-glycine is not well understood. It has been postulated that the presence of electrolytes can modify the packing arrangement of glycine molecules[102]. This is a result of Coulombic interactions between the ions and glycine molecules. Cyclic dimers, which are the growth units of α-glycine, may be disrupted by the presence of sodium chloride, while the formation of head-to-tail open chains, which are the growth units of γ-glycine, may be promoted[102]. The sodium chloride may contribute to an ionic atmosphere which results in the charging and aligning of glycine molecules to a head-to-tail chain arrangement. It has also been suggested that an increased ratio of charged glycine molecules to zwitterions is important for γ- glycine nucleation [102].

Computational studies have shown that the addition of sodium chloride alters the structure of polar γ-glycine nuclei[99]. When in pure aqueous solution, the γ- glycine nucleus was found to develop a melted layer of amorphous glycine around the nucleus; the addition of sodium chloride was found to result in a double layer forming that stabilised the γ-glycine nuclei and eliminated the surface melted layer[99]. On the other hand, non-polar α-glycine nuclei were largely unaffected by the presence of sodium chloride. The addition of sodium chloride was also found to affect the surface tension of α-glycine and γ-glycine nuclei- when 80 mg/ml was added, the interfacial free energy of a γ-glycine nucleus decreased by 7.7 mJ/m^2, suggesting it became more stable, while the interfacial free energy of a α-glycine nucleus increased by 3.1 mJ/m^2, suggesting that it became less stable[99].

It would be expected that the use of other salts to produce the same ionic strength as that used for NaCl would also result in a double layer forming that would stabilise the γ-glycine nuclei, however, experiments found that only salts which contained sodium were effective in promoting the formation of γ-glycine over α-glycine (calcium and magnesium salts were not effective). This supported the idea of the inhibition of α-glycine resulting in the formation of γ-glycine[90].

Other Methods to Obtain γ -glycine

Lasers have been demonstrated as capable of inducing γ-glycine formation via a non-photochemical mechanism[17, 37]. As mentioned, γ-glycine is polar and is made from open chains of glycine zwitterions that are connected head-to-tail by hydrogen bonds[95, 99]. The use of linearly polarised light from a laser was thought to induce alignment of the helical structures that form γ-glycine more effectively than the cyclic dimers that form α-glycine[17]. The application of a D.C. field was thought to have a similar effect[53].

1.5.3 Glycine Self-Association

Several studies suggest that glycine molecules undergo self-association in supersaturated solutions. Dimers were thought to be the most prevalent form of glycine in aqueous solution and as mentioned, this was a potential reason why α-glycine, which is made from layers of cyclic dimers, formed preferentially over the more stable γ-glycine which is not formed from dimers[99]. Evidence for the presence of dimers came from atomic force microscopy, small angle x-ray studies[38, 108] and measurements of diffusivities[109]. The study of diffusivities also showed glycine solutions to contain trimers and a small number of species containing hundreds of monomers[109].

Recent studies, however, suggest that cyclic dimers may not actually be the most prevalent form of glycine in aqueous solution. For example a study, based on freezing point depression and self-diffusion measurements, found that zwitterionic monomers were the most prevalent form of glycine in aqueous solution (up to 70%) with the rest existing as dimers[95]. Monomers were also found to be more common than dimers in theoretical studies[110-112]. Other studies have shown that catemers are the most prevalent paired structure in aqueous solutions[110, 111]. Therefore, taking into consideration the suspected role of cyclic dimers on the nucleation of α-glycine, it may be that the concentration of cyclic dimers in aqueous solutions is not particularly high or low, but sufficient for cyclic dimers to be the precursors for the nucleation of α-glycine[93].

Various studies suggest that in supersaturated, aqueous glycine solutions, larger molecular clusters with liquid-like properties exist and have a role in nucleation. Small angle x-ray scattering suggested that the first step of crystallisation involves

the formation of liquid-like clusters of a few hundred nanometres with a second step involving the reorganisation of the structures into crystalline structures[38, 108, 113]. Glycine dimers were thought to form mass fractal aggregates in supersaturated solutions, which were then transformed into surface fractal structures, prior to nucleation. The transformation was attributed to the organisation of disordered liquid-like structures in to more ordered lattice structures[38].

Another study, which used dynamic light scattering, reported that glycine rich mesoscale clusters (nanodroplets) of around 250nm diameter with liquid-like properties exist in aqueous glycine solutions, both undersaturated and supersaturated. The nanodroplets were not metastable and existed at a fixed size and concentration, in thermodynamic equilibrium with glycine crystals. They were estimated to have a very low mole fraction of total glycine solute (less than 10^{-6}) and coexisted with small sub-nanometre molecular clusters and molecular solution[85, 113].

The nanodroplets were not thought to be directly involved in productive crystal nucleation (e.g. a 6 fold increases in their concentration did not affect the number of crystals formed or the time taken for the crystals to appear) but they could be coalesced to form larger nanodroplets (>750 nm diameter) which gave access to a more rapid nucleation pathway (a significantly shorter time was required for the appearance of crystals, and a much larger number of crystals was produced)[85]. The larger droplets were only observed in stirred solutions and they were not observed under quiescent conditions. Therefore they were thought to form due to the coalescence of the smaller nanodroplets[85, 113]. The larger glycine nanodroplets were thought to have the same compositions as the smaller nanodroplets, but with a much larger total mass. The size of the coalesced nanodroplets was larger than the clusters reported in other studies that proposed a two-step nucleation theory[5, 6, 38].

For the more rapid nucleation pathway, it was proposed that productive nucleation of glycine occurred in the large glycine-rich nanodroplets, but occurred non-productively in the smaller 250nm nanodroplets[85, 113]. Each time nucleation was initiated in a glycine-rich nanodroplet, growth would have occurred until the local high concentration of glycine within the nanodroplet was exhausted. When this happened, the nascent crystal would have been exposed to the bulk solution. If the crystal was large enough, it would have survived and grown, however, if it was too small, it would have redissolved into the bulk solution or become a cluster again[66].

With this scenario, due to the larger mass of glycine in the coalesced nanodroplets, nucleation may have occurred productively in the larger nanodroplets since the crystals formed would have been above a critical size. For smaller nanodroplets, nucleation would have been largely non-productive as the crystals would not have reached the critical size.

Glycine anions or cations may also help explain the presence of liquid-like glycine clusters in solution according to a study[93]. The glycine ions themselves may not undergo self-aggregation, but they may interact strongly with glycine zwitterions due to the ion-dipole interaction. This may result in one glycine ion interacting with one glycine zwitterion, leading to the formation of a charged dimer. Charged dimers may then interact with other zwitterions through strong ion-dipole interactions, leading to the formation of a higher n-mer. This would be particularly likely when the concentration of anions or cations was low, since one ion would be surrounded by many zwitterions and would interact with them readily. When the concentration of anions/ cations was higher, there would be fewer zwitterions so the interaction between one glycine ion and surrounding zwitterions would be less likely. This would weaken the effectiveness of the formation of liquid-like glycine clusters[93].

Since literature has various possible explanations for how glycine exists in solution, it remains unclear as to what the most prevalent form of glycine in solution is and how this affects nucleation. The wide variation of possibilities is likely due to differences in experimental technique used.

1.5.4 Influence of Shear on Glycine Nucleation

Few previous studies exist on the role that fluid shear has on glycine nucleation. As mentioned previously, the use of a magnetic stirrer was found to result in enhanced nucleation rates and this was thought to be due to the coalescence of glycine nanodroplets, which led to a more rapid nucleation pathway[85]. A main drawback of this study was that the use of magnetic stirrer bars resulted in unquantifiable shear rates due to the possible interactions between the magnetic stir bar and the bottom of the vial. The work in this thesis on the influence of controlled flow conditions on glycine nucleation therefore improves and clarifies the existing understanding in this area.

1.6 Measurement of Nucleation Rates

There are several methods of estimating nucleation rates in the literature and some of the more interesting examples are given here. The measurement of nucleation rates is difficult and reproducibility is hard to achieve. Part of this is due to the stochastic nature of nucleation; often a large number of repetitions are required for reliable trends to be deduced. Other difficulties arise since the critical nucleus size is often in the range of 100-1000 atoms, which is difficult to measure using standard experimental methods[114]. Nuclei also only exist for short times and they freely diffuse around the solution volume, making it difficult to detect them in the volume of solution that is being examined. Therefore, rather than directly measuring the nucleation rate, the methods tend to involve techniques such as:

- counting the number of crystals formed (e.g. double pulse method, integral method)
- measuring particle size distributions (e.g. mixed-suspension, mixed-product removal method)
- measuring metastable zone widths
- measuring induction times
- transmission measurements

and relating these to the rate of nucleation.

1.6.1 Double Pulse Method

Principles of the Method

A technique that allows the direct determination of nucleation rates from the number of crystals appearing in a certain solution volume in a given time has been produced by Galkin and Vekilov[115, 116]. The technique is based on separating nucleation from ensuing growth stages, and the principles are centred on the dependence of solubility on temperature that exists for many substances[115, 117].

Solution depletion can be a problem with nucleation studies. It happens because crystals typically grow very rapidly at the supersaturation required for nucleation which results in the depletion of supersaturation and therefore a reduced nucleation rate over time. The technique proposed by Galkin and Vekilov[115] overcomes this issue since once nucleation has occurred initially at a fairly constant rate, the

supersaturation is lowered to levels where the nucleation rate is zero. The crystals/ nuclei already formed can then grow to detectable dimensions, without further nuclei being formed.

Experimental Method

A diagram of an experimental setup for the double pulse method is given in Figure 1. 10. The most reliable nucleation rates were found using a large number of independent trials: 400 identical lysozyme solution droplets (0.1-2.5µl) were contained within wells cut into a block of Teflon. A Peltier temperature controller was used to control the temperature of a brass block, and the Teflon block was in contact with the brass plate. 5 identical blocks, independently controlled, were used, allowing for 2000 samples at a time.

At the start of an experiment, the solute temperature was set to T_1. T_1 corresponded to the temperature that resulted in the desired level of supersaturation for nucleation. After a period of time at this temperature (Δt_1) which was sufficient for nucleation to occur at a constant supersaturation level, the temperature was then changed to T_2. T_2 corresponded to a temperature where the supersaturation was sufficiently low that further nucleation did not take place, but allowed existing nuclei to grow to a detectable size. Once the crystals had grown to a detectable size, samples were studied using a microscope and the number of crystals in each sample (N) was counted. The nucleation rate was then estimated:

$$J = \frac{N}{V \Delta t_1}$$

(1. 32)

Here V is the volume of each droplet.
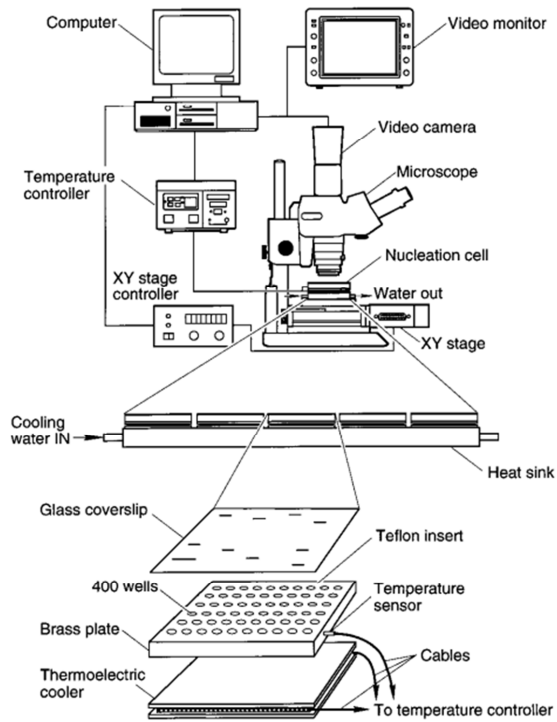
Figure 1. 10
Experimental setup for the double pulse method of measuring nucleation rates[115].

The principles behind this method of determining nucleation rates have been widely used in literature, with slight variations in procedure/ analysis being reported [118-120]. In some of these, microfluidics have been used. A microfluidic device can generate hundreds of droplets, giving a large sample of independent nucleation events. A main drawback of the double pulse method is that industrial crystallisation processes will strongly differ from the small and stagnant solution volumes used.

1.6.2 Metastable Zone Width (MSZW) Measurements

Principles of the Method

Measurements of metastable zone widths can provide useful information on nucleation. It is a relatively simple method for obtaining relative nucleation data[23], and it is particularly useful for studying the effects of a variable on nucleation rates[3]. Generally small MSZW result in shorter induction times and higher rates of nucleation[23]. The MSZW depends on many factors including temperature, agitation, thermal history of the solution and cooling rate [1, 3].

The basic principles of MSZW measurements can be explained using Figure 1. 11. Point A represents an undersaturated solution, where the solution is stable and crystals to do not form. It can be cooled from point A to point B on the solubility curve; point B represents a saturated solution. The solution can be further cooled, and when this happens, the solution is supersaturated: the solute concentration is greater than the saturation (equilibrium) concentration. When cooled between points B (solubility curve) and C (metastable boundary), solid is not spontaneously precipitated in a short time to achieve equilibrium in the solutions. If, however, it was cooled beyond point C in to the labile region, spontaneous crystallisation would be probable[1]. The metastable boundary is therefore the point at which crystals will quickly and spontaneously appear. The MSZW can therefore be determined by the difference between the saturation temperature (T^*) and the metastable boundary temperature ($T_{MSZW\ limit}$). This is often known as the maximum allowable cooling (ΔT_{max}) of solution of a given concentration.

$$\Delta T_{max} = T^* - T_{MSZW\ limit} \qquad \textbf{(1. 33)}$$

Measurements of ΔT_{max} can be used to estimate the rate of nucleation in a solution[23, 121, 122].

The maximum obtainable supersaturation in the solutions at a given temperature (Δc_{max}) can be found from the difference in concentration between the saturated solution (c^*) and the solution at the metastable boundary ($c_{MSZW\ limit}$). In Figure 1. 11, this is illustrated by the difference in concentration at points C and D.

$$\Delta c_{max} = c_{MSZW\ limit} - c^* \qquad \textbf{(1. 34)}$$
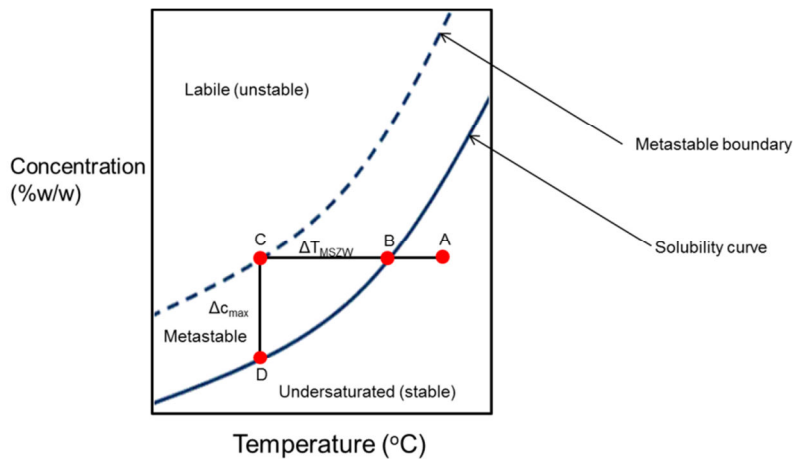
Figure 1. 11
Example solubility curve for 2 phase system with a positive relationship between temperature and solubility.

Experimental Methods

The MSZW (ΔT_{max}) can be measured in 2 main ways- isothermal or polythermal measurements[123]. The measurements made are very equipment dependent.

A typical procedure for measuring ΔT_{max} using the polythermal method is as follows[1, 123]. A just-saturated solution is placed in a vessel with temperature control and is allowed to thermally equilibrate. The solution is kept stirred at a constant rate and is cooled slowly until small crystals are formed. The temperature of the solution is then increased slowly until the crystals disappear. The temperature at which the last crystal has disappeared is taken as the saturation temperature (T^*) of the solutions.

The solution is then heated slightly above this saturation (by 1-5°C or so) and it is maintained at this higher temperature for ~ 30 minutes. The solution is then cooled at a constant rate and the temperature at which the first crystal appears is denoted $T_{MSZW\ limit}$. This can then be repeated multiple times and for different cooling rates[3, 23, 123].

Nucleation rates can then be estimated from the ΔT_{max} measurements. One method involves examining the stochastic distributions of ΔT_{max} values obtained from repetitions of an experiment at a given set of conditions[23, 121, 122]. The probability distributions of ΔT_{max} can be fitted with a theoretical equation and solved for nucleation rates[23, 121, 122].

A second, more conventional method involves measuring ΔT_{max} for different cooling rates and plotting $\log(\text{cooling rate})$ versus $\log(\Delta T_{max})$.[1, 3, 123] This should yield a straight line and the gradient and intercept can be used to deduce the constants in the Becker-Doering empirical relation for nucleation rates (Eqn. (1. 27)) [1, 3, 123].

Isothermal measurements involve cooling a solution rapidly until it becomes supersaturated/ metastable. The supersaturation is held constant and the time taken for crystals to form is then measured[123].

1.6.3 Mixed-Suspension, Mixed-Product Removal (MSMPR)

Experimental Method

Nucleation rates and crystal growth rates can be measured simultaneously using an idealised mixed-suspension, mixed-product removal (MSMPR) crystalliser model. It is analogous to the use of CSTR models in chemical engineering and is the simplest crystalliser to analyse.

A typical setup is given in Figure 1. 12. Solution enters the fixed-volume vessel where it is well-mixed to ensure that there is no variation of concentration, temperature, size distribution, etc. within the solution volume. Supersaturation can be introduced through cooling, reaction, evaporation, etc. Nuclei form and these can grow into crystals. The outlet flow is assumed to have the same composition as the solution in the vessel. Due to the crystals having a probabilistic variation of residence time in the crystalliser, there will be a crystal size distribution. Once the system has reached a steady state, the crystal size distribution of the outlet flow can be measured.
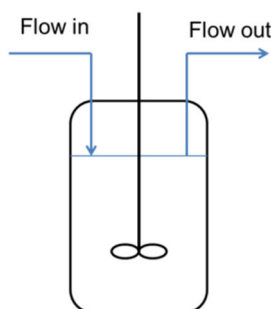
Figure 1. 12
Simplified MSMPR diagram.

Principles of the Method

Nucleation rates and growth rates can be estimated from the crystal size distribution measured. The theory used to deduce these is based on a population balance and applies the laws of conservation. Several assumptions can be made to simplify the theory. These include steady state operation with no accumulation in the system; no crystals are assumed to be present in the feed; all crystals are assumed to be of the same shape characterized by a chosen linear dimension size (L); the crystal growth rate (G) is assumed to be independent of crystal size and crystals are assumed to not break down by attrition [1, 3, 123, 124].

Taking these assumptions into consideration, the crystal population density (n), which is the number of crystals per unit size per unit volume, can be written as a function of crystal size:

$$n = n_0 e^{-\frac{L}{G\tau}}$$

(1. 35)

Here n_0 is the population density of zero sized crystals (nuclei) and τ is the mean residence time in the crystalliser.

Eqn. (1. 35) can be linearised by taking logarithms:

$$\ln(n) = \ln(n_0) - \frac{L}{G\tau}$$

(1. 36)

The experimentally measured crystal size distribution can then be plotted as $\ln(n)$ versus L and the slope of the plot should be equal to $-\frac{1}{G\tau}$ and the intercept should be equal to $\ln(n_0)$. From the slope value, the growth rate can be deduced if the residence time is known. The growth rate can then be used to find the nucleation rate.

$$J = \lim_{L \to 0} \frac{dN}{dt} = \lim_{L \to 0} \left[\frac{dN}{dL} \frac{dL}{dt} \right] = n_0 G$$

(1. 37)

Here N is the number of crystals per unit volume and t is time.

The assumptions made for the MSMPR model are unlikely to hold precisely. For example, attrition and breakage due to mechanical stress can occur, and particles are unlikely to exist as discrete entities and may instead agglomerate. Insufficient mixing could be an issue and conditions might not be steady state. Although increasing the stirrer speed could improve mixing, attrition may then become more of an issue, so there are often trade-offs to get conditions close to the assumptions. These various factors can confound MSMPR data[1, 123, 124].

1.6.4 T or Y Mixers (Integral Method of Determination)
Principles of the Method

The integral method of determination uses a precise time interval, within which nucleation takes place. The total number of nuclei generated in this time can be deduced and a rate of nucleation can therefore be found. T-mixers and Y-mixers allow a precise nucleation time to be used. The nucleation time is based on the residence time of the outlet tube[123, 125]. This nucleation time holds provided that the solution is quenched directly at the outlet of the mixer (see Figure 1. 13). Advantages of using these devices include the ability to achieve intensive mixing in a small volume[123]. This setup is generally applicable for reactive/ anti-solvent crystallisation processes[125].

If the desupersaturation proceeds slowly, the supersaturation and therefore rate of nucleation will remain constant along the length of the outlet tube. At the end of the tube, the solution will still be supersaturated so it must be rapidly quenched in a saturated solution to reduce the supersaturation and inhibit further nucleation. This is illustrated in Figure 1. 13. The nucleation rate can be estimated from the particle number concentration (N) and the residence time of the sample within the outlet tube (t_r).

$$J = \frac{N}{t_r}$$
(1. 38)
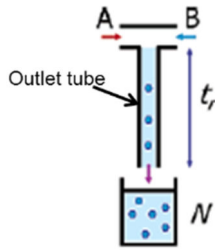
Figure 1. 13
T-mixer setup for constant supersaturation along length of tube [125].

A differential method can also be used as shown in Figure 1. 14. The nucleation rate can be estimated from the difference in number concentration (ΔN) and difference in residence times (Δt_r) between each setup.

$$J = \frac{\Delta N}{\Delta t_r}$$ **(1. 39)**
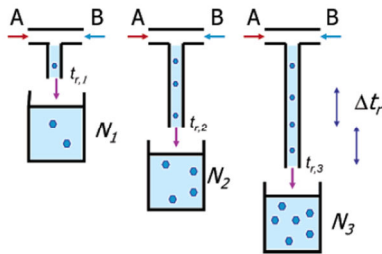
Figure 1. 14
Differential T-mixer setup for constant supersaturation along length of tube [125].

In some cases the supersaturation is rapidly depleted because many nuclei form and grow rapidly. This means that the supersaturation may only be high enough for nucleation to take place in the initial section of the outlet tube, corresponding to residence time t_t (see Figure 1. 15). In the remaining length of outlet tube, the crystals may then grow, consuming the remaining supersaturation, but no more nuclei will form. The nucleation rate can then be estimated from:

$$J = \frac{N}{t_t}$$ **(1. 40)**

t_t is defined as the residence time of the length of outlet tube to the point where the nucleation rate drops to a value where the nucleation becomes insignificant[125]. This

can be estimated from induction time measurements or more laboriously through a population balance model[125].
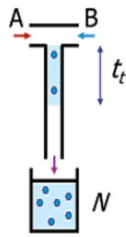
Figure 1. 15
T-mixer setup for depletion of supersaturation along length of tube [125].

Experimental Method

Since nuclei are small, standard particle counters, which usually have a lower size detection limit in the region of 1μm, are usually not sufficient to count the number of nuclei/ crystals exiting the tube[123]. To overcome this, an experimental setup that consists of a nucleator (T-mixer or Y-mixer with an outlet tube) followed by a growth vessel can be used. The growth vessel allows the nuclei to grow to a detectable size.

A volume of reactant is fed to the mixer where rapid mixing occurs. Provided that the mixing time and chemical reaction/ precipitation times are very short compared with the residence time of the outlet tube, the supersaturation should reach its nominal value at the entrance to the outlet tube. At the end of the tube outlet, the nuclei will typically be in the size range of nanometers[123]. After the solution exits the outlet tube, nucleation is inhibited by instantly diluting the suspension upon entering a (agitated) vessel. Although nucleation is inhibited, the nuclei/ crystals continue to grow. A low supersaturation is used so that nucleation will be negligible but moderate growth can occur[123]. Once crystals reach a sufficient size, they can then be counted.

Rather than growing the nuclei and counting them, the nucleation rate can also be determined by measuring the particle size distribution and the total mass precipitated[125]. Dynamic light scattering could also be used[123]. For this, the experimental setup would be similar to that mentioned previously, but rather than quenching in a solution that would enable growth, the solution would be quenched in

a solution that contains surfactants. These would stop nucleation and hinder agglomeration[123].

1.6.5 Other Methods

A number of other techniques exist for estimating nucleation rates. There is a levitating droplet technique, whereby a 'containerless' environment is produced by suspending a droplet between two oils of different density. One oil will have a higher density than the droplet (and precipitate) and the other oil will have a lower density[126, 127]. The number of crystals forming in the droplets can then be counted. The method reduces the effects of heterogeneous nucleation, since the droplets are not in contact with a solid surface. Levitating droplets, however, have the problem of evaporation from the air-liquid interface, which can hinder reproducibility. Oil can also affect the crystallisation process[126, 127].

Other techniques that have been found to produce very good results for measuring the rate of nucleation of small molecules, but are not applicable to solution crystallisation, include the cloud chamber technique and supersonic nozzle expansion technique. These are applicable to vapour-liquid transitions[115].

1.6.6 Limitations of the Measurement Techniques

The various techniques outlined so far for measuring nucleation rates are not appropriate for the controlled flow, cooling crystallisation experiments carried out in the work for this thesis. For example, with the double pulse method, no shearing of the solutions took place and with the MSZW and MSMPR methods, stirring was required and this would not result in the well-controlled fluid shear desired for the experiments carried out in this thesis. The T- or Y-mixer method is not well suited to cooling crystallisation experiments. Methods that required the number of crystals to be counted, such as the double pulse and T- or Y-mixer methods, can also be very error prone.

A more suitable method of measuring nucleation rates for the experiments detailed in this thesis was through measuring induction times and relating these to the rate of primary nucleation[128]. This method was advantageous as it was non-intrusive to the controlled shear experimental setups and in-situ measurements could easily be

taken. Chapter 3 outlines the principles of induction time measurements and the methods that were used to measure them in the experiments carried out. In Chapter 4 Section 4.5.2, it is shown how induction time measurements can be related to the rate of primary nucleation.

1.7 Conclusions

Crystal nucleation from solution is not well understood to date. It is generally accepted that classical nucleation theory has many shortcomings when applied to the nucleation of crystals from solution, so non-classical nucleation theories may be better suited.

Measuring nucleation rates is difficult. There are various possible methods to measure nucleation rates in the literature, but these are often intrusive and error prone. Measuring induction times and relating these to the rate of nucleation is a non-intrusive method, and it can easily be applied to the controlled flow experiments carried out for the work in this thesis.

The influence of controlled fluid shear on the nucleation of small organic molecules is not well understood. Many studies suggest that it can enhance nucleation under certain conditions. The nucleation of glycine, the small organic compound studied for the work in this thesis, has previously been found to be enhanced by fluid shear. The shear enhancement of its nucleation was thought to be due to the coalescence of mesoscale clusters, which led to a more rapid nucleation pathway. The nucleation of glycine is also strongly influenced by pH and presence of sodium chloride.

The work in this thesis aims to improve understanding on the influence of controlled fluid shear on glycine nucleation and how fluid shear, pH and the presence of sodium chloride can affect mesoscale clustering in the solutions.

1.8 References and Nomenclature

1.8.1 References

(1)   Mullin, J. W., *Crystallization*. 4th ed.; Heineman: 2002.

(2)   Davey, R.; Garside, J., *From Molecules to Crystallizers. An Introduction to Crystallization.* ed.; Oxford University Press: 2000.

(3)   Myerson, A., *Handbook of Industrial Crystallization*. 2nd ed.; Butterworth-Heinemann: 2001.

(4)   Kashchiev, D., *Nucleation: Basic Theory and Applications*. ed.; Butterworth-Heinemann: 2000.

(5)   Erdemir, D.; Lee, A. Y.; Myerson, A. S., Nucleation of Crystals from Solution: Classical and Two-Step Models. *Accounts of Chemical Research* **2009,** 42, (5), 621-629.

(6)   Vekilov, P. G., The two-step mechanism of nucleation of crystals in solution. *Nanoscale* **2010,** 2, (11), 2346-2357.

(7)   Mullin, J. W.; Raven, K. D., Influence Of Mechanical Agitation On Nucleation Of Some Aqueous Salt Solutions. *Nature* **1962,** 195, (4836), 35-&.

(8)   Mullin, J. W.; Raven, K. D., Nucleation In Agitated Solutions. *Nature* **1961,** 190, (477), 251-&.

(9)   Nyvlt, J.; Skrivane.J; Gottfrie.J; Krickova, J., Uber Kristallisation .19. Einfluss Der Durchmischung Auf Die Breite Der Metastabilen Zone. *Collection of Czechoslovak Chemical Communications* **1966,** 31, (5), 2127-&.

(10)   Joshi, M. S.; Antony, A. V., Nucleation In Super-Saturated Potassium Dihydrogen Ortho-Phosphate Solutions. *Journal of Crystal Growth* **1979,** 46, (1), 7-9.

(11)   Young, S. W., Mechanical stimulus to crystallization in supercooled liquids. *Journal of the American Chemical Society* **1911,** 33, 148-162.

(12)   Young, S. W.; Cross, R. J., The mechanical stimulus to crystallization. II. *Journal of the American Chemical Society* **1911,** 33, 1375-1388.

(13)   Young, S. W.; Van Sicklen, W. J., The mechanical stimulus to crystallization. *Journal of the American Chemical Society* **1913,** 35, 1067-1078.

(14)   Berkeley, Solubility and supersolubility from the osmotic standpoint. *Philosophical Magazine* **1912,** 24, (140), 254-268.

(15)   Taleb, M.; Didierjean, C.; Jelsch, C.; Mangeot, J. P.; Capelle, B.; Aubry, A., Crystallization of proteins under an external electric field. *Journal of Crystal Growth* **1999,** 200, (3-4), 575-582.

(16)   Sazaki, G.; Yoshida, E.; Komatsu, H.; Nakada, T.; Miyashita, S.; Watanabe, K., Effects of a magnetic field on the nucleation and growth of protein crystals. *Journal of Crystal Growth* **1997,** 173, (1-2), 231-234.

(17)   Zaccaro, J.; Matic, J.; Myerson, A. S.; Garetz, B. A., Nonphotochemical, laser-induced nucleation of supersaturated aqueous glycine produces unexpected gamma-polymorph. *Crystal Growth & Design* **2001,** 1, (1), 5-8.

(18)   Delucas, L. J.; Suddath, F. L.; Snyder, R.; Naumann, R.; Broom, M. B.; Pusey, M.; Yost, V.; Herren, B.; Carter, D.; Nelson, B.; Meehan, E. J.; McPherson, A.; Bugg, C. E., Preliminary Investigations Of Protein Crystal-Growth Using The Space-Shuttle. *Journal of Crystal Growth* **1986,** 76, (3), 681-693.

(19)   Ruecroft, G.; Hipkiss, D.; Ly, T.; Maxted, N.; Cains, P. W., Sonocrystallization: The use of ultrasound for improved industrial crystallization. *Organic Process Research & Development* **2005,** 9, (6), 923-932.

(20)   Kashchiev, D.; van Rosmalen, G. M., Review: Nucleation in solutions revisited. *Crystal Research and Technology* **2003,** 38, (7-8), 555-574.

(21)   Vekilov, P. G., Nucleation. *Crystal Growth & Design* **2010,** 10, (12), 5007-5019.

(22)   Oxtoby, D. W.; Kashchiev, D., A General Relation Between The Nucleation Work And The Size Of The Nucleus In Multicomponent Nucleation. *Journal of Chemical Physics* **1994,** 100, (10), 7665-7671.

(23)   Kulkarni, S. A.; Kadam, S. S.; Meekes, H.; Stankiewicz, A. I.; ter Horst, J. H., Crystal Nucleation Kinetics from Induction Times and Metastable Zone Widths. *Crystal Growth & Design* **2013,** 13, (6), 2435-2440.

(24)   Laaksonen, A.; McGraw, R.; Vehkamaki, H., Liquid-drop formalism and free-energy surfaces in binary homogeneous nucleation theory. *Journal of Chemical Physics* **1999,** 111, (5), 2019-2027.

(25)   Drenth, J.; Haas, C., Nucleation in protein crystallization. *Acta Crystallographica Section D-Biological Crystallography* **1998,** 54, 867-872.

(26)   Knezic, D.; Zaccaro, J.; Myerson, A. S., Nucleation induction time in levitated droplets. *Journal of Physical Chemistry B* **2004,** 108, (30), 10672-10677.

(27)   Zurek, W. H.; Schieve, W. C., Multistep Clustering And Nucleation. *Journal of Physical Chemistry* **1980,** 84, (12), 1479-1482.

(28)   Strey, R.; Viisanen, Y., Measurement Of The Molecular Content Of Binary Nuclei - Use Of The Nucleation Rate Surface For Ethanol-Hexanol. *Journal of Chemical Physics* **1993,** 99, (6), 4693-4704.

(29)   Oxtoby, D. W., Nucleation of first-order phase transitions. *Accounts of Chemical Research* **1998,** 31, (2), 91-97.

(30) Yau, S. T.; Vekilov, P. G., Direct observation of nucleus structure and nucleation pathways in apoferritin crystallization. *Journal of the American Chemical Society* **2001,** 123, (6), 1080-1089.

(31) Oxtoby, D. W., Phase transitions - Catching crystals at birth. *Nature* **2000,** 406, (6795), 464-465.

(32) Vekilov, P. G., Dense liquid precursor for the nucleation of ordered solid phases from solution. *Crystal Growth & Design* **2004,** 4, (4), 671-685.

(33) Vorontsova, M.; Maes, D.; Vekilov, P., Recent advances in the understanding of two-step nucleation of protein crystals. *Faraday Discussions* **2015**.

(34) Anwar, J.; Boateng, P. K., Computer simulation of crystallization from solution. *Journal of the American Chemical Society* **1998,** 120, (37), 9600-9604.

(35) Shore, J. D.; Perchak, D.; Shnidman, Y., Simulations of the nucleation of AgBr from solution. *Journal of Chemical Physics* **2000,** 113, (15), 6276-6284.

(36) tenWolde, P. R.; Frenkel, D., Enhancement of protein crystal nucleation by critical density fluctuations. *Science* **1997,** 277, (5334), 1975-1978.

(37) Garetz, B. A.; Matic, J.; Myerson, A. S., Polarization switching of crystal structure in the nonphotochemical light-induced nucleation of supersaturated aqueous glycine solutions. *Physical Review Letters* **2002,** 89, (17), 4.

(38) Chattopadhyay, S.; Erdemir, D.; Evans, J. M. B.; Ilavsky, J.; Amenitsch, H.; Segre, C. U.; Myerson, A. S., SAXS study of the nucleation of glycine crystals from a supersaturated solution. *Crystal Growth & Design* **2005,** 5, (2), 523-527.

(39) Pan, W. C.; Kolomeisky, A. B.; Vekilov, P. G., Nucleation of ordered solid phases of proteins via a disordered high-density state: Phenomenological approach. *Journal of Chemical Physics* **2005,** 122, (17).

(40) Filobelo, L. F.; Galkin, O.; Vekilov, P. G., Spinodal for the solution-to-crystal phase transformation. *Journal of Chemical Physics* **2005,** 123, (1).

(41) Pan, W.; Vekilov, P. G.; Lubchenko, V., Origin of Anomalous Mesoscopic Phases in Protein Solutions. *Journal of Physical Chemistry B* **2010,** 114, (22), 7620-7630.

(42) Lomakin, A.; Chung, D. S.; Benedek, G. B.; Kirschner, D. A.; Teplow, D. B., On the nucleation and growth of amyloid beta-protein fibrils: Detection of nuclei and quantitation of rate constants. *Proceedings of the National Academy of Sciences of the United States of America* **1996,** 93, (3), 1125-1129.

(43) Krishnan, R.; Lindquist, S. L., Structural insights into a yeast prion illuminate nucleation and strain diversity. *Nature* **2005,** 435, (7043), 765-772.

(44) Pan, W.; Galkin, O.; Filobelo, L.; Nagel, R. L.; Vekilov, P. G., Metastable mesoscopic clusters in solutions of sickle-cell hemoglobin. *Biophysical Journal* **2007,** 92, (1), 267-277.

(45)   Galkin, O.; Nagel, R. L.; Vekilov, P. G., The kinetics of nucleation and growth of sickle cell hemoglobin fibers. *Journal of Molecular Biology* **2007,** 365, (2), 425-439.

(46)   Galkin, O.; Pan, W.; Filobelo, L.; Hirsch, R. E.; Nagel, R. L.; Vekilov, P. G., Two-step mechanism of homogeneous nucleation of sickle cell hemoglobin polymers. *Biophysical Journal* **2007,** 93, (3), 902-913.

(47)   Savage, J. R.; Dinsmore, A. D., Experimental Evidence for Two-Step Nucleation in Colloidal Crystallization. *Physical Review Letters* **2009,** 102, (19).

(48)   Leunissen, M. E.; Christova, C. G.; Hynninen, A. P.; Royall, C. P.; Campbell, A. I.; Imhof, A.; Dijkstra, M.; van Roij, R.; van Blaaderen, A., Ionic colloidal crystals of oppositely charged particles. *Nature* **2005,** 437, (7056), 235-240.

(49)   Gebauer, D.; Voelkel, A.; Coelfen, H., Stable Prenucleation Calcium Carbonate Clusters. *Science* **2008,** 322, (5909), 1819-1822.

(50)   Pouget, E. M.; Bomans, P. H. H.; Goos, J. A. C. M.; Frederik, P. M.; de With, G.; Sommerdijk, N. A. J. M., The Initial Stages of Template-Controlled CaCO3 Formation Revealed by Cryo-TEM. *Science* **2009,** 323, (5920), 1455-1458.

(51)   Gebauer, D.; Kellermeier, M.; Gale, J. D.; Bergstrom, L.; Colfen, H., Pre-nucleation clusters as solute precursors in crystallisation. *Chemical Society Reviews* **2014,** 43, (7), 2348-2371.

(52)   Meldrum, F. C.; Sear, R. P., Materials Science Now You See Them. *Science* **2008,** 322, (5909), 1802-1803.

(53)   Aber, J. E.; Arnold, S.; Garetz, B. A.; Myerson, A. S., Strong dc electric field applied to supersaturated aqueous glycine solution induces nucleation of the gamma polymorph. *Physical Review Letters* **2005,** 94, (14).

(54)   Garetz, B. A.; Matic, J.; Myerson, A. S., Polarization switching of crystal structure in the nonphotochemical light-induced nucleation of supersaturated aqueous glycine solutions. *Physical Review Letters* **2002,** 89, (17).

(55)   Garetz, B. A.; Aber, J. E.; Goddard, N. L.; Young, R. G.; Myerson, A. S., Nonphotochemical, polarization-dependent, laser-induced nucleation in supersaturated aqueous urea solutions. *Physical Review Letters* **1996,** 77, (16), 3475-3476.

(56)   Pontoni, D.; Narayanan, T.; Rennie, A. R., Nucleation and growth kinetics of colloidal silica. In *Trends in Colloid and Interface Science Xvi*, Miguel, M. G. B. H. D., Ed. 2004; Vol. 123, pp 227-230.

(57)   Igarashi, K.; Azuma, M.; Kato, J.; Ooshima, H., The initial stage of crystallization of lysozyme, a differential scanning calorimetric (DSC) study. *Journal of Crystal Growth* **1999,** 204, (1-2), 191-200.

(58)   Galkin, O.; Chen, K.; Nagel, R. L.; Hirsch, R. E.; Vekilov, P. G., Liquid-liquid separation in solutions of normal and sickle cell hemoglobin. *Proceedings of the*

National Academy of Sciences of the United States of America **2002,** 99, (13), 8479-8483.

(59)   Nicolis, G.; Nicolis, C., Enhancement of the nucleation of protein crystals by the presence of an intermediate phase: a kinetic model. *Physica a-Statistical Mechanics and Its Applications* **2003,** 323, 139-154.

(60)   Gavezzotti, A., Molecular aggregation of acetic acid in a carbon tetrachloride solution: A molecular dynamics study with a view to crystal nucleation. *Chemistry-a European Journal* **1999,** 5, (2), 567-576.

(61)   Soga, K. G.; Melrose, J. R.; Ball, R. C., Metastable states and the kinetics of colloid phase separation. *Journal of Chemical Physics* **1999,** 110, (4), 2280-2288.

(62)   Talanquer, V.; Oxtoby, D. W., Crystal nucleation in the presence of a metastable critical point. *Journal of Chemical Physics* **1998,** 109, (1), 223-227.

(63)   Lutsko, J. F.; Nicolis, G., Theoretical evidence for a dense fluid precursor to crystallization. *Physical Review Letters* **2006,** 96, (4).

(64)   Haas, C.; Drenth, J., The interface between a protein crystal and an aqueous solution and its effects on nucleation and crystal growth. *Journal of Physical Chemistry B* **2000,** 104, (2), 368-377.

(65)   Sear, R. P., Nucleation via an unstable intermediate phase. *Journal of Chemical Physics* **2009,** 131, (7).

(66)   Jawor-Baczynska, A.; Moore, B.; Sefcik, J., Effect of mixing, concentration and temperature on the formation of mesostructured solutions and their role in the nucleation of dl-valine crystals. *Faraday Discussions* **2015**.

(67)   Keller, A., Polymer Crystals. *Reports on Progress in Physics* **1968,** 31, 623-625.

(68)   Mackley, M. R.; Keller, A., Flow Induced Polymer-Chain Extension And Its Relation To Fibrous Crystallization. *Philosophical Transactions of the Royal Society a-Mathematical Physical and Engineering Sciences* **1975,** 278, (1276), 29-+.

(69)   Kumaraswamy, G.; Kornfield, J. A.; Yeh, F. J.; Hsiao, B. S., Shear-enhanced crystallization in isotactic polypropylene. 3. Evidence for a kinetic pathway to nucleation. *Macromolecules* **2002,** 35, (5), 1762-1769.

(70)   Monasse, B., Nucleation And Anisotropic Crystalline Growth Of Polyethylene Under Shear. *Journal of Materials Science* **1995,** 30, (19), 5002-5012.

(71)   Coccorullo, I.; Pantani, R.; Titomanlio, G., Spherulitic Nucleation and Growth Rates in an iPP under Continuous Shear Flow. *Macromolecules* **2008,** 41, (23), 9214-9223.

(72)   Jay, F.; Haudin, J. M.; Monasse, B., Shear-induced crystallization of polypropylenes: effect of molecular weight. *Journal of Materials Science* **1999,** 34, (9), 2089-2102.

(73)   Penkova, A.; Pan, W. C.; Hodjaoglu, F.; Vekilov, P. G., Nucleation of protein crystals under the influence of solution shear flow. *Interdisciplinary Transport Phenomena in the Space Sciences* **2006,** 1077, 214-231.

(74)   Gliko, O.; Pan, W.; Katsonis, P.; Neumaier, N.; Galkin, O.; Weinkauf, S.; Vekilov, P. G., Metastable liquid clusters in super- and undersaturated protein solutions. *Journal of Physical Chemistry B* **2007,** 111, (12), 3106-3114.

(75)

(76)   Roberts, M. M.; Heng, J. Y. Y.; Williams, D. R., Protein Crystallization by Forced Flow through Glass Capillaries: Enhanced Lysozyme Crystal Growth. *Crystal Growth & Design* **2010,** 10, (3), 1074-1083.

(77)   Reis, N. M.; Chirgadze, D. Y.; Blundell, T. L.; Mackley, M. R., The effect of protein-precipitant interfaces and applied shear on the nucleation and growth of lysozyme crystals. *Acta Crystallographica Section D-Biological Crystallography* **2009,** 65, 1127-1139.

(78)   Chen, D. L.; Gerdts, C. J.; Ismagilov, R. F., Using microfluidics to observe the effect of mixing on nucleation of protein crystals. *Journal of the American Chemical Society* **2005,** 127, (27), 9672-9673.

(79)   Ackerson, B. J.; Pusey, P. N., Shear-Induced Order In Suspensions Of Hard-Spheres. *Physical Review Letters* **1988,** 61, (8), 1033-1036.

(80)   Haw, M. D.; Poon, W. C. K.; Pusey, P. N., Direct observation of oscillatory-shear-induced order in colloidal suspensions. *Physical Review E* **1998,** 57, (6), 6859-6864.

(81)   Amos, R. M.; Rarity, J. G.; Tapster, P. R.; Shepherd, T. J.; Kitson, S. C., Fabrication of large-area face-centered-cubic hard-sphere colloidal crystals by shear alignment. *Physical Review E* **2000,** 61, (3), 2929-2935.

(82)   Palberg, T.; Monch, W.; Schwarz, J.; Leiderer, P., Grain-Size Control In Polycrystalline Colloidal Solids. *Journal of Chemical Physics* **1995,** 102, (12), 5082-5087.

(83)   Butler, S.; Harrowell, P., Kinetics Of Crystallization In A Shearing Colloidal Suspension. *Physical Review E* **1995,** 52, (6), 6424-6430.

(84)   Blaak, R.; Auer, S.; Frenkel, D.; Lowen, H., Homogeneous nucleation of colloidal melts under the influence of shearing fields. *Journal of Physics-Condensed Matter* **2004,** 16, (38), S3873-S3884.

(85)   Jawor-Baczynska, A.; Sefcik, J.; Moore, B. D., 250 nm Glycine-Rich Nanodroplets Are Formed on Dissolution of Glycine Crystals But Are Too Small To Provide Productive Nucleation Sites. *Crystal Growth & Design* **2013,** 13, (2), 470-478.

(86)   Liang, K. P.; White, G.; Wilkinson, D.; Ford, L. J.; Roberts, K. J.; Wood, W. M. L., An examination into the effect of stirrer material and agitation rate on the

nucleation of L-glutamic acid batch crystallized from supersaturated aqueous solutions. *Crystal Growth & Design* **2004,** 4, (5), 1039-1044.

(87)   Liu, J.; Rasmuson, A. C., Influence of Agitation and Fluid Shear on Primary Nucleation in Solution. *Crystal Growth & Design* **2013,** 13, (10), 4385-4394.

(88)   Liu, J.; Svard, M.; Rasmuson, A. C., Influence of Agitation and Fluid Shear on Nucleation of m-Hydroxybenzoic Acid Polymorphs. *Crystal Growth & Design* **2014,** 14, (11), 5521-5531.

(89)   Sypek, K.; Burns, I. S.; Florence, A. J.; Sefcik, J., In Situ Monitoring of Stirring Effects on Polymorphic Transformations during Cooling Crystallization of Carbamazepine. *Crystal Growth & Design* **2012,** 12, (10), 4821-4828.

(90)   Towler, C. S.; Davey, R. J.; Lancaster, R. W.; Price, C. J., Impact of molecular speciation on crystal nucleation in polymorphic systems: The conundrum of gamma glycine and molecular 'self poisoning'. *Journal of the American Chemical Society* **2004,** 126, (41), 13347-13353.

(91)   Darvey, I. G., What Fraction Of Glycine Molecules Are Nonionic In A Solution Of Glycine At A Ph Value Equal To The Isoelectric Point Of Glycine. *Biochemical Education* **1995,** 23, (3), 141-143.

(92)   Lu, J.; Wang, X.-J.; Yang, X.; Ching, C.-B., Solubilities of glycine and its oligopeptides in aqueous solutions. *Journal of Chemical and Engineering Data* **2006,** 51, (5), 1593-1596.

(93)   Han, G.; Thirunahari, S.; Chow, P. S.; Tan, R. B. H., Resolving the longstanding riddle of pH-dependent outcome of glycine polymorphic nucleation. *Crystengcomm* **2013,** 15, (6), 1218-1224.

(94)   Han, G. J.; Chow, P. S.; Tan, R. B. H., Direct Comparison of alpha- and gamma-Glycine Growth Rates in Acidic and Basic Solutions: New Insights into Glycine Polymorphism. *Crystal Growth & Design* **2012,** 12, (5), 2213-2220.

(95)   Huang, J.; Stringfellow, T. C.; Yu, L., Glycine exists mainly as monomers, not dimers, in supersaturated aqueous solutions: Implications for understanding its crystallization and polymorphism. *Journal of the American Chemical Society* **2008,** 130, (42), 13973-13980.

(96)   Srinivasan, K., Crystal growth of alpha and gamma glycine polymorphs and their polymorphic phase transformations. *Journal of Crystal Growth* **2008,** 311, (1), 156-162.

(97)   Bernal, J. D., Short notifications and notes - The crystal structure of the natural amino acids and related compounds. *Zeitschrift Fur Kristallographie* **1931,** 78, (3/4), 363-369.

(98)   Iitaka, Y., Crystal Structure Of Gamma Glycine. *Acta Crystallographica* **1961,** 14, (1), 1-5.

(99)   Duff, N.; Dahal, Y. R.; Schmit, J. D.; Peters, B., Salting out the polar polymorph: Analysis by alchemical solvent transformation. *Journal of Chemical Physics* **2014,** 140, (1), 11.

(100)   Weissbuch, I.; Lahav, M.; Leiserowitz, L., Toward stereochenical control, monitoring, and understanding of crystal nucleation. *Crystal Growth & Design* **2003,** 3, (2), 125-150.

(101)   Weissbuch, I.; Leisorowitz, L.; Lahav, M., Tailor-Made And Charge-Transfer Auxiliaries For The Control Of The Crystal Polymorphism Of Glycine. *Advanced Materials* **1994,** 6, (12), 952-956.

(102)   Yang, X.; Lu, J.; Wang, X.-J.; Ching, C.-B., Effect of sodium chloride on the nucleation and polymorphic transformation of glycine. *Journal of Crystal Growth* **2008,** 310, (3), 604-611.

(103)   Di Profio, G.; Reijonen, M. T.; Caliandro, R.; Guagliardi, A.; Curcio, E.; Drioli, E., Insights into the polymorphism of glycine: membrane crystallization in an electric field. *Physical Chemistry Chemical Physics* **2013,** 15, (23), 9271-9280.

(104)   Iitaka, Y., Crystal Structure Of Beta-Glycine. *Nature* **1959,** 183, (4658), 390-391.

(105)   Ferrari, E. S.; Davey, R. J.; Cross, W. I.; Gillon, A. L.; Towler, C. S., Crystallization in polymorphic systems: The solution-mediated transformation beta to alpha glycine. *Crystal Growth & Design* **2003,** 3, (1), 53-60.

(106)   Yu, L.; Ng, K., Glycine crystallization during spray drying: The pH effect on salt and polymorphic forms. *Journal of Pharmaceutical Sciences* **2002,** 91, (11), 2367-2375.

(107)   Akers, M. J.; Milton, N.; Byrn, S. R.; Nail, S. L., Glycine Crystallization During Freezing - The Effects Of Salt Form, Ph, And Ionic-Strength. *Pharmaceutical Research* **1995,** 12, (10), 1457-1461.

(108)   Erdemir, D.; Chattopadhyay, S.; Guo, L.; Ilavsky, J.; Amenitsch, H.; Segre, C. U.; Myerson, A. S., Relationship between self-association of glycine molecules in supersaturated solutions and solid state outcome. *Physical Review Letters* **2007,** 99, (11).

(109)   Myerson, A. S.; Lo, P. Y., Diffusion And Cluster Formation In Supersaturated Solutions. *Journal of Crystal Growth* **1990,** 99, (1-4), 1048-1052.

(110)   Chen, J.; Trout, B. L., A Computational Study of the Mechanism of the Selective Crystallization of alpha- and beta-Glycine from Water and Methanol-Water Mixture. *Journal of Physical Chemistry B* **2010,** 114, (43), 13764-13772.

(111)   Yani, Y.; Chow, P. S.; Tan, R. B. H., Glycine Open Dimers in Solution: New Insights into alpha-Glycine Nucleation and Growth. *Crystal Growth & Design* **2012,** 12, (10), 4771-4778.

(112)   Hamad, S.; Hughes, C. E.; Catlow, C. R. A.; Harris, K. D. M., Clustering of glycine molecules in aqueous solution studied by molecular dynamics simulation. *Journal of Physical Chemistry B* **2008,** 112, (24), 7280-7288.

(113)   Jawor-Baczynska, A.; Moore, B. D.; Lee, H. S.; McCormick, A. V.; Sefcik, J., Population and size distribution of solute-rich mesospecies within mesostructured aqueous amino acid solutions. *Faraday Discussions* **2013,** 167, 425-440.

(114)   Schuth, F.; Bussian, P.; Agren, P.; Schunk, S.; Linden, M., Techniques for analyzing the early stages of crystallization reactions. *Solid State Sciences* **2001,** 3, (7), 801-808.

(115)   Galkin, O.; Vekilov, P. G., Direct determination of the nucleation rates of protein crystals. *Journal of Physical Chemistry B* **1999,** 103, (49).

(116)   Galkin, O.; Vekilov, P. G., Nucleation of protein crystals: critical nuclei, phase behavior, and control pathways. *Journal of Crystal Growth* **2001,** 232, (1-4), 63-76.

(117)   Vekilov, P. G.; Galkin, O., On the methods of determination of homogeneous nucleation rates of protein crystals. *Colloids and Surfaces a-Physicochemical and Engineering Aspects* **2003,** 215, (1-3), 125-130.

(118)   Wantha, L.; Flood, A. E., Nucleation Kinetics of the gamma-Polymorph of DL-Methionine. *Chemical Engineering & Technology* **2012,** 35, (6), 1024-1030.

(119)   Ildefonso, M.; Candoni, N.; Veesler, S., Using Microfluidics for Fast, Accurate Measurement of Lysozyme Nucleation Kinetics. *Crystal Growth & Design* **2011,** 11, (5).

(120)   Selimovic, S.; Jia, Y. W.; Fraden, S., Measuring the Nucleation Rate of Lysozyme using Microfluidics. *Crystal Growth & Design* **2009,** 9, (4), 1806-1810.

(121)   Kadam, S. S.; Kulkarni, S. A.; Ribera, R. C.; Stankiewicz, A. I.; ter Horst, J. H.; Kramer, H. J. M., A new view on the metastable zone width during cooling crystallization. *Chemical Engineering Science* **2012,** 72, 10-19.

(122)   Kadam, S. S.; Kramer, H. J. M.; ter Horst, J. H., Combination of a Single Primary Nucleation Event and Secondary Nucleation in Crystallization Processes. *Crystal Growth & Design* **2011,** 11, (4), 1271-1277.

(123)   Garside, J., *Measurement of Crystal Growth and Nucleation Rates*. 2nd ed.; IChemE: 2002.

(124)   Jones, A., *Crystallization Process Systems*. ed.; Butterworth-Heinemann: 2002.

(125)   Roelands, C. P. M.; ter Horst, J. H.; Kramer, H. J. M.; Jansens, P. J., Analysis of nucleation rate measurements in precipitation processes. *Crystal Growth & Design* **2006,** 6, (6), 1380-1392.

(126)   Chayen, N. E., A novel technique for containerless protein crystallization. *Protein Engineering* **1996,** 9, (10), 927-929.

(127) Chayen, N. E., Crystallization with oils: a new dimension in macromolecular crystal growth. *Journal of Crystal Growth* **1999,** 196, (2-4), 434-441.

(128) Jiang, S. F.; ter Horst, J. H., Crystal Nucleation Rates from Probability Distributions of Induction Times. *Crystal Growth & Design* **2011,** 11, (1), 256-261.

1.8.2 Main Nomenclature

A = pre-exponential factor

$A_c(n)$= cluster surface area

a= activity

a_s= activity of solute in solution

a_{sat}= activity of solute at equilibrium

b = nucleation order

c = concentration of solute

c^*= concentration of solution when saturated

$c_{MSZW\ limit}$= concentration of solution when at the metastable boundary

c_{sat}= equilibrium concentration of solute

Δc = concentration driving force

Δc_{max}= maximum obtainable supersaturation in the solutions at a given temperature

G= crystal growth rate

ΔG = free energy change for creating a cluster

$\Delta G(n)$ = free energy change to form a cluster of n molecules

ΔG_{crit}= critical free energy change

ΔG_S = surface free energy change

ΔG_V = volume free energy change

J = primary nucleation rate

k = Boltzmann constant

k_n= nucleation rate constant

L = size of crystal characteristic dimension

N = number of crystals in each sample or number of crystals per unit volume

ΔN= difference in number concentration

n = number of molecules in cluster or crystal population density

n^*= critical nucleus size

n_0= population density of zero sized crystals

S = supersaturation

T = absolute temperature

T^* = temperature at which solution was saturated

$T_{MSZW\ limit}$ = temperature at which the metastable boundary was reached

ΔT_{max} = maximum allowable cooling of solutions at a given concentration

t = time

t_r = residence time of the sample within the tube

t_t = the residence time of the length of tube to the point where the nucleation rate drops to a value where the nucleation becomes insignificant

Δt_1 = time solution was held at temperature T_1

Δt_r = difference in residence times

V = volume of each droplet

υ = molecular volume

β = shape coefficient

γ = interfacial tension/ surface energy

γ_{ef} = effective surface tension

γ_s = activity coefficient for solute in solution

γ_{sat} = activity coefficient for solute at equilibrium

θ = wetting angle

μ = chemical potential

$\Delta\mu$ = difference in chemical potential between the solute in the solution and the solute at equilibrium

μ^o = standard chemical potential

$\mu_{crystal}$ = chemical potential of the crystallising material in crystal form

μ_s = chemical potential of solute in the solution

μ_{sat} = chemical potential of the solute at equilibrium

σ = relative supersaturation

τ = mean residence time in the crystalliser

$\phi(n)$ = total surface energy of the cluster

ψ = wetting angle factor

2. Shearing Devices

Chapter Outline and Contents

In industrial processes, fluid shear is widely encountered, for example through agitation in a vessel or transport through pipes, however, as detailed in Chapter 1 Section 1.4, the influence of fluid shear on the primary nucleation of small organic molecules is not well understood at present. In order to gain a better understanding of the role that fluid shear has on primary nucleation from solution, the nucleation of glycine in aqueous solution was investigated under well-controlled flow conditions. As mentioned in Chapter 1, previous studies often involved flow conditions which could not be easily quantified e.g. stirring using a magnetic stirrer bar, so for the work carried out in this thesis, it was desirable to have flow conditions in which parameters such as shear rate and velocity could be well quantified. Quantifiable flow was desired so that the effect of controlled flow on the nucleation of glycine from solution could be studied accurately and systematically.

Therefore, flow devices in which well-characterised flow of Newtonian fluids could be obtained were designed and constructed. These were a capillary flow system and a cylindrical Couette cell. The capillary flow system was based on using a syringe pump to make fluid flow back and forth along a capillary, while the Couette flow setup was based on the flow between two concentric cylinders, the outer one of which was rotated. Checks and calculations were carried out to ensure that the flow was predominantly streamlined over the conditions of the experiments carried out for the work in this thesis.

The capillary flow system is used in Chapter 4 and the Couette cell setups are used in Chapters 4 to 6 to investigate the influence of controlled fluid shear on the nucleation of glycine from aqueous solution.

This chapter covers:

- Basic theory on fluid shear in capillaries and cylindrical Couette flow.
- The general setup of the capillary flow device.
- The general setup of the Couette flow device.

2.1 Theory on the Controlled Shearing of a Newtonian Fluid

This section outlines the basic theory on how shear rates could be calculated for flow in the capillary and Couette flow devices.

2.1.1 Newtonian Fluids

Liquids with simple molecular structures often exhibit Newtonian behaviour. This means that their viscosity (which is a measure of its resistance to deformation by a shear stress, or a measure of its rate of energy dissipation) is independent of what is done to the fluid (e.g. a stress applied or the rate at which it is sheared) and the time for which it is subjected to shear.

For Newtonian fluids, a linear relationship therefore exists between shear stress (the force applied per unit area) and shear rate (the rate of fluid deformation). Viscosity is the proportionality constant between the two and is therefore an indicator of the internal resistance of a fluid to deformation. Newton's law of viscosity describes the relationship between shear stress (τ), shear rate or shear strain ($\dot{\gamma}$) and apparent viscosity (η).

$$\tau = \eta\dot{\gamma} \qquad\qquad \textbf{(2. 1)}$$

The fluid will not deform if no stress is applied and Newtonian fluids behave in a purely viscous manner. For Newtonian fluids at constant temperature and pressure, the shear rate will therefore increase linearly with increasing shear stress over a wide range of stresses[1, 2].

More complex liquids, such as polymer solutions and colloidal suspensions generally exhibit non-Newtonian behaviour, meaning that their viscosity is dependent on what it done to the fluid (e.g. a stress applied or the rate at which it is sheared) and/or the time for which they are subjected to shear. They can also display elastic properties where the input energy is stored, rather than dissipated. Their flow is therefore much more complicated than Newtonian fluids[1, 2].

The theory outlined here deals primarily with Newtonian fluids since rheology studies showed that the aqueous glycine solutions used in the experiments displayed Newtonian behaviour[3].

2.1.2 Shearing of a Newtonian Fluid

A fluid can be sheared (deformed) by flow and applied external forces due to the frictional effects exhibited by molecules moving relative to one another. This behaviour is seen in all fluids and is due to their viscosities.

When a fluid flows over a surface, the fluid in contact with the surface is brought to rest (same velocity as surface), and the adjacent layers are retarded by the viscous drag of the fluid. This means that the velocity of fluid in proximity to a surface changes with the distance perpendicular to the direction of flow.

In order to gain a better understanding of the concept of fluid shear, it is useful to first consider the simple case of flow between a pair of parallel plates. Two parallel plates of area A can be placed a distance apart (y), with a thin layer of Newtonian fluid between them. The lower plate is fixed while the upper plate moves in the x direction at a velocity relative to the lower plate (u_x) due to the application of a shearing force (F). This causes the fluid to deform and is shown in Figure 2. 1.
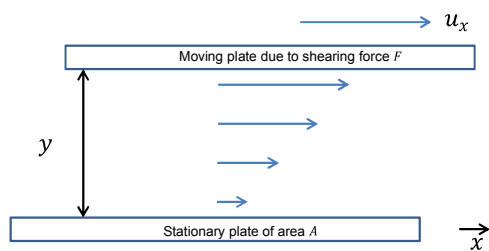
Figure 2. 1
Shearing of a fluid between parallel plates.

When conditions are steady, the shearing force is balanced by the internal forces in the fluid due to its viscosity, and the top plate will move at a constant velocity. Provided that the distance between the plates is small, the velocity of the fluid increases linearly from zero (where fluid in contact with the stationary bottom plate), to u_x (where fluid in contact with the moving upper plate). The velocity gradient (shear rate) is therefore constant over the distance between the two plates. The shearing force per unit area (shear stress) is proportional to the velocity gradient (shear rate/ rate of deformation) of the fluid, i.e. Newton's law of viscosity (Eqn. (2. 1)):

$$\tau = \frac{F}{A} \propto \frac{u_x}{y} \propto \frac{du_x}{dy} \qquad\qquad \textbf{(2. 2)}$$

2.1.3 Flow through a Capillary

2.1.3.1 Derivation of the Hagen-Poiseuille Equation

Much of the theory on the flow of a Newtonian material through a capillary is centred on the derivation of the Hagen-Poiseuille equation which relates pressure drop to volumetric flow rate. For fluid flowing through a capillary, due to the geometry, the shear rate (and shear stress) are a function of radial position i.e. distance from the capillary axis. Shearing is highest at the walls of the capillary and lowest at the centre.

The theory that follows derives the Hagen-Poiseuille equation and is based on laminar (streamlined) flow through a perfectly cylindrical, horizontal capillary. Flow through a capillary is generally classed as streamlined if the Reynolds number (Re) is less than 2000[1]. Details of the Reynolds numbers encountered in the capillary experiments carried out here in this thesis are given in Section 2.2.

$$Re = \frac{inertial\ forces}{viscous\ forces}$$

$$Re = \frac{\rho u_{avg} d}{\eta} \qquad\qquad \textbf{(2. 3)}$$

Here ρ is the fluid's density, u_{avg} is the average velocity of fluid in the capillary and d is the inner diameter of the capillary.

Force Balance for Fluid Flowing Through a Capillary

The pressure change due to friction (ΔP) along a length of capillary can be related to the shear stress at the capillary walls (τ_w). A force balance across a horizontal capillary of length (l) and inner radius ($\mathcal{R}$) is given in Eqn. (2. 4) (see Figure 2. 2).

$$(-\Delta P)\pi \mathcal{R}^2 = 2\pi \mathcal{R} l \tau_w \qquad\qquad \textbf{(2. 4)}$$

A force balance can also be taken across a central core of fluid of radius s, as given in Eqn. (2. 5). Note that the pressure drop per unit length $\left(\frac{\Delta P}{l}\right)$ is independent of radial position.

$$(-\Delta P)\pi s^2 = 2\pi s l \tau_s \qquad\qquad \textbf{(2. 5)}$$

Here, τ_s is the shear stress at a distance s from the capillary axis.
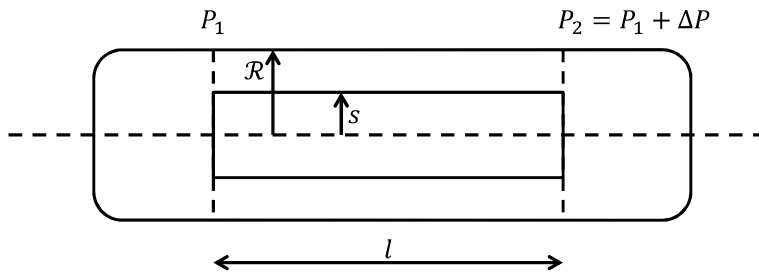
Figure 2. 2
Diagram showing a central core of fluid in a capillary.

Velocity Profile for Laminar Flow in a Capillary

The velocity profile over a cross section of a capillary is parabolic, as shown in Figure 2. 3. This is a result of the shear stress applied to the fluid varying with distance from the capillary axis. An equation that describes the velocity as a function of distance from the capillary axis can be derived as follows.
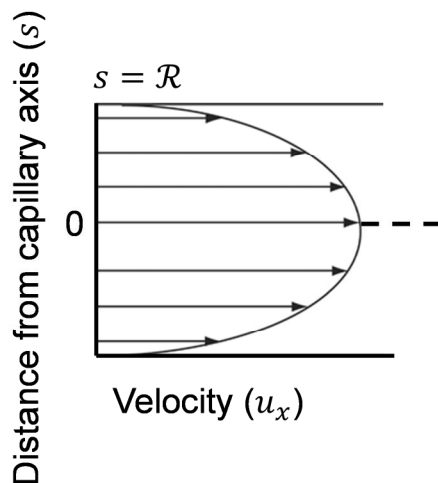
Figure 2. 3
Velocity profile across a capillary.

Assuming a Newtonian fluid and taking the definition of shear stress being equal to the viscosity multiplied by the velocity gradient (Newton's law of viscosity), the shear stress in terms of the distance from the capillary axis can be written as:

$$\tau_s = -\eta \frac{du_x}{ds} \qquad\qquad \text{(2. 6)}$$

The negative sign in present since $\frac{du_x}{ds}$ is negative: as s increases, u_x decreases.

Eqn. (2. 6) can be substituted into the force balance taken across a central core of fluid of radius s (Eqn. (2. 5)) giving:

$$(-\Delta P)\pi s^2 = 2\pi s l\left(-\eta\frac{du_x}{ds}\right) \qquad \textbf{(2. 7)}$$

This can be rearranged to give:

$$\Delta P s = 2l\eta\frac{du_x}{ds} \qquad \textbf{(2. 8)}$$

Eqn. (2. 8) can be separated and integrated and no slip boundary conditions ($u_x = 0$ when $= \mathcal{R}$) can be applied.

$$\int_0^{u_x} du_x = \frac{\Delta P}{l}\frac{1}{2\eta}\int_{\mathcal{R}}^{s} s\, ds \qquad \textbf{(2. 9)}$$

$$u_x = \frac{(-\Delta P)}{l}\frac{1}{4\eta}(\mathcal{R}^2 - s^2) \qquad \textbf{(2. 10)}$$

Equation (2. 10) shows that the velocity across a capillary's cross section has a parabolic variation with distance from the capillary axis. The maximum velocity (u_{max}) occurs when $s = 0$, at the centre of the capillary:

$$u_{max} = \frac{1}{4\eta}\frac{(-\Delta P)}{l}\mathcal{R}^2 = \frac{1}{16\eta}\frac{(-\Delta P)}{l}d^2 \qquad \textbf{(2. 11)}$$

The fluid velocity therefore reaches a maximum at the centre of the capillary and is zero at the capillary walls.

The ratio of velocity at position s (u_x) to the maximum velocity (u_{max}) is:

$$\frac{u_x}{u_{max}} = 1 - \frac{s^2}{\mathcal{R}^2} \qquad \textbf{(2. 12)}$$

Volumetric Flow rate in a Capillary

To determine the volumetric flow rate (Q) in a capillary, a capillary's cross section can be split into annular elements, as shown in Figure 2. 4. An annulus can be considered to be between radius s and $(s + ds)$. It can be assumed that the velocity is constant within a thin annular element.
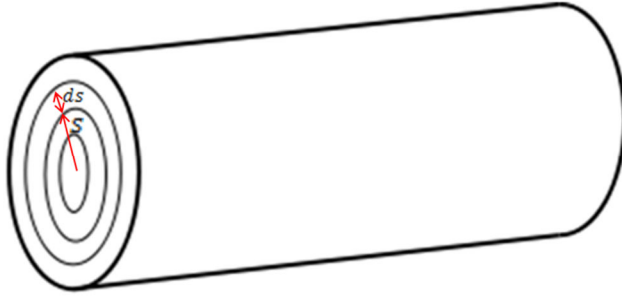
Figure 2. 4
Cross section split into annular elements.

The volumetric flow rate in an annulus is:

$$dQ = u_x\, 2\pi s\, ds \qquad \textbf{(2. 13)}$$

The total volumetric flow rate can be found by integrating Eqn. (2. 13) across the whole capillary radius, and Eqn. (2. 10) can be substituted in for u_x.

$$\int_0^Q dQ = 2\pi \int_0^{\mathcal{R}} u_x\, s\, ds \qquad \textbf{(2. 14)}$$

This yields the Hagen-Poiseuille equation, which relates pressure drop and volumetric flow rate for the laminar flow of Newtonian fluids:

$$Q = \frac{(-\Delta P)}{l}\frac{\pi}{8\eta}\mathcal{R}^4 \qquad \textbf{(2. 15)}$$

2.1.3.2 Fluid Velocities in a Capillary

The average velocity (u_{avg}) of fluid in the capillary is equal to the volumetric flow rate divided by the cross sectional area of the capillary:

$$u_{avg} = \frac{Q}{\pi \mathcal{R}^2} \qquad \textbf{(2. 16)}$$

The Hagen-Poiseuille equation (Eqn. (2. 15)) can be substituted in giving:

$$u_{avg} = \frac{(-\Delta P)}{l}\frac{1}{8\eta}\mathcal{R}^2 \qquad \textbf{(2. 17)}$$

As mentioned earlier, the maximum velocity (at the centre of the pipe) is given by:

$$u_{max} = \frac{1}{4\eta}\frac{(-\Delta P)}{l}\mathcal{R}^2 \qquad \textbf{(2. 18)}$$

Comparing the terms for the maximum and average velocities, it can be seen that:

$$u_{avg} = \frac{u_{max}}{2} \qquad \textbf{(2. 19)}$$

An expression for the velocity at a distance s from the capillary axis (u_x) in terms of the average velocity is therefore (combining Eqn. (2. 10) and Eqn. (2. 17)):

$$u_x = 2u_{avg}\left(1 - \frac{s^2}{\mathcal{R}^2}\right) \qquad \textbf{(2. 20)}$$

2.1.3.3 Shear Rates and Shear Stresses in a Capillary

As mentioned, the shear rate and shear stress are functions of radial position. Combining Eqn. (2. 4) and Eqn. (2. 5), the ratio of the shear stress at a distance s from the capillary axis (τ_s) to the shear stress at the capillary walls (τ_w) can be written as:

$$\frac{\tau_s}{\tau_w} = \frac{s}{\mathcal{R}} \qquad \textbf{(2. 21)}$$

This shows that the shear stress (and shear rate since $\tau = \eta\dot{\gamma}$ for Newtonian fluids) increases linearly from zero at the centre of the capillary to a maximum at the capillary walls (see Figure 2. 5). This is expected since the velocity profile across a capillary is a parabolic function of radial position. Since the shear rate is equal to the velocity gradient (derivative of a velocity profile), the shear stress and shear rate would be a linear function of radial position.
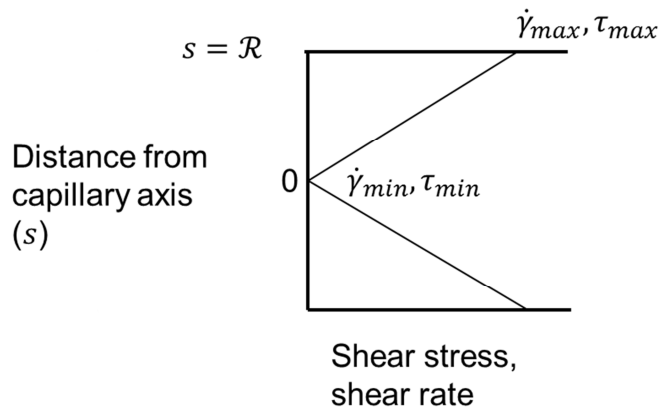
Figure 2. 5
Linear shear profile for capillary.

Average and Maximum Shear Rates

A term for the shear rate that occurs at any point from the capillary axis can be obtained by differentiating the velocity profile (Eqn. (2. 20)) with respect to s (the shear rate is the velocity gradient).

$$\dot{\gamma}(s) = -\frac{du_x}{ds} = \frac{4su_{avg}}{\mathcal{R}^2} \qquad \textbf{(2. 22)}$$

At the capillary walls, $s = \mathcal{R}$ and the maximum shear rate occurs. The maximum shear rate ($\dot{\gamma}_{max}$) is therefore:

$$\dot{\gamma}_{max} = \frac{4u_{avg}}{\mathcal{R}} \qquad \textbf{(2. 23)}$$

The average shear rate ($\dot{\gamma}_{avg}$) across the capillary can be found from:

$$\dot{\gamma}_{avg} = \frac{1}{\mathcal{R}-0}\int_0^{\mathcal{R}} \dot{\gamma}(s)\, ds = \frac{2u_{avg}}{\mathcal{R}} \qquad \textbf{(2. 24)}$$

Shear Stresses in a Capillary

For a Newtonian fluid, $\tau = \eta\dot{\gamma}$. Therefore, the equations for the maximum and average shear stress and how the shear stress varies as a function of radial position can be obtained by multiplying those deduced for the shear rate by the viscosity.

The shear stress as a function of the distance from the capillary axis is:

$$\tau(s) = \frac{4\eta s u_{avg}}{\mathcal{R}^2} \qquad \textbf{(2. 25)}$$

At the capillary walls, the shear stress is at a maximum (τ_{max}):

$$\tau_{max} = \frac{4\eta u_{avg}}{\mathcal{R}} \qquad \textbf{(2. 26)}$$

The average shear stress (τ_{avg}) that occurs across the capillary can be found from:

$$\tau_{avg} = \frac{1}{\mathcal{R}-0}\int_0^{\mathcal{R}} \tau(s)\, ds = \frac{2\eta u_{avg}}{\mathcal{R}} \qquad \textbf{(2. 27)}$$

2.1.4 Cylindrical Couette Flow
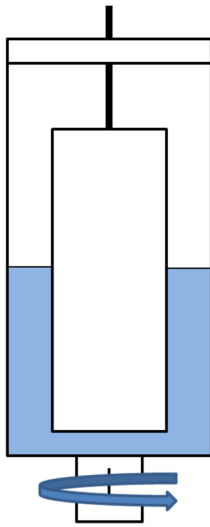
Figure 2. 6
Basic Couette cell diagram. Fluid (blue) is contained within the gap between the cylinders.

Cylindrical Couette flow arises from the shear flow in the gap between the vertical walls of concentric cylinders, one of which cylinders is rotated (Figure 2. 6). Commonly, the inner cylinder is rotated while the outer cylinder is kept fixed. With this arrangement, for low angular flow velocities, the flow is stable and is known as cylindrical Couette flow. Beyond a critical angular velocity, however, the flow may become unstable resulting in instabilities[4].

The instabilities are known as Taylor-Couette instabilities and are characterised by the formation of vortices superimposed on the laminar Couette flow. The vortices can cause energy redistributions within the gap due to high-speed fluid near the rotating inner cylinder being carried outwards and low-speed fluid near the stationary outer cylinder being carried inwards[5].

The vortices arise due to centrifugal instability. In simple Couette flow, the centrifugal force pushing fluid away from the rotating inner cylinder is balanced by the centripetal radial pressure gradient force pushing fluid inwards. If, however, a fluid particle is moved outwards slightly from its initial radius (perturbed even by an infinitesimal amount), it reaches a region where the inward force due to the pressure gradient is slightly less than the outward centrifugal force on the particle (the outward force is based on the particle's initial position because its angular momentum is conserved). This results in the particle continuing outwards. Similarly,

a fluid particle moved slightly inwards from its initial radius will continue inwards as the inward force due to the pressure gradient is slightly greater than the outward forces on the particle[6]. When rotational rates are low, these instabilities can be suppressed by viscosity since this damps out the perturbations. i.e. viscosity delays the onset of centrifugal instability [6, 7].

If the inner cylinder is kept fixed and the outer cylinder is rotated, these vortical instabilities do not occur[4]. This is because the instabilities only occur when the pressure gradient force decreases with increasing radius. This is the case when the inner cylinder is rotated and the outer cylinder is kept fixed. When the outer cylinder is rotated and the inner cylinder is kept fixed, the pressure gradient force increases with increasing radius, and the flow remains stable [6].

The theory outlined here is based on a fixed inner cylinder with a rotating outer cylinder, corresponding to what was done in all Couette flow experiments in this thesis. This arrangement was chosen to ensure that vortices did not form since they could have affected the nucleation process. The theory is also based on laminar (streamlined) flow. For Couette cells with a fixed inner cylinder and a rotating outer cylinder, the Reynolds number can be calculated from:

$$Re = \frac{\rho(2\pi N r_{out})(r_{out} - r_{in})}{\eta} \qquad \textbf{(2. 28)}$$

Critical Reynolds numbers depend on the geometry used and can be found experimentally[2, 8]. More information on the stability of the flow encountered during the experiments carried out here is given in Section 2.3.

2.1.4.1 Velocity Profile for Cylindrical Couette Flow

The velocity (v) profile across the gap of the Couette cell can be approximated by solving a momentum balance across the system (from the Navier-Stokes equation) assuming steady state operation$\left(\frac{\partial v}{\partial t} = 0\right)$.

$$\frac{\partial v}{\partial t} = \mu_k \left[\frac{\partial}{\partial r}\left(\frac{1}{r}\frac{\partial}{\partial r}(rv)\right)\right] = 0 \qquad \textbf{(2. 29)}$$

Here r is radial position, μ_k is kinematic viscosity and t is time.

The kinematic viscosity cannot equal zero, so

$$\left[\frac{\partial}{\partial r}\left(\frac{1}{r}\frac{\partial}{\partial r}(rv)\right)\right] = 0 \qquad \textbf{(2. 30)}$$

Integrating Eqn. (2. 30) with respect to r once gives:

$$\frac{\partial}{\partial r}(rv) = Cr \qquad \textbf{(2. 31)}$$

Here C is a constant.

Integrating again with respect to r gives:

$$rv = Ar^2 + B \qquad \textbf{(2. 32)}$$

Here A and B are constants.

Therefore, the velocity profile can be written as:

$$v(r) = Ar + \frac{B}{r} \qquad \textbf{(2. 33)}$$

The constants A and B can then be determined by using boundary conditions ($v = 0$ when $r = r_{in}$; $v = 2\pi N r_{out}$ when $r = r_{out}$). Here N is the rotational rate, r_{out} is the radius (inner) of the outer cylinder and r_{in} is the radius (outer) of the inner cylinder.

When $r = r_{in}$, $v = 0$ so Eqn. (2. 33) becomes:

$$0 = Ar_{in} + \frac{B}{r_{in}} \qquad \textbf{(2. 34)}$$

Rearranging for A gives:

$$A = -\frac{B}{r_{in}^2} \qquad \textbf{(2. 35)}$$

Substituting Eqn. (2. 35) back into the velocity equation (Eqn. (2. 33)) gives:

$$v(r) = B\left(\frac{1}{r} - \frac{r}{r_{in}^2}\right) \qquad \textbf{(2. 36)}$$

When $r = r_{out}$, $v = 2\pi N r_{out}$ so Eqn. (2. 36) becomes:

$$v(r) = B\left(\frac{1}{r_{out}} - \frac{r_{out}}{r_{in}^2}\right) = 2\pi N r_{out} \qquad \textbf{(2. 37)}$$

Rearranging for B gives:

$$B = \frac{2\pi N r_{out}}{\left(\frac{1}{r_{out}} - \frac{r_{out}}{r_{in}^2}\right)}$$

(2. 38)

Substituting Eqn. (2. 38) back into Eqn. (2. 36) gives an equation for the velocity profile (non-linear):

$$v(r) = 2\pi N r_{out} \frac{r_{out}}{r} \frac{\left(1 - \frac{r^2}{r_{in}^2}\right)}{\left(1 - \frac{r_{out}^2}{r_{in}^2}\right)}$$

(2. 39)

The velocity profile remained close to linear across the gap for conditions used in the experimental setups detailed in this thesis, as shown in Section 2.3. The velocity increased from zero at the stationary inner cylinder to $2\pi N r_{out}$ at the rotating outer cylinder, as shown in Figure 2. 7. The linear approximation for the velocity profile is:

$$v(r) = 2\pi N r_{out} \frac{r - r_{in}}{r_{out} - r_{in}}$$

(2. 40)
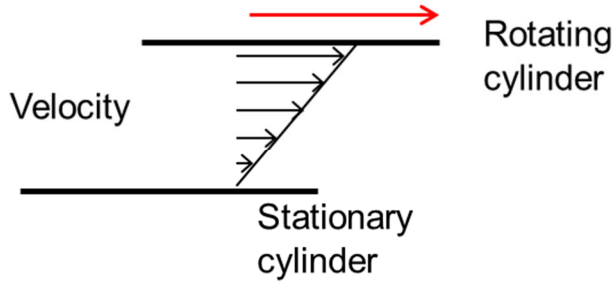
Figure 2. 7
Linear velocity profile across Couette cell's gap between the cylinders' vertical walls.

2.1.4.2 Shear Rates for Cylindrical Couette Flow

An expression for the shear rate across the gap can be found by differentiating the non-linear velocity profile (Eqn. (2. 39)) with respect to radius.

$$\dot{\gamma}(r) = \frac{dv(r)}{dr} = 2\pi N r_{out} \frac{\left(-\frac{1}{r^2} - \frac{1}{r_{in}^2}\right)}{\left(\frac{1}{r_{out}} - \frac{r_{out}}{r_{in}^2}\right)}$$

(2. 41)

The average shear rate across the gap can be calculated from:

$$\dot{\gamma}_{avg} = \frac{1}{r_{out} - r_{in}} \int_{r_{in}}^{r_{out}} \dot{\gamma}(r) \, dr = \frac{2\pi N r_{out}}{r_{out} - r_{in}}$$

(2. 42)

An expression for the shear rate across the gap can also be calculated based on a linear velocity profile (Eqn. (2. 40)) and is identical to Eqn. (2. 42):

$$\dot{\gamma}_{avg} = \frac{2\pi N r_{out}}{r_{out} - r_{in}} \qquad \textbf{(2. 43)}$$

For the cylinder arrangement used for the experiments in this thesis, due to the linear nature of the velocity profile, the shear rate varied only slighly across the gap. The shear rate was largest at stationary inner cylinder and lowest at the rotating outer cyliner.
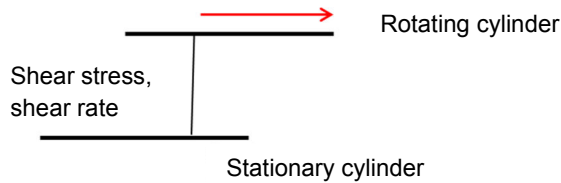
Figure 2. 8
Constant shear profile across Couette cell's gap between the cylinders' vertical walls.

2.1.4.3 Shear Stresses for Cylindrical Couette Flow

Using Newton's law of viscosity and Eqn. (2. 41), an expression for the shear stress that occurs across the gap can be obtained:

$$\tau(r) = \eta 2\pi N r_{out} \frac{\left(-\frac{1}{r^2} - \frac{1}{r_{in}^2}\right)}{\left(\frac{1}{r_{out}} - \frac{r_{out}}{r_{in}^2}\right)} \qquad \textbf{(2. 44)}$$

The average shear stress that occurs across the gap can be found from:

$$\tau_{avg} = \frac{\eta 2\pi N r_{out}}{r_{out} - r_{in}} \qquad \textbf{(2. 45)}$$

2.2 Capillary Setup

This section describes the general setup of the capillary flow device. The capillary setup was designed to allow the effect of controlled, laminar capillary flow on nucleation to be investigated. More specific information on the setup's use in glycine nucleation experiments is given in Chapter 4 Section 4.3.

2.2.1 Capillary Equipment Design and Operation

A capillary flow system was set up as shown in Figure 2. 9.
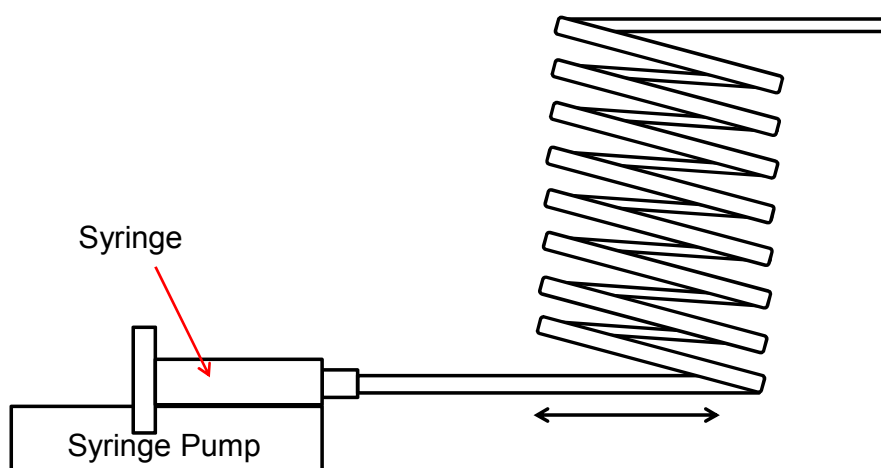
Figure 2. 9
General capillary setup.

12.5 metres of Nalgene PVC tubing (2 mm I.D., 4 mm O.D.) was attached to a 50 ml syringe. Close attachment was achieved by attaching a gauge 18 needle (1.27 mm O.D.) to the syringe tip using a luer adapter; 2 cm of 1 mm I.D. (2 mm O.D.) Nalgene PVC tubing was connected to the needle and the 2 mm I.D. tubing was connected over the 1 mm I.D. tubing. This ensured a very tight connection that was resistant to high pressure build ups. Due to the length of tubing used, it was coiled around a cylindrical vessel. The diameter of the cylindrical vessel was large (10 cm) compared to the diameter of the tubing. This was to ensure that bends were not tight and that the flow would follow typical Poiseuille flow.

The syringe was attached to a programmable syringe pump (Cole Parmer 74905-54). The pump allowed flow rates to be controlled and it could be operated in infusion and withdrawal modes sequentially, to result in continuous, periodic 'square wave' operation. This type of continuous operation was necessary since single

passes of the capillary did not provide sufficient residence times over which nucleation could occur.

To achieve this continuous operation, the capillary was first filled with solution (it had ~40 ml capacity) and a chosen volume of fluid (10 ml), which corresponded to ~3.2 m length of capillary, was withdrawn back into the syringe and then infused back into the capillary continuously at a chosen flow rate. This resulted in the fluid passing back and forth along the capillary periodically. The syringe pump bar pulled the syringe plunger at a constant velocity, withdrawing fluid into the syringe, resulting in steady flow at a fixed average velocity along the capillary in a negative direction. This was then followed by the syringe pump bar pushing the syringe plunger at a constant velocity, infusing fluid back into the capillary, resulting in steady flow at a fixed average velocity along the capillary in a positive direction. This was repeated, resulting in continuous, periodic flow back and forth along the capillary in 'square waves'. Visually, it could be seen that flow passed back and forth along the capillary.

2.2.2 Capillary Flow Parameters

A typical average velocity profile of fluid in the capillary is given in Figure 2. 10. Various parameters such as the average velocities and maximum shear rates used for the capillary experiments carried out for the work in this thesis are given in Table 2. 1.
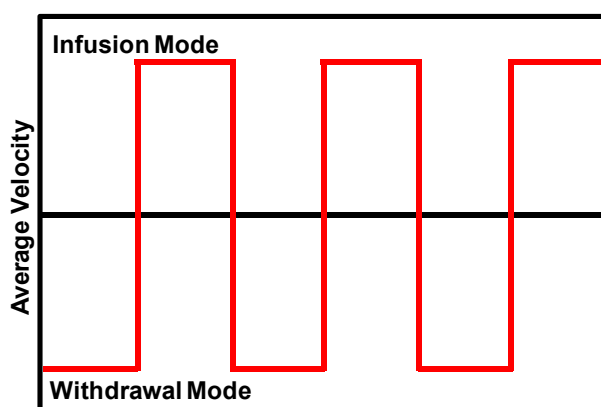
Figure 2. 10
Average velocity profile of fluid in the capillary. Scales can be deduced using the data in Table 2. 1.

Table 2. 1
Capillary setup parameters

Flow rate of Fluid in Capillary (ml/min)	Average Velocity of Fluid in Capillary (m/s)	Wall (Maximum) Shear Rate (s^{-1}) (The average shear rate is half the maximum)	Square Wave Frequency (min^{-1})	Reynolds Number (based on glycine solutions used in experiments)
25	0.125	500	1.25	200
50	0.25	1000	2.5	400
100	0.5	2000	5	800

Due to the 'square wave' nature of the operation and the low Reynolds numbers encountered, shear rates were calculated on the assumption of laminar flow of a Newtonian fluid in a horizontal, cylindrical capillary (theory outlined in Section 2.1.3). Entry lengths[2] (length of capillary before flow becomes fully developed L_{ent}) were calculated to be negligible compared with the length of the capillary and half-length of square waves (see Eqn. (2. 46)).

$$\frac{L_{ent}}{d} = 0.370 \exp(-0.148Re) + 0.0550Re + 0.260 \quad \textbf{(2. 46)}$$

As given in Table 2. 1, the frequency of the 'square waves' was low (maximum of 5 cycles per minute) and the amplitude (average velocity) was large in the capillary (0.13 ms^{-1} for the lowest shear rate used here and 0.5 ms^{-1} for the largest shear rate used here). The time taken for the syringe pump bar to reach its operating velocity was negligible compared to the duration at which it ran at its constant operating velocity (it would have taken a small amount of time for the syringe pump to stabilise pressure within the syringe). A lag time of under 1 s occurred when the syringe pump switched between infusion and withdrawal modes. This time was significantly greater than the relaxation time of the fluid[9].

2.3 Couette Setup

This section describes the general setup of the Couette flow device. The Couette cell setup was designed to allow the effect of controlled, laminar, cylindrical Couette flow on nucleation to be investigated. More specific information on its setup for use in glycine nucleation experiments is given in Chapter 4 Section 4.2, Chapter 5 Section 5.2 and Chapter 6 Section 6.3.

2.3.1 Couette Equipment Design and Operation

2.3.1.1 Initial Setup with Fixed Surface to Volume Ratio

The Couette flow system was set up as shown in Figure 2. 11 and Figure 2. 12. The setup used an outer cylinder with an inner diameter of 38 mm. The inner cylinder had an outer diameter of 30 mm. Cylinders were hollow and made of glass. The inner cylinder was kept fixed using a clamp stand, and the outer cylinder was rotated by means of a motor (Como Drills, RS Components 420-665) powered by a variable D.C. power supply. The motor had a 16:1 gearbox which allowed accurate control over the rotational rate of the outer cylinder. A digital tachometer was used to measure the rotational rate of the outer cylinder. A Perspex lid was present to minimise evaporation.
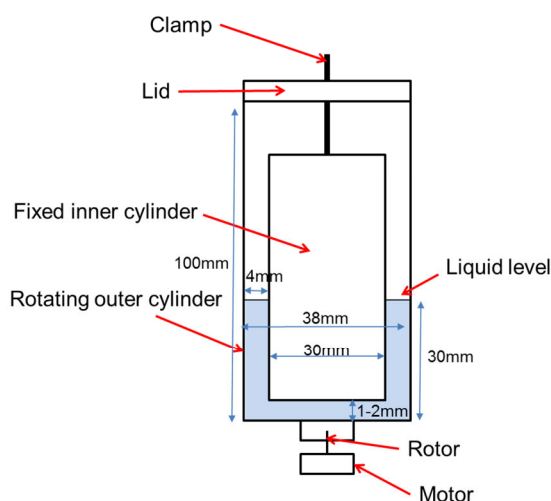
Figure 2. 11
Diagram of the initial Couette cell setup, with a surface to volume ratio of 5 cm^2/cm^3.

Figure 2. 12
Photograph of Couette flow setup.

The geometry resulted in a 4 mm gap between the vertical inner and outer cylinder walls. 15 ml solution was used in each of the Couette flow experiments carried out, resulting in the depth of solution in the gap between the vertical cylinder walls being approximately 3 cm. The area of glass surface that was exposed to each millilitre of solution contained within the gap between the vertical cylinder walls was 5 cm^2/cm^3.

A gap of 1-2 mm was kept between the base of the inner and outer cylinders. The flow in this bottom gap cannot be characterised quantitatively, so the setup was designed so that the volume of solution in the bottom gap was very low compared to the volume of solution contained in the gap between the vertical cylinder walls (which could be accurately quantified, as detailed in Section 2.1.4). Visual observations showed that nucleation began in solution contained within the gap between the vertical cylinder walls[8] (when solutions nucleated, they rapidly became turbid and the "cloudiness" originated from solution contained within the gap between the vertical cylinder walls, rather than solution in the base gap). Further evidence that the bottom gap was not having a dominant role on the nucleation came from a range of experiments that were carried out which involved using different diameters of inner cylinders (see Section 2.3.1.2 and Chapter 5). These showed that the setup that used the smallest diameter of inner cylinder resulted in the slowest nucleation for a particular average shear rate. Since an inner cylinder with a smaller diameter resulted in a larger gap between the inner and outer vertical cylinder walls, larger rotational rates had to be used to achieve the required shear rates. Despite higher rotational rates (and therefore higher shear rates in the gap at

the bottom), nucleation occurred more slowly. This confirmed that the controlled shear in the vertical gap between the cylinder walls had the main effect on nucleation[8].

2.3.1.2 Setups with Different Surface to Volume Ratios

In addition to the Couette flow system detailed in Section 2.3.1.1 with a fixed surface to volume ratio of 5 cm^2/cm^3, additional geometries were used to vary the surface area that a fixed volume of solution was exposed to. This was achieved by changing the diameter of the Couette cell's inner cylinder. Increasing the inner cylinder's diameter resulted in a narrower gap between the vertical walls of the inner and outer cylinder. This meant that a fixed volume of solution was exposed to a larger surface area. The converse is true for using a smaller diameter of inner cylinder. The setups used are shown in Figure 2. 13. When solution was exposed to a larger surface to volume ratio, the solution had a smaller free surface area (air-solution interface).

The setups were identical to the setup detailed in Section 2.3.1.1, but rather than using only an inner cylinder with a 30 mm outer diameter, 22 mm and 34 mm inner cylinders were used as well.

The 34 mm, 30 mm and 22 mm diameter inner cylinder geometries resulted in a 2mm, 4 mm or 8 mm gap respectively between the vertical inner and outer cylinder walls. 15 ml solution was used in each of the Couette flow experiments carried out, resulting in the depth of solution in the gaps between the vertical cylinder walls being approximately 6 cm, 3 cm and 1.5 cm for each setup respectively. The area of glass surface that was exposed to each millilitre of solution contained within the gap between the vertical cylinder walls was 10 cm^2/cm^3, 5 cm^2/cm^3 and 2.5 cm^2/cm^3 respectively.

A gap of 1-2 mm was kept between the base of the inner and outer cylinders for each setup. Since the gap between the bases of the cylinders was kept constant for each setup, the volume of solution in the bottom gap was constant for all experiments. This meant that the volume of solution that was exposed to the well-controlled flow conditions was constant for each experiment. This was important as the volume of solution affects nucleation statistics[10, 11].
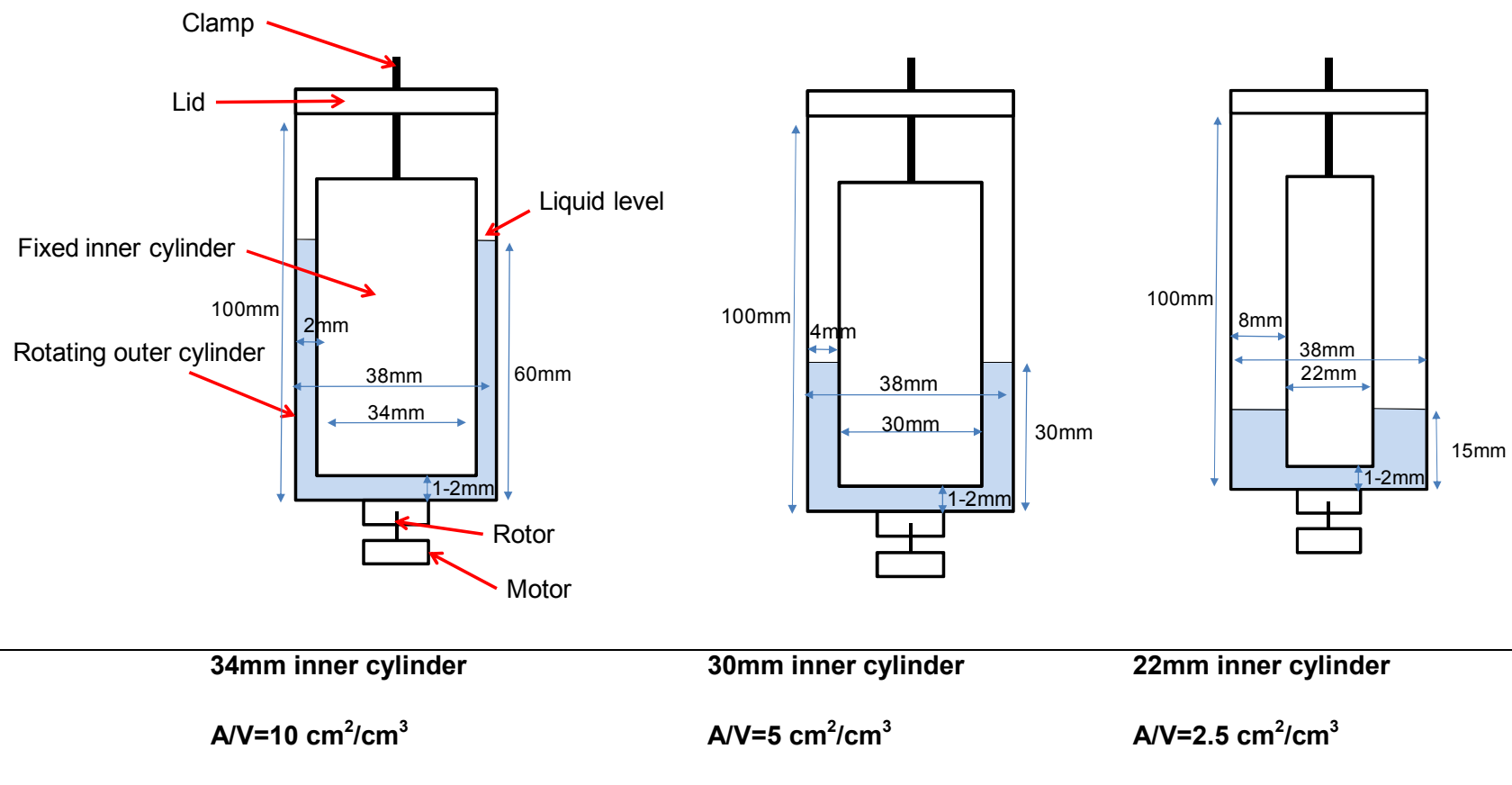
Figure 2. 13
Diagrams of the 3 Couette cell setups that were used to expose different surface areas to a fixed volume of solution.

2.3.2 Couette Flow Parameters

The range of outer cylinder rotational rates, average shear rates and Reynolds numbers that could be covered by each Couette cell setup is given in Table 2. 2. Calculations were based on the theory outlined in Section 2.1.4. The upper ranges were limited by equipment instabilities.

Table 2. 2
Ranges of rotational rates, shear rates and Reynolds numbers achievable using each setup.

Surface Area per Millilitre Solution Contained Within Vertical Cylinder Gap (cm^2/cm^3)	Rotational Rate of Outer Cylinder Range (RPM)	Average Shear Rate Range (s^{-1})	Reynolds Number Range
2.5	100-500	25-125	1100-5500
5	50-500	25-250	280-2800
10	25-250	25-250	70-700

In order to be able to accurately quantify the shear rates that occurred in the gap between the vertical cylinder walls in the Couette cells using the theory outlined in Section 2.1.4, checks were made to ensure that the flow remained streamlined over the conditions of the experiments carried out. Firstly, the fixed inner/rotating outer cylinder geometry did not result in the Taylor instabilities which would have occurred in a fixed outer/ rotating inner cylinder geometry for the conditions used[4, 8]. To ensure that the critical Reynolds number for the geometries used in the experiments was not surpassed, rheoscopic fluid (suspension of mica platelets that align with the flow) and dye injections were used in the Couette cells, and the flow was visualised for the range of conditions used in each experimental setup.

Even at the highest rotational rate used for each Couette cell geometry, the flow did not show significant turbulence (the rheoscopic fluid scattered light uniformly). Some minor turbulence (the light scattered by the rheoscopic fluid occasionally showed small, localised regions of heterogeneity) was observed with the geometry that used the smallest inner cylinder diameter (22 mm) for 500 rpm (125 s^{-1}) experiments. These conditions resulted in the highest Reynolds number and it was also more difficult to check that the cylinders were accurately aligned due to the relatively large gap between the vertical cylinder walls. These findings therefore suggested that flow

in the gap between the vertical cylinder walls was predominantly streamlined for the conditions studied. This meant that the shear rates in the gap between the two cylinders could be accurately quantified by solving the Navier-Stokes equation using the theory outlined in Section 2.1.4.

It was noted that large instabilities were observed experimentally when the inner cylinders were rotated and the outer cylinder was kept fixed, in agreement with what would be expected from theory[4]. Instabilities were also observed when cylinders were not concentrically aligned, as shown in Figure 2. 14.

Figure 2. 14
Images of cylinders containing rheoscopic fluid being rotated at 500 rpm (30 mm inner cylinder geometry) showing that turbulence was observed when the cylinders were not aligned concentrically.

The velocity profiles of fluid across the gap between the vertical cylinder walls were calculated using the equation derived from Navier Stokes (Eqn. (2. 39)). They were also calculated on the assumption of a perfectly linear velocity profile (Eqn. (2. 40)). The profiles obtained using the Navier-Stokes derivation showed a small departure from a perfectly linear profile. The largest departure was 20% and occurred when the 22 mm inner cylinder setup was used to produce a shear rate of 125 s^{-1}. The maximum departures from the linear profiles for each geometry are given in Table 2. 3. When shear rates are mentioned with regards to results in this thesis, average shear rates are quoted so the departure from linearity would not have affected this value (see Eqn. (2. 42)).

Table 2. 3
Maximum estimated departures from linearity for the Navier Stokes derived velocity profiles.

Inner Cylinder Diameter (mm)	Maximum Departure from Linearity	Corresponding Shear Rate (s^{-1})
22	20%	125
30	10%	250
34	5%	250

2.4 Conclusions

Flow devices in which well-characterised flow of Newtonian fluids could be obtained were designed and constructed. These were a capillary flow system and a cylindrical Couette flow cell. The capillary flow system was based on using a syringe pump to make fluid flow back and forth along a capillary, while the Couette flow setup was based on the flow between two concentric cylinders, the outer one of which was rotated. Checks and calculations were carried out to ensure that the flow was predominantly streamlined over the conditions of the experiments carried out for the work in this thesis. Methods of quantifying the flow in the Couette and capillary flow setups were also given.

The capillary flow system is used in Chapter 4 and the Couette flow setups are used in Chapters 4 to 6 to investigate the influence of controlled fluid shear on the nucleation of glycine from aqueous solution.

2.5 Summary

- Two flow devices (Couette cell and capillary system) were designed and constructed to allow quantifiable laminar flow conditions to be obtained.
- The capillary flow system was based on using a syringe pump to make fluid flow back and forth along a capillary.
- The flow in the capillary was typical Poiseuille flow for the conditions studied, with a parabolic velocity profile. The shear rate increased linearly from zero at the centre of the capillary to a maximum at the capillary walls.
- The Couette cell flow geometry was based on the flow between two concentric cylinders. The inner cylinder was kept fixed while the outer cylinder was rotated using a motor.
- The flow in the Couette cell was not affected by Taylor instabilities and remained predominantly streamlined for the conditions studied. The velocity profile was close to linear for the conditions studied so the shear rate remained approximately constant across the gap between the vertical cylinder walls.

2.6 References and Nomenclature
2.6.1 References

(1)   Blackhurst; Harker; Coulson; Richardson, *Coulson and Richardson's Volume 1*. 6th ed.; Butterworth-Heinemann Ltd: 1999.

(2)   Green, D.; Perry, R., *Perry's Chemical Engineers' Handbook*. 8 ed.; McGraw-Hill Professional: 2007.

(3)   Myerson, A., *Handbook of Industrial Crystallization*. 2nd ed.; Butterworth-Heinemann: 2001.

(4)   Taylor, G. I., Stability of a viscous liquid contained between two rotating cylinders. *Philosophical Transactions of the Royal Society of London Series a-Containing Papers of a Mathematical or Physical Character* **1923,** 223, 289-343.

(5)   Wereley, S. T.; Lueptow, R. M., Spatio-temporal character of non-wavy and wavy Taylor-Couette flow. *Journal of Fluid Mechanics* **1998,** 364, 59-80.

(6)   Lueptow, R. Taylor-Couette flow, Scholarpedia. Accessed 04/05/15. http://www.scholarpedia.org/article/Taylor-Couette_flow

(7)   Avila, M. Taylor-Couette Flow. Accessed 04/05/15. http://wwwfa.upc.es/websfa/fluids/marc/tc.php?lang=eng

(8)   Forsyth, C.; Mulheran, P. A.; Haw, M. D.; Burns, I. S.; Sefcik, J., Influence of Controlled Fluid Shear on Nucleation Rates in Glycine Aqueous Solutions. *Crystal Growth & Design* **2015,** 15, (1), 94-102.

(9)   Mullin, J. W., *Crystallization*. 4th ed.; Heineman: 2002.

(10)   Kadam, S. S.; Kramer, H. J. M.; ter Horst, J. H., Combination of a Single Primary Nucleation Event and Secondary Nucleation in Crystallization Processes. *Crystal Growth & Design* **2011,** 11, (4), 1271-1277.

(11)   Kubota, N., Effect of sample volume on metastable zone width and induction time. *Journal of Crystal Growth* **2012,** 345, (1), 27-33.

2.6.2 Main Nomenclature

A = area of plate or constant

B = constant

C = constant

d = capillary diameter (inner)

F = shearing force

l = pipe length

L_{ent} = entry length

N = rotational rate

ΔP = pressure change due to friction

Q = volumetric flow rate

$\mathcal{R}$ = inner radius of capillary

r = radial position

r_{in} = radius (outer) of the inner cylinder

r_{out} = radius (inner) of the outer cylinder

s = distance from pipe axis

t = time

u_{avg} = average velocity in x direction

u_{max} = maximum velocity in x direction

u_x = velocity in x direction

v = velocity

y = perpendicular distance from surface

$\dot{\gamma}$ = shear rate

$\dot{\gamma}_{avg}$ = average shear rate

$\dot{\gamma}_{max}$ = maximum shear rate

η = dynamic viscosity

μ = kinematic viscosity $\frac{\eta}{\rho}$

ρ = solution density

τ = shear stress

τ_{avg} = average shear stress

τ_{max} = maximum shear stress

τ_s = shear stress at a distance s from the capillary axis

τ_w = shear stress at capillary walls

3. Induction Time Measurements

Chapter Outline and Contents

To gain an improved understanding of the nucleation of glycine from aqueous solution while the solution was subjected to controlled fluid shear, induction times of glycine from solution were measured while the glycine solutions were sheared in the capillary and Couette flow setups described in Chapter 2. The measured induction times were then used to estimate nucleation rates, which is discussed in Chapter 4 and Chapter 5[1, 2]. This method of obtaining nucleation rates from induction times was advantageous over the methods outlined in Chapter 1 Section 1.6 as it was simple and could be done in-situ without hindering the controlled flow conditions.

In this chapter, the methods used to measure induction times are described. Three main methods were used: (1) visual observation, (2) imaging or (3) simultaneous scattering and transmission measurements. When induction times were reached, solutions became turbid over a short timescale, leading to a sharp increase in scattering, decrease in transmission and increase in the mean pixel intensity of the images. Induction times were obtained by finding the point of inflection of the rising (or falling) signals. The imaging and transmission/ scattering methods gave complementary results, which suggested that they detected induction times with similar resolutions. The transmission/ scattering method had more scope than the imaging method to obtain further information on the system under investigation, such as particle sizes and number concentrations (see Chapter 6 and Chapter 8).

For capillary flow experiments, only the visual method of obtaining induction times was used. For Couette flow experiments, a mixture of visual, imaging and scattering/ transmission measurements were used. Experimental procedures and results from the induction time experiments are given in Chapter 4 and Chapter 5.

This chapter covers:

- Basic theory on induction time measurements.
- The setup and method of obtaining induction times visually (qualitative) and from images and transmission/ scattering measurements (quantitative).
- A comparison of the quantitative methods.

3.1 Induction Times

The induction time is a measure of the 'ability' of a system to remain in a metastable state[3]. A period of time usually exists between the achievement of supersaturation and the appearance of crystals so measuring induction times involves measuring the time between the creation of supersaturation and the formation of a new crystalline phase[4]. The induction time is sensitive to factors such as the level of supersaturation, agitation, the presence of impurities, temperature and viscosity[4].

3.1.1 Experimental Methods of Measuring Induction Times

There are various experimental techniques that can be used to measure induction times and these will detect induction times with different resolutions. The induction times measured may therefore not have identical values when measured by different techniques. The best way to measure induction times is to continuously monitor a property they will change when nucleation and crystal growth proceed. Crystals have to grow to reach detectable levels. Properties that can potentially be monitored include[5]:

Temperature- nucleation and growth reduces the free energy of the system so usually heat is evolved. Direct temperatures could be measured or differential scanning calorimetry could be used.

Volume- when a solution nucleates (and the nucleated crystals then grow), its volume may change by a measurable amount. A technique such as dilatometry could be used to measure the volume of a crystallising system with time.

Concentration- when a solution nucleates (and the nucleated crystals then grow), the solution concentration will decrease. Concentration dependent physical properties, such as conductivity, density or refractive index could therefore be monitored over time.

Optical Transmittance- nucleation and growth cause the turbidity of the solution to change so transmission, scattering, etc. can be measured to monitor this. Changes in turbidity or the formation of visible crystals can be detected by eye, however, this is error prone due to the variability of human judgement.

3.1.2 Principles of Induction Time Measurements

From classical nucleation theory (presented in Chapter 1 Section 1.3.1), one would not expect induction times to exist. It assumes ideal steady-state conditions whereby nuclei are present immediately once the solution becomes supersaturated[4]. The induction time can therefore be considered comprised of multiple parts. These include a relaxation time (t_r) which is the time required for the system to achieve a quasi-steady state distribution of molecular clusters; a nucleation time (t_n) which is the time required to form a stable nucleus; and a growth time (t_g) which is the time for the nucleus to grow to a detectable size.

The induction time (t_{ind}) can therefore be considered:

$$t_{ind} = t_r + t_n + t_g \qquad \textbf{(3. 1)}$$

It is thought to be difficult (even impossible) to determine these quantities separately[4]. The relaxation time depends strongly on the system viscosity and therefore diffusivity- in low viscosities the relaxation time can be very low, but in more viscous systems, it can be high. It has been shown to be unimportant in aqueous solutions of moderate supersaturation and viscosities[6], however, in some cases, for example at very low supersaturation, it cannot be ignored[7]. The nucleation time will depend on the supersaturation and hence critical nucleus size, and the growth time will depend on the size that the nuclei are detectable (this could be a size at which secondary nucleation of a crystal sharply increases, causing cloudiness of a previously transparent solution[8]). It cannot be assumed that the growth rate of the nucleus is the same as that of a macro-crystal; there will likely be a difference in mechanism and rate[4].

A latent period lag time may also occur in some systems, and this can be considered the onset of a significant change in the system e.g. substantial solution de-supersaturation/ significant nucleation.

The times mentioned are illustrated in Figure 3. 1. Supersaturation is created at time zero (A) and crystals are detected after an induction time t_{ind} (B). The nucleation time t_n (B') is less than the induction time since critical nuclei have to grow to a detectable size. In some systems, after point B, no change may occur for a considerable time until point C. Point C can be considered the end of the latent period, t_{lp}. After the end of the latent period, rapid desupersaturation can occur (D);

crystal growth and/or nucleation predominate during this region and supersaturation is depleted. Eventually, the system will reach equilibrium (E).
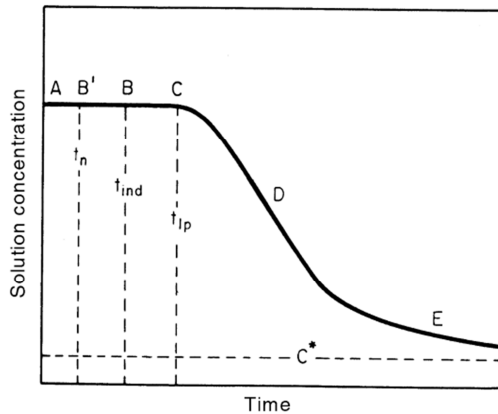
Figure 3. 1
De-supersaturation curve[4].

If the relaxation time can be ignored, the induction time becomes a function of the nucleation and growth times. Three cases exist:

$t_n \gg t_g$; $t_n \approx t_g$ and $t_n \ll t_g$

In the simplest case for true homogeneous nucleation, assuming $t_n \gg t_g$ and t_r is negligible, the rate of primary nucleation (J) is inversely proportional to the induction time[4].

$$t_{ind} \propto \frac{1}{J} \qquad\qquad (3.\ 2)$$

The other cases are more complicated and are outlined in textbooks[3, 7]. Calculating nucleation rates from these methods can be difficult since they require knowledge of quantities that can be difficult to measure, such as wetting angles, pre-exponential factors, interfacial tension and diffusion coefficients.

An easier method that allows the rate of primary nucleation and growth times to be estimated from the probability distributions of induction times has been proposed by Jiang and ter Horst[1]. This method is used widely in this thesis and is discussed in Chapter 4 and Chapter 5.

3.2 Induction Times from Visual Monitoring

For some experiments carried out for the work done in this thesis, induction times were measured visually. For these, a torch was used to illuminate the sample under investigation and the sample was monitored visually. The induction times measured through this method would have had significant uncertainty. Therefore, more quantitative methods of measuring induction times (imaging/ transmission/ scattering measurements) were used where possible.

The quantitative methods were not possible to use with capillary experiments due to the poor optical quality of the capillaries. The quantitative methods could also not be used for experiments where the turbidity of the solution did not change significantly with the onset of crystallisation, for example, in experiments where solutions were unsheared. When solutions were not sheared, only a small number of crystals formed in the solutions and these were not sufficient to have an effect on the measured signals. In experiments where solutions were sheared, a large number of crystals generally formed and solutions became turbid so induction times for these experiments could be easily detected by the quantitative means.

3.3 Induction Times from Imaging

A simple way to measure induction times quantitatively was achieved by using a camera to image the ambient light scattered by incipient solutions as they were sheared in the Couette flow setups. Images could then be analysed to find the induction time.

A webcam (Logitech Webcam 300) was used to take images. It was placed 15cm from the Couette flow device. Images were taken periodically (once every second) using time lapse software (TNL Soft Solutions). To ensure that measurements could be fairly compared, automatic camera settings (brightness, exposure time, etc.) were switched off and it was ensured that identical camera settings were used each time the experiments were run. It was also ensured that background lighting was constant for each experiment. Matlab code was written to allow the average pixel intensity in a region of interest in the images to be calculated and plotted as a function of time. The main steps in the code were:

- Loading images and converting them to grey scale. The formula[9] used to convert to grey scale was $0.2989 Red + 0.5870 Green + 0.1140 Blue$. The formula meant that the luminance of the grey scale image equalled the luminance of the original colour image[9].

- Subtracting a background image from every image. The first image taken (time zero) was used as the background image.

- Allowing the user to select a region of interest from the image.

- Calculating the mean pixel intensity (plus the standard deviation) in the region of interest for each image with the background subtracted.

- Using the time elapsed between each image to plot the mean pixel intensity as a function of time.

An example plot of the mean pixel intensity obtained as a function of time is given in Figure 3. 2. When the induction time was reached, solutions became turbid over a short timescale, leading to a sharp increase in mean pixel intensity. Induction times were obtained by finding the time intercept of the main inflection in the average pixel intensity plots, as shown in Figure 3. 2.
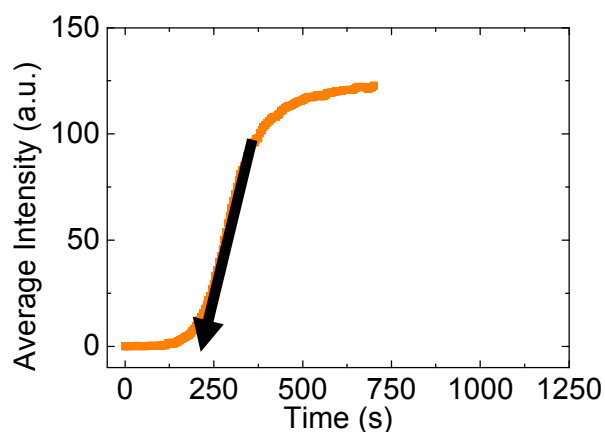
Figure 3. 2
Example plot of mean pixel intensity as a function of time for a solution that nucleated after an 'induction time' and rapidly became turbid.

This method of obtaining induction times was simple and reliable, but its main drawback was that little further information (other than gradients, etc.) could be easily extracted from the images, unlike the transmission/ scattering detection method.

3.4 Induction Times from Transmission/ Scattering Measurements

A novel, custom made instrument was setup to take simultaneous transmission and scattering measurements of solutions as they were sheared in the Couette flow setups. Software was written to record the measured data and induction times could be deduced from the measurements.

This method of obtaining induction times offered greater scope than the imaging method since transmission and scattering data could potentially be used to obtain further information on the system. For example, models can be developed and the transmission data can be used to calculate the number concentration of crystals formed (see Chapter 8). Scattering data can be used to estimate the sizes of particles in a system (see Chapter 6). The ratio of scattering and transmission data can also potentially be used to monitor polymorph formation[10].

3.4.1 Hardware Setup

Hardware capable of measuring the intensity of laser light incident on a sample, transmitted through a sample and scattered by a sample was set up as shown in Figure 3. 3. This setup was similar in principle to one used previously for in-situ monitoring of stirring effects on crystallisation of carbamazepine[10], but was redesigned and set up for the purposes of the experiments here.

Figure 3. 3
Setup of the instrument that was used to measure scattering and transmission simultaneously from solutions as they were sheared in a Couette flow device.

The beam from a helium-neon laser (Thorlabs HRP170; 17 mW; beam diameter ~ 1 mm) was directed through the centre of the Couette cell, via a range of neutral density filters (if required). The purpose of the neutral density filters w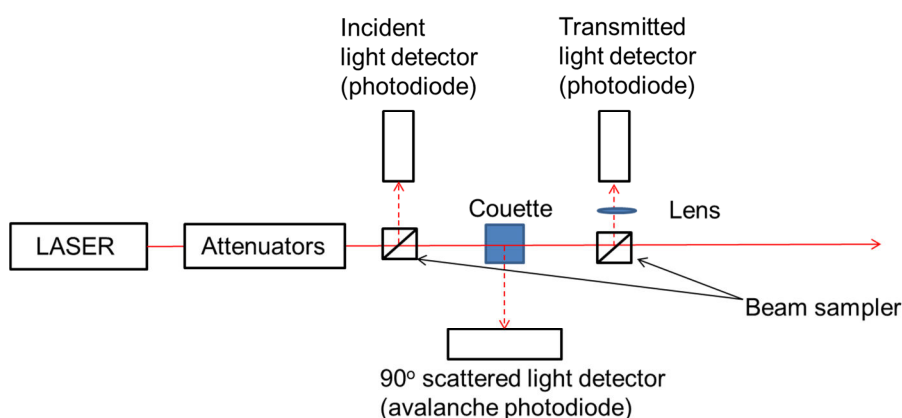as to attenuate the laser beam to ensure that the intensity of light incident on the detectors was suitably low so that they would not become saturated. The transmission % of the five filters available is given in Table 3. 1.

Table 3. 1
% Transmission of neutral density filters. (Attenuators on Figure 3. 3.)

Neutral Density Filter (numbered on hardware)	Transmission (%)
1	7.4
2	1.3
3	0.1
4	0.1
5	33.3

To measure the intensities of the incident and transmitted beams, beam sampler plates were used to weakly reflect a portion of the beam onto photodiode detectors (Thorlabs PDA36A-EC). The beam samplers made use of Fresnel reflection- due to differences in refractive index of air and the beam sampler (silica), part of the beam incident on the plate was reflected and part was transmitted. One side of the beam sampler was uncoated while the other had an anti-reflection coating to minimise ghosting. The laser was incident on the uncoated side. A lens (25 mm focal length bi-convex lens (Thorlabs LB1471-A)) was placed between the beam sampler for the transmitted light and the transmitted light detector. This was necessary as due to cylinder rotation, the transmitted beam moved slightly meaning that the sample of transmitted light sometimes failed to reach the detector. The lens de-magnified the sampled light and focussed it onto the detector, reducing the movement of the sample of light. The lens was placed approximately 10 cm from the beam sampler (S_o) and 3.3 cm from the detector (S_i). This resulted in magnification $\left(M = \frac{-S_i}{S_o} \right)$ of around 0.3. A more sensitive avalanche photodiode (Hamamatsu APD C5460) was used to measure the intensity of light scattered at 90º.

The photodiode detectors worked in the photoconductive (reverse bias) mode. Light incident on the detectors was converted to current and since the current was passed through a known resistance, the output measured was a voltage. The measured voltage was indicative of the illumination since the voltage produced was approximately linearly proportional to the intensity of light incident on the detector.

The detectors were connected to the computer using a LabVIEW connector block (BNC-2120). Signals were digitised by a data-acquisition card (National Instruments PCI-6221) and recorded using LabVIEW.

When experiments were carried out, a box was placed over the equipment or the lights were switched off to ensure that the intensity of laser light reaching the detectors was significantly greater than the intensity of background light reaching the detectors.

3.4.2 Data Acquisition Software

Software was written using LabVIEW to record the signals output from the detectors[11]. The user could choose a sampling rate (number of measurements per minute) on the front panel (Figure 3. 6) and the LabVIEW code accordingly recorded the voltages output from the detectors. Plots of the voltages measured as a function of time updated on the front panel so that the user could monitor the measurements. Once the measurements had been carried out for the desired duration, the code saved 4 columns of data: time, incident light detector voltage, transmitted light detector voltage and scattered light detector voltage. Here, the main purposes of the LabVIEW code (Figure 3. 4) are described. Labelled (numbered) diagrams are also given (Figure 3. 5) and each label is explained.

3.4.2.1 Code Description

User Inputs

The first step of the code was to obtain any parameters input by the user from the front panel. These were:

- The sampling rate (measurements to be taken per minute)
- Boolean status (on or off). If the Boolean was off, the code did not execute the while loop.

Rate of Measurements

The sampling rate input by the user was used to ensure that measurements were taken at the desired rate. The sampling rate was converted to the time between measurements in milliseconds. This value entered the while loop and became the millisecond multiple. The millisecond multiple was connected to a function that had a millisecond timer. The timer function waited until the timer's value became a multiple of the millisecond multiple before executing the next loop. These features resulted in the while loop running according to the sampling rate input by the user.

Obtaining Time Data

The time corresponding to each loop was calculated. There were three elements to the timing aspect of the code:

1. Collecting all of the time data, for use after all of the loops had run.
2. Obtaining time data (current and past) so that graphs could be updated on the front panel while the program was running.
3. Displaying how much time had passed since the program was started, on the front panel.

1. A millisecond timer (tick count) within the while loop got the time from the computer's clock at the start of each loop. These values exited the loop and formed an array. An index array function was used to extract the computer's clock value for the first loop (index 0). This clock value from the first loop was then subtracted from the clock value for each loop to deduce the time (in milliseconds) since the execution of the first loop. Times in milliseconds were then converted to seconds. These steps resulted in the formation of an array of complete time data once all of the loops had been executed i.e. Boolean switched to off.

2. Shift registers were used to pass information from one execution of the loop to subsequent executions. In this case, the time from computer's clock at the start of each previous loop was passed to the subsequent loops. This allowed graphs to be plotted on the front panel that contained the results from the previous loops, plus the current loop. The graphs updated with each loop, allowing 'live' monitoring.

The time from the computer's clock at start of a loop was added to an array that contained the times from the computer's clock at the start of each previous loop. An index array function was used to extract the computer's clock value for the first loop (index 0). This clock value for the first loop was then subtracted from the clock value

for each loop to deduce the time (in milliseconds) associated with each loop. The times were converted from milliseconds to seconds and represented the time data for the current and all previous loops.

3. The clock value for the first loop was subtracted from the clock value for the current loop to deduce the time (in milliseconds) that had passed since the first loop. This time was converted from milliseconds to seconds and was displayed on the front panel.

Obtaining Scattering, Transmission and Incident Signal Data

Each time the while loop was executed, a stacked sequence structure ran within the loop. With the stacked structure, frames operated sequentially and each frame ran a data acquisition task to record the voltage output from a detector. Since there were three detectors, three frames were run sequentially.

Each data acquisition task took 20,000 measurements at a rate of 200,000 Hz. These raw data exited the stacked structure and were plotted and displayed on the front panel (the times displayed on the plots were arbitrary values). The mean of the 20,000 measurements was also found and was displayed on the front panel. Mean values of the 20,000 measurements were found since the individual values showed some noise fluctuations and would have resulted in too much data being collected.

The mean values exited the loop and formed arrays. Three arrays were therefore built up and contained the mean value of the transmitted, incident or scattered light signals for each loop. Once all the loops had run (Boolean was switched off), the arrays therefore contained the complete set of mean transmitted, incident and scattered signals.

Shift registers were used to pass information on the measurements from one execution of the loop to subsequent executions. Here, the mean values of the transmitted, incident or scattered light signals from previous loops were passed to the subsequent loops. This allowed graphs to be plotted on the front panel that contained the results from the previous loops, plus the current loop, allowing 'live' monitoring. Describing this stage in more detail, the mean transmitted, incident and scattered light signals from a loop were added to arrays that contained the mean transmitted, incident and scattered light signals from each previous loop. These

were bundled into clusters with the time data associated with each loop. The clusters were then plotted individually on the front panel.

Displaying and Saving Data

Once the Boolean was switched to off, the while loop stopped running and the complete mean signal data arrays and time data array were bundled into clusters (each cluster had time data and either incident, scattered or transmitted light data) and the clusters were concatenated into a single array which was input to a multi-plot XY-Graph function, with each cluster forming a plot on the graph. This was displayed on the front panel.

The complete mean signal data arrays and time arrays were concatenated into a single, larger array. This was then sent to a function that wrote the data to a text file. The data were transposed and had 4 columns (time, incident light data, transmitted light data and scattered light data).

3.4.2.2 Diagrams and Key

Main features of the code have been labelled between 1 and 30 (Figure 3. 5). A brief description of what is represented by each label is given:

1. Gets sampling rate from front sheet.

2. Calculates time between each measurement (in minutes).

3. Converts time between each measurement from minutes to seconds.

4. Converts time between each measurement from seconds to milliseconds.

5. This value is the 'millisecond multiple' and is fed to the loop.

6. The Boolean status is obtained from the front panel. The loop only runs if the status is on.

7. The code waits until a millisecond multiple has passed before executing the next loop.

8. A millisecond timer (tick count) within the while loop gets the time from computer's clock at start of each loop.

9. These computer clock values exit the loop and form an array.

10. An index array function is used to extract the computer's clock value for the first loop (index 0).

11. The clock value for the first loop is subtracted from the clock value for each loop to deduce the time (in milliseconds) associated with each loop.

12. The times are converted from milliseconds to seconds and represent the time data.

13. Shift registers are used to pass information from one execution of the loop to subsequent executions. The time from computer's clock at the start of each previous loop is passed to the subsequent loops. This ultimately allows graphs to be plotted on the front panel that contain the results from the previous loops, plus the current loop, allowing 'live' monitoring.

14. The time from the computer's clock at the start of a loop is added to an array that contains the time from computer's clock at the start of each previous loop.

15. An index array function is used to extract the computer's clock value for the first loop (index 0).

16. The clock value for the first loop is subtracted from the clock value for each loop to deduce the time (in milliseconds) associated with each loop.

17. The times are converted from milliseconds to seconds and represent the time data for the current and all previous loops.

18. The clock value for the first loop is subtracted from the clock value for the current loop to deduce the time (in milliseconds) that has passed since the first loop.

19. The time is converted from milliseconds to seconds and displayed on the front panel.

20. Each time the while loop is run, a stacked sequence structure runs within the loop.

21. With the stacked structure, frames operate sequentially and each frame runs a data acquisition task to record the voltage output from a detector. Since there are three detectors, three frames are run sequentially. Each data acquisition task takes 20,000 measurements at a rate of 200,000 Hz.

22. The raw data exit the stacked structure and are plotted and displayed on the front panel (the times displayed on the plots are arbitrary values). The mean of the 20,000 measurements is found and is displayed on the front panel.

23. The mean values exit the loop and form arrays.

24. Shift registers are used to pass the mean values of transmitted, incident or scattered light signals from previous loops to the subsequent loops.

25. The mean transmitted, incident and scattered light signals from a loop are added to arrays that contain the mean transmitted, incident and scattered light signals from each previous loop.

26. The mean signals from the previous and current loops are bundled into clusters with the time associated with each loop. These clusters are plotted individually on the front panel allowing 'live' monitoring.

27. Once the Boolean is switched to off, the while loop stops running and the mean value from the arrays containing the mean transmission, scattering and incident signal data are found and plotted on the front panel. These data were not useful for the work done here.

28. The mean signal data arrays and time data array are bundled into clusters.

29. The clusters are concatenated into a single array which is input to a multi-plot XY-Graph function, and each cluster forms a plot on the graph. This is plotted on the front panel.

30. The mean signal data arrays and time arrays are concatenated into a single, larger array. This is then sent to a function that writes the data to a text file. The data are transposed.
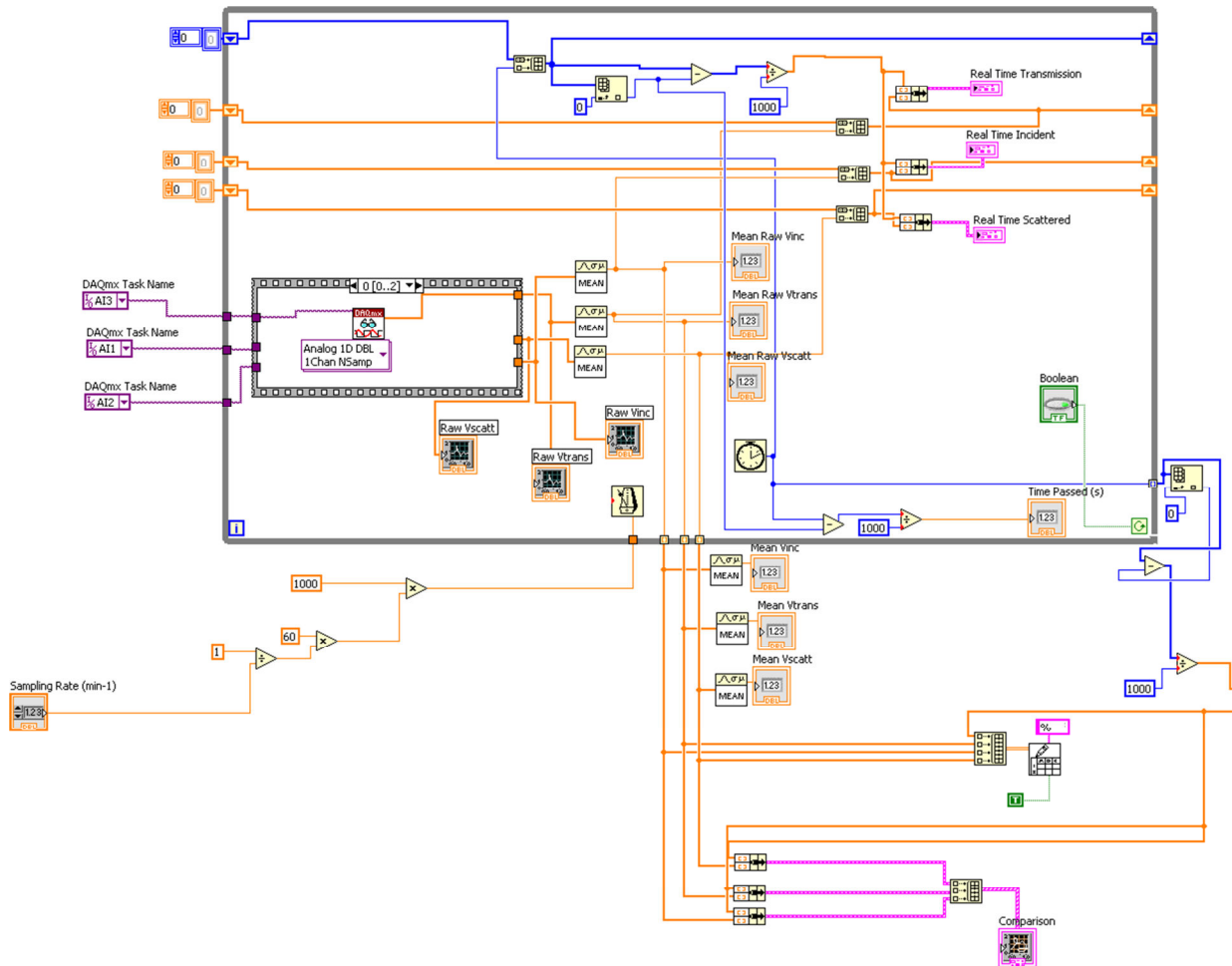
Figure 3. 4
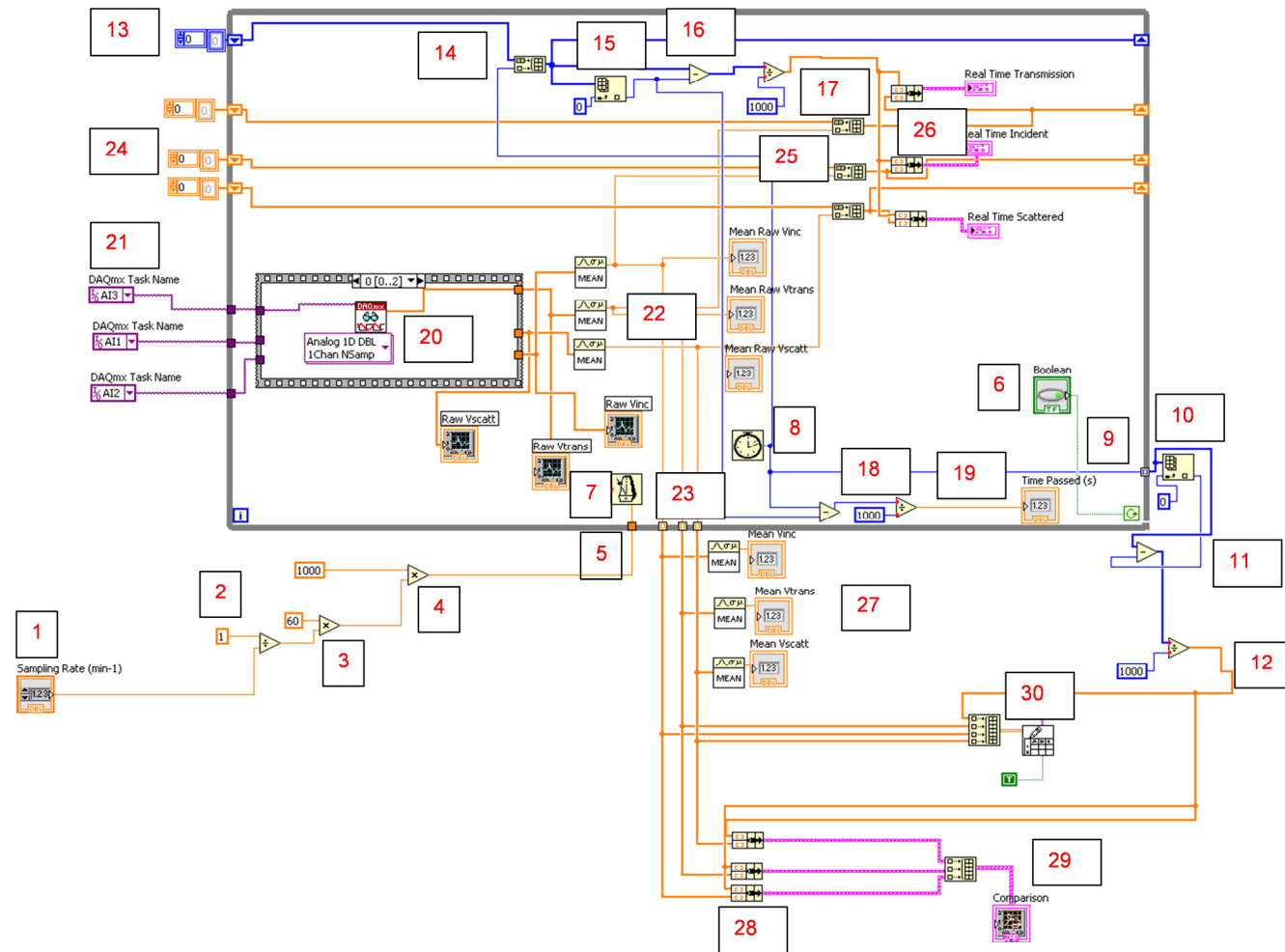LabVIEW code used for recording data from the detectors.

Figure 3. 5
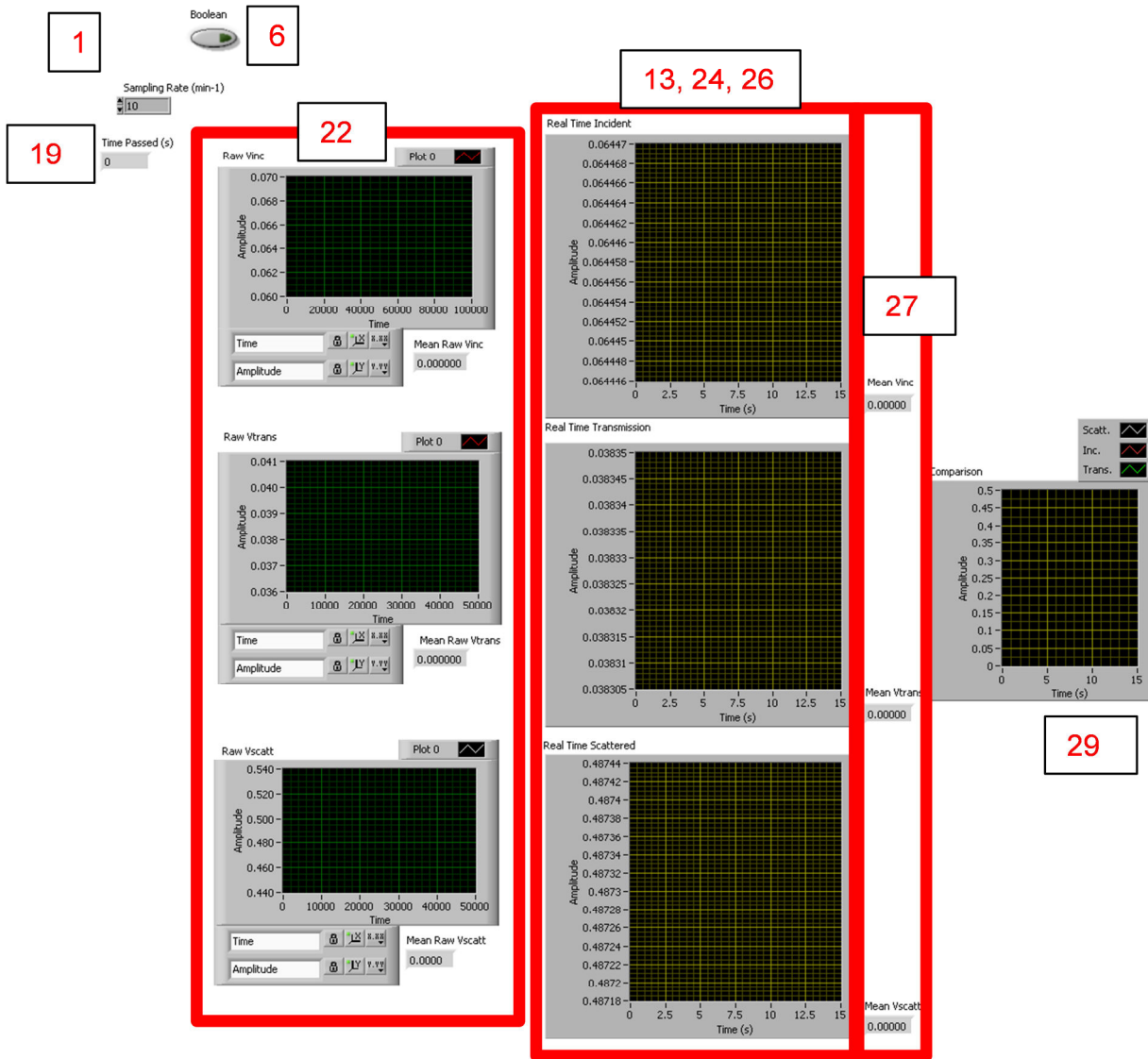Numbered LabVIEW code used for recording data from the detectors.

Figure 3. 6
Numbered LabVIEW front panel corresponding to the code used
for recording data from the detectors.

3.4.3 Data Processing

The data recorded for the incident, transmitted and scattered light measurements had to be corrected due to photodiode calibrations and background signals before they could be used to obtain induction times. The incident and transmitted signals were also used to calculate the transmission of light through the Couette setups. The steps required for these data processing aspects are detailed here.

3.4.3.1 Photodiode Calibration and Data Correction

The voltages output from the photodiodes (incident and transmitted light signals) were calibrated to allow relative intensities to be deduced since this was necessary to determine transmission values. Calibration was required because if each photodiode was irradiated with an identical intensity of laser light, different voltages were output. This was because the voltages output from the photodiodes were unique to each detector and each detector received different background intensities of light.

To calibrate the photodiodes, it was assumed that when a non-scattering/non-absorbing sample was present (e.g. Couette cell containing water/ transparent aqueous glycine solution), the intensity of incident laser light (I_o) was equal to the intensity of transmitted laser light (I_t).

$$I_o = I_t \qquad \text{(3. 3)}$$

For photodiodes, theoretically the intensity of light incident on a detector should proportional to the voltage output.

$$aV_i = bV_t \qquad \text{(3. 4)}$$

Here V_i is the voltage due to the intensity of incident laser light, V_t is the voltage due to the intensity of transmitted laser light and a and b are proportionality constants.

The voltage due to the intensity of incident or transmitted laser light was equal to the measured value minus the background reading. The background reading was obtained by having the laser switched off. Here subscript m refers to the measured voltage and subscript b refers to the background voltage.

$$V_i = V_{im} - V_{ib} \qquad \text{(3. 5)}$$

$$V_t = V_{tm} - V_{tb} \qquad \text{(3. 6)}$$

Since the intensity of incident and transmitted light should be equal when a non-scattering/non-absorbing sample was present, a calibration factor ($\frac{a}{b}$) was deduced.

$$a(V_{im} - V_{ib}) = b(V_{tm} - V_{tb}) \qquad \textbf{(3. 7)}$$

$$\frac{a}{b} = \frac{(V_{tm} - V_{tb})}{(V_{im} - V_{ib})} \qquad \textbf{(3. 8)}$$

This calibration factor allowed the measured incident and transmitted voltage values to be corrected, and the corrected incident and transmitted voltages could be fairly compared to obtain transmission values.

For scattering measurements, the scattering voltage from the non-scattering/non-absorbing sample was subtracted from the measured experimental voltage for a scattering/ interacting sample. This allowed the voltage due to the presence of the scattering/ interacting sample to be deduced. This level of data processing was sufficient as scattering measurements were not compared relatively, unlike the incident and transmitted light detector signals.

3.4.3.2 Basic Light Transmission Theory

Once the data were corrected, the incident and transmitted light signal data could be used to calculate the transmission of light through the solutions and the associated attenuation coefficient. Basic theory on how transmission and attenuation coefficients are related to the corrected incident and transmitted signals is given here. Light incident on a sample can be transmitted, scattered or absorbed, as shown in Figure 3. 7. The extinction of incident light is therefore due to absorption and/or scattering.
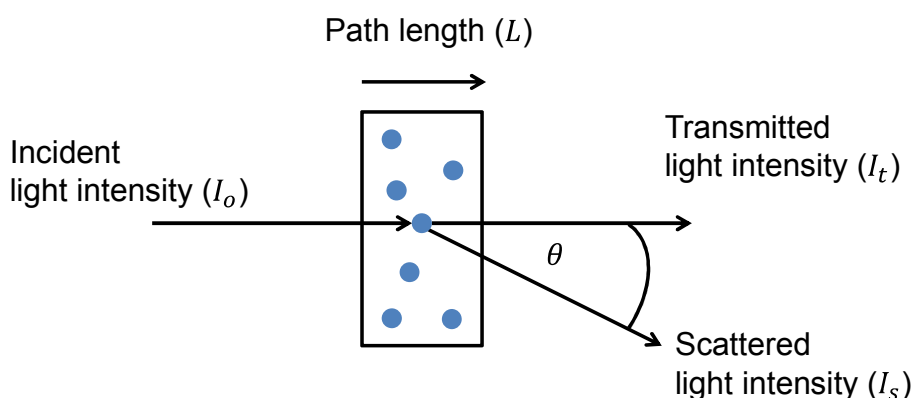

Figure 3. 7
Extinction of incident beam.

The variation of intensity (I) with optical path length (L) can be expressed as:

$$dI = -\tau I dL \qquad \text{(3. 9)}$$

Here τ is the attenuation coefficient, which takes the sources of extinction of incident light into account.

$$\text{(3. 10)}$$
$$\tau = \sum_{i}^{n} C_i^{ext} N_i$$

C_i^{ext} is the extinction cross section of particle i, N_i is the number of particles i per unit volume, $i = 1, 2, ..., n$ where n is the total number of types of particle.

The extinction cross section of particle i can be written in terms of the scattering cross section of particle i (C_i^{sca}) and absorption cross section of particle i (C_i^{abs}).

$$\tau = \sum_{i}^{n} C_i^{sca} N_i + C_i^{abs} N_i \qquad \text{(3. 11)}$$

Eqn. (3. 9) can be separated and integrated between the limits of: intensity I_o when the path length is zero (i.e. incident light intensity) and I_t when the path length is L (i.e. transmitted intensity).

$$\int_{I_o}^{I_t} \frac{dI}{I} = -\tau \int_0^L dL \qquad \text{(3. 12)}$$

The result is the Beer-Lambert law.

$$I_t = I_o e^{-\tau L} \qquad \text{(3. 13)}$$

The transmission (T) can be defined as:

$$\text{(3. 14)}$$
$$T = \frac{I_t}{I_o} = e^{-\tau L}$$

This can be calculated using the corrected incident and transmitted light voltages, mentioned in Section 3.4.3.1.

The attenuation coefficient can be estimated from transmission values:

$$\tau = \frac{-\ln(T)}{L} \qquad \text{(3. 15)}$$

If it is assumed that extinction due to molecular absorption is negligible, all extinction will be due to scattering (Eqn. (3. 11)) and the attenuation coefficient will therefore represent the total scattering integrated across the whole range of angles.

Transmission can be related to absorbance (A) through:

$$A = -\log(T)$$ **(3. 16)**

3.4.3.3 Obtaining Induction Times from Transmission/ Scattering Plots

An example plot of the transmission and scattering measured for supersaturated glycine solution being sheared in the Couette cell as a function of time is given in Figure 3. 8. When the induction time was reached, solutions became turbid over a short timescale, leading to a sharp increase in scattering and decrease in transmission. Induction times were obtained by finding the time intercept of the main inflection in the transmission/ scattering plots, as shown in the diagram.
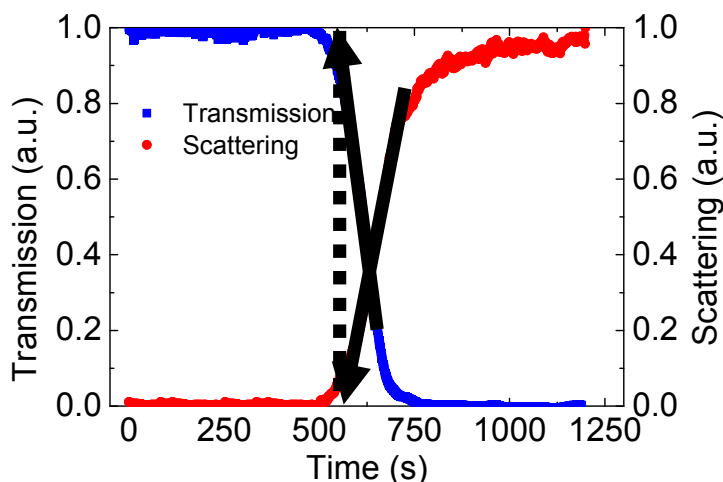

Figure 3. 8
Example plot of scattering/ transmission as a function of time for a solution that rapidly became turbid once an induction time had passed.

The simultaneous scattering and transmission measurements gave similar induction times. Since solutions quickly became very turbid, sensitivity differences between the detection methods were not very important[2].

3.5 Comparison of the Quantitative Induction Time Measurement Methods

The imaging and transmission/ scattering measurement methods could not be used simultaneously. For imaging, the sample had to be well illuminated, however, for transmission/ scattering measurements, background lighting had to be low so that the intensity of light reaching detectors from the laser was not masked. Therefore direct comparisons between the methods could not be made. Experiments were repeated using both methods multiple times (see Chapter 4 Section 4.4.1) and the times where inflections occurred using the imaging method were of a similar time range to those obtained through transmission/ scattering measurements. This suggested that the methods detected induction times with similar resolutions[2].

The imaging method of obtaining induction times was cheaper and easier to use than the transmission/ scattering method, however, not much further information could easily be obtained from the average pixel intensity data. Image analysis could potentially be useful, however, due to the cloudy nature of the solutions that had nucleated here, and the fact that the images were obtained while the cylinder was rotating, obtaining further information from the images would be difficult.

As mentioned, the transmission/ scattering method had more scope for obtaining further information on the system studied, such as the number of crystals formed (Chapter 8), the size of particles (Chapter 6) and polymorph formation[10].

3.6 Conclusions

Three methods of measuring the induction times of supersaturated glycine solutions exposed to controlled flow conditions in the Couette cell or capillary flow system (detailed in Chapter 2) were described and discussed. These methods were visual monitoring, imaging and simultaneous scattering and transmission measurements.

When induction times were reached, solutions became turbid over a short timescale, leading to a sharp increase in scattering, decrease in transmission and increase in the mean pixel intensity of the images. Induction times were obtained by finding the point of inflection of the rising (or falling) signals.

The imaging and transmission/scattering methods gave complementary results, which suggested that they detected induction times with similar resolutions. The

transmission/ scattering method, however, had more scope than the imaging method for obtaining further information from the system being studied, such as particle sizes (Chapter 6) and number concentrations (Chapter 8). The induction times measured can be used to estimate the rates of primary nucleation that occurred in the experiments. This is shown in Chapter 4 and Chapter 5.

3.7 Summary

- Measuring induction times is a straightforward method for obtaining information on nucleation rates in solutions while solutions were sheared in the controlled flow devices.

- Three methods to measure induction times were used- visual monitoring, imaging and simultaneous scattering and transmission measurements.

- The qualitative visual method was more error prone than the quantitative methods.

- The imaging method involved imaging the light scattered by incipient crystals and calculating the mean pixel intensity as a function of time. When solutions nucleated, the mean pixel intensity increased.

- The transmission/scattering method involved making simultaneous measurements using photodiodes. When solutions nucleated, the scattering intensity increased and the transmission decreased.

- The imaging and transmission/scattering methods gave complementary results, which suggested that they detected induction times with similar resolutions.

- The transmission/scattering method had more scope than the imaging method for obtaining further information on the system being studied

3.8 References and Nomenclature

3.8.1 References

(1)   Jiang, S. F.; ter Horst, J. H., Crystal Nucleation Rates from Probability Distributions of Induction Times. *Crystal Growth & Design* **2011,** 11, (1), 256-261.

(2)   Forsyth, C.; Mulheran, P. A.; Haw, M. D.; Burns, I. S.; Sefcik, J., Influence of Controlled Fluid Shear on Nucleation Rates in Glycine Aqueous Solutions. *Crystal Growth & Design* **2015,** 15, (1), 94-102.

(3)   Kashchiev, D., *Nucleation: Basic Theory and Applications*. ed.; Butterworth-Heinemann: 2000.

(4)   Mullin, J. W., *Crystallization*. 4th ed.; Heineman: 2002.

(5)   Davey, R.; Garside, J., *From Molecules to Crystallizers. An Introduction to Crystallization.* ed.; Oxford University Press: 2000.

(6)   Sohnel, O.; Mullin, J. W.; Jones, A. G., Crystallization And Agglomeration Kinetics In The Batch Precipitation Of Strontium Molybdate. *Industrial & Engineering Chemistry Research* **1988,** 27, (9), 1721-1728.

(7)   Myerson, A., *Handbook of Industrial Crystallization*. 2nd ed.; Butterworth-Heinemann: 2001.

(8)   Kadam, S. S.; Kramer, H. J. M.; ter Horst, J. H., Combination of a Single Primary Nucleation Event and Secondary Nucleation in Crystallization Processes. *Crystal Growth & Design* **2011,** 11, (4), 1271-1277.

(9)   Matlab Help. Accessed 04/05/15. http://uk.mathworks.com/help/matlab/

(10)   Sypek, K.; Burns, I. S.; Florence, A. J.; Sefcik, J., In Situ Monitoring of Stirring Effects on Polymorphic Transformations during Cooling Crystallization of Carbamazepine. *Crystal Growth & Design* **2012,** 12, (10), 4821-4828.

(11)   Travis, J.; Kring, J., *Labview for Everyone: Graphical Programming Made Easy and Fun*. ed.; Prentice Hall: 2006.

3.8.2 Main Nomenclature

A = absorbance

a = proportionality constant

b = proportionality constant

C_i^{abs} = absorption cross section of particle i

C_i^{ext} = extinction cross section of particle i

C_i^{sca} = scattering cross section of particle i

I = intensity

I_o = intensity when the path length is zero (i.e. incident light intensity)

I_s = scattered light intensity

I_t = transmitted light intensity

J = nucleation rate

L = path length

M = magnification

N_i = number of particles i per unit volume

n = number of types of particle

S_i = distance from the lens to the image (detector)

S_o = distance from the object (beam sampler) to the lens

T = transmission

t_i = induction time

t_g = growth time

t_n = nucleation time

t_r = relaxation time

V_i = voltage due to the intensity of incident laser light (subscript m refers to the measured voltage and subscript b refers to the background voltage)

V_t = voltage due to the intensity of transmitted laser light (subscript m refers to the measured voltage and subscript b refers to the background voltage)

τ = attenuation coefficient

4. Influence of Controlled Fluid Shear on Nucleation Rates in Glycine Aqueous Solutions

Chapter Outline and Contents

The controlled flow devices detailed in Chapter 2 and the induction time measurement procedures detailed in Chapter 3 were used to investigate the nucleation of glycine in supersaturated aqueous solutions exposed to well-controlled fluid shear under isothermal conditions. Average shear rates between 25 s^{-1} and 1000 s^{-1} were studied using the Couette and capillary flow devices. Induction times were obtained from imaging, transmission and scattering measurements or visual monitoring. Great care was taken to eliminate any seeding in order to avoid secondary nucleation preceding the formation of the first crystals through primary nucleation.

Induction times obtained under shearing in the Couette or capillary setups were found to be considerably lower than those in unsheared solutions. The probability distributions of the induction times appeared to closely follow a distribution based on a previously published model by Jiang and ter Horst[1]. Using their model, where the induction time is related to the rate of formation of primary nuclei and the time it takes for them to grow to the size where the secondary nucleation becomes significant, it was found that both the primary nucleation rate and the growth time were strongly dependent on the shear rate imposed. Moreover, increasing the average shear rate reduced the mean induction time in a power law relationship: $t_{ind} \propto \dot{\gamma}_{avg}^{-0.61 \pm 0.16}$.

Due to the stochastic nature of nucleation, experiments were repeated multiple times and a detailed statistical analysis, which involved bootstrapping and Monte Carlo simulations, was carried out to ensure that the number of repetitions was sufficient for trends to be statistically valid.

This chapter covers:

- The glycine solution preparation method.
- The experimental procedure for Couette flow experiments.
- The experimental procedure for capillary flow experiments.
- The induction time results obtained from the experiments.
- The probability distributions of induction times and how they can be related to primary nucleation rates.
- Statistical trends and the impact of sample size.

4.1 Glycine Solution Preparation

Glycine (CAS Number 56-40-6) of ≥99% purity was purchased from Sigma Aldrich (item G8898) and used without further purification. Two concentrations (c) of solution were prepared by dissolving glycine in deionised water- 307 g glycine/kg water and 325 g glycine/kg water. During experiments, these solutions were cooled to 20°C and 23°C respectively. The solubility (c^*) of glycine was 219 g glycine/kg water at 20°C and 232 g glycine/kg water at 23°C[2]. Cooling therefore resulted in a supersaturation (S) of 1.4 for both solutions, where

$$S = \frac{c}{c^*} \qquad \text{(4. 1)}$$

Solutions were prepared in sealed glass bottles and were stirred at 55°C for 24 hours to ensure that glycine was fully dissolved. When the solutions were at 55°C, they were undersaturated. For the work detailed in this chapter, Couette cell experiments were performed at 23°C and capillary experiments were performed at 20°C.

It is noted that supersaturations were very sensitive to temperature. Solubility data[2] were used to estimate the effect that changes in temperature would have on the supersaturation of the two solutions used (S=1.4 at 20°C and 23°C). These results are given in Figure 4. 1 and showed that small changes in temperature can result in significant changes in supersaturation. For all experiments performed, it was ensured that temperatures did not vary by more than 1°C. Induction times were generally fairly short so the temperature would not have varied by much throughout an experiment.
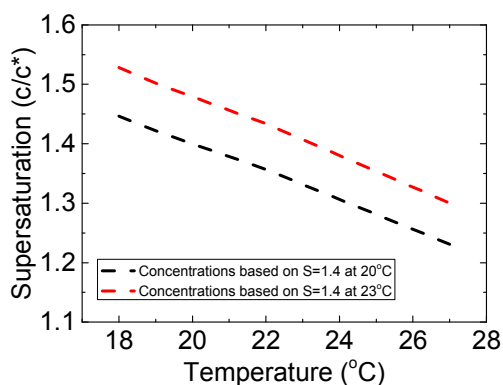

Figure 4. 1
Effect of changes in temperature to the supersaturation of prepared solutions.

4.2 Couette Cell Experimental Procedure

For the Couette cell experiments detailed in this chapter, the Couette cell geometry that used the 30mm inner Couette was used (see Chapter 2 Section 2.3 for more details on the construction and setup of the Couette cell).

15 ml undersaturated glycine solution (325 g glycine/kg water in incubator at 55°C) was filtered using preheated 0.2 µm SFCA disposable syringe filters (with the exception of 250 rpm (125 s^{-1}) imaging experiments for which solutions were unfiltered) into a preheated Couette cell by syringe. The filters, syringe and Couette cell were preheated to 55°C in the incubator, and the filtration procedure took place inside the incubator to minimise the rate of heat loss.

The filled Couette cell was removed from the incubator and attached to a monitoring instrument that was set up to allow induction times to be obtained quantitatively. The monitoring instrument was setup as shown in Chapter 3 Section 3.4 and it allowed transmission/ scattering measurements to be taken simultaneously. A camera was also in place to image the solution as it was sheared (see Chapter 3 Section 3.3). Since transmission and scattering measurements were found to result in similar induction times, as detailed in Chapter 3 Section 3.4.3.3, transmission measurements were analysed herein to estimate induction times.

To minimise evaporation at the solution/ air interface, a lid was secured to the Couette cell and parafilm was used to ensure that it was well sealed. The solution was left to cool in the surrounding air (23°C) for 30 minutes in order to reach ambient temperature and the desired level of supersaturation. There was no cylinder rotation during cooling. During cooling, a fan was used to speed up heat transfer.

The temperature profile of the solution during cooling (shown in Figure 4. 2) was measured to validate that the 30 minute cooling time was sufficient to ensure that the solutions had reached the desired temperature after this time. More information on how the temperature profile was obtained is given later in this section. The supersaturation was also plotted using solubility data[2].
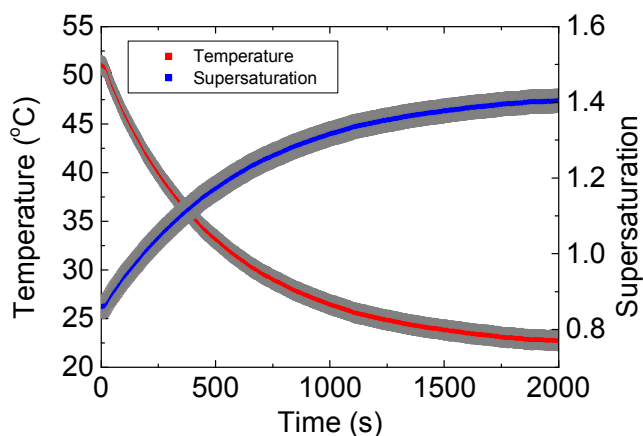
Figure 4. 2
Cooling and supersaturation profiles of the solution in the Couette. The thermocouple's error was approximately $\pm 1^{o}$C, which corresponded to an error in supersaturation in the region of ± 0.03.

The ambient temperature remained constant so the solution remained isothermal once it had cooled to 23°C. Since shearing of the solutions took place under isothermal conditions (the temperature of the solution was equal to the temperature of its surroundings), the effect of controlled fluid shear on induction times was not linked to heat transfer.

Once the solution cooling period had finished, the fan was switched off and the motor and relevant monitoring equipment were started. If the solution was being monitored via transmission measurements, a box was placed over the instrument to reduce the intensity of background light reaching the detectors.

Rotational rates (50 rpm, 125 rpm, 250 rpm or 500 rpm), which corresponded to average shear rates of 25 s^{-1}, 62.5 s^{-1}, 125 s^{-1} and 250 s^{-1} (see Chapter 2 Section 2.1.4 for the calculation of shear rates), were measured using a digital tachometer and the voltage was adjusted to obtain the desired rotational rate. Once the solution had become visibly turbid, the motor and monitoring equipment were switched off. Data were then analysed to obtain induction times. Experiments were repeated at least 10 times, which was sufficient for statistically reliable trends to be deduced, as is shown in Section 4.6.

Induction times were also obtained for experiments that involved no shearing i.e. 0 rpm. This was done visually as only a small number of crystals formed in unsheared solutions (fewer than 5, typically 1 or 2) which meant solutions did not become turbid.

For induction time measurements, time= 0 s is defined as the time at which the motor was started and cylinder rotation began. This happened after the solution had cooled to 23°C and therefore reached the desired level of supersaturation i.e. time= 0 s was 30 minutes after the filled Couette cell was removed from the incubator.

Temperature Data Logger

As mentioned, cooling profiles were measured to validate that the 30 minute cooling time was sufficient for solutions to reach ambient conditions. This was achieved by using a thermocouple connected to a data acquisition setup. Thermocouples work on the Seebeck effect and are cheap devices that allow temperature measurements to be made. They typically consist of 2 dissimilar metals that touch to make a contact point. The contact point produces a voltage that is a function of temperature. The voltage produced depends on the temperature difference between the contact point and the junction where the voltage is being measured across. Therefore to know the absolute temperature of the contact point, the temperature at the junction where the voltage is being measured across (the cold junction) must be specified.

Figure 4. 3 illustrates a thermocouple that is being used to measure the temperature of a sample. The circuit has 3 junctions between dissimilar metals. The voltage produced across the cold junction (J2 and J3) is proportional to the temperature difference between sample (J1) and the cold junction (J2 and J3). J2 and J3 should be close enough together that they are at the same temperature.
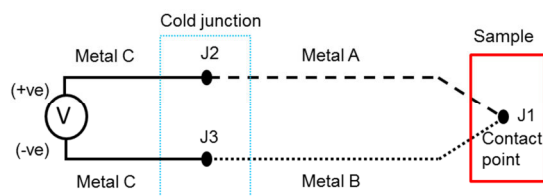

Figure 4. 3
Thermocouple circuit.

To measure the temperature profile of a solution while it was cooling, a thermocouple (type K) was connected to the computer using a LabVIEW connector block (BNC-2120). Signals were digitised by a data-acquisition card (National Instruments PCI-6221) and recorded using LabVIEW. Data acquisition software, similar in principle to the software described in detail in Chapter 3 Section 3.4.2, was written so that the temperature data could be recorded. Plots of the temperature measured as a function of time updated on the front panel so that the user could monitor the measurements. The user could specify the rate of temperature measurements. For measurements done here, one measurement per second was chosen.

To calculate the temperature from the thermocouple, the cold junction temperature had to be specified. This could either be kept at a constant value input by the user, or the value measured by the LabVIEW connector block could be used. Here, a constant value of 23^oC was input as the connector block's temperature measurement did not appear to be well calibrated. Checks were regularly made between the value measured by the thermocouple and a standard alcohol thermometer. The values were generally within 1^oC of each other.

4.3 Capillary Experimental Procedure

For the capillary experiments detailed in this chapter, the capillary flow device was set up as shown in Figure 4. 4. More details on the construction and setup of the capillary flow device are given in Chapter 2 Section 2.2.
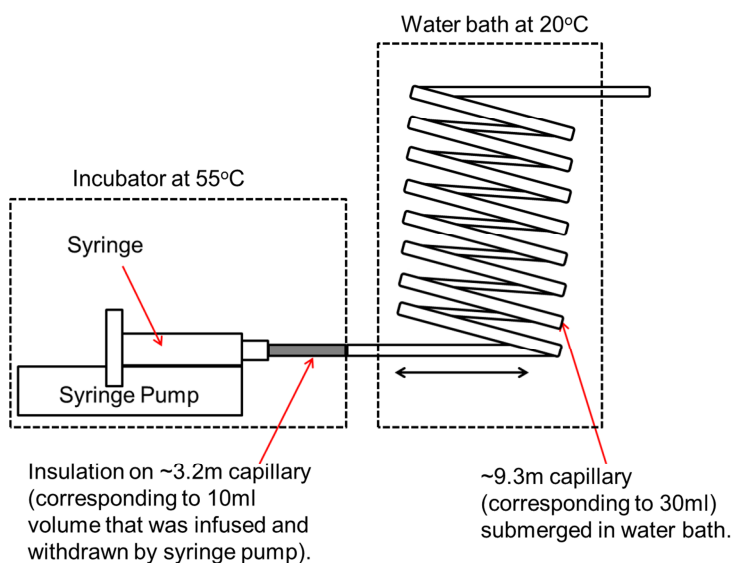

Figure 4. 4
Capillary setup including details of temperature control.

50 ml undersaturated solution (307 g glycine/kg water from the incubator at 55°C) was filtered using preheated 0.2 µm SFCA syringe filters into a preheated 60 ml syringe, and the syringe tip was attached to the capillary as described in Chapter 2 Section 2.2. The syringe was attached to the syringe pump, and the syringe pump, syringe and ~3.2 m of adjacent capillary were kept incubated at 55°C. The ~3.2 m of capillary was also covered with insulation.

This length of capillary was kept incubated and insulated since the length corresponded to the volume of solution that was withdrawn and infused by the syringe pump continuously (a 10 ml volume was withdrawn/infused, which equated to approximately 3.2 m of capillary). By keeping the syringe and first ~3.2 m of capillary incubated, the solution that entered and left the syringe during continuous operation remained undersaturated. Since the solubility of glycine in water decreases with decreasing temperature, keeping the solution that was entering and leaving the syringe incubated was necessary to ensure that it did not become supersaturated- entering and exiting the syringe was found to strongly enhance nucleation in supersaturated glycine solutions, leading to blockages. The remaining length of capillary (~9.3 m) was submerged in a water bath at 20°C.

The 50 ml of solution in the syringe was infused from the syringe through the capillary; the first 10 ml that emerged from the end of the capillary was discarded leaving 40 ml in the capillary. The 30 ml solution in the non-incubated/ uninsulated length of capillary was left to cool in the water bath (20°C) for 10 minutes. Once the solution had cooled, the syringe pump was operated in a continuous mode whereby 10 ml solution was passed back and forth periodically at a chosen flow rate (25 ml/min, 50 ml/min or 100 ml/min), which corresponded to average shear rates of 250 s^{-1}, 500 s^{-1} and 1000 s^{-1} (see Chapter 2 Section 2.1.3 for how shear rates were calculated), while staying isothermal at 20°C in the non-incubated/ un-insulated length of capillary (in the water bath).

The solution in the capillary was monitored visually and the induction time was noted. The section of capillary monitored corresponded to solution that was not exposed to the first 3.2 m or final 3.2 m of capillary. This was to avoid any possible influence of solution entering and exiting the syringe or exposure to the air-solution interface on induction time results. A submersible torch was placed in the water

bath and directed towards the capillary to allow for easier crystal detection by eye. Induction times were also obtained for experiments that involved no shearing, i.e. the flow rate was 0 ml/min.

For induction time measurements, time= 0 s is defined as the time at which the syringe pump was started and flow back and forth along the capillary began. This happened after the solution in the non-incubated length of capillary had cooled to $20^{\circ}C$ and therefore reached the desired level of supersaturation i.e. time= 0 s was 10 minutes after the capillary was submerged in the water bath and infused with undersaturated ($55^{\circ}C$) solution. Checks were done to validate that 10 minutes was sufficient for solutions to cool to $20^{\circ}C$. This was achieved by collecting a solution that had been cooled in the capillary for 10 minutes and using a thermocouple to measure its temperature. This was then repeated to ensure it was consistent.

4.4 Induction Time Results

Induction times of aqueous glycine solutions that underwent controlled fluid shear in Couette or capillary flow devices were obtained. A wide range of average shear rates were covered, from 25 s^{-1} to 1000 s^{-1}.

4.4.1 Couette Results

Figure 4. 5 shows the induction times that were obtained at each rotational rate for Couette flow experiments. By increasing the rotational rate (and therefore flow velocity and shear rate), smaller mean induction times were obtained. At 50 rpm, the induction times obtained were approaching the induction times measured for unsheared solutions, however, at higher rotational rates, the induction times measured were considerably smaller. Values obtained from both measurement methods ((1) simultaneous measurements of static light scattering at the scattering angle of 90° and transmitted light intensity; (2) imaging the nucleation process and then analysing the images) overlapped and had similar mean values, as shown in Figure 4. 6. As mentioned in Chapter 3, the simultaneous scattering and transmission measurements gave identical induction times. Since solutions quickly became very turbid, sensitivity differences between the detection methods were therefore not very important.
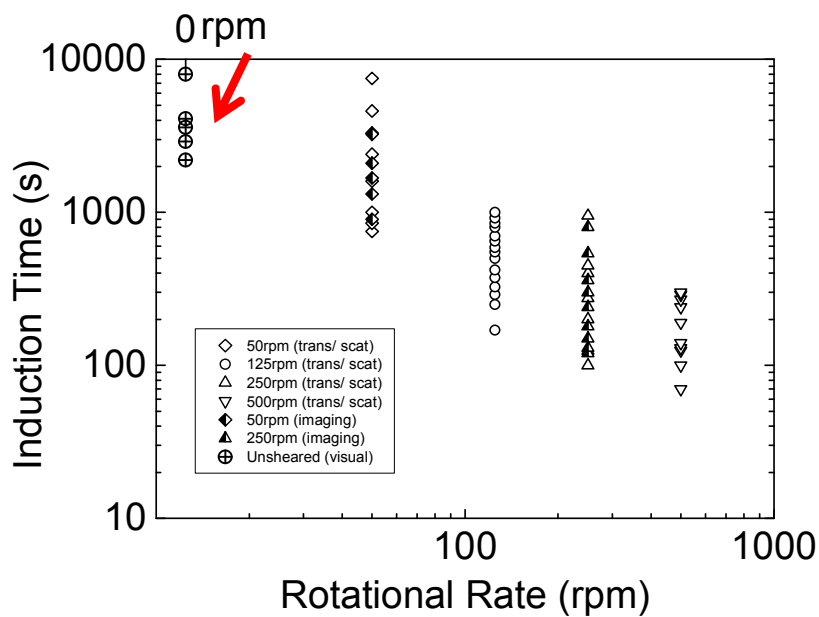
Figure 4. 5
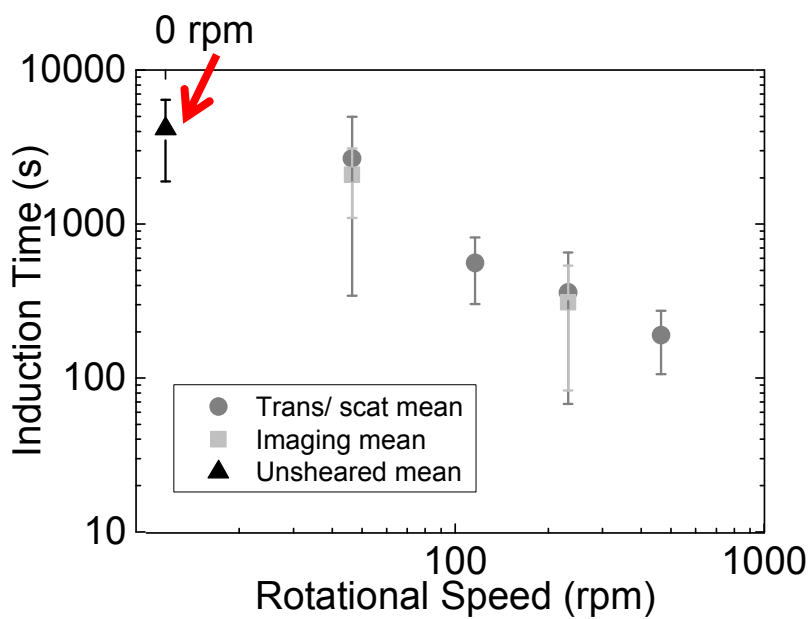Induction times obtained using Couette cell for a range of rotational rates.

Figure 4. 6
Mean induction times (using transmission/ scattering or imaging methods) obtained using Couette cell for a range of rotational rates. Error bars represent one standard deviation.

4.4.2 Capillary Results

Figure 4. 7 shows the induction times that were obtained at each flow rate for capillary flow experiments. By increasing the flow rate (and therefore flow velocity and shear rate), smaller mean induction times were obtained, as shown in Figure 4. 8. The induction times obtained for all flow rates used were considerably smaller than those of unsheared solutions.
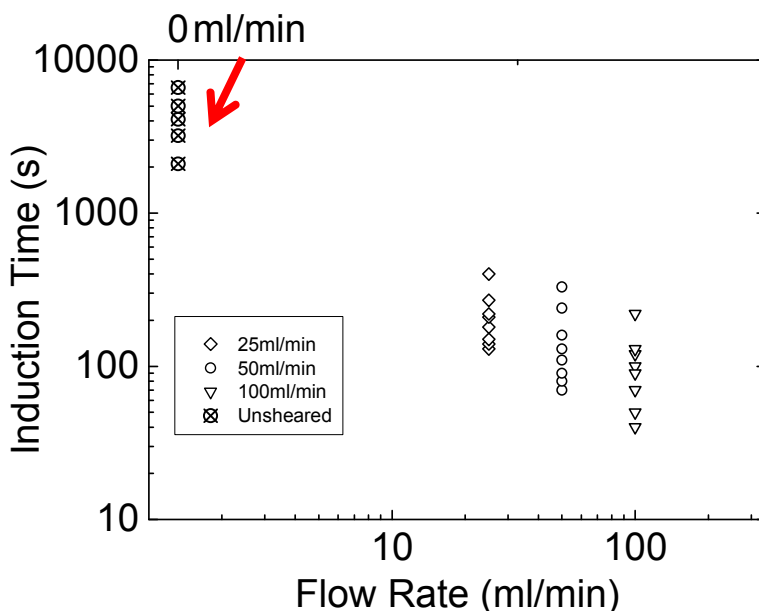

Figure 4. 7
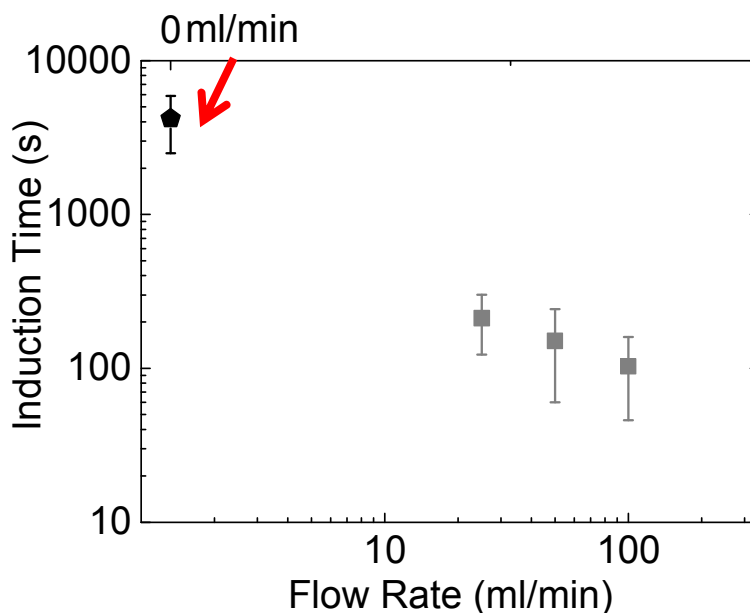Induction times obtained using capillary setup for a range of flow rates.

Figure 4. 8
Mean induction times obtained using capillary setup for a range of flow rates. Error bars represent one standard deviation.

4.4.3 Comparison of Couette and Capillary Results

Figure 4. 9 shows the measured induction times for the Couette and capillary experiments as a function of the average shear rate. Figure 4. 10 shows the mean and median of capillary and Couette results presented together as a function of the average shear rate. Both flow geometries gave similar mean induction times when solutions were sheared at the same average shear rate (500 rpm and 25 ml/min).

Figure 4. 9
Induction times obtained using Couette and capillary setups as a function of the average shear rate. For capillary experiments, the maximum shear rate, which occurs at the walls, would be twice the average shear rate.
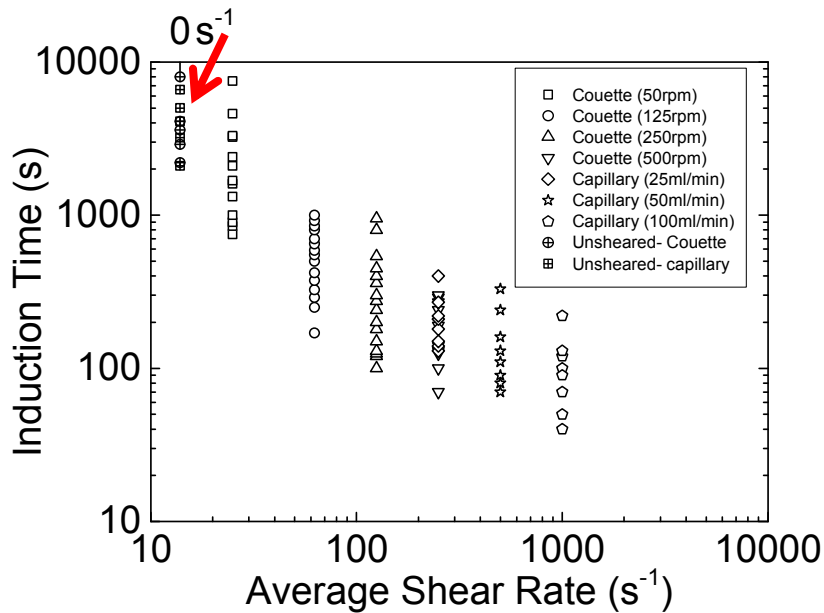

Figure 4. 10
Mean induction times obtained using Couette and capillary setups as a function of the average shear rate. For capillary experiments, the maximum shear rate, which occurs at the walls, would be twice the average shear rate. Error bars represent one standard deviation.
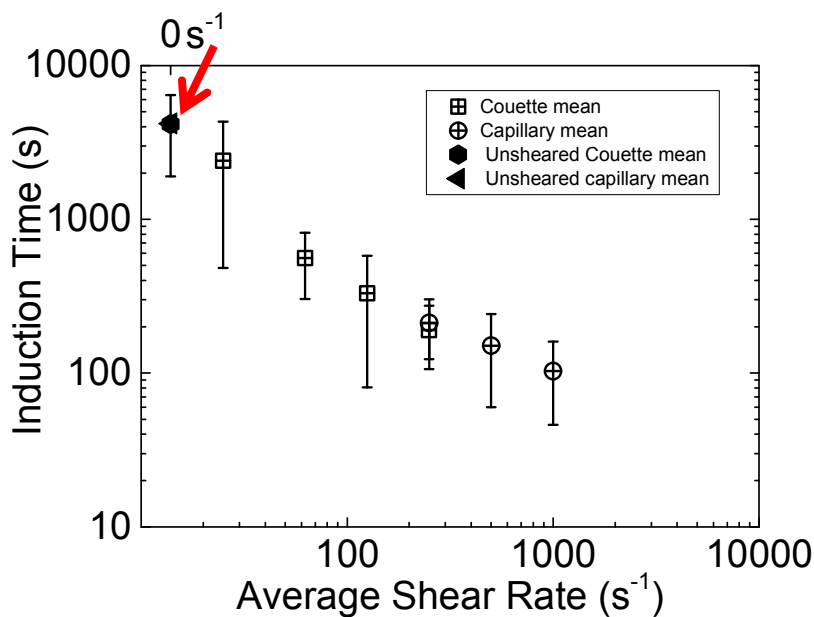
4.4.4 Discussion of Couette and Capillary Results

4.4.4.1 Role of Fluid Shear on Primary and Secondary Nucleation

Shearing was hypothesised to have an influence on both primary and secondary nucleation. Since induction times were notably smaller for higher shear conditions than for unsheared solutions, it is important to distinguish effects on primary and secondary nucleation, respectively.

Preheating and filtration of solutions was done to ensure that no crystals were initially present in aqueous glycine solutions. In order to eliminate any seed crystals that were present at the glass walls of Couette cylinders or in plastic capillaries, these were extensively cleaned with hot water after each experiment. No crystals were seen after inspection under an optical microscope. In order to ensure this was indeed the case, observations were made under quiescent (unsheared) conditions and it was invariably seen that a small number of crystals (typically 1 or 2 after 4 hours) appeared at the base of the Couette cylinder. After 4h, the largest dimension observed was 6 mm, and using growth rates from literature (~60 μm per minute for the supersaturation and temperature used here[3]), the longest axis would be expected to be at least 14 mm if a crystal was already present at the start of the experiment. Growth rates were also verified experimentally by placing a seed crystal in the supersaturated solution and monitoring its growth. This shows that there were no crystals present in the system at the start, neither in the bulk nor on the walls exposed to the solution.

When solutions were not sheared, fewer than 5 crystals (usually 1 or 2) typically formed (shown in Figure 4. 11) and these would have been formed through primary nucleation, as discussed above. When solutions were sheared, however, a very large number of crystals formed in close succession, causing solutions to rapidly go turbid (shown in Figure 4. 12). The large number of crystals formed over such a short timescale was thought to be most likely due to the secondary nucleation of a shear-enhanced primary crystal, rather than a sudden, large increase in primary nucleation[1, 4-8].

It can therefore be concluded that the crystals formed at higher shear rates were due to shear enhanced primary nucleation of a nucleus, followed by extensive secondary nucleation. This is in agreement with studies carried out by ter Horst et al. which suggested that the crystallisation mechanism was due to the nucleation of a single parent crystal, followed by the attrition of the single parent crystal to form secondary nuclei[1, 5, 8].

Figure 4. 11
Image of crystals formed when solution was not sheared in the Couette cell.

Figure 4. 12
Image of solution that had been sheared in the Couette cell.

4.4.4.2 Influence of Low Rates of Fluid Shear on Primary and Secondary Nucleation

For 50 rpm Couette flow experiments, the formation of the primary nucleus may not have been greatly shear enhanced, since induction times were fairly similar to those in unsheared solutions. Solutions sheared at 50 rpm, however, became turbid, unlike unsheared solutions, so secondary nucleation was likely to still have been enhanced by the flow conditions.

The relatively small effect that the 50 rpm experiments had on the induction times compared to unsheared experiments was unexpected since the shear rate was still

considerable (25 s^{-1}) and often very low levels of fluid shear can affect nucleation [9, 10]. There is often a substantial difference between no shear/agitation and just a little shear/agitation.

One reason to account for this is that an overestimation of induction times may have occurred when the shear rate was low (50 rpm experiments). The rate at which turbidity increased with 50 rpm experiments was notably lower than the other rotational rates, which suggested slower secondary nucleation. It is noted that the induction time detection method for 50 rpm experiments was transmission/ imaging, while for unsheared experiment, induction times were measured visually. For experiments that involved shearing, sufficient secondary nucleation had to take place before measured signals were substantially affected to obtain clear induction times, meaning that an overestimation of induction times may have occurred when comparing to unsheared solution induction times.

The unsheared induction times would also technically have been larger than stated, particularly for Couette flow experiments due to the slow cooling process. Monitoring began 30 minutes after the solutions were removed from the incubator (they were left for 30 minutes to cool to ambient temperature), however, from glycine solubility data[2], the solutions would have become supersaturated once they had cooled to temperatures below 41°C. Looking at the cooling profile in Figure 4. 2, this shows that solutions were supersaturated long before the 30 minute cooling period had finished. Preliminary experiments on unsheared solutions showed that nucleation proceeded significantly faster when supersaturations exceeded 1.35 (unsheared induction times were of a few hours rather than several hours/ days). This supersaturation was reached after around 1300 s cooling, so perhaps an additional 500 s should have been added to the unsheared induction times. Sheared solutions would also have had this 500 s of 'high' supersaturation prior to shear, however, the duration of applied shear was the most important aspect with regards to induction times for those experiments. From growth rates and monitoring crystal sizes, a nucleation event would not have occurred during this 500 s.

4.5 Distribution of Induction Times

The distributions of induction times obtained were further investigated to gain a better understanding of underlying nucleation phenomena.

For a given set of conditions, a number of induction times (t_i) were observed (where $i = 1,2,\dots \mathrm{M}$), and these were ordered from shortest to longest. The observed experimental cumulative probability distribution of induction times ($O(t_i)$) was then:

$$O(t_i) = \frac{i}{M} \qquad \textbf{(4. 2)}$$

There have been several approaches in previous literature to analyse induction time distributions based on probabilistic arguments[1, 11, 12]. Here two different approaches to analysing the distributions were taken. The first was to assume that the induction times were log-normally distributed and the second was to assume that they followed a model proposed by Jiang and ter Horst[1].

4.5.1 Log-Normal Distribution

A simple approach was to assume that the induction times were log-normally distributed, since log-normal distributions have been often observed to fit probabilistic outcomes of various natural phenomena[13]. In this case, the cumulative distribution of the logarithm of induction times follows the cumulative distribution function ($Q(t_i)$):

$$Q(t_i) = \frac{1}{2}\left[1 + \mathrm{erf}\left(\frac{\log(t_i) - \overline{\log(t_i)}}{\sigma\sqrt{2}}\right)\right] \qquad \textbf{(4. 3)}$$

Here, erf is the error function, $\overline{\log(t_i)}$ is the mean of the log induction times and σ is the standard deviation of the log induction times.

These data were calculated for each set of induction times recorded at each experimental condition (see Figure 4. 9) and the log-normal distributions calculated were then compared to the observed cumulative distribution functions. Residuals were calculated and coefficients of determination (R^2) were calculated from:

$$R^2 = 1 - \frac{SS_R}{SS_T} \qquad\qquad \textbf{(4. 4)}$$

Here SS_T is the total sum of squares and SS_R is the sum of squared residuals.

$$SS_T = \sum_{i=1}^{M} \left(O(t_i) - \overline{O(t_i)} \right)^2 \qquad\qquad \textbf{(4. 5)}$$

$$SS_R = \sum_{i=1}^{M} \left(Q(t_i) - O(t_i) \right)^2 \qquad\qquad \textbf{(4. 6)}$$

Even if a log-normal distribution described induction time data well, there is no clear way to deduce further information about underlying physical phenomena from the shape of a distribution of induction times.

4.5.2 Jiang and ter Horst Distribution

In order to obtain quantitative insight into nucleation phenomena from experimentally observed distributions of induction times, a model proposed by Jiang and ter Horst[38] was also considered. In the model it was assumed that, due to the stochastic nature of nucleation in small volumes, the probability of forming a particular number of crystals over a time interval followed a Poisson distribution[38,42]. Assumptions required for the Poisson distribution included that the primary nucleation events were independent and occurred at a constant average rate over the time interval. The assumption of a constant nucleation rate was initially thought to be sufficient since during the induction period, the supersaturation was constant which would suggest the rate of nucleation was constant. This is discussed in more detail in Chapter 6 Section 6.6.

The Poisson probability mass function (p_m) is:

$$p_m = \frac{N^m}{m!} \exp(-N) \qquad\qquad \textbf{(4. 7)}$$

Here, N is the average number of nuclei that form in the time interval and m is the number of nuclei that form in a time interval.

If no nuclei are formed within the time interval, the probability of this (p_0) can be expressed as:

$$p_0 = \exp(-N) \qquad \text{(4. 8)}$$

The average number of nuclei formed (N) in time (T) and volume (V) can be related to the nucleation rate through:

$$N = JVT \qquad \text{(4. 9)}$$

Here J is the nucleation rate per unit volume and V is the volume of the solution in the vessel. As mentioned in Chapter 1, the nucleation rate in general depends on supersaturation and temperature, and may also vary depending on other process parameters, such as the shear rate.

The probability that the first nucleation event occurs between time T and $T + dT$ is given by the probability that no nucleation event occurs up to time T multiplied by the probability that a nucleation event occurs in the interval dT:

$$p(T).dT = \exp(-JVT) \times JV.dT \qquad \text{(4. 10)}$$

The cumulative distribution function of nucleation times ($P(t_n)$), which is the likelihood that the first nucleation event occurs up to time (t_n) is then:

$$P(t_n) = \int_0^{t_n} p(T).dT = 1 - \exp(-JVt_n) \qquad \text{(4. 11)}$$

i.e. it is equal to 1 minus the probability that no crystals formed during time t_n.

The induction time (t_i) that is observed in the experiments is the time at which the solution becomes clouded by many crystals to a detectable level. The second element of the Jiang and ter Horst model is that the first nucleation event (due to primary nucleation) occurring at time t_n leads to the observed clouding at a later time:

$$t_i = t_n + t_g \qquad \text{(4. 12)}$$

Here t_g is interpreted as the time taken for the first crystal formed through primary nucleation to grow to a sufficient size at which secondary nucleation occurs, causing the solutions to rapidly become turbid i.e. a detectable change in transmission occurs.

Thus the cumulative probability of observations made by time t_i having crystallised to a detectable level is $(P(t_i))$:

$$P(t_i) = 1 - \exp\bigl(-JV(t_i - t_g)\bigr) \qquad \text{(4. 13)}$$

The observed cumulative probability distribution of induction times (Eqn. (4. 2) was used to find the best fit values for J and t_g in Eqn. (4. 13) for each set of experimental conditions. This was done using least squares fitting. Residuals were calculated and coefficients of determination (R^2) were calculated from:

$$R^2 = 1 - \frac{SS_R}{SS_T} \qquad \text{(4. 14)}$$

$$SS_T = \sum_{i=1}^{M} \bigl(O(t_i) - \overline{O(t_i)}\bigr)^2 \qquad \text{(4. 15)}$$

$$SS_R = \sum_{i=1}^{M} \bigl(P(t_i) - O(t_i)\bigr)^2 \qquad \text{(4. 16)}$$

Using Matlab, best estimates for J and t_g were obtained at the various shear rates, so it was possible to determine whether nucleation rates and growth times showed dependence on shear rates under the conditions investigated here.

4.5.3 Comparison of Distributions

In Figure 4. 13 and Figure 4. 14, experimental data for the Couette and capillary systems are shown (Eqn. (4. 2)) respectively, together with log-normal distribution curves from Eqn. (4. 3) using the mean and standard deviation of the log induction times for each set of data, and also with the best fit of the Jiang and ter Horst model from Eqn. (4. 13).

While log-normal distributions agreed with experimental data reasonably well, the functional form of the model by Jiang and ter Horst did seem to be better suited to describing the data under all conditions investigated here (see Figure 4. 15). This would perhaps be expected since the Jiang and ter Horst model involved least squares fitting to the experimental data, whereas the log-normal method was just based on the mean and standard deviation of log induction times.
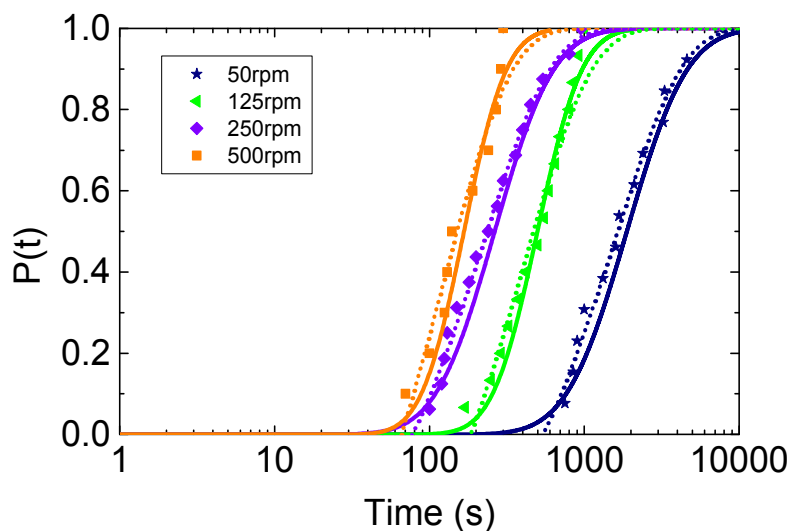

Figure 4. 13
Cumulative distribution functions for induction times obtained using Couette setup. Symbols represent experimental data (Eqn. (4. 2)), dashed line is the best fit for the model by Jiang and ter Horst (Eqn. (4. 13)) and solid line is the log-normal distribution (Eqn. (4. 3)).

Figure 4. 14
Cumulative distribution functions for induction times obtained using capillary setup. Symbols represent experimental data (Eqn. (4. 2)), dashed line is the best fit for the model by Jiang and ter Horst (Eqn. (4. 13)) and solid line is the log-normal distribution (Eqn. (4. 3)).
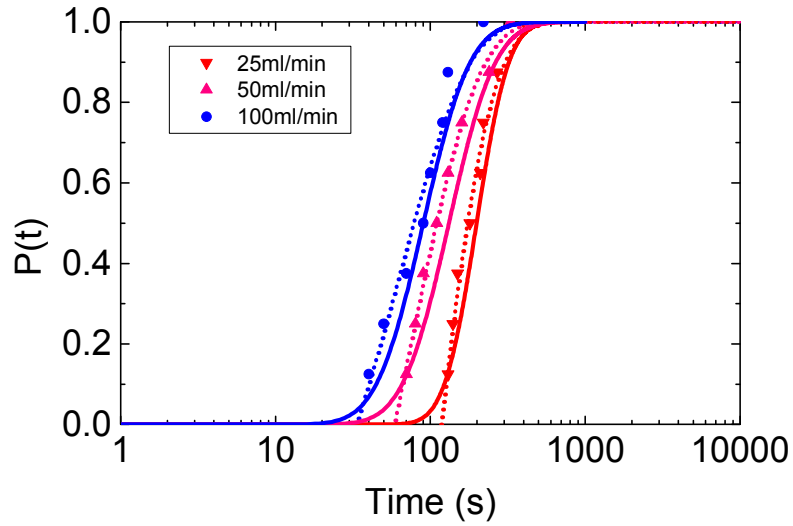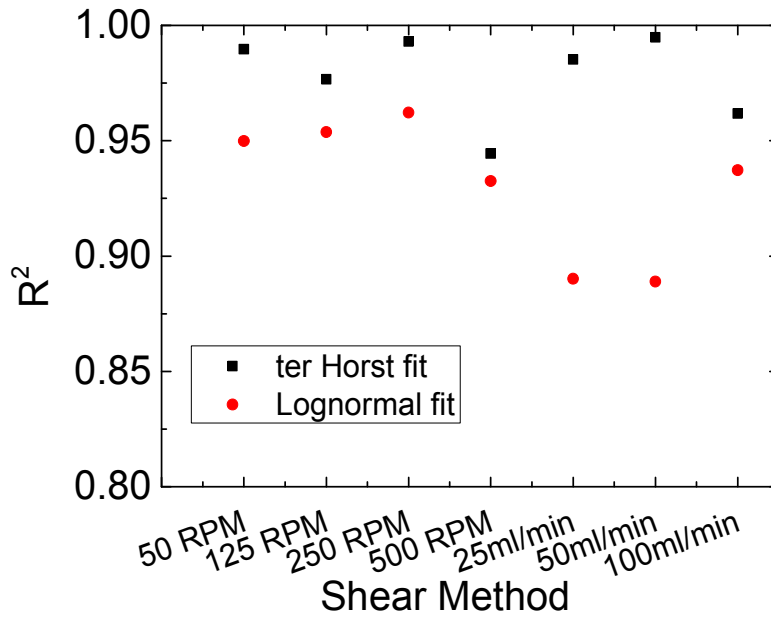

Figure 4. 15
Coefficients of determination for the best fit of the model by Jiang and ter Horst and for the log-normal distribution.

4.5.4 Influence of Controlled Fluid Shear on Nucleation Rates and Growth Times

Nucleation rates (J) and growth times (t_g) obtained from the best fit of the model by Jiang and ter Horst fit are shown in Figure 4. 16. It has already been seen that the observed induction times decreased with increasing shear rate (cf. Figure 4. 9), so it would be expected that the nucleation rate increases with increasing shear rate, and/or the growth time decreases with increasing shear rate.

As shown in Figure 4. 16, nucleation rates increased fairly sharply at lower shear rates (<100 s^{-1}) followed by a slower increase at higher shear rates (>100 s^{-1}), and there was good agreement between values obtained from Couette and capillary measurements with the same average shear rate. It can be seen that nucleation rates can be enhanced by at least one order of magnitude by laminar shear flow in the flow setups used here.

The increase of nucleation rate with increasing shear rate, as shown in Figure 4. 16, could be explained by several possible factors such as improved molecular alignment[10, 14, 15], cluster aggregation[16-18] or mass transfer[19-21], resulting in higher nucleation rates[16, 18]. These possible reasons are discussed in detail in Chapter 5 Section 5.7 and Chapter 6 Section 6.6.

It can be also seen in Figure 4. 16 that growth times decreased significantly with increasing shear rates. This could have been due to enhanced mass transfer to the growing crystals, meaning that crystals grew to an attrition size more quickly. Higher levels of shear could also mean that size of crystals at which attrition occurred became smaller. Another reason is that secondary nucleation increased with increasing shear rate, meaning that a detectable amount of crystals formed more quickly as the solution's turbidity increased rapidly. If there were more secondary nuclei, they would not have had to grow to as large a size to be detected. The effect of shear on growth times is discussed in more detail in Chapter 5 Section 5.7.
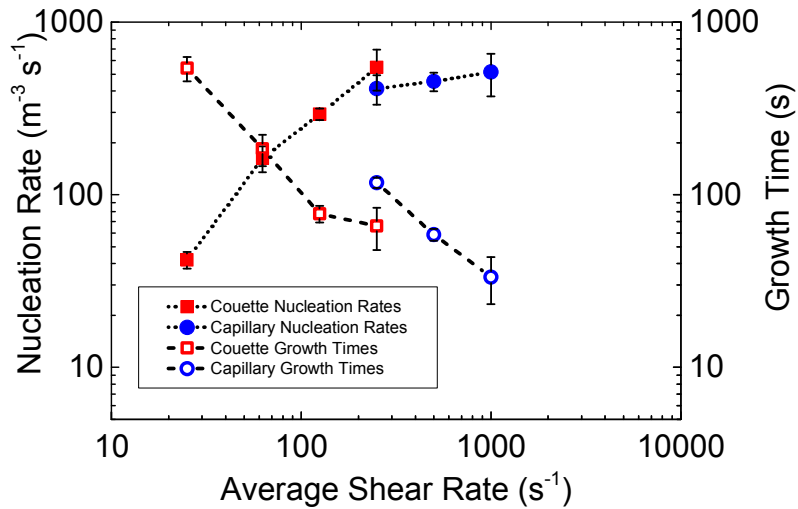
Figure 4. 16

Nucleation rates J and growth times t_g estimated from the best fit of the model by Jiang and ter Horst. Error bars represent 95% confidence intervals.

4.6 Statistical Trends and Impact of Sample Size

Recent literature suggests that due to the stochastic nature of nucleation in small volumes, a large number of repetitions (on the order of 100-1000) should be carried out to obtain accurate results[1, 6, 7, 18, 22]. Here, a detailed statistical analysis of the induction time experimental data has been carried out, and it has been found that far fewer repetitions were sufficient to deduce reliable trends for how the nucleation rates vary with shear rate for the system investigated here[23].

The approach used was to generate model datasets of varying sample size at each shear rate using the bootstrapping or Monte Carlo simulations described below. A linear regression was then fitted to the log(induction time) versus log(average shear rate) plots of these model data. The slope of the regression varied from one model dataset to another, so the effect of sample size on the mean and standard deviation of the regression slopes was investigated. As shown below, it was found that the number of experimental repetitions performed was indeed sufficient to obtain

statistically reliable results. Furthermore, the best fit slope for the experimental data and its confidence interval were calculated.

Since plots of log(induction time) versus log(average shear rate) showed linear dependence, this meant that the induction times were related to the average shear rate through a power law relationship.

$$\log(t_i) = \log(a) + k \log(\dot{\gamma}_{avg}) \qquad \textbf{(4. 17)}$$

$$t_i = a\dot{\gamma}_{avg}{}^{k} \qquad \textbf{(4. 18)}$$

Here t_i is the induction time, $\dot{\gamma}_{avg}$ is the average shear rate, a is a constant term and k is the power/ slope.

4.6.1 Bootstrapping Method

Bootstrapping of the data was done to estimate the reliability of the regression slopes obtained from linear least squares fits to the log(induction time) data as a function of log(average shear rate)[23, 24]. The bootstrapping approach has proved useful in estimating standard deviations in other nucleation systems[25]. Excel macros were written to carry out the bootstrapping procedure.

For bootstrapping, the experimental data were randomly resampled (with replacement so that a given data point could be re-selected) for each set of conditions. Resampling was done by assigning a number to each measured induction time for a particular set of conditions and then using a random number generator to select which induction time data points were to be resampled.

Full and partial bootstraps were done. For the full bootstraps, the number of resamples was equal to the number of measurements in each data-set taken at the various experimental conditions; if a data set contained 5 induction times, 5 resamples were taken. For partial bootstraps, the number of resamples was varied from 1 to 10.

The resampled induction times were plotted as a function of shear rate (log(induction time) versus log(average shear rate)) and the slope of the plot was calculated from a linear least squares fit. This procedure of resampling and calculating the slope of log(induction time) versus log(average shear rate) was repeated 400 times and the mean slope and standard deviation were found.

4.6.2 Monte Carlo Simulation Method

Monte Carlo simulations were carried out by assuming that the induction times followed a log-normal distribution or the Jiang and ter Horst model. Parameters for these (mean and standard deviation of log induction times for log-normal distribution and nucleation rate, growth time and their errors for the Jiang and ter Horst model) were obtained for each set of data, as described previously in Section 4.5.

For each modelled distribution, a large number of samples (induction times) were drawn in the usual Monte Carlo procedure, as explained in the following section, allowing the effect of sample size to be investigated more robustly than in the bootstrap method.

As with the bootstrapping, the slope from the least squares fit of the sampled log(induction time) versus log(shear rate) was calculated for each simulated data set, and the procedure was repeated 400 times. From the repetitions, the mean slope and the corresponding standard deviation were found.

4.6.2.1 Lognormal Method

When sample data were drawn based on a log-normal distribution of induction times, the procedure used the mean and standard deviation of log induction times obtained for a set of experiments carried out at particular experimental conditions. The data set was generated by assuming that the standard deviation was normally distributed. A normal deviate ($x_{deviate}$) was used for this, as shown in Eqn.(4. 19). Normal deviates are discussed in Section 4.6.2.3.

$$\log(t_i)_{gen} = \overline{\log(t_i)} + \sigma x_{deviate} \sqrt{2} \mathrm{erf}^{-1}(2P_{rand} - 1) \qquad \textbf{(4. 19)}$$

Here $\log(t_i)_{gen}$ is the generated log induction time, $\overline{\log(t_i)}$ is the mean of the log induction times obtained from a set of experiments based on fixed experimental conditions, σ is the standard deviation of these and P_{rand} is a randomly generated probability between 0 and 1.

4.6.2.2 Jiang and ter Horst Method

When sample data were generated based on the Jiang and ter Horst model, the procedure used the nucleation rate and growth time (and their 95% confidence intervals) obtained for a set of experiments carried out at particular experimental conditions. The data set was generated by assuming that the value of the errors on the nucleation rate and growth rate were normally distributed. 2 normal deviates were used for this, as shown in Eqn. (4. 20).

$$(t_i)_{gen} = t_g + \frac{t_g^{error}}{1.96} x_{deviate1} - \frac{\ln(1 - P_{rand})}{V(J + \frac{J_{error}}{1.96} x_{deviate2})} \qquad \text{(4. 20)}$$

Here $(t_i)_{gen}$ is the generated induction time, t_g^{error} is the 95% confidence interval for the growth time, J_{error} is the 95% confidence interval for the nucleation rate and $x_{deviate1}$ and $x_{deviate2}$ are normal deviates. 95% confidence is approximately 1.96 standard deviations.

4.6.2.3 Normal Deviate

The normal deviates were obtained by a rejection method. A random number between -5 and 5 was generated (x). This range was chosen since it is the typical range of x axis values for a normal distribution with a mean value of zero and standard deviation of 1, as shown in Figure 4. 17 (5 standard deviations represent well over 99.999% confidence). The probability density function value (p) was calculated based on this randomly generated x value, a mean of zero and standard deviation of 1.

$$p = \frac{1}{\sigma\sqrt{2\pi}} \exp\left(\frac{(x-\mu)^2}{2\sigma^2}\right) \qquad \text{(4. 21)}$$

Here σ is the standard deviation which was made equal to 1, μ is the mean which was made equal to zero and x is the randomly generated value between -5 and 5.
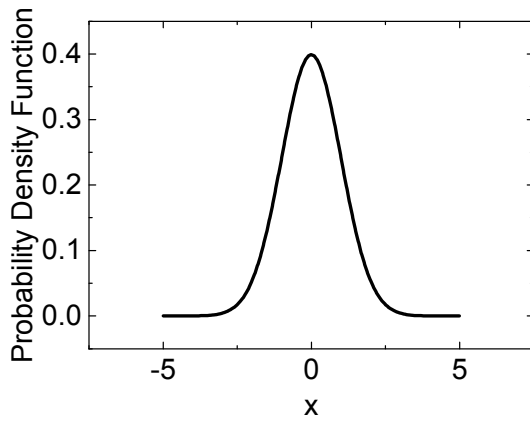
Figure 4. 17
Normal distribution with a mean value of zero and standard deviation of 1.

A random number between 0 and 1 (probability) (N_{rand}) was generated and this was compared to the calculated probability density function, p. If the random number (N_{rand}) was greater than the calculated probability density function (p), the random deviate (x) was rejected. The procedure of generating a random deviate (x), calculating the probability density function (p) based on the random deviate, and comparing the probability density function to a random number between 0 and 1 was repeated until the random number generated was less than or equal to the calculated probability density function i.e. it lay under the normal distribution curve in Figure 4. 17. When this was the case, the x value was accepted and became the normal deviate, $x_{variate}$.
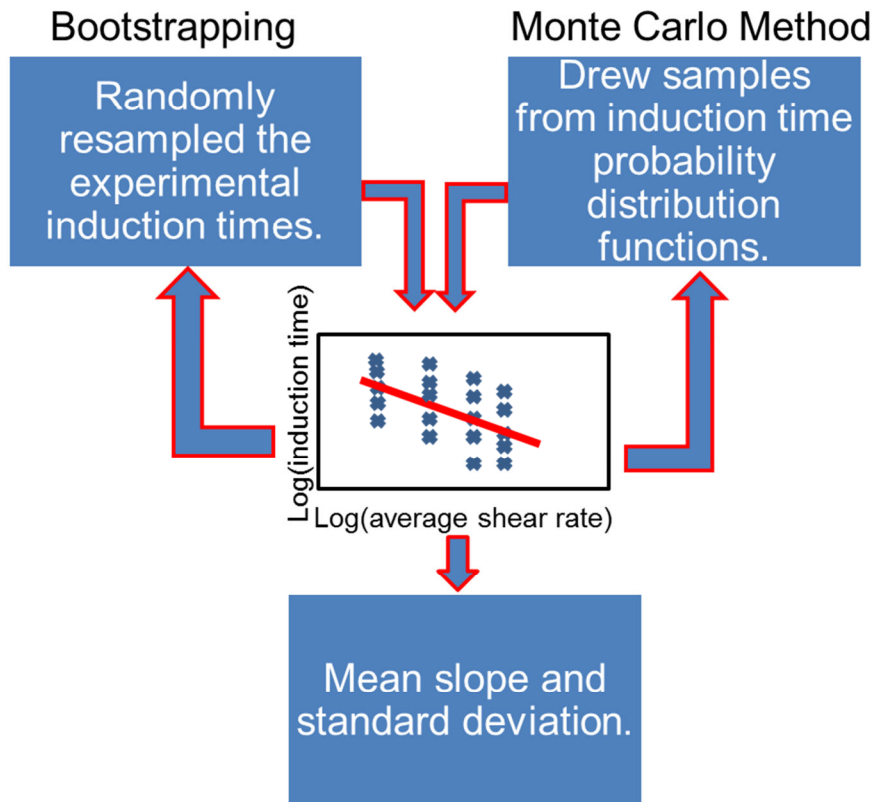
4.6.3 Statistical Analysis Summary Diagram

Figure 4. 18
Diagram summarising the bootstrapping and Monte Carlo procedures carried out.

4.6.4 Effect of Sample Size

The standard deviation of the calculated slopes was found to decrease with increasing the sample size (number of experimental repetitions), as shown in Figure 4. 19. Although Monte Carlo simulations showed that increasing the number of repetitions (samples) to 100 would ensure much lower uncertainties as would be expected, the statistical significance of the observed trend could be established with far fewer repetitions. For the work done in this thesis, each experiment was repeated at least 10 times which was enough for trends to be reliable.
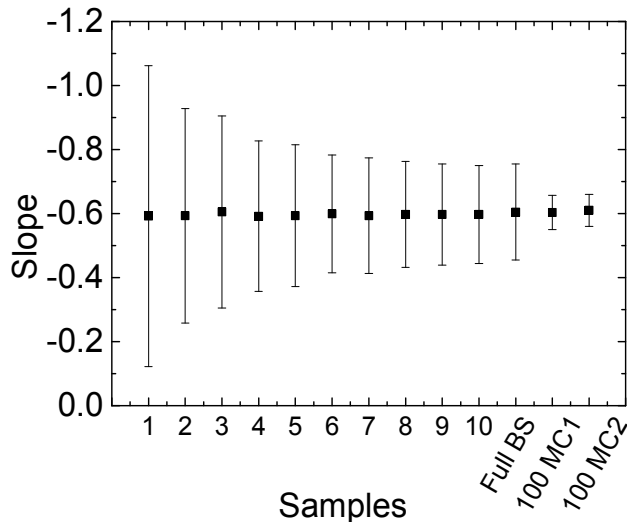

Figure 4. 19
Slopes found from bootstrapping (1-10 resamples and full) and 100 sample Monte Carlo simulations. MC1 is for lognormal model (Eqn.(4. 3)). MC2 is for Jiang and ter Horst model (Eqn. (4. 13)). Slopes are based on experimental data from Couette (excluding 50 rpm) and capillary setups. Error bars represent 2 standard deviations.

4.6.5 Influence of Chosen Data Sets

The slope values for log(induction time) versus log(average shear rate) obtained through each method (bootstrapping and Monte Carlo) depended on which data were included in the analysis. Since distributions of induction times for 50 rpm (the lowest rotational rate used) overlapped significantly with those for unsheared solutions, fits were done including and excluding these. The slopes and standard deviations found from full bootstraps of different data sets are shown in Table 4.1. Importantly, the slopes found were always negative within their confidence intervals. This confirmed that it was valid to conclude that increasing shear rates were associated with smaller induction times for the system investigated here.

Table 4. 1

Slopes and standard deviations from full bootstraps of various data sets

Data used	Slope from full bootstrap	2 Standard Deviations
Couette	-1.07	0.22
Couette excluding 50 rpm data	-0.79	0.28
Capillary	-0.57	0.32
Couette and capillary	-0.81	0.12
Couette and capillary excluding 50 rpm data	-0.61	0.16

Excluding the 50 rpm data had a significant effect on all slopes, which suggested that nucleation may have been occurring by a different mechanism for these conditions compared to the other Couette and capillary data. The 50 rpm induction times may also have been overestimated due to the slower rate of secondary nucleation that occurred for these experiments, compared to higher rotational rates, as mentioned earlier.

When 50 rpm data were excluded, slopes were within confidence intervals of each other for Couette and capillary results, as shown in Figure 4. 20. This suggested that shear enhanced primary nucleation may potentially have been occurring through similar mechanisms in both flow setups. The slopes found from analyses based on multiple Couette and capillary data sets had reasonably low standard deviations, particularly when the number of samples exceeded 5. This indicated that the slopes obtained reliably represented the trend of the experimental data. Standard deviations were larger when analyses were based on fewer data sets or a smaller number of samples per data set, as expected.

The slopes obtained from Monte Carlo simulations compared closely to the slopes obtain from bootstrapping the data. This suggested that the distributions assumed matched the experimental data well.

The slopes (and therefore powers in the power law dependence of the mean induction time on the average shear rate) found therefore suggested that when

anomalous data (50 rpm) were excluded, $t_i \propto \dot{\gamma}_{avg}^{-0.61 \pm 0.16}$ based on a full bootstrap to the Couette and capillary data.
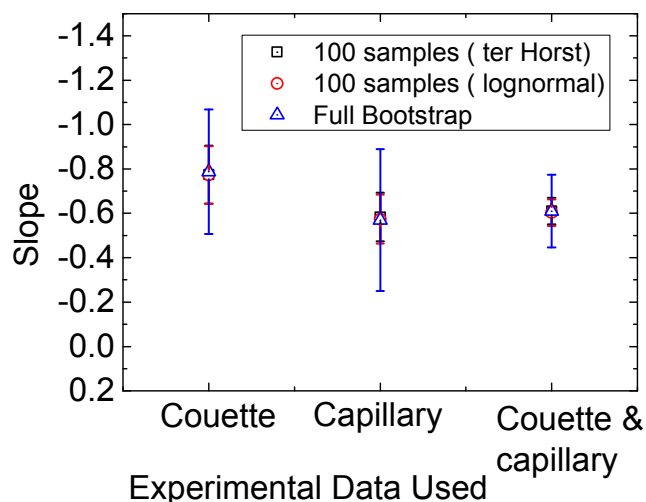

Figure 4. 20
Slopes found for Couette and capillary data (excluding 50 rpm data) using full bootstraps and 100 sample Monte Carlo simulations). Error bars represent 2 standard deviations.

4.7 Conclusions

The nucleation of glycine was investigated in supersaturated aqueous solutions exposed to well-controlled fluid shear under isothermal conditions. Well characterised flow geometries based on Couette and capillary setups were used over a wide range of average shear rates (25 s^{-1} and 1000 s^{-1}) and induction times were estimated using a range of techniques, including imaging, transmission measurements and visual monitoring. Due to the stochastic nature of nucleation, experiments were repeated multiple times and a statistical analysis was performed to show that this number of repetitions was sufficient for accurate trends to be deduced. Great care was taken to eliminate any seeding in order to avoid secondary nucleation preceding the formation of the first crystals through primary nucleation.

Induction times obtained under shearing in the Couette and capillary flow setups were found to be considerably lower than those in unsheared solutions. Distributions of induction times appeared to closely follow a distribution based on a previously published model by Jiang and ter Horst[1]. Using their model, where the induction time is related to the rate of formation of primary nuclei and the time it takes for them to grow to the size where the secondary nucleation becomes significant, it was found that both the primary nucleation rate and the growth time were strongly

dependent on the shear rate imposed. Moreover, increasing the average shear rate reduced the mean induction time in a power law relationship: $t_{ind} \propto \dot{\gamma}_{avg}^{-0.61 \pm 0.16}$.

Using the model by Jiang and ter Horst, it was found that the primary nucleation rate increased and at the same time, the growth time decreased with increasing shear rate. The nucleation rates increased fairly sharply at lower shear rates (<100 s^{-1}) followed by a slower increase at higher shear rates (>100 s^{-1}), and there was good agreement between the values obtained from Couette and capillary setups. The nucleation rates were enhanced by at least one order of magnitude by laminar shear in the flow systems studied here.

4.8 Summary

- Controlled fluid shear was obtained using Couette and capillary flow setups.
- Induction times were measured while solutions were sheared.
- Imaging and simultaneous transmission and scattering measurements were used to measure induction times and gave complementary results.
- Induction times for sheared solutions were less than for solutions that were not sheared.
- Shear was proposed to enhance the primary nucleation of a nucleus, which then underwent extensive secondary nucleation.
- A plot of log(induction time) versus log(average shear rate) was linear, suggesting a power law relationship between induction time and average shear rate.
- The probability distributions of induction times were analysed and compared well to log-normal distributions and a model proposed by Jiang and ter Horst[1].
- The model proposed by Jiang and ter Horst showed that as the average shear rate increased, the nucleation rate increased and growth time decreased.
- Bootstrapping and Monte Carlo simulations were used to show that the number of repetitions carried out here was sufficient for reliable trends to be deduced.

4.9 References and Nomenclature

4.9.1 References

(1)   Jiang, S. F.; ter Horst, J. H., Crystal Nucleation Rates from Probability Distributions of Induction Times. *Crystal Growth & Design* **2011,** 11, (1), 256-261.

(2)   JelinskaKazimierczuk, M.; Szydlowski, J., Isotope effect on the solubility of amino acids in water. *Journal of Solution Chemistry* **1996,** 25, (12), 1175-1184.

(3)   Dowling, R.; Davey, R. J.; Curtis, R. A.; Han, G. J.; Poornachary, S. K.; Chow, P. S.; Tan, R. B. H., Acceleration of crystal growth rates: an unexpected effect of tailor-made additives. *Chemical Communications* **2010,** 46, (32), 5924-5926.

(4)   Mullin, J. W., *Crystallization*. 4th ed.; Heineman: 2002.

(5)   Kadam, S. S.; Kramer, H. J. M.; ter Horst, J. H., Combination of a Single Primary Nucleation Event and Secondary Nucleation in Crystallization Processes. *Crystal Growth & Design* **2011,** 11, (4), 1271-1277.

(6)   Kadam, S. S.; Kulkarni, S. A.; Ribera, R. C.; Stankiewicz, A. I.; ter Horst, J. H.; Kramer, H. J. M., A new view on the metastable zone width during cooling crystallization. *Chemical Engineering Science* **2012,** 72, 10-19.

(7)   Kulkarni, S. A.; Kadam, S. S.; Meekes, H.; Stankiewicz, A. I.; ter Horst, J. H., Crystal Nucleation Kinetics from Induction Times and Metastable Zone Widths. *Crystal Growth & Design* **2013,** 13, (6), 2435-2440.

(8)   Kulkarni, S. A.; Meekes, H.; ter Horst, J. H., Polymorphism Control through a Single Nucleation Event. *Crystal Growth & Design* **2014,** 14, (3), 1493-1499.

(9)   Parambil, J. V.; Schaepertoens, M.; Williams, D. R.; Heng, J. Y. Y., Effects of Oscillatory Flow on the Nucleation and Crystallization of Insulin. *Crystal Growth & Design* **2011,** 11, (10), 4353-4359.

(10)   Penkova, A.; Pan, W. C.; Hodjaoglu, F.; Vekilov, P. G., Nucleation of protein crystals under the influence of solution shear flow. *Interdisciplinary Transport Phenomena in the Space Sciences* **2006,** 1077, 214-231.

(11)   Sear, R. P., On the interpretation of quantitative experimental data on nucleation rates using classical nucleation theory. *Journal of Physical Chemistry B* **2006,** 110, (43), 21944-21949.

(12)   Sear, R. P., Quantitative studies of crystal nucleation at constant supersaturation: experimental data and models. *Crystengcomm* **2014,** 16, (29), 6506-6522.

(13)   Limpert, E.; Stahel, W. A.; Abbt, M., Log-normal distributions across the sciences: Keys and clues. *Bioscience* **2001,** 51, (5), 341-352.

(14)   Keller, A., Polymer Crystals. *Reports on Progress in Physics* **1968,** 31, 623-&.

(15)   Vekilov, P. G., The two-step mechanism of nucleation of crystals in solution. *Nanoscale* **2010,** 2, (11), 2346-2357.

(16)   Jawor-Baczynska, A.; Sefcik, J.; Moore, B. D., 250 nm Glycine-Rich Nanodroplets Are Formed on Dissolution of Glycine Crystals But Are Too Small To Provide Productive Nucleation Sites. *Crystal Growth & Design* **2013,** 13, (2), 470-478.

(17)   Gebauer, D.; Voelkel, A.; Coelfen, H., Stable Prenucleation Calcium Carbonate Clusters. *Science* **2008,** 322, (5909), 1819-1822.

(18)   Liu, J.; Rasmuson, A. C., Influence of Agitation and Fluid Shear on Primary Nucleation in Solution. *Crystal Growth & Design* **2013,** 13, (10), 4385-4394.

(19)   Mullin, J. W.; Raven, K. D., Nucleation In Agitated Solutions. *Nature* **1961,** 190, (477), 251-&.

(20)   Mullin, J. W.; Raven, K. D., Influence Of Mechanical Agitation On Nucleation Of Some Aqueous Salt Solutions. *Nature* **1962,** 195, (4836), 35-&.

(21)   Nyvlt, J.; Skrivane.J; Gottfrie.J; Krickova, J., Uber Kristallisation .19. Einfluss Der Durchmischung Auf Die Breite Der Metastabilen Zone. *Collection of Czechoslovak Chemical Communications* **1966,** 31, (5), 2127-&.

(22)   Galkin, O.; Vekilov, P. G., Direct determination of the nucleation rates of protein crystals. *Journal of Physical Chemistry B* **1999,** 103, (49).

(23)   Forsyth, C.; Mulheran, P. A.; Haw, M. D.; Burns, I. S.; Sefcik, J., Influence of Controlled Fluid Shear on Nucleation Rates in Glycine Aqueous Solutions. *Crystal Growth & Design* **2015,** 15, (1), 94-102.

(24)   Press, W. H.; Teukolsky, S. A.; Vetterling, W. T.; Flannery, B. P., *Numerical Recipes in Fortran 77*. ed.; Cambridge University Press: New York, 2006.

(25)   O'Neill, K. P.; Grinfeld, M.; Lamb, W.; Mulheran, P. A., Gap-size and capture-zone distributions in one-dimensional point-island nucleation and growth simulations: Asymptotics and models. *Physical Review E* **2012,** 85, (2), 8.

4.9.2 Main Nomenclature

a= constant

c= concentration

c^*= solubility concentration

erf = error function

J = nucleation rate per unit volume

J_{error} = 95% confidence interval for the nucleation rate

k = power/ slope

$\log(t_i)_{gen}$= generated log induction time

M= total number of experiments carried out for a given set of conditions

m = number of nuclei that form in a time interval

N = average number of nuclei that form in the time interval

N_{rand}= random number between 0 and 1

$O(t_i)$= cumulative distribution of observed induction times

p = probability density function

p_m= Poisson probability mass function

p_0= probability that no crystals form in a time interval

P_{rand}= randomly generated probability between 0 and 1

$P(t_i)$ = cumulative distribution of induction times for the Jiang and ter Horst model

$P(t_n)$ = cumulative distribution of nucleation times for the Jiang and ter Horst model

$Q(t_i)$= cumulative distribution of induction times for the lognormal distribution

R^2= coefficient of determination

S= supersaturation

SS_R = sum of squared residuals

SS_T = total sum of squares

T= time

t_g= growth time

t_i= induction time where $i = 1,2,\dots M$

$(t_i)_{gen}$ = generated induction time

t_g^{error} = 95% confidence interval for the growth time

t_n= nucleation time

V = volume of the solution in the vessel

x = randomly generated value between -5 and 5

$x_{deviate}$= normal deviate

$\dot{\gamma}_{avg}$= average shear rate

μ = mean

σ = standard deviation

5. Influence of Controlled Fluid Shear and Surface Area on Nucleation Rates in Glycine Aqueous Solutions

Chapter Outline and Contents

In Chapter 4, it was shown that controlled fluid shear could enhance nucleation rates in aqueous glycine solutions by at least one order of magnitude. In this chapter, this work is extended and the effect of the area of surface that the solution was exposed to while it was being sheared in the Couette cell was investigated.

The nucleation of glycine was investigated in supersaturated aqueous solutions exposed to well-controlled fluid shear in a Couette cell under isothermal conditions. A wide range of average shear rates (25 s^{-1} to 250 s^{-1}) were used and the surface area that the solution was exposed to was varied (2.5 cm^2 per ml solution to 10 cm^2 per ml solution). Care was taken to eliminate any seeding in order to avoid secondary nucleation preceding the formation of the first crystals through primary nucleation. Induction times were estimated using a range of techniques including imaging, transmission measurements and visual monitoring. Due to the stochastic nature of nucleation, experiments were repeated multiple times.

Induction times obtained under shearing were found to be considerably lower than those in unsheared solutions for each of the surface to volume ratios used. Exposure to larger surface areas also resulted in shorter induction times.

The model proposed by Jiang and ter Horst (see Chapter 4) showed that as the shear rate and surface area increased, the primary nucleation rate increased and growth time decreased.

The induction times were found to decrease with increased shear rates and increased surface areas in a power law relationship: $t_i \propto (\dot{\gamma}_{avg}A)^{-0.83\pm0.2}$. The probability distributions of induction times were found to scale with shear rate and surface area and master equations were fitted to the scaled data with low errors. This suggested that all processes that took place during nucleation were measured on one key timescale, which was proportional to $\frac{1}{\dot{\gamma}_{avg}A}$. These findings therefore suggested that the total deformation of solutions and the surface area that solutions were exposed to were important in determining induction times and hence rates of primary nucleation. Shear and surface enhanced cluster aggregation may potentially help explain the behaviour seen.

This chapter covers:

- The glycine solution preparation method.
- The experimental procedure for Couette experiments.
- The induction time results obtained from the experiments.
- A Design of Experiments (DoE) analysis of the induction time results.
- The probability distributions of induction times.
- The scaling of induction times.
- Possible explanations for the behaviour seen.

5.1 Glycine Solution Preparation

Glycine (CAS Number 56-40-6) of ≥99% purity was purchased from Sigma Aldrich (item G8898) and used without further purification. Two concentrations (c) of solution were prepared by dissolving glycine in deionised water- 307 g glycine/kg water and 325 g glycine/kg water. During experiments, these solutions were cooled to 20°C and 23°C respectively. The solubility (c^*) of glycine was 219 g glycine/kg water at 20°C and 232 g glycine/kg water at 23°C[1]. Cooling therefore resulted in a supersaturation (S) of 1.4 for both solutions, where

$$S = \frac{c}{c^*}$$

(5. 1)

Solutions were prepared in sealed glass bottles and were stirred at 55°C for 24 hours to ensure that glycine was fully dissolved. When the solutions were at 55°C, they were undersaturated.

For the work detailed in this chapter, Couette cell experiments that used a 30 mm inner cylinder were performed at 23°C and Couette cell experiments that used a 22 mm or 34 mm inner cylinder were performed at 20°C.

5.2 Couette Experimental Procedure

The Couette experimental procedure was similar to the procedure detailed in Chapter 4, however, here three diameters of inner cylinder were used (22 mm, 30 mm and 34 mm), rather than the one diameter (30 mm) that was used in Chapter 4. More details on the construction and setup of the Couette cells are given in Chapter 2.

15 ml undersaturated glycine solution (in incubator at 55°C) was filtered using preheated 0.2 µm SFCA disposable syringe filters (with the exception of 125 s^{-1} 30 mm inner cylinder imaging experiments for which solutions were unfiltered) into a preheated Couette cell by syringe. The filters, syringe and Couette cell were preheated to 55°C in the incubator, and the filtration procedure took place inside the incubator to minimise the rate of heat loss.

For 30 mm inner cylinder induction time experiments, solutions with a concentration of 325 g glycine/kg water were used since they were eventually cooled to 23°C. For

22 mm and 34 mm inner cylinder experiments, solutions with a concentration of 307 g glycine/kg water were used since they were cooled to 20°C. All resulted in solutions of S=1.4 when cooled.

The filled Couette cell was removed from the incubator and attached to a monitoring instrument that was set up to allow induction times to be obtained quantitatively (as described in Chapter 3). The monitoring instrument allowed transmission/ scattering measurements to be taken simultaneously. For the experiments here, induction times were obtained from transmission measurements (scattering data were not collected/ used). Scattering and transmission methods were previously found to give identical induction times, as mentioned in Chapter 3. A camera was also in place to image the solution as it was sheared; induction times could be obtained by analysing the images.

To minimise evaporation at the solution/ air, a lid was secured to the Couette Cell and parafilm was used to ensure it was well sealed. The solution was left to cool in the surrounding air for 30 minutes in order to reach ambient temperature and the desired level of supersaturation. For 30 mm inner cylinder induction time experiments, the ambient air was 23°C while for 34 mm and 22 mm inner cylinder experiments, it was 20°C. There was no cylinder rotation during cooling. During cooling, a fan was used to speed up heat transfer.

The temperature profile of the solution during cooling was measured to validate that the 30 minute cooling time was sufficient to ensure that the solutions had reached ambient temperature after this time. The ambient temperature remained constant throughout an experiment so the solution remained isothermal once it had cooled to ambient temperature. Since shearing of the solutions took place under isothermal conditions (the temperature of the solution was equal to the temperature of its surroundings), the effect of laminar shear on induction times was not linked to heat transfer.

Once the solution cooling period had finished, the fan was switched off and the motor and monitoring equipment were started. Rotational rates were measured using the digital tachometer and the voltage was adjusted to obtain the rotational rate necessary to give the desired shear rate for a particular cylinder arrangement. If the solution was being monitored via transmission measurements, a box was placed

over the instrument to reduce the intensity of background light reaching the detectors.

Once the solution had become visibly turbid, the motor and monitoring equipment were switched off. Data were then analysed to obtain induction times. Induction times were also obtained for experiments that involved no shearing i.e. 0 rpm. This was done visually as only a small number of crystals formed in unsheared solutions (fewer than 5, typically 1 or 2) which meant solutions did not become turbid.

For induction time measurements, time= 0 s is defined as the time at which the motor was started and cylinder rotation began. This happened after the solution had cooled to ambient temperature and therefore reached the desired level of supersaturation i.e. time= 0 s was 30 minutes after the filled Couette cell was removed from the incubator.

Induction time measurements were carried out for a wide range of shear rates and surface areas, as shown in Figure 5. 1. Since each shear rate (with the exception of 250 s^{-1}) was repeated for each cylinder geometry, a robust Design of Experiments analysis could be carried out on the data. Experiments were repeated at least 10 times. 10 repetitions had proven to be sufficient to allow reliable statistical trends to be obtained from induction time data that were measured through a similar method before[2], as detailed in Chapter 4 Section 4.6.
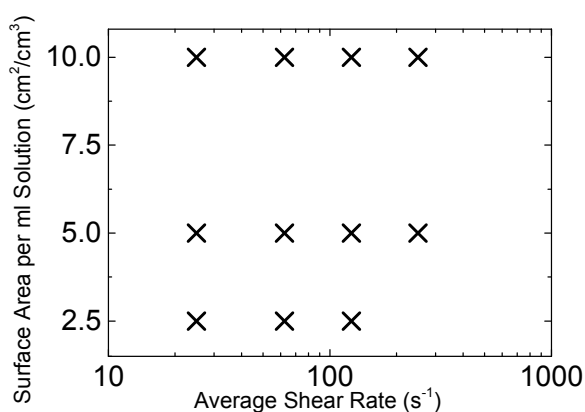

Figure 5. 1
The different combinations of shear rate and surface area that were used in the induction time experiments.

5.3 Induction Time Results

5.3.1 Induction Time Results for Each Setup

Induction times of supersaturated aqueous glycine solutions that underwent controlled fluid shear in the Couette flow devices were obtained. A wide range of average shear rates were covered: 25 s^{-1} to 250 s^{-1}. A large range of surface areas were also studied: 2.5 cm^2/ml solution to 10 cm^2/ml solution.

The induction times measured for each Couette cell geometry are shown in Figure 5. 2, Figure 5. 3 and Figure 5. 4. The mean values and standard deviation of these data are shown in Figure 5. 5. Figure 5. 6 shows the means, medians and spread of induction times. The data for the experiments where the surface to volume ratio was 5 cm^2/cm^3 are the same as those detailed in Chapter 4.

Figure 5. 2
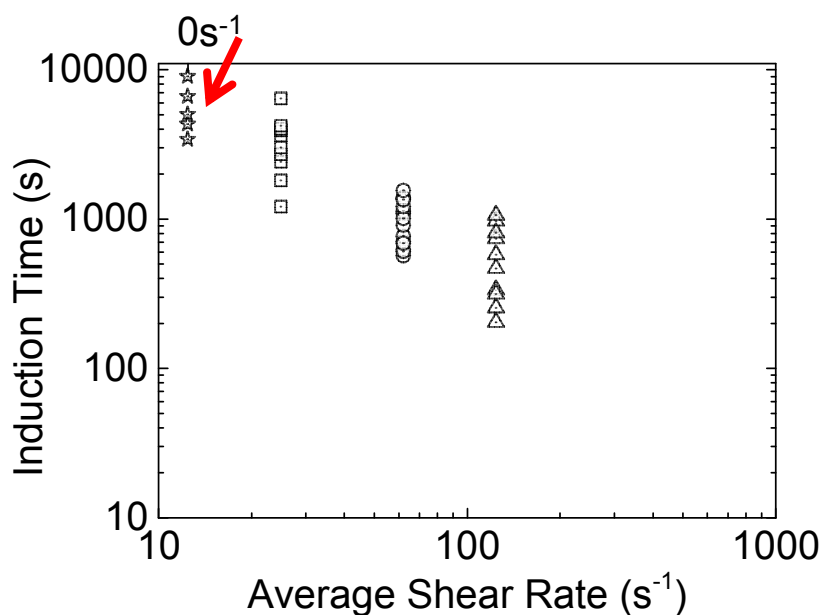Induction times measured for each shear rate when the surface to volume ratio was 2.5 cm^2/cm^3.
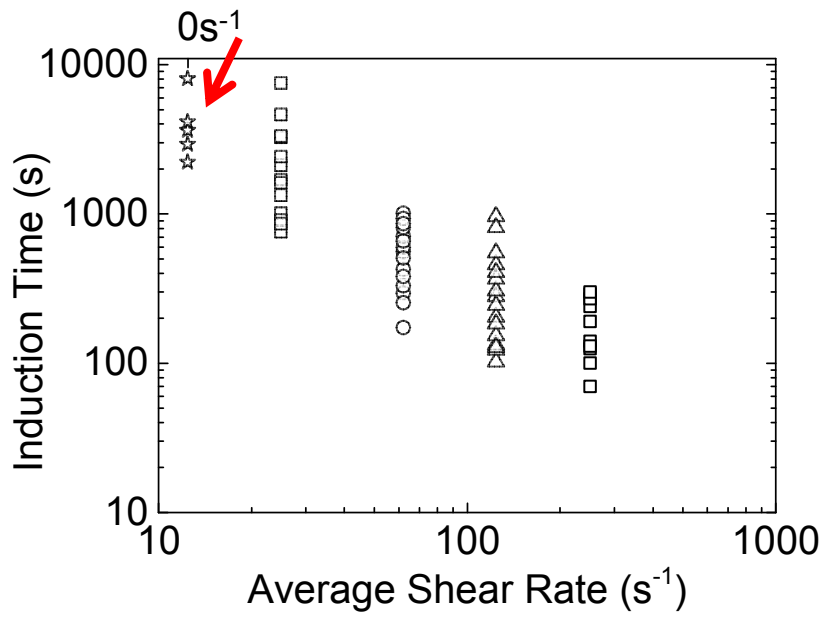
Figure 5. 3
Induction times measured for each shear rate when the surface to volume ratio was 5 cm^2/cm^3.
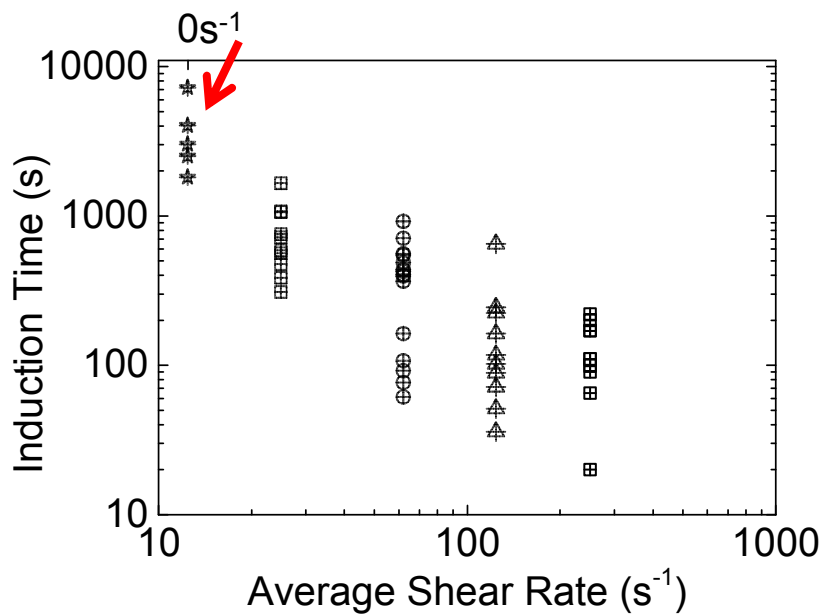

Figure 5. 4
Induction times measured for each shear rate when the surface to volume ratio was 10 cm^2/cm^3.
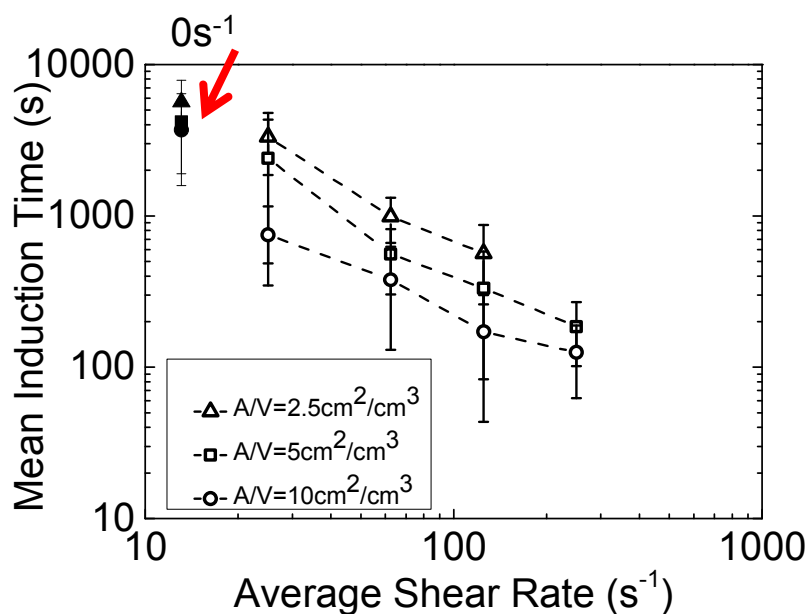
Figure 5. 5
Mean induction times measured for each shear rate/ cylinder arrangement. Error bars represent one standard deviation.
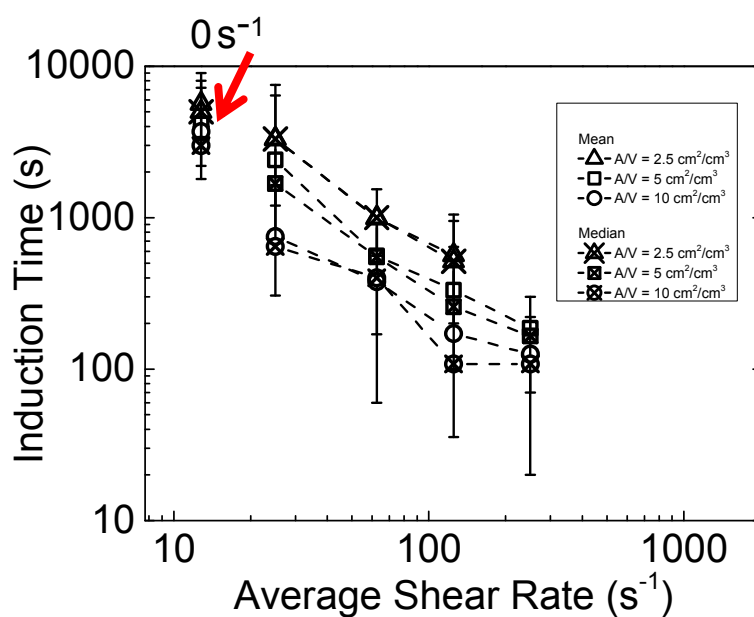

Figure 5. 6
Mean and median induction times. Error bars represent the full range of induction times measured.

Induction time measurements showed that increasing the shear rate led to shorter induction times for every cylinder surface arrangement studied. For each shear rate studied, cylinder arrangements which exposed the glycine solutions to larger surface

areas resulted in shorter induction times than cylinder arrangements with smaller surface areas. These trends are shown clearly in Figure 5. 5 and Figure 5. 6.

5.3.2 Discussion of Induction Time Results

5.3.2.1 Role of Fluid Shear on Primary and Secondary Nucleation

As concluded in Chapter 4 Section 4.4.4, shearing was hypothesised to have an influence on both primary and secondary nucleation. The crystals formed under shear were thought to be due to shear enhanced primary nucleation of a nucleus, followed by extensive secondary nucleation of the primary crystal. This was in agreement with work carried out by Jiang and ter Horst[3] which suggested that the crystallisation mechanism was due to the nucleation of a single parent crystal, followed by the attrition of the single parent crystal to form secondary nuclei.

5.3.2.2 Influence of Low Rates of Fluid Shear on Primary and Secondary Nucleation

The induction times for sheared solutions were considerably shorter than for unsheared solutions for all shear rates used with the 10 cm^2/cm^3 cylinder arrangement, however, the induction times measured for 25 s^{-1} average shear rate experiments using the 2.5 cm^2/cm^3 and 5 cm^2/cm^3 cylinder arrangements were fairly close to the unsheared induction times. The formation of the primary nucleus/nuclei may therefore not have been greatly shear enhanced for 25 s^{-1} experiments using the 2.5 cm^2/cm^3 and 5 cm^2/cm^3 cylinder arrangements since their induction times were similar to the induction times measured for unsheared solutions. Solutions sheared at these conditions, however, became turbid, unlike unsheared solutions, so secondary nucleation was likely to still have been enhanced by the flow conditions.

Normally it would be expected that even small levels of shear would significantly reduce induction times[4, 5] so a reason to account for the behaviour seen is that an overestimation of induction times may have occurred for 25 s^{-1} experiments using the 2.5 cm^2/cm^3 and 5 cm^2/cm^3 cylinder arrangements (as mentioned in Chapter 4 Section 4.4.4). The rate at which turbidity increased with these experiments was

notably lower than the other setups, which suggested slower secondary nucleation. The induction time detection method for these experiments was transmission/ imaging, while for unsheared experiments, induction times were measured visually. For sheared experiments, sufficient secondary nucleation had to take place before measured signals were substantially affected, meaning that an overestimation of induction times may have occurred when secondary nucleation was slow.

5.3.2.3 Consideration of Capillary Results

Couette flow results in this chapter showed that increasing the surface area resulted in shorter induction times. In Chapter 4 Section 4.4.2, it was shown that when a capillary flow setup was used, the induction times were reduced, but the reduction appeared to be due to the increasing shear rate. The reduction of induction times with increasing shear rates in the capillary setup followed the trend of the reduction in induction times with increasing shear rates in the Couette setups, despite the capillary exposing solution to a larger surface area (and larger free interface).

Therefore, from the results in this chapter, it would have been expected that if the capillary had a similar effect on induction times as the Couette flow setups (shear and surface area both influencing induction times), induction times would have been reduced due to both the increasing shear rate and also the larger surface area that solution was exposed to. The capillary exposed the solution to 20 cm^2 per ml of solution which is double the largest surface to volume ratio in the Couette flow setups used here. The capillary induction times measured in Chapter 4 were therefore larger than expected if shear and surface area both influenced the induction times obtained in a similar way to the Couette flow experiments. The capillary setup also exposed solution to a larger air-solution interface than Couette flow setups and it would generally be expected that larger solution- air interfaces would lead to shorter induction times.

There are some reasons which may account for results obtained. Firstly, the capillary was made from PVC so factors such as material and wetting angle may have had an effect. A drop of water on PCV has a wetting angle close to 90° so does not wet the surface well. Water on glass has a wetting angle close to 30° so wets the surface readily[6]. As reviewed in Chapter 1 Section 1.3.1.2, increased wetting of a surface can reduce the free energy barrier for nucleation, resulting in

higher nucleation rates, so glass might have been a more favourable surface for heterogeneous nucleation to take place, compared to PVC.

The results may also have been influenced by the shear profile of each setup. As detailed in Chapter 2, the capillary setup resulted in a parabolic velocity profile so the shear rate varied with radial position. This was different than the Couette cell setup which had a close to linear velocity profile and therefore constant shear rate.

Capillary induction times were measured visually and it was difficult to see through the capillary walls. Secondary nucleation in the capillary was also much slower than the Couette flow setups, which meant that a relatively small number of crystals formed in the capillary and they had to grow to sufficient sizes before they could be detected by eye. These reasons could have led to an overestimation of induction times for capillary experiments. The visual method of measuring induction times is also very error prone.

Due to the large differences in materials, setup, detection method and interface, it is therefore perhaps better not to directly compare the capillary and Couette flow setup results, as was done in Chapter 4.

5.4 Design of Experiments Analysis of Induction Time Results

5.4.1 Chosen Factors and their Levels

Minitab was used to perform a Design of Experiments (DoE) analysis of the induction time results[7]. The analysis was based on 2 factors (shear rate and surface area), each with 3 levels (25 s^{-1}, 62.5 s^{-1} and 125 s^{-1} for shear rate; 2.5 cm^2/cm^3, 5 cm^2/ cm^3 and 10 cm^2/ cm^3 for surface area). Since every possible combination of factor level was used, it represented a full factorial design. Each replicate therefore contained 9 different factor level combinations (treatments), as shown in Table 5. 1.

A factorial design, whereby every possible combination of factor levels is covered, was advantageous over a typical change one variable at a time approach since it allowed interactions between the variables to be discovered. Choosing 3 levels of each factor was better than choosing 2 levels since it allowed curvature to be detected[7].

Table 5. 1
Treatments used in DoE factorial design.

Treatment	Average Shear Rate (s^{-1})	Surface Area per ml Solution (cm^2/cm^3)
1	25	2.5
2	25	5
3	25	10
4	62.5	2.5
5	62.5	5
6	62.5	10
7	125	2.5
8	125	5
9	125	10

5.4.2 Interaction and Main Effect Plots

As mentioned, a main benefit of factorial experiments over the change one factor at a time approach is that interactions between factors can be discovered, and it is straightforward to find out if interactions exist. An interaction exists if the difference in response between levels of one factor is not the same at all levels of the other factor. This can be illustrated through two factor interaction plots, as shown in Figure 5. 7 and Figure 5. 8. If the lines are parallel, the factors do not interact significantly. The plots on Figure 5. 7 and Figure 5. 8 are fairly parallel which suggests that there was not significant interaction between the shear rate and surface factors. The main non-linearity arose due to the induction time results based on experiments with an average shear rate of 25 s^{-1} and exposed surface areas of 2.5 cm^2/cm^3 or 5 cm^2/cm^3. As discussed earlier (Section 5.3.2.2), an overestimation of induction times may have occurred for these conditions due to the slower secondary nucleation that took place.
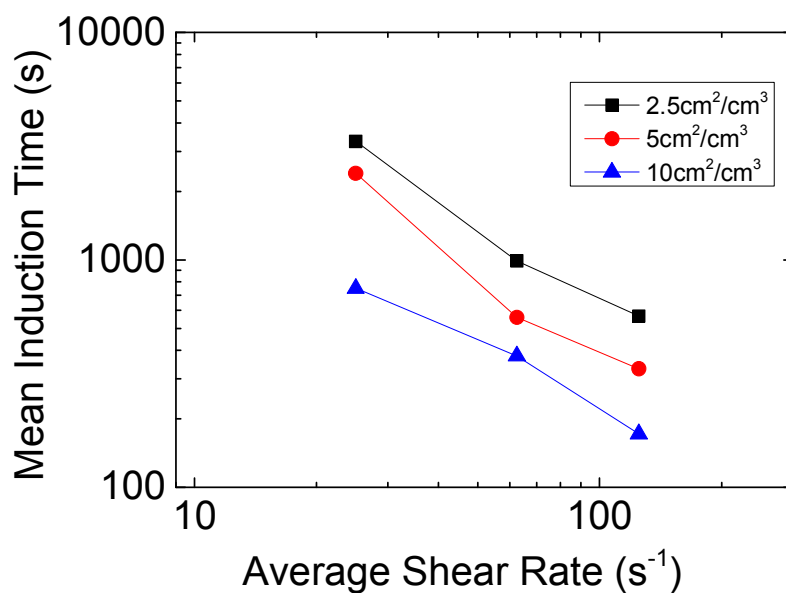

Figure 5. 7
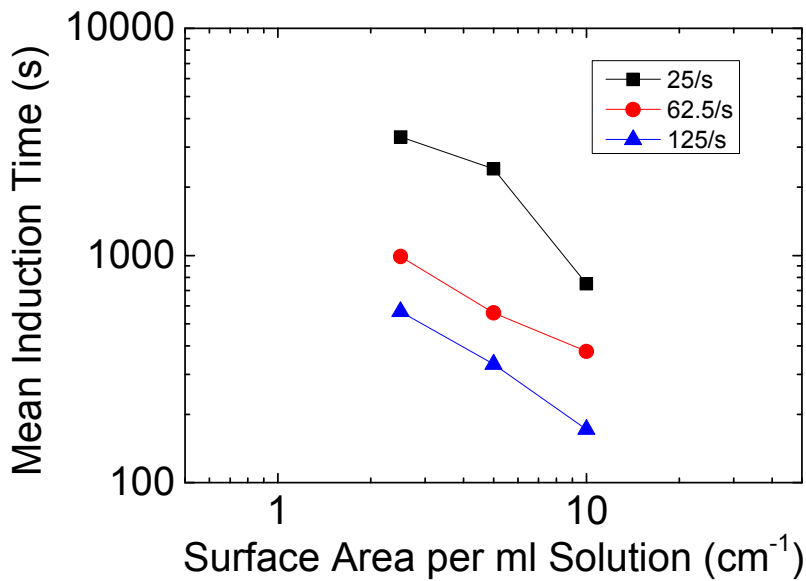Mean induction time versus average shear rate (log-log).

Figure 5. 8
Mean induction time versus surface area per ml solution (log-log).

The main effect of each factor was plotted (Figure 5. 9 and Figure 5. 10). The effect of a factor is the change in response produced by changing the level of a factor. A main effect plot is therefore a plot of the mean response values at each level of a factor. The gradient of the plot tells the direction of the effect and the magnitude of the slope indicates the strength of the effect. Since the gradients for the factors were both negative (mean induction time versus shear rate or surface area), it shows that increasing the level of each factor reduced the mean induction time.
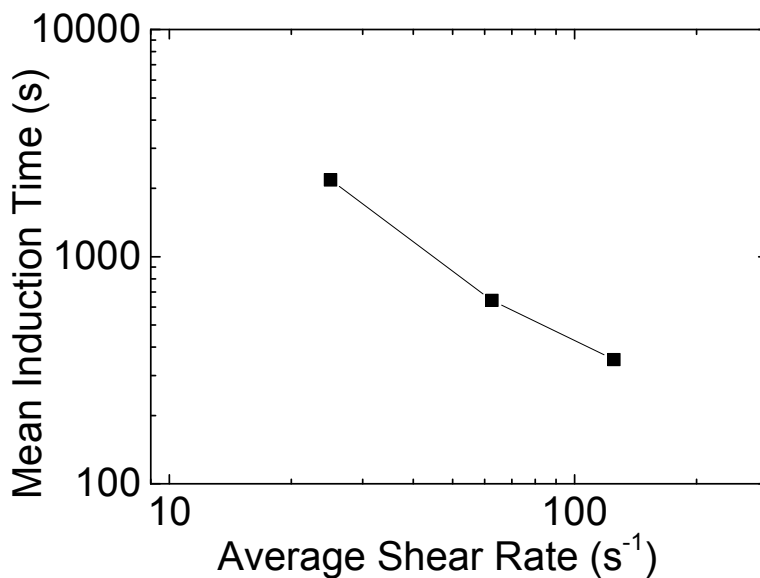

Figure 5. 9
Mean induction time versus average shear rate (log-log). Each point is the average of the 3 different surface levels.
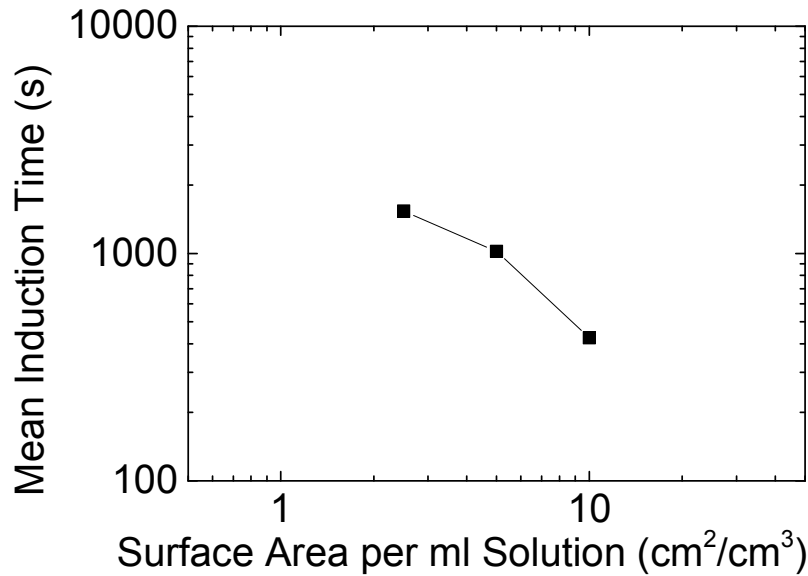
Figure 5. 10
Mean induction time versus surface area per ml solution (log-log). Each point is the average of the different shear rate levels.

5.4.3 DOE Minitab Statistical Analysis

The observations made from the graphs were confirmed by performing an analysis of variance using the DoE analysis feature in Minitab. Induction times, shear rates and surface areas were logged to linearise the plots. The main theory behind a two factor factorial experiment is given in the appendix. The theory summarises the calculations carried out by Minitab for DoE analyses. Full theory and explanations can be found in texts such as Montgomery's Applied Statistics and Probability for Engineers [7, 8].

The main outputs from the Minitab DoE analysis are given in Table 5.2. The analysis showed that shear rate and surface area affected the induction times, and there did not appear to a significant interaction between the factors. No interaction was expected as the plots on Figure 5. 5 (and Figure 5. 7 and Figure 5. 8) were fairly parallel[7]. For the analysis, the level of significance was 0.05 i.e. the analysis was based on 95% confidence. The residuals were found to be well represented by a normal distribution.

Table 5. 2
Main results from DoE analysis using Minitab.

Source	Degrees of Freedom	Sum of Squares	Mean Squares	F Statistic (f_0)	P-Value
Main Effects					
Shear rate	2	10.7	5.4	69.0	$<10^{-5}$
Surface	2	6.0	3.0	38.8	$<10^{-5}$
2-Way Interactions					
Shear rate*surface	4	0.2	0.04	0.5	0.8
Error	105	8.2			
Total	113				

<u>Main Effects</u>: from an F distribution chart, $f_{0.05,2,105} = 3.0$. Since $f_0 = 69.0$ for the effect of shear rate and $f_0 = 38.8$ for the effect of surface (both are significantly greater than 3), the null hypotheses (shear rate and surface had no effect on the induction times) could be rejected and it could be concluded that these factors affected the induction time.

<u>Interactions</u>: from an F distribution chart, $f_{0.05,4,105} = 2.5$. Since $f_0 = 0.5$ for the interaction between shear rate and surface (smaller than 2.5), the null hypothesis (there was no interaction between the factors) could not be rejected and it could therefore be concluded that there did not appear to be a significant interaction between the factors. These conclusions compared well with what was shown graphically in the interaction and main effect plots (lines parallel and negative gradient).

5.5 Distribution of Induction Times

The distributions of induction times obtained were further investigated to gain a better understanding of underlying nucleation phenomena. A similar procedure to that detailed in Chapter 4 Section 4.5 was carried out. The experimental cumulative probability distribution functions were compared to log-normal distributions and a model proposed by Jiang and ter Horst[3].

5.5.1 Comparison of Distributions

Figure 5. 11 shows the experimental data Eqn. (4.2) together with log-normal distribution curves from Eqn. (4.3), and also the best fit of the Jiang and ter Horst model from Eqn. (4.13). Both models appeared to fit the experimental data well, but the Jiang and ter Horst model generally had higher coefficients of determination (Figure 5. 12). This is in agreement with what was found in the analysis of the experiments detailed in Chapter 4 and would be expected since the Jiang and ter Horst model involved linear least squares fitting to the experimental data, whereas the log-normal method was based only on the mean and standard deviation of log induction times.
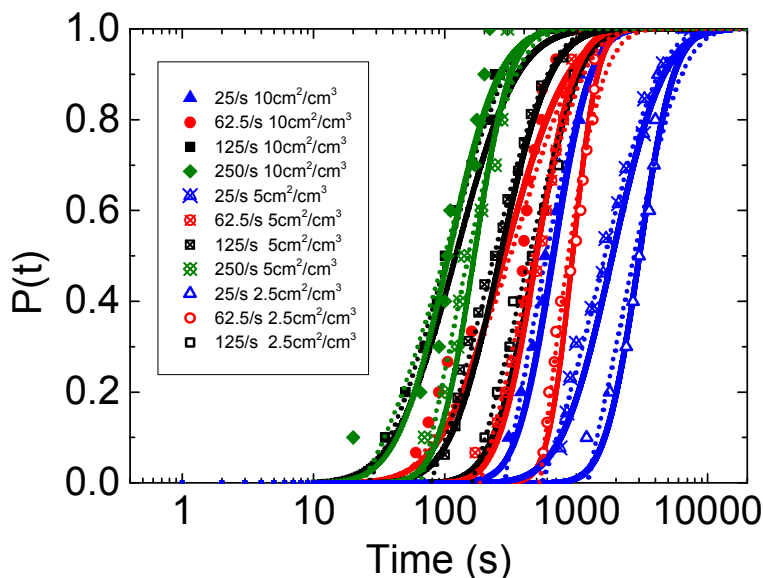

Figure 5. 11
Cumulative distribution functions for induction times for each setup. Symbols represent experimental data (Eqn. (4.2)), dashed line is the best fit for the model of Jiang and ter Horst (Eqn. (4.13)) and solid line is the log-normal distribution (Eqn. (4.3)).
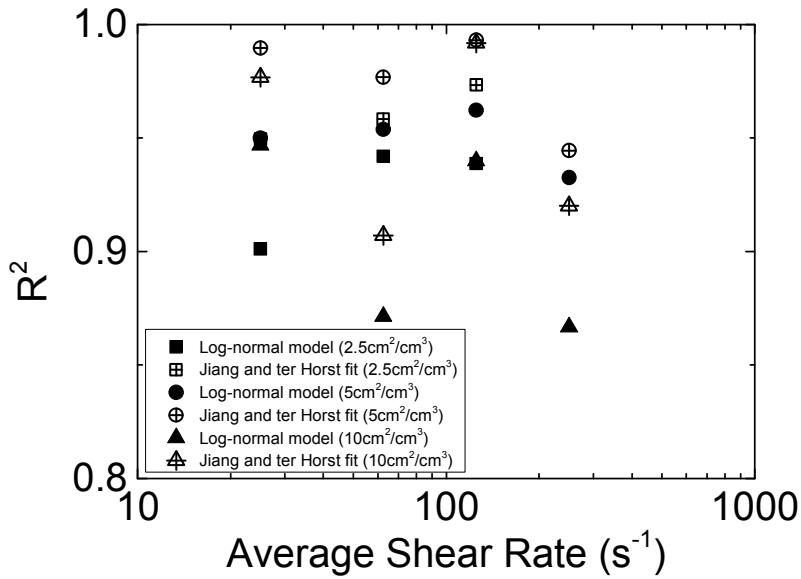
Figure 5. 12
Coefficients of determination for the best fit of the model by Jiang and ter Horst and for the log-normal model.

5.5.2 Influence of Controlled Fluid Shear on Nucleation Rates and Growth Times

Nucleation rates (J) and growth times (t_g) obtained from the best fit of the model by Jiang and ter Horst fit are shown in Figure 5. 13 and Figure 5. 14 respectively. It has already been seen that the observed induction times decrease with increasing shear rate and surface area (cf. Figure 5. 5), so it would be expected that the nucleation rate increases with increasing shear rate and surface area, and/or the growth time decreases with increasing shear rate and surface area. This is in agreement with what is shown in Figure 5. 13 and Figure 5. 14. It can be seen that nucleation rates can be enhanced significantly by laminar shear. It can also be seen that growth times decrease significantly with increasing shear rates. Nucleation rates are shown to increase with increasing surface area and growth times are shown to decrease with increasing surface area. Possible explanations for these observations is discussed more in Section 5.7
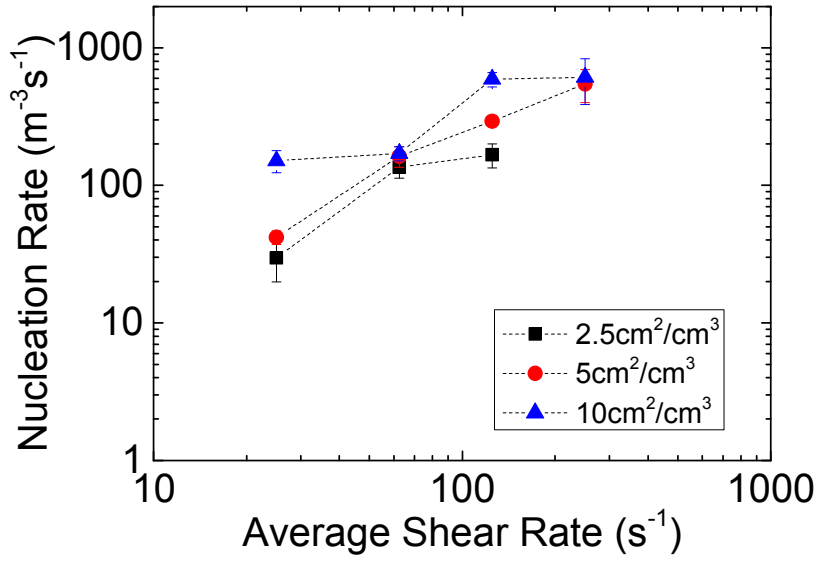
Figure 5. 13
Nucleation rates J estimated from the best fit of the model by Jiang and ter Horst. Error bars represent 95% confidence intervals.
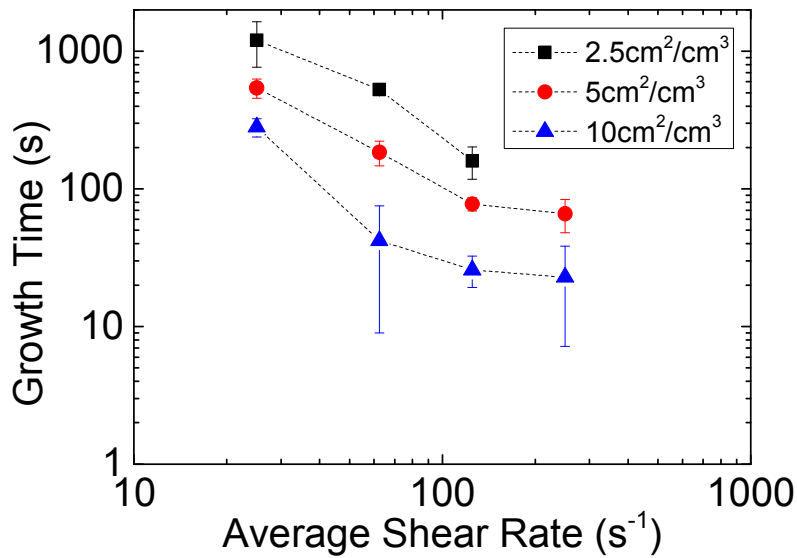

Figure 5. 14
Growth times t_g estimated from the best fit of the model by Jiang and ter Horst. Error bars represent 95% confidence intervals.

5.6 Statistical Trends and Scaling

The concept of scaling was investigated to see whether the distributions of induction times appeared to scale by shear rate and surface area. The observed cumulative probability distribution of induction times are shown in Figure 5. 15 and were calculated from Eqn. (4.2).
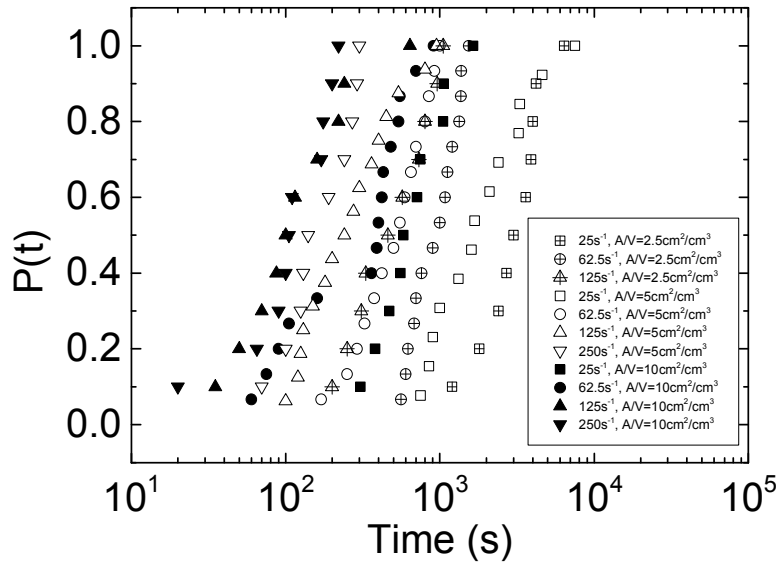

Figure 5. 15
Experimental cumulative distribution functions of induction times for each setup.

When induction times were scaled, for a given set of experimental conditions, the scaled times, $t_{scaled\,i}$ (where $i = 1,2,...M$) were ordered from shortest to longest. The observed cumulative probability distribution of scaled induction times $O(t_{scaled\,i})$ was calculated from:

$$O(t_{scaled\,i}) = \frac{i}{M} \qquad\qquad (5.\,2)$$

5.6.1 Scaling by Shear Rate

The induction times were first scaled by shear rate:

$$t_{scaled\ i} = \dot{\gamma}_{avg} t_i \qquad \textbf{(5. 3)}$$

Here $\dot{\gamma}_{avg}$ is the average shear rate and t_i is the induction time where $i = 1, 2, \ldots M$

This scaled time was equal to the total strain. The total strain can be defined as the total distance travelled by a fixed point at the surface of the rotating outer cylinder, divided by the size of the gap between the cylinders.

$$\gamma = \frac{v(r_{out}) t_i}{gap} = \frac{2\pi N r_{out} t_i}{r_{out} - r_{in}} = \dot{\gamma}_{avg} t_i \qquad \textbf{(5. 4)}$$

Here γ is the total strain, $v(r_{out})$ is the velocity of the outer cylinder, N is the rotational rate, r_{out} is the radius (inner) of the outer cylinder, r_{in} is the radius (outer) of the inner cylinder and $gap = r_{out} - r_{in}$.

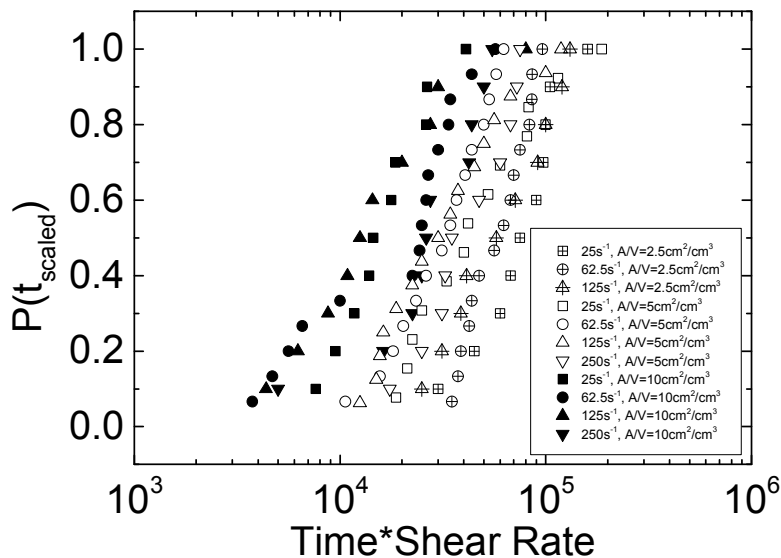The cumulative distribution of scaled times was found, as shown in Figure 5. 16.

Figure 5. 16
Experimental cumulative distribution functions of induction times scaled by shear rate for each setup.

The cumulative distributions of the scaled times were found to converge into three groups (one for each surface to volume ratio used). The findings therefore showed that for a fixed surface area that the solution was exposed to, the probability distribution of induction times scaled with shear rate and suggested that the total strain/ deformation (shear history) was important for the onset of nucleation.

5.6.2 Scaling by Shear Rate and Surface Area

Next, the induction times were scaled by both the shear rate and the surface area, and the cumulative probability distributions of the scaled times were found. All of the cumulative probability distributions for each set of conditions converged as shown in Figure 5. 17. This suggested that the area of surface (A) that the solution was exposed to was important for the onset of nucleation.

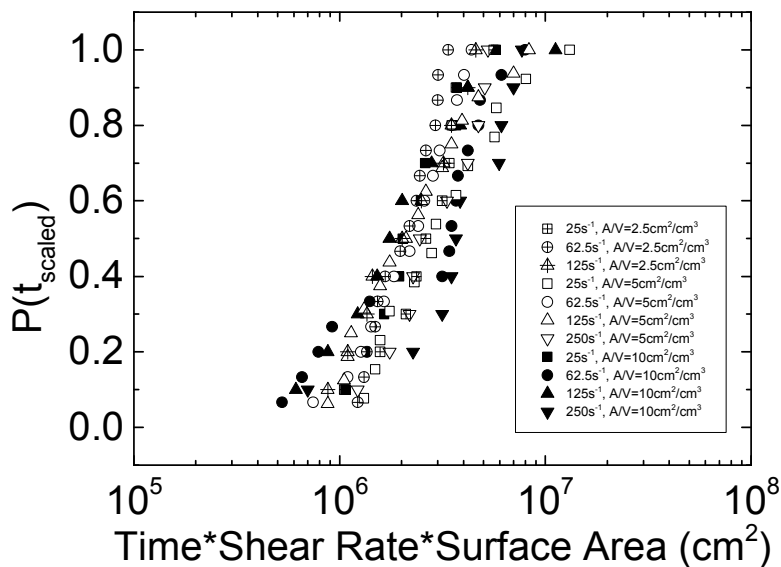$$t_{scaled\ i} = \dot{\gamma}_{avg} t_i A = \gamma A \qquad \textbf{(5. 5)}$$

Figure 5. 17
Experimental cumulative distribution functions of induction times scaled by the shear rate and surface area for each setup.

Since the induction times appeared to scale with shear rate and surface area, this suggested that all processes that occurred could be measured on one key

timescale, proportional to $\frac{1}{\dot{\gamma}_{avg}A}$ i.e. there was a single dominant time scale. The processes that occurred were the stochastic formation of a crystal and the non-stochastic growth phase. When dealing with the stochastic formation of a crystal, the timescale potentially appears rational as it would be expected that nucleation rates could be enhanced by increased shear rates (see Chapter 4) and surface areas (see Chapter 1 Section 1.3.1.2). The timescale, however, was more difficult to rationalise for the non-stochastic growth phase, particularly why a larger surface area would result in shorter growth times. This is reviewed in more detail in Section 5.7.

Rearranging Newton's law of viscosity and writing the shear stress in terms of a force (F) per unit area (A), the product of shear rate and area could be written in terms of force and viscosity. This suggested that the timescale was proportional to $\frac{1}{F}$.

$$\dot{\gamma}_{avg}A = \frac{F}{\eta} \qquad\qquad \textbf{(5. 6)}$$

5.6.3 Master Equations

An overall cumulative distribution function of the scaled induction time data (induction times scaled by average shear rate and surface area) was produced and is shown in Figure 5. 18. Since the log-normal distribution and Jiang and ter Horst model closely matched the experimental distributions of induction times, these were also used to produce master fits to the scaled induction time data, as shown in Figure 5. 18.

For the master log-normal distribution, a log-normal cumulative distribution was written in terms of scaled induction times, $Q(t_{scaled\ i})$:

$$Q(t_{scaled\ i}) = \frac{1}{2}\left[1 + \mathrm{erf}\left(\frac{\log(t_{scaled\ i}) - \overline{\log(t_{scaled\ i})}}{\sigma\sqrt{2}}\right)\right] \qquad \textbf{(5. 7)}$$

$\overline{\log(t_{scaled\ i})}$ is the mean of all of the log scaled induction times, across all conditions studied and σ is the standard deviation of these.

The master equation provided a good fit to the individual experimental cumulative distribution functions, with $R^2 = 0.81$.

For the Jiang and ter Horst model, Eqn. (4.13) was written in terms of the scaled induction times and fitting parameters α and β, giving $P(t_{scaled\,i})$.

For simplicity, experimental induction times were written in terms of scaled induction times using scaling factor φ:

$$t_i = \frac{t_{scaled\,i}}{\varphi} \quad\quad\quad\quad \text{(5. 8)}$$

Here, $\varphi = \dot{\gamma}_{avg}A$.

$$P(t_{scaled\,i}) = 1 - e^{-JV\left(\frac{t_{scaled\,i}}{\varphi} - t_g\right)} \quad\quad\quad\quad \text{(5. 9)}$$

Here V is the solution volume.

Taking the scaling factor outside:

$$P(t_{scaled\,i}) = 1 - e^{-\frac{JV}{\varphi}(t_{scaled\,i} - t_g\varphi)} \qu\quad\quad\quad \text{(5. 10)}$$

This could be rewritten in terms of fitting parameters α and β:

$$P(t_{scaled\,i}) = 1 - e^{-\alpha V(t_{scaled\,i} - \beta)} \qu\quad\quad\quad \text{(5. 11)}$$

If required, nucleation rates and growth times could be obtained from the fitting parameters (α and β) using the scaling factor.

$$J = \alpha\varphi \qu\quad\quad\quad \text{(5. 12)}$$

$$t_g = \frac{\beta}{\varphi} \qu\quad\quad\quad \text{(5. 13)}$$

A master equation was obtained by finding the best fit values of α and β (see Table 5. 3) to the scaled data (Figure 5. 18). The master equation provided a good fit to the individual experimental cumulative distribution functions, with $R^2 = 0.81$.
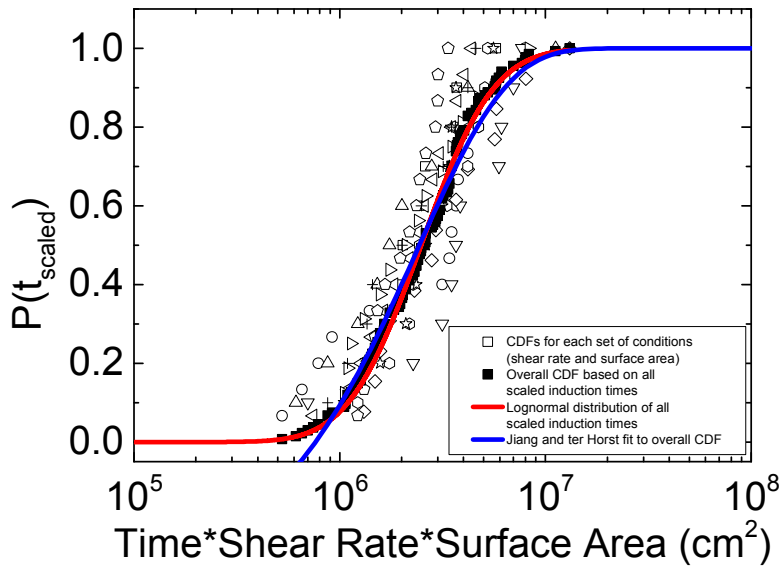
Figure 5. 18
Experimental cumulative distribution functions of induction times for each setup scaled by shear rate and surface area. Plot also shows an overall experimental cumulative distribution function and cumulative distributions based on a log-normal distribution of scaled times and Jiang and ter Horst fits to the data.

Table 5. 3
Fitting parameters obtained when scaling induction time by shear rate and total surface area. Errors represent 95% confidence intervals.

α	β
0.028 cm^{-2}.m^{-3} ±0.001	762000 cm^2 ±45000

5.6.4 Slopes of Induction Time versus Shear Rate * Area

A plot of the mean induction times for each experimental setup as a function of the product of shear rate and surface area is given in Figure 5. 19. A plot of the median induction time for each experimental setup as a function of the product of shear rate and surface area is given in Figure 5. 20. These plots show a linear dependence of $\log(t_i)$ as a function of $\log(\dot{\gamma}_{avg}A)$, suggesting a power law relationship.

A plot of each induction time measured as a function of the product of shear rate and surface area is shown in Figure 5. 21 and had a slope of -0.83±0.2 (95%

confidence). Therefore $t_i \propto (\dot{\gamma}_{avg}A)^{-0.83 \pm 0.2}$. Due to uncertainties with the reliability of the 25 s^{-1} data for the 2.5 cm^2/cm^3 and 5 cm^2/cm^3 setups, these data were excluded from the slope calculation.
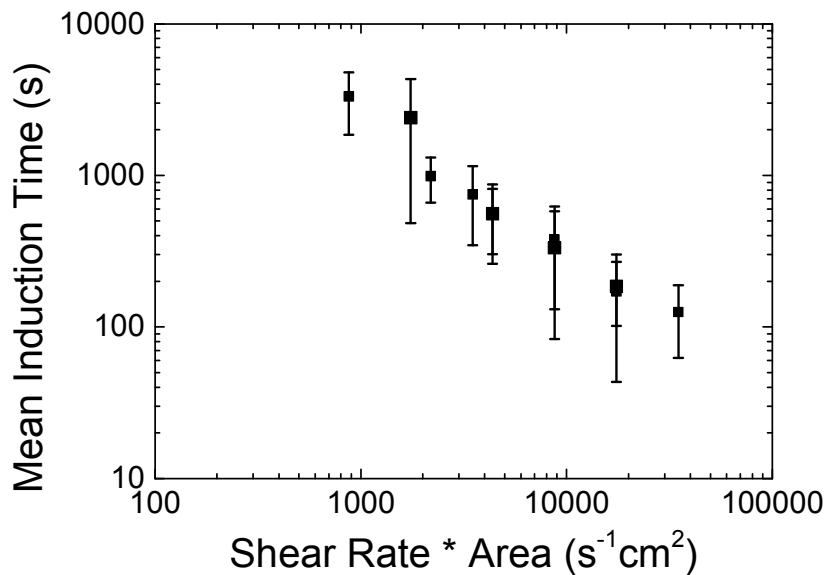

Figure 5. 19
Mean induction time measured for each setup as a function of the product of shear rate and surface area. Error bars represent 1 standard deviation.
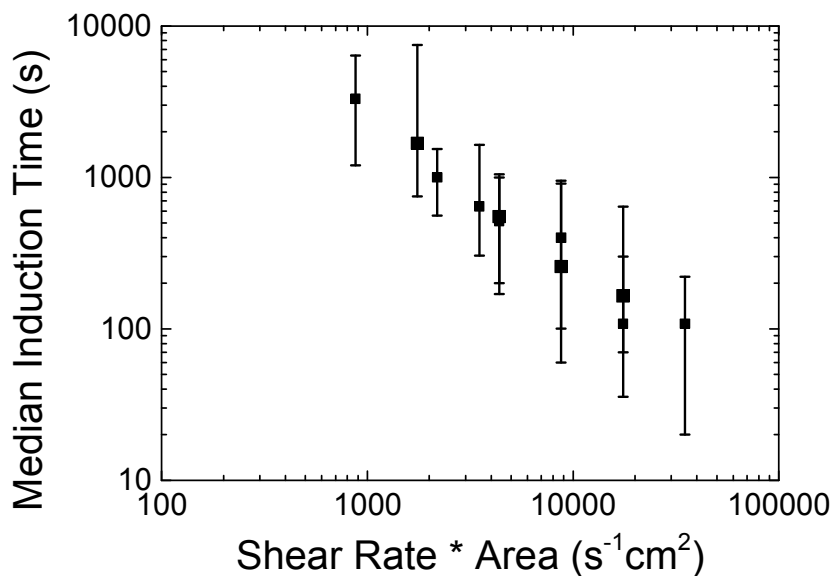

Figure 5. 20
Median induction time measured for each setup as a function of the product of shear rate and surface area. Error bars represent the full spread of measured induction times.
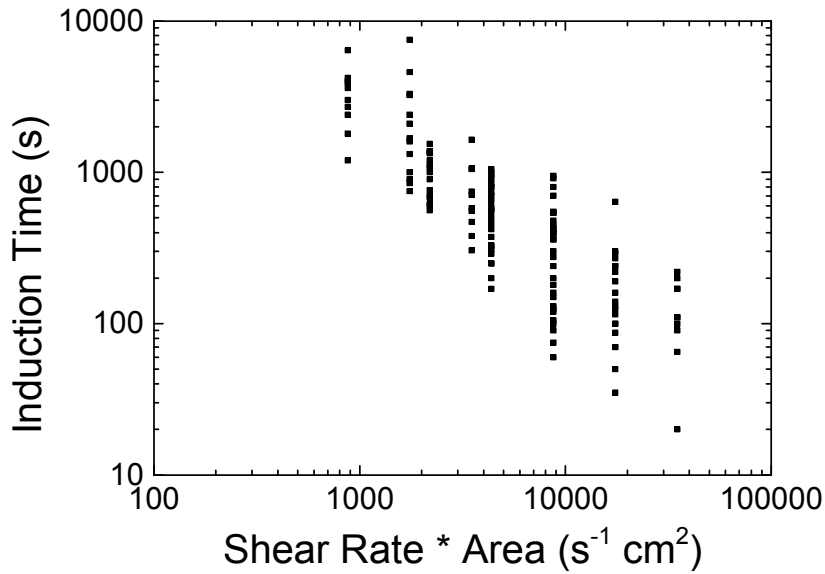
Figure 5. 21
Measured induction times for each setup as a function of the product of shear rate and surface area.

5.6.5 Nucleation Rates and Growth Times versus Product of Shear Rate and Surface Area

Since the product of the shear rate and surface area that solution was exposed to appeared to be important for nucleation kinetics in the setups studied here, nucleation rates and growth times obtained using the model by Jiang and ter Horst (see section 5.5) were plotted as a function of the product of shear rate and surface area. These are shown in Figure 5. 22 and Figure 5. 23. The plots suggested a linear dependence of $\log(J)$ and $\log(t_g)$ as a function of $\log(\dot{\gamma}_{avg}A)$, suggesting a power law relationship with exponents of 0.66±0.2 and -1.25±0.2 (95% confidence intervals) respectively excluding the anomalous 25s^{-1} data. This shows that the product of shear rate and surface area were important for the nucleation rates and growth times deduced.
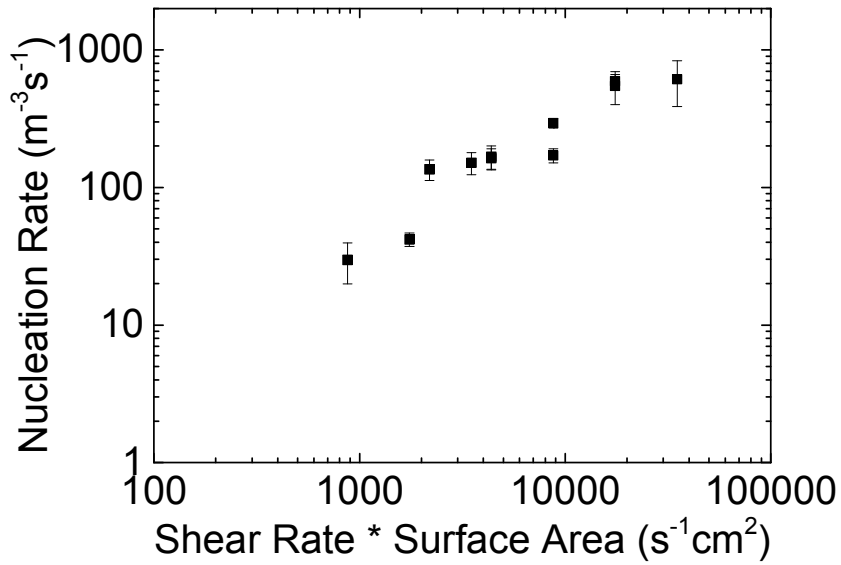
Figure 5. 22
Nucleation rates *J* estimated from the best fit of the model by Jiang and ter Horst plotted as a function of shear rate and surface area. Error bars represent 95% confidence intervals.

Figure 5. 23
Growth times t_g estimated from the best fit of the model by Jiang and ter Horst plotted as a function of shear rate and surface area. Error bars represent 95% confidence intervals.
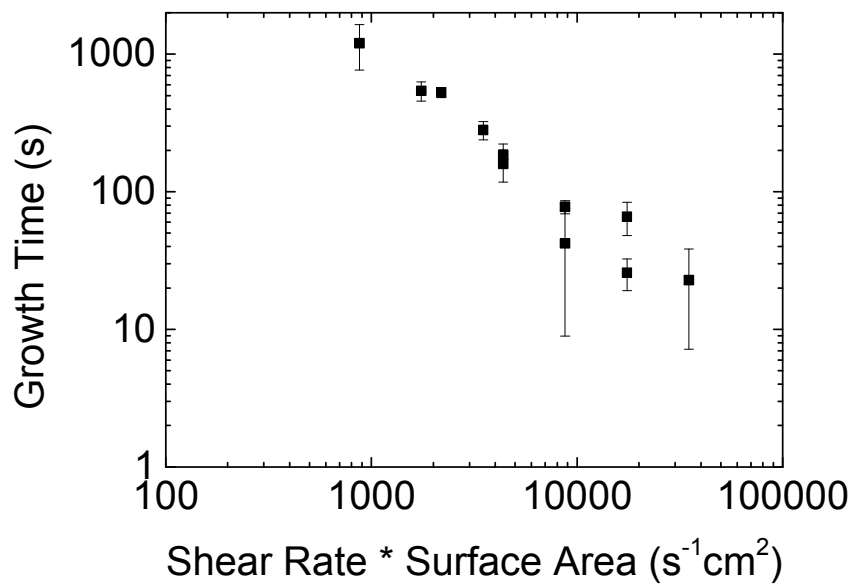
5.6.6 Bootstrapping

Slopes from bootstrapping the data were also found. Full bootstraps were done, using a method identical to that detailed in Chapter 4 Section 4.6. The value of the slope depended on which shear rates were included in the analysis, as shown in Figure 5. 24. For each surface to volume ratio used, the slope of $\log(t_i)$ as a function of $\log(\dot{\gamma}_{avg})$ was generally within confidence intervals of -1, which suggested that the total deformation was important for the onset of nucleation, as mentioned previously. Full bootstraps were also done to $\log(t_i)$ versus $\log(A)$. The slopes and errors found for each shear rate are given in Figure 5. 25. These were also generally within the region of -1.
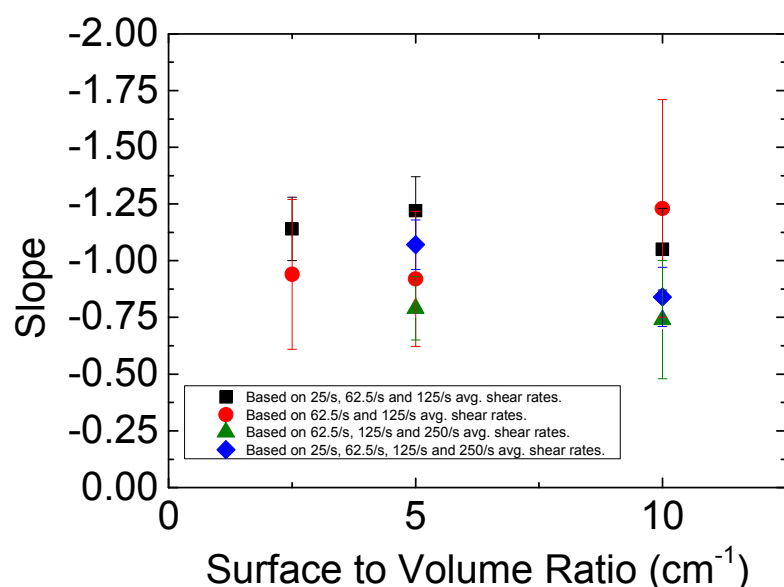

Figure 5. 24
Slopes found from full bootstraps to $\log(t_i)$ data as a function of $\log(\dot{\gamma}_{avg})$. Error bars represent 1 standard deviation.
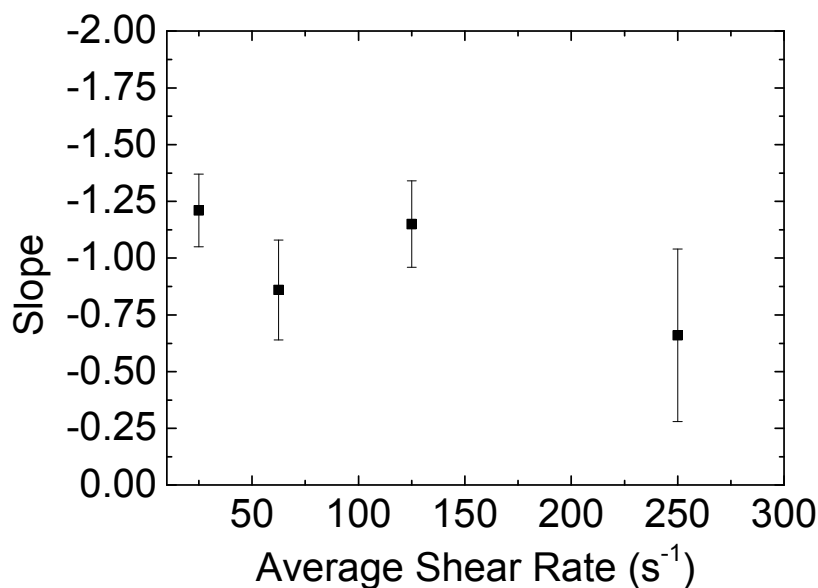
Figure 5. 25
Slopes found from full bootstraps to $\log(t_i)$ data as a function of $\log(A)$. Error bars represent 1 standard deviation.

5.7 Consideration of Results

The results showed that glycine nucleation (nucleation rates and growth times) was affected by both fluid shear and exposure to surface (Figure 5. 13 and Figure 5. 14). Here reasoning behind such behaviour is considered.

5.7.1 Effect of Shear and Surface on Nucleation Rates

Increased shear rates and surface areas resulted in shorter nucleation times, as shown in Figure 5. 13.

5.7.1.1 Influence of Shear Rate on Nucleation Rates

Reasons behind the role that fluid shear has on nucleation are unclear. The increase of nucleation rates with increasing shear rate, as shown in Figure 5. 13, could potentially be explained by several possible factors such as improved molecular alignment[5, 9, 10], cluster aggregation[11-13] or mass transfer[14-16], resulting in higher nucleation rates[11, 13].

Mass Transfer.

It has been suggested in literature that nucleation rates can be enhanced by increasing the rate of mass transfer[14-16]. To gain an appreciation of the likely role that mass transfer may have had on the system here, Sherwood Numbers (Sh) were calculated. Sherwood numbers represent the ratio of the total rate of mass transfer to the rate of diffusive mass transport alone.

$$Sh = \frac{total\ rate\ of\ mass\ transfer}{diffusive\ rate\ of\ mass\ transfer}$$

$$Sh = \frac{KL}{D} \qquad \textbf{(5. 14)}$$

Here K is the mass transfer coefficient, L is the characteristic length scale and D is the diffusion coefficient. For single, non-interacting spherical particles undergoing Brownian motion at low Reynolds numbers, the diffusion coefficient can be estimated though the Stokes-Einstein equation.

There are many empirical correlations from which the Sherwood Number for mass transfer to spherical particles can be calculated and these often take a general form of[17]:

$$Sh = \alpha' + \beta' Re_p^{0.5} Sc^{0.33} \qquad \textbf{(5. 15)}$$

Here Sc is the Schmidt Number ($Sc = \frac{\mu}{D}$) and α' and β' are empirical constants. Typically $\alpha' = 2$ to account for diffusion and $0.3 < \beta' < 1$. The right hand term represents the forced convection mass transfer contribution.

The Reynolds Number for a spherical particle (Re_p) was calculated from:

$$Re_p = \frac{u d_p}{\mu} \qquad \textbf{(5. 16)}$$

Here μ is the kinematic viscosity of the solution, d_p is the diameter of the particle and u is the relative velocity of the spherical particle and fluid some distance away from the spherical particle.

Assuming that $\alpha' = 2$ and varying the value of β' between 0.3 and 1, the Sherwood Numbers did not notably exceed 2 (2.05-2.15), suggesting that the forced

convection term was negligible compared to the diffusion contribution. The diameter of particle used was equal to the diameter of a nanodropet (250nm)[11] (see Chapter 6) and the velocity was taken as the relative velocity across a distance of 250nm based on the velocity gradients of the Couette cell setups.

It therefore appeared unlikely that mass transfer was notably enhanced by the application of fluid shear. Mass transfer could therefore not be attributed to the enhanced nucleation rates measured under higher shear rates. These conclusions were similarly drawn on previous work on the influence of fluid shear on primary nucleation[13].

Molecular Alignment.

Shear induced molecular alignment has been widely reported to affect the nucleation of large, elongated molecules e.g. polymers[9, 18-20]. The effect's significance would be expected to increase with increasing shear rate or increasing molecular length of solute[13]. For long molecules, e.g. polypropylene, low shear rates (0.5 s^{-1} to 10 s^{-1}) can be used to stretch and order molecules[13, 21]. For smaller molecules, non-equilibrium molecular dynamics simulations suggest that extremely high shear rates ($>10^{10}$ s^{-1}) are required for the ordering of molecules[22]. Glycine is a small molecule and the shear rates encountered in the experiments (25 s^{-1}- 1000 s^{-1}) were significantly smaller than those that would be expected to be required for shear induced molecular alignment.

Aggregation of Clusters.

From dynamic light scattering measurement results (Chapter 6) and a previous study on glycine nucleation from aqueous solution[11], it has been proposed that the coalescence of liquid-like, glycine rich mescoscale clusters (nanodroplets) may occur and the coalesced nanodroplets can lead to a more rapid nucleation pathway. The aggregation of clusters has been proposed in other recent studies on nucleation. For example, supersaturated solutions of calcium carbonate were found to contain distinct cluster sizes and this was interpreted as nucleation taking place by cluster aggregation[12, 23, 24]. A study of butyl paraben undergoing flow in a Couette cell concluded that enhanced cluster aggregation was a plausible outcome for the enhanced nucleation rates seen under flow[13], and a further study on the influence of Couette flow on m-hydroxybenzoic acid was also supportive of the theory of

enhanced cluster aggregation[25]. A study on the effect of mixing on mesoscale clusters in DL-valine solutions suggested that mixing resulted in the presence of larger mesoscale clusters than in quiescent solutions, and the presence of larger clusters corresponded to faster nucleation. The larger clusters were thought to form through shear-induced coalescence or surface-assisted coalescence[26].

Further explanations on the proposed mechanism of cluster aggregation are given in Chapter 6 Section 6.6.

5.7.1.2 Influence of Surface Area on Nucleation Rates

The increase of nucleation rates with increased surface areas, as shown in Figure 5. 13, could potentially be explained as follows. It is widely accepted that true homogenous nucleation is uncommon so nucleation that occurs heterogeneously is most likely[27]. According to classical nucleation theory, the overall free energy change for heterogeneous nucleation is less than the corresponding free energy change for homogeneous nucleation, and the overall free energy change for heterogeneous nucleation decreases with increasing surface wettability[28] (see Chapter 1). Therefore, it would be expected that increased exposure to surfaces would make heterogeneous nucleation more probable and enhance nucleation rates. Having a larger surface area means there are more possible sites for heterogeneous nucleation to take place, which makes the probability of a nucleation event taking place after a particular time higher. Therefore higher nucleation rates would be expected for glycine solutions exposed to larger surface areas.

Inspection of the Couette walls after an experiment suggested that a small number of crystals grew on the glass walls (see Figure 5. 26), supporting the idea that primary nucleation occurred preferentially at surfaces. Increased surface areas may also have enhanced the coalescence of mesoscale clusters, with the larger, coalesced clusters leading to a more rapid nucleation pathway (see Chapter 6)[26].

Exposing solution to larger surface to volume ratios resulted in the solution being exposed to smaller solution-air interfaces, so the effects seen could not be attributed to the exposure to a larger free interface. Solutions exposed to larger surface to volume ratios would also have cooled faster than solutions exposed to smaller surface to volume ratios. This effect should have been small since solutions had all cooled to ambient temperature by the end of the cooling period.
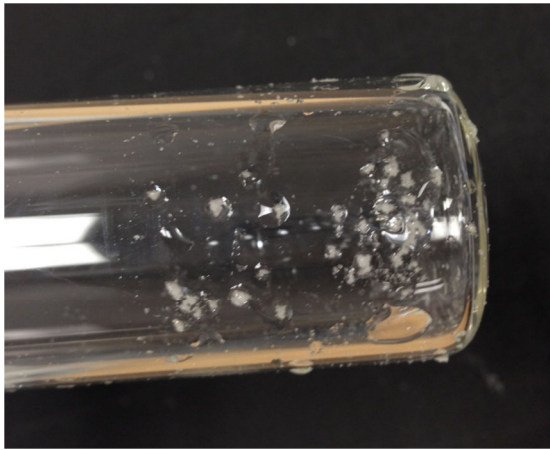
Figure 5. 26
Image of an inner cylinder of the Couette cell following an experiment giving clear evidence that nucleation was heterogeneous.

5.7.2 Effect of Shear and Surface on Growth Times

Increased shear rates and surface areas resulted in shorter growth times, as shown in Figure 5. 14.

5.7.2.1 Influence of Shear Rate on Growth Times

Larger shear rates may have resulted in the size of crystal at which attrition takes place, causing solutions to become turbid, to be smaller. This would have resulted in crystallisation reaching a detectable level more quickly. At higher shear rates, secondary nucleation was also more extensive, meaning that a detectable amount of crystals formed more quickly; if there were more secondary nuclei, they would not have had to grow to as large a size to be detected. Enhanced mass transfer to the growing crystals may also have occurred, but the analysis of the Sherwood Number suggested that this was not the case.

5.7.2.2 Influence of Surface Area on Growth Times

The decrease of growth time with increased surface area was not expected and is more difficult to rationalise. If flow showed small deviations from being perfectly streamlined, more secondary nucleation may have been occurring when solutions

were exposed to larger surface areas due to increased contact of crystals with the Couette cell's walls[27].

Another possibility is that multiple crystals may have formed through primary nucleation during the induction time. If multiple crystals formed through primary nucleation during the induction time, it would be expected that the growth time would be shorter since these multiple crystals would each eventually undergo secondary nucleation, leading to a faster decrease in transmission. With larger surface areas, the chances of multiple crystals forming through primary nucleation would have been higher since nucleation occurs preferentially at surfaces in the case of heterogeneous nucleation.

To see whether it was likely that multiple crystals could form through primary nucleation during the induction time, the nucleation rates and growth times obtained using Jiang and ter Horst's model were analysed to see whether they supported the idea that multiple crystals may have formed, mainly if additional crystals were likely to have formed during the growth time. The product of JVt_g varied between 0.1 and 1.1 which was of a similar magnitude to JVt_n values calculated (0.03-5.6). This suggested that additional crystals may have potentially formed through primary nucleation during the growth time, however, JVt_g decreased with increasing surface area. This therefore did not support the possibility that increased surface areas led to a greater likelihood that additional crystals formed during the growth time.

The Jiang and ter Horst model was then adapted to obtain probability distribution functions for forming at least a certain number of crystals (the published form of the model was based on forming at least one crystal and did not specify how many crystals). The adapted forms of the model (for up to 5 crystals) did not provide good fits to the data, but these attempts to modify the model were too limited as more than 5 crystals may have formed. Using a polynuclear model may therefore be more suited to the experiments carried out here. With a progressive polynuclear model, it is usually assumed that many nuclei continuously appear and grow during the induction time. The crystals being detected would therefore be a direct result of primary nucleation and growth, rather than attrition and growth[28, 29]. An instantaneous polynuclear model would correspond to the case of all primary nuclei forming instantaneously at an initial moment and then growing until the phase transformation was complete[28, 29]. An adapted form of a progressive polynuclear

model may be more suitable for the work done here, for example, a model that represents on-going primary nucleation and growth, as well as attrition of crystals.

As will be mentioned in Chapter 6, the model by Jiang and ter Horst may not have been fully suitable for the induction time data measured here. For example, the assumption of a constant nucleation rate in the model may not have been valid if the coalescence of nanodroplets was occurring since coalesced nanodroplets were thought to lead to higher nucleation rates. The assumption of a Poisson distribution of the number of crystals forming after a particular time may also not have been valid.

As a further analysis, the measured induction time data were looked at. First of all, each measured induction time for a given set of conditions was divided by the shortest induction time measured for that set of conditions $\left(\frac{t_i}{t_{i_{min}}}\right)$. This is shown in Figure 5. 27. As the surface area increased, $\frac{t_i}{t_{i_{min}}}$ generally increased overall on average- larger surface areas generally resulted in a greater spread of induction times. These findings were supportive that multiple crystals may have formed during the induction time since the measured induction times were often considerably longer than the shortest time measured.
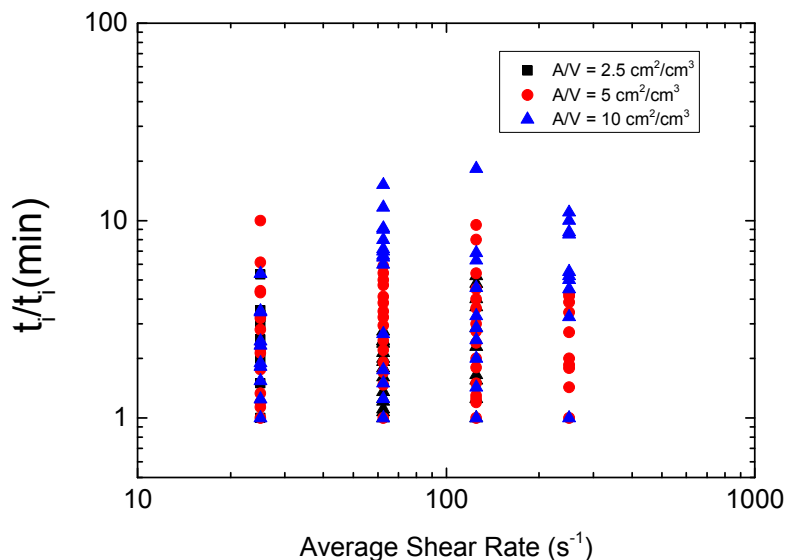

Figure 5. 27
Each measured induction time divided by the minimum measured induction time for each set of experimental conditions.

Another aspect that may have affected results was that Couette cell setups with different surface areas resulted in solution being filled to different depths in the gap between the vertical cylinder walls. This meant that the laser beam went through different relative depths of solution e.g. at the highest surface to volume ratio, the laser beam went through the lower half of the solution, whereas at the lowest surface to volume ratio, the laser went through the upper half of solution. The error due to these differences should have been fairly low as the solutions usually became cloudy throughout (the small size of the large number of crystals formed meant that their sedimentation time was large), with the exception of using the lowest shear rates studied.

5.8 Conclusions

The nucleation of glycine was investigated in supersaturated aqueous solutions exposed to well-controlled fluid shear under isothermal conditions. A wide range of average shear rates (25 s^{-1} to 250 s^{-1}) and surface areas (2.5 cm^2 per ml solution to 10 cm^2 per ml solution) were used and induction times were estimated using a range of techniques, including imaging, transmission measurements and visual monitoring. Due to the stochastic nature of nucleation, experiments were repeated multiple times. Care was taken to eliminate any seeding in order to avoid secondary nucleation preceding the formation of the first crystals through primary nucleation.

Induction times obtained under shearing were found to be considerably lower than those in unsheared solutions and increasing the surface area that solution was exposed to resulted in shorter induction times. The model proposed by Jiang and ter Horst showed that as the shear rate and surface area increased, the primary nucleation rate increased and growth time decreased. The induction times were found to decrease with increased shear rates and increased surface areas in a power law relationship: $t_i \propto (\dot{\gamma}_{avg} A)^{-0.83 \pm 0.2}$.

The distributions of induction times were found to scale with shear rate and surface area and master equations were fitted to the scaled data with low errors. This suggested that all processes that took place during nucleation were measured on one key timescale, which was proportional to $\frac{1}{\dot{\gamma}_{avg} A}$.

Possible reasons for the observations made were analysed and shear and surface enhanced cluster aggregation, which is discussed more in Chapter 6, remains the most likely explanation.

5.9 Summary

- Controlled fluid shear was obtained using a Couette flow setup.
- The area that aqueous glycine solution was exposed to while it was being sheared was varied by changing the diameter of the inner cylinder of the Couette cell.
- Induction times for sheared solutions were less than for solutions that were not sheared. Induction times were also lower for solutions that were exposed to larger surface areas.
- A full factorial design of experiments analysis confirmed that shear rate and surface area affected the induction times measured.
- The probability distributions of induction times were analysed and compared well to a log-normal distribution and a model proposed by Jiang and ter Horst[3].
- The model proposed by Jiang and ter Horst showed that as the shear rate and surface area increased, the primary nucleation rate increased and growth time decreased.
- The distributions of induction times were found to scale with shear rate and surface area. The findings suggested that all processes that took place during nucleation were measured on one key timescale, which was proportional to $\frac{1}{\dot{\gamma}_{avg}A}$.
- A plot of log(induction time) versus log(average shear rate*surface area) was linear, suggesting a power law relationship: $t_i \propto (\dot{\gamma}_{avg}A)^{-0.83\pm0.2}$.
- Shear and surface enhanced cluster aggregation seems to be the most plausible explanation for the behaviour seen.

5.10 References and Nomenclature

5.10.1 References

(1)   JelinskaKazimierczuk, M.; Szydlowski, J., Isotope effect on the solubility of amino acids in water. *Journal of Solution Chemistry* **1996,** 25, (12), 1175-1184.

(2)   Forsyth, C.; Mulheran, P. A.; Haw, M. D.; Burns, I. S.; Sefcik, J., Influence of Controlled Fluid Shear on Nucleation Rates in Glycine Aqueous Solutions. *Crystal Growth & Design* **2015,** 15, (1), 94-102.

(3)   Jiang, S. F.; ter Horst, J. H., Crystal Nucleation Rates from Probability Distributions of Induction Times. *Crystal Growth & Design* **2011,** 11, (1), 256-261.

(4)   Parambil, J. V.; Schaepertoens, M.; Williams, D. R.; Heng, J. Y. Y., Effects of Oscillatory Flow on the Nucleation and Crystallization of Insulin. *Crystal Growth & Design* **2011,** 11, (10), 4353-4359.

(5)   Penkova, A.; Pan, W. C.; Hodjaoglu, F.; Vekilov, P. G., Nucleation of protein crystals under the influence of solution shear flow. *Interdisciplinary Transport Phenomena in the Space Sciences* **2006,** 1077, 214-231.

(6)   Sumner, A. L.; Menke, E. J.; Dubowski, Y.; Newberg, J. T.; Penner, R. M.; Hemminger, J. C.; Wingen, L. M.; Brauers, T.; Finlayson-Pitts, B. J., The nature of water on surfaces of laboratory systems and implications for heterogeneous chemistry in the troposphere. *Physical Chemistry Chemical Physics* **2004,** 6, (3), 604-613.

(7)   Montgomery, D.; Runger, G., *Applied Statistics and Probability for Engineers*. 4th ed.; John Wiley & Sons: 2006.

(8)   Antony, J., *Design of Experiments for Engineers and Scientists*. ed.; Elsevier: 2004.

(9)   Keller, A., Polymer Crystals. *Reports on Progress in Physics* **1968,** 31, 623-625

0)   Vekilov, P. G., The two-step mechanism of nucleation of crystals in solution. *Nanoscale* **2010,** 2, (11), 2346-2357.

(11)   Jawor-Baczynska, A.; Sefcik, J.; Moore, B. D., 250 nm Glycine-Rich Nanodroplets Are Formed on Dissolution of Glycine Crystals But Are Too Small To Provide Productive Nucleation Sites. *Crystal Growth & Design* **2013,** 13, (2), 470-478.

(12)   Gebauer, D.; Voelkel, A.; Coelfen, H., Stable Prenucleation Calcium Carbonate Clusters. *Science* **2008,** 322, (5909), 1819-1822.

(13)   Liu, J.; Rasmuson, A. C., Influence of Agitation and Fluid Shear on Primary Nucleation in Solution. *Crystal Growth & Design* **2013,** 13, (10), 4385-4394.

(14)   Mullin, J. W.; Raven, K. D., Nucleation In Agitated Solutions. *Nature* **1961,** 190, (477), 251-&.

(15)   Mullin, J. W.; Raven, K. D., Influence Of Mechanical Agitation On Nucleation Of Some Aqueous Salt Solutions. *Nature* **1962,** 195, (4836), 35-&.

(16)   Nyvlt, J.; Skrivane.J; Gottfrie.J; Krickova, J., Uber Kristallisation .19. Einfluss Der Durchmischung Auf Die Breite Der Metastabilen Zone. *Collection of Czechoslovak Chemical Communications* **1966,** 31, (5), 2127-&.

(17)   Blackhurst; Harker; Coulson; Richardson, *Coulson and Richardson's Volume 1*. 6th ed.; Butterworth-Heinemann Ltd: 1999.

(18)   Mackley, M. R.; Keller, A., Flow Induced Polymer-Chain Extension And Its Relation To Fibrous Crystallization. *Philosophical Transactions of the Royal Society a-Mathematical Physical and Engineering Sciences* **1975,** 278, (1276), 29-+.

(19)   Tan, V.; Gogos, C. G., Flow-Induced Crystallization Of Linear Polyethylene Above Its Normal Melting-Point. *Polymer Engineering and Science* **1976,** 16, (7), 512-525.

(20)   Tribout, C.; Monasse, B.; Haudin, J. M., Experimental study of shear-induced crystallization of an impact polypropylene copolymer. *Colloid and Polymer Science* **1996,** 274, (3), 197-208.

(21)   Somani, R. H.; Yang, L.; Zhu, L.; Hsiao, B. S., Flow-induced shish-kebab precursor structures in entangled polymer melts. *Polymer* **2005,** 46, (20), 8587-8623.

(22)   Gray, R. A.; Warren, P. B.; Chynoweth, S.; Michopoulos, Y.; Pawley, G. S., Crystallization Of Molecular Liquids Through Shear-Induced Nucleation. *Proceedings of the Royal Society-Mathematical and Physical Sciences* **1995,** 448, (1932), 113-120.

(23)   Meldrum, F. C.; Sear, R. P., Materials Science Now You See Them. *Science* **2008,** 322, (5909), 1802-1803.

(24)   Gebauer, D.; Kellermeier, M.; Gale, J. D.; Bergstrom, L.; Colfen, H., Pre-nucleation clusters as solute precursors in crystallisation. *Chemical Society Reviews* **2014,** 43, (7), 2348-2371.

(25)   Liu, J.; Svard, M.; Rasmuson, A. C., Influence of Agitation and Fluid Shear on Nucleation of m-Hydroxybenzoic Acid Polymorphs. *Crystal Growth & Design* **2014,** 14, (11), 5521-5531.

(26)   Jawor-Baczynska, A.; Moore, B.; Sefcik, J., Effect of mixing, concentration and temperature on the formation of mesostructured solutions and their role in the nucleation of dl-valine crystals. *Faraday Discussions* **2015**.

(27)   Mullin, J. W., *Crystallization*. 4th ed.; Heineman: 2002.

(28)   Kashchiev, D., *Nucleation: Basic Theory and Applications*. ed.; Butterworth-Heinemann: 2000.

(29)   Kashchiev, D.; van Rosmalen, G. M., Review: Nucleation in solutions revisited. *Crystal Research and Technology* **2003,** 38, (7-8), 555-574.

5.10.2 Main Nomenclature

A= surface area that solutions were exposed to

c= concentration

c^*= solubility concentration

D = diffusion coefficient

d_p = diameter of the particle

F= force

f_0= f statistic

J = nucleation rate per unit volume

K = mass transfer coefficient

L = characteristic length scale

N = rotational rate

$O(t_{scaled\ i})$= cumulative distribution of observed scaled induction times

$P(t_{scaled\ i})$= cumulative distribution of scaled induction times for the Jiang and ter Horst model

$Q(t_{scaled\ i})$= cumulative distribution of scaled induction times for the lognormal distribution

r_{in} = radius (outer) of the inner cylinder

r_{out}= radius (inner) of the outer cylinder

S= supersaturation

t_g= growth time

t_i= induction time where $i = 1,2,\ldots M$

$t_{scaled\ i}$= scaled experimentally observed induction time

u = relative velocity of the spherical particle and fluid some distance away from the spherical particle

V = volume of the solution

$v(r_{out})$ = the velocity of the outer cylinder

α = fitting parameter

α' = empirical constant

β' = empirical constant

β = fitting parameter

γ= total strain

$\dot{\gamma}_{avg}$= average shear rate

η= dynamic viscosity

μ= kinematic viscosity

σ =standard deviation.

τ= shear stress

φ = scaling factor

6. In-Situ Dynamic Light Scattering Measurements of Aqueous Glycine Solution Undergoing Controlled Fluid Shear

Chapter Outline and Contents

In Chapter 4 and Chapter 5, it was shown that exposing aqueous glycine solutions to controlled fluid shear and increased surface areas could enhance nucleation rates. A possible reason for this was that the glycine rich, liquid-like, mesoscale clusters that exist in aqueous glycine solutions could be coalesced and the larger coalesced clusters could lead to a more rapid nucleation pathway.

In this chapter, an improved understanding of what was happening to the mesoscale clusters in glycine solutions as they were sheared was obtained by performing in-situ dynamic light scattering (DLS) measurements on supersaturated aqueous glycine solutions exposed to well-controlled fluid shear in a Couette cell under isothermal conditions.

Solutions were exposed to a range of average shear rates (25 s^{-1} and 125 s^{-1}) and surface areas (2.5 cm^2 per ml solution and 5 cm^2 per ml solution). Dynamic light scattering equipment was set up so that measurements could be taken from solution that was contained within the Couette cell. The procedure involved shearing a solution for a chosen duration of time, stopping shearing and taking DLS measurements. Due to the stochastic nature of nucleation, experiments were repeated multiple times. The autocorrelation functions output from the DLS measurements were analysed using cumulant and CONTIN methods, allowing an idea of mesoscale cluster sizes and size distributions to be obtained.

The in-situ dynamic light scattering measurements showed that shearing caused the average size of mesoscale clusters in the solutions to increase, which may have been due to the coalescence of clusters. Larger shear rates and surface areas resulted in a faster rate of increase in average cluster size. Since induction times could also be decreased by larger shear rates and surface areas, the increase in average cluster size seen was thought to be linked to the onset of nucleation. This showed agreement with previous studies which indicated that glycine nucleation rates could be enhanced by the shear-enhanced coalescence of clusters[1].

This chapter covers:

- Dynamic light scattering theory.
- The setup of the dynamic light scattering hardware.
- The experimental procedure for Couette flow dynamic light scattering experiments.
- Dynamic light scattering results and statistical analyses.
- A consideration of the nucleation pathway.

6.1 Dynamic Light Scattering Theory

This section outlines basic light scattering theory that is used for the analysis of the measured light scattering data.

6.1.1 Light Scattering Introduction

Light is rarely observed directly from its source- most of the light that reaches our eyes does so in an indirect way, for example as scattered light. Light scattering is the change in intensity and direction of a beam of incident light that hits an object[2]. Light scattering is the reason why a leaf looks green: green light is scattered effectively, whereas red light, for example, is absorbed by the leaf[2].

The oscillating electric field from light interacts with matter. By interacting with electrons in the atoms/molecules, it can induce oscillatory electric dipole moments, and the oscillating dipole moments form sources of radiation. This radiation is scattered light[3-5]. A diagramatic representation of this is given in Figure 6. 1.
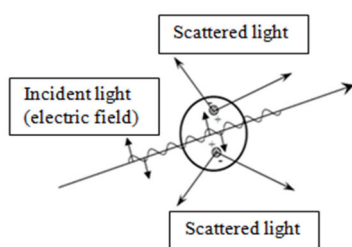

Figure 6. 1
Light scattering by induced dipoles, due to incident light wave.

The scattered light observed depends on the cooperative effect of the individual scattering by molecules/ atoms in the material: their arrangement is crucial. If light passes through a perfectly homogeneous, isotropic material, no scattered light is detected[2, 3]. A perfect crystal at absolute zero has molecules arranged in a highly regular way, such that scattered waves from individual atoms/ molecules interfere destructively and no real scattering is observed[2].

On the other hand, a (pure) gas or fluid results in real scattering since the molecules are randomly arranged and subject to fluctuations, e.g. density fluctuations. Therefore all waves cannot interfere destructively[2]. Light travelling through such media is therefore scattered due to inhomogeneities[2, 3]. Scattering from multi-component systems, e.g. a suspension of particulates, is largely a result of differences in optical properties (essentially differences in refractive index) between the dispersed phase and the dispersion medium[3]. This is why fish can be seen swimming in the water of a pond.

Scattered light can produce a speckle pattern (Figure 6. 2). If the particles that are causing the scattering are stationary, the speckle pattern will remain constant. When the waves of scattered light interfere destructively, dark spaces are produced, and when they interfere constructively, bright patches are produced. If the particles that are scattering are moving (e.g. by Brownian motion), the speckle pattern will constantly fluctuate due to the changing phases of scattered light. The rate of fluctuations is therefore related to the motion of particles- the faster the particles move (smaller particles), the more rapid the fluctuations[6]. The intensity of light scattered in any particular direction relative to the incident beam will depend on the arrangement of particles at any given moment. This fact is used in light scattering measurements to reveal structures and dynamics.
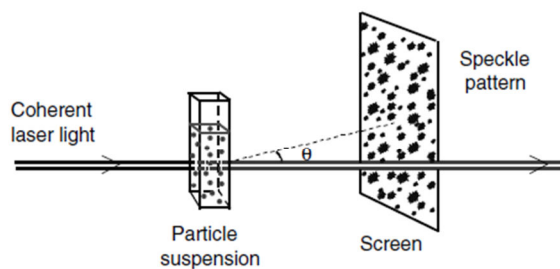

Figure 6. 2
Speckle pattern[6].

6.1.2 Typical Light Scattering Setup

In a typical light scattering setup, a sample is illuminated by an incident laser beam. Some of the radiation incident on the sample is scattered due to inhomogeneities (e.g. density fluctuations/ refractive index differences) and scattered light is measured by a detector at an angle, θ. A simplified setup is given in Figure 6. 3. Laser light is used since it is sufficiently coherent (all waves have the same phase difference and frequency), collimated (waves are parallel to each other) and quasi-monochromatic (virtually constant wavelength)[7].
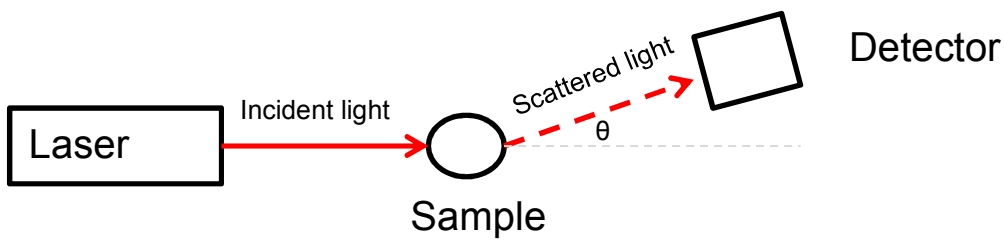
Figure 6. 3
Simplified experimental setup.

Experiments can be classified as static or dynamic[8]. Static light scattering (SLS) experiments are based on measuring the average intensity of scattered light during an observation time at a particular angle[3].

$$I(\theta) = \lim_{T_{obs} \to \infty} \frac{1}{T_{obs}} \int_0^{T_{obs}} I(\theta, t)\, dt \qquad \textbf{(6. 1)}$$

Here T_{obs} is the total observation time, t is the time and I is the intensity of scattered light.

Scattering is commonly measured at different scattering vectors (see Section 6.1.3) since this corresponds to measuring structures at different length scales. A plot of average intensity versus scattering vector can provide useful information[9]. Since only static properties are measured, structural information such as particle shapes and arrangements can be deduced[10]. Static light scattering is not considered any further in this thesis (with the exception of Chapter 7 where average intensities of scattered light at a fixed angle are calculated) and the following theory is based largely on dynamic light scattering.

6.1.3 Scattering Vector

An important value used in light scattering analyses is the scattering vector (q). It is the difference in magnitude of the incident and scattered light vectors and can be derived through trigonometric relations.

$$q = \frac{4\pi n}{\lambda} sin\left(\frac{\theta}{2}\right)$$

(6. 2)

Here λ is the wavelength of laser light used in a vacuum and n is the refractive index of the dispersion medium.

The reciprocal of the scattering vector has dimensions of length and is related to the length scale of structures most strongly contributing to scattering. Through the application of Bragg's law, the following rough equivalence can be found:

$$L \approx \frac{2\pi}{q}$$

(6. 3)

Therefore, at a given q, scattering is most strongly contributed to by inhomogeneities (variations in refractive index or density), corresponding to length scale, L. At an angle of 90°, this corresponds to length scales of a few hundred nanometres. A particle's form factor describes the angular variation of intensity as a function of particle size.

6.1.4 Dynamic Light Scattering

Dynamic light scattering involves measuring temporal variations of intensity and is based on the random Brownian motion of particles in solution. It allows time-dependent information to be determined and properties based on particle motion, including diffusion coefficients, can therefore be deduced[3, 6]. The theory outlined here is based on single scattering (a photon is scattered once).

The theory of DLS is based on the electric field of scattered light (E) however, intensity is easily measured by detectors, and the electric field and intensity are easily related[6].

$$I = |E|^2 \qquad \text{(6. 4)}$$

The measured intensity of scattered light fluctuates with time, as shown in Figure 6. 4 and the rate of fluctuations are related to particle size. The intensity fluctuates due to the random Brownian motion of particles: scattered light will interfere constructively or destructively so the intensity of light picked up by the detector will vary depending on the movement of the particles. Intensity measurements can be converted to autocorrelation functions and usable information can be deduced from these [6].
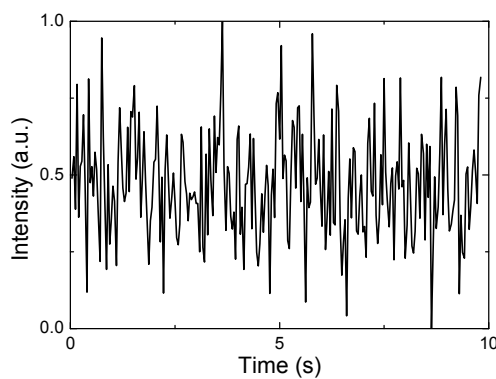
Figure 6. 4
Example of fluctuating intensity with time.

An intensity autocorrelation function ($G_2(\tau)$) can be defined as:

$$G_2(\tau) = \langle I(t)I(t+\tau) \rangle \qquad \text{(6. 5)}$$

Here τ is a delay time.

The normalised intensity autocorrelation function ($g_2(\tau)$) is given by:

$$g_2(\tau) = \frac{G_2(\tau)}{\langle I(t) \rangle^2} = \frac{\langle I(t)I(t+\tau) \rangle}{\langle I(t) \rangle^2} \qquad \text{(6. 6)}$$

The intensity autocorrelation function effectively compares a signal with a delayed version of itself. For short delay times, the intensities of scattering from the particles

are highly correlated, whereas after longer delays, due to the random movement of the particles, intensities are no longer correlated[6, 7]. At short delay times, there has been little movement to destroy correlation, while after longer delays, increased movement has reduced the correlation.

The normalised intensity autocorrelation function can be written in terms of the normalised electric field autocorrelation function ($g_1(\tau)$) through the use of a Siegert relation[6, 7].

$$g_2(\tau) = 1 + |g_1(\tau)|^2 \qquad \textbf{(6. 7)}$$

Often an experimental coherence factor (β) is included giving[6]:

$$g_2(\tau) = 1 + \beta|g_1(\tau)|^2 \qquad \textbf{(6. 8)}$$

The normalised electric field autocorrelation function represents a single exponential decay with the delay time for a monodisperse sample undergoing normal free diffusion.

$$g_1(\tau) = \sqrt{g_2(\tau) - 1} = e^{-\tau\Gamma} \qquad \textbf{(6. 9)}$$

Here Γ is the decay rate of the correlation function.

From Eqn. (6. 9), it can be seen that by taking a plot of the natural logarithm of $g_1(\tau)$, a straight line relation should be obtained with a slope whose magnitude is equal to Γ, the decay rate.

$$\ln\bigl(g_1(\tau)\bigr) = -\tau\Gamma \qquad \textbf{(6. 10)}$$

This method of obtaining the decay rate applies only to truly monodisperse systems. For systems with small amounts of polydispersity, which is common in practice, the straight line relationship is not followed so closely. With a polydisperse sample, differently sized particles show different decays (smaller particles decay more quickly than larger particles) so the measured correlation function will have multiple decays.

A cumulant analysis is therefore commonly carried out for samples with low levels of polydispersity. Cumulant analyses are favoured due to their simplicity, and they are not greatly affected by experimental noise[7, 11].

6.1.4.1 Cumulant Analysis

A cumulant analysis involves fitting a polynomial to $\ln(g_1(\tau))$. For the analysis done here, non-linear regression in Matlab was used.

$$ln\big(g_1(\tau)\big) = a + b\tau + c\tau^2 + d\tau^3 \qquad \textbf{(6. 11)}$$

Here a, b, c and d are coefficients of the polynomial fit.

Eqn. (6. 11) represents a 3rd order fit- any fits greater is unwarranted due to lack of precision in the data and it leads to other parameters being less precise[7]. The coefficient of the first cumulant represents the decay rate, as can be seen from the equations.

$$|b| \approx \Gamma$$

The decay rate represents an average decay rate of the particles in the solution and is related to the average diffusion coefficient (D) through the magnitude of the scattering vector.

$$\Gamma = Dq^2 \qquad \textbf{(6. 12)}$$

The average hydrodynamic radius (R_h) can be determined using the average diffusion coefficient in the Stokes-Einstein equation. The Stokes-Einstein equation is based on assumptions such as single, non-interacting spheres undergoing Brownian motion in viscous liquids at low Reynolds numbers. The hydrodynamic radius represents the radius of a hard sphere diffusing at the same rate as the given particle.

$$R_h = \frac{k_B T}{6\pi\eta D} \qquad \textbf{(6. 13)}$$

Here k_B is the Boltzmann constant and T is the absolute temperature.

From the theory, at a fixed scattering vector, small particles have larger diffusion coefficients, and their correlations decay at a higher rate than larger particles. This is illustrated in Figure 6. 5.
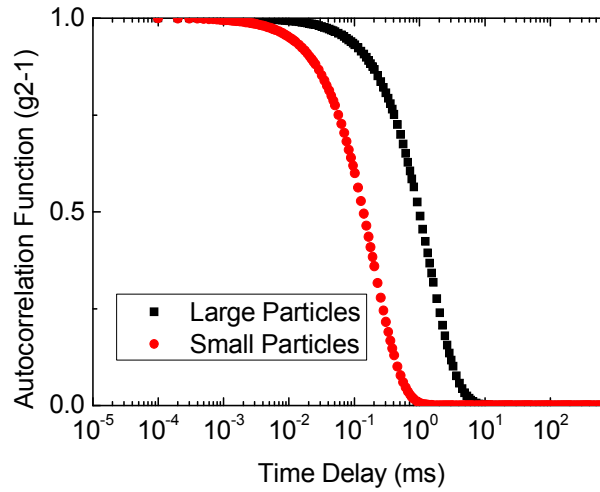

Figure 6. 5
Example of normalised intensity autocorrelation functions for monodisperse samples of differently sized spherical.

6.1.4.2 CONTIN Analysis

Since many of the autocorrelation functions obtained in the experimental work did not represent perfect, single exponential decays, the 'Non- Linear Regularised Fit' program from ALV software was used to fit multiple exponential decays to the correlation data and obtain particle size distributions (PSDs). The software used the CONTIN method by Provencher[12]. It performed a Laplace inversion of the correlation functions using a constrained regularisation method.

The normalised electric field correlation function could be written as:

$$g_1(\tau) = \sqrt{g_2(\tau) - 1} = \int_{\Gamma_{min}}^{\Gamma_{max}} e^{-\Gamma\tau} G(\Gamma) d\Gamma \qquad \textbf{(6. 14)}$$

Here $G(\Gamma)$ is the decay rate distribution function.

This is the Laplace transform of $G(\Gamma)$ with respect to Γ[6]. Therefore, an inverse Laplace transformation of the measured correlation function yields $G(\Gamma)$ and hence information on the distribution of particle sizes[3, 6, 13].

The following model was fitted to the data. Fitting the intensity correlation function, $g_2(\tau)$, was chosen over fitting $g_1(\tau)$ since it gave smoother distribution functions and fewer artefact peaks[14].

$$g_2(\tau) - 1 = \left(\int_{\Gamma_{min}}^{\Gamma_{max}} e^{-\Gamma\tau} G(\Gamma) d\Gamma \right)^2 \qquad \textbf{(6. 15)}$$

The inversion of the correlation function is very unstable so CONTIN uses methods to try and stabilise the solutions. The inversion is very unstable because it is an ill-conditioned process; a small, inevitable amount of statistical or systematic error in the measured correlation function can lead to a large error in the recovered $G(\Gamma)$ and hence particle size distribution[3, 6].

To try and find more stable solutions, regularisation is used. This tries to stabilise the solution by imposing penalties for improbable solutions. More information on regularisation is given in the appendix.

Once the decay rate distributions are known, particle size distributions can be obtained through the Stokes-Einstein relation[14]. The particle size distributions were intensity weighted size distributions (c_i) as these are the fundamental output from DLS measurements. The intensity weighted particle size distributions were also converted to number weighted distributions ($c_{i,n}$). This was achieved by assuming that scattering was in the Rayleigh-Debye regime (Eqn. (6. 16)). This regime is limited to radius values smaller than $\frac{\lambda}{2}$ (~300 nm). It is further limited if the difference in refractive index between the clusters and solvent is large[14]. The refractive indices for glycine and water are 1.46 and 1.33 respectively.

$$c_{i,n} = \frac{c_i}{R_i{}^6 \, P(q,R_i)} = \frac{c_i}{(\sin(qR_i) - qR_i \cos(qR_i))^2} \qquad \textbf{(6. 16)}$$

Here P is the form factor and R_i is the particle radius.

6.2 Dynamic Light Scattering Hardware Setup

As discussed in Chapter 1 and Chapter 5, mesoscale clusters (nanodroplets) exist in glycine solutions and the clusters may be involved in a more rapid nucleation pathway[1]. In order to gain an understanding of the sizes of clusters in the glycine solutions and whether their sizes were affected by fluid shear, dynamic light scattering hardware was setup to allow DLS measurements to be taken from solution that was contained within the Couette cell. This was significantly advantageous over using a commercial DLS instrument as transferring solution from the Couette cells to the commercial instrument strongly influenced the nucleation process. Using a dropper/ syringe to transfer solution was found to cause the solutions to quickly crystallise.

6.2.1 Hardware Setup Summary

To allow in-situ dynamic light scattering measurements to be made, hardware was set up as shown in Figure 6. 6. The components used are listed in Table 6. 1. The beam emerging from the laser (helium-neon laser Thorlabs HRP170, 17 mW) was focussed from 1 mm diameter to a narrow beam waist of ~100 μm diameter using Lens 1 (150 mm focal length plano-convex lens, Thorlabs LA1433-A). This was necessary to obtain a measurement volume (calculated from cross section of beam and aperture of pinhole) that was small enough that fluctuations in scattering intensity would not be averaged over. The beam was focussed in the centre of the gap between the vertical inner and outer Couette cell cylinders.

Light scattered at 90° was imaged onto a 'pinhole' (plastic external aperture of the optical fibre) and collected by an optical fibre (200 μm diameter multimode optical fibre, Thorlabs M72L02). The light was imaged onto the fibre at 1:1 magnification using Lens 2 (25 mm focal length bi-convex lens, Thorlabs LB1471-A). A 2 mm iris was present close to the Couette cell to stop strong reflections from reaching the fibre and limit the range of angles reaching the detector.

The optical fibre was connected to a detector (Excelitas Single Photon Counting Module, SPCM-AQRH-14-FC) that was connected to a correlator (ALV-7004/USB) and computer.
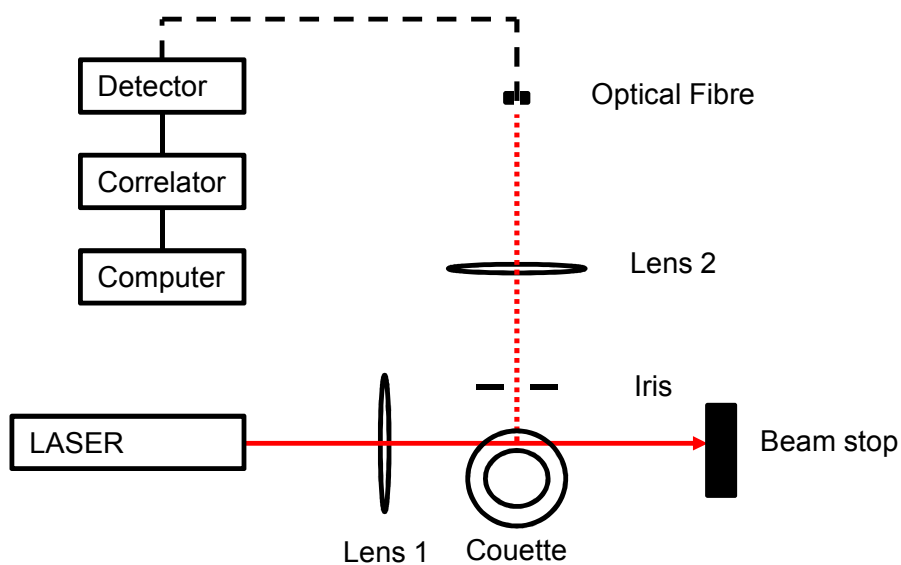
Figure 6. 6
DLS hardware layout.

Table 6. 1
DLS hardware

Laser	Thorlabs HRP170 HeNe
Correlator	ALV-7004/USB
Detector	Excelitas Single Photon Counting Module (SPCM-AQRH-14-FC)
Fibre	200 µm diameter multimode optical fibre (Thorlabs M72L02)
Iris	Standard iris (Thorlabs SM1D12) 2 mm diameter
Lens 1	150 mm focal length plano-convex lens (Thorlabs LA1433-A)
Lens 2	25 mm focal length bi-convex lens (Thorlabs LB1471-A)

Neutral density filters were also present to reduce the intensity of incident light, if required. Details of these filters are given in Chapter 3. For the DLS measurements carried out here, no filters were used due to the relatively low intensity of scattered light that was collected.

6.2.2 Beam Delivery Optics

Beam delivery optics were required to reduce the diameter of the beam going through the sample to a size at which a suitably sized measurement volume was obtained. The measurement volume is defined as the cross section of the incident beam and aperture of the pinhole (here, this was taken as the diameter of the fibre). Without reducing the beam's diameter, measurement volumes were too large, which meant that fluctuations in scattering intensity were averaged over and correlation data could therefore not be obtained.

To achieve a reduction in beam diameter, a plano-convex lens (lens 1) was used to focus the incident collimated laser beam to a spot of a desired size at the lens' focal point. An incident ray travelling parallel to the principal axis of a converging lens will refract through the lens and pass through the focal point on the opposite side of the lens. This is shown in Figure 6. 7. A plano convex lens was chosen as plano convex lenses result in lower spherical aberrations than bi-convex lenses, meaning a more uniform beam waist could be achieved. The beam was incident on the curved surface of the lens.
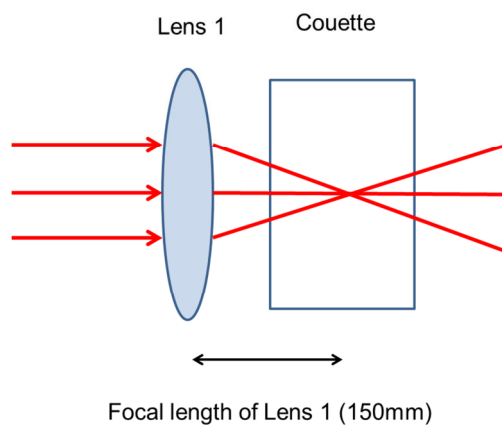
Figure 6. 7
Delivery optics.

The focal length of convex lens capable of focussing the laser beam to a spot in the region of 100 μm was estimated using the following equation for a Gaussian beam. This diameter was chosen since it compared similarly to the diameter used in commercial instruments[14].

$$d_{spot} = \frac{4f\lambda}{\pi D_{lens}}$$ **(6. 17)**

Here d_{spot} is the diameter of focussed spot (beam waist), f is the focal length of the lens and D_{lens} is the diameter of laser beam incident on the lens.

The diameter of beam incident on the lens was calculated using the diameter of the beam at the laser's output (0.98 mm from manufacturer), the beam divergence (0.82 mrad full divergence from manufacturer) and the distance from the laser's output to the lens (55 cm). Using trigonometry, the diameter of beam incident on the lens was calculated to be 1.43 mm. (See Figure 6. 8)

Lens 1

Laser

Distance from laser's output to Lens 1 (55cm)
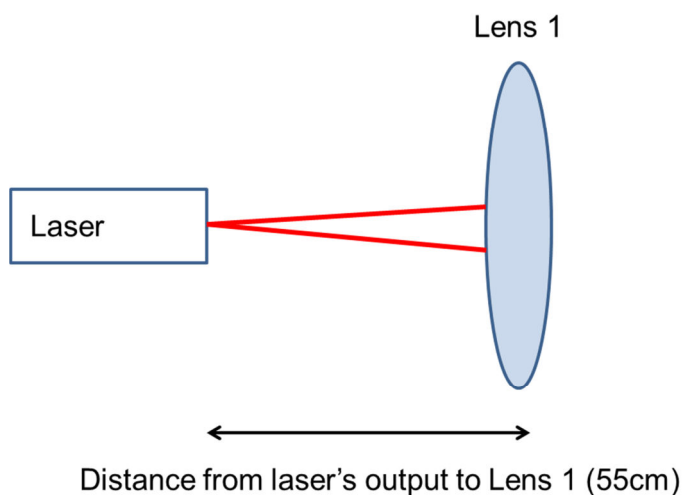
Figure 6. 8
Beam divergence.

Using Eqn. (6. 17), the required focal length was found to be 178 mm. A focal length of 150 mm was chosen as it was commercially available and resulted in a suitable spot size of 85 µm assuming negligible spherical aberrations.

6.2.3 Scattered Light Collection Optics

The aim of the collection optics was to get light scattered from the measurement volume at 90° into an optical fibre that was connected to the single photon counting module detector. The optics were designed to image the light scattered from the measurement volume onto the fibre.
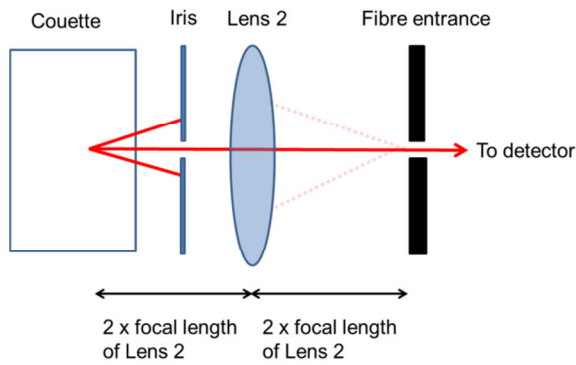
Figure 6. 9
Collection optics.

A bi-convex lens (lens 2) was placed two focal distances away from the beam waist, and the fibre's opening was placed two focal distances from the lens. This arrangement resulted in 1:1 magnification as can be seen by inspecting Eqn. (6. 18) and Eqn. (6. 19).

$$\frac{1}{f} = \frac{1}{S_o} + \frac{1}{S_i} \qquad \textbf{(6. 18)}$$

$$M = \frac{y_i}{y_o} = \frac{-S_i}{S_o} \qquad \textbf{(6. 19)}$$

Here S_o is the distance from the object (measurement volume) to the lens, S_i is the distance from the lens to the image (fibre entrance), y_i is the size of the image, y_o is the size of object and M is the magnification.

A focal length of 25 mm was chosen as this short focal length had the benefit of the imaging lens being closer to the sample, so the intensity of scattered light that was collected by the lens was larger than if the imaging lens was placed further away from the sample (there would have been an inverse square law variation of intensity with distance of imaging lens from beam waist). 1:1 magnification also ensured that the intensity of light reaching the detector was sufficient- higher magnifications were tested but these resulted in lower intensities of light scattered by the measurement volume being incident on the detector.

A 200 μm diameter fibre was used as this resulted in a good amount of scattered light being detected. When smaller diameters were used, the intensity of light reaching the detector was lower due to the smaller measurement volume.

An iris was used to limit the range of angles of scattered light being collected and to block out reflections. When a 2 mm iris was placed 2 cm from the measurement volume, the range of angles passing through the iris was 90 ± 3°. See Figure 6. 10. The range of angle incident on the lens was 90 ± 2°
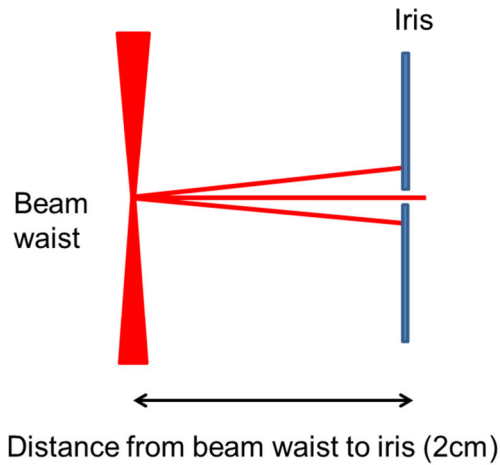

Figure 6. 10
Range of angles passing through iris.

The imaging lens, iris and fibre were built into a single piece of collection optics hardware using a lens tube. The iris was screwed onto the front end of the tube, the lens was positioned accurately at the required distance inside the tube. A fibre adapter plate (Thorlabs SM1FC) was positioned within an x-y translation mount (LM1XY/M) and the translation mount was screwed onto the other end of the tube. The fibre was then connected to the fibre adapter plate. By having these components connected together, alignment was made a lot easier and the tube blocked out unwanted light. The collection optics hardware was attached to an x, y, z stage and this allowed for alignment fine tuning. The other end of the fibre was connected to the detector and the detector was attached to the correlator. The correlator was connected to a PC.

6.3 Experimental Procedures

Dynamic light scattering measurements were carried for two shear rates and two surface area setups, as shown in Table 6. 2. The ranges were more limited than for the induction time measurements (see Chapter 5) since for DLS measurements, the laser beam was directed through the gap between the vertical cylinder walls and alignment became very difficult when the gap was less than 4 mm. Equipment instability (therefore alignment) was also problematic at shear rates beyond 125 s^{-1} for the 22 mm inner cylinder experiments (surface to volume ratio of 2.5 cm^2/cm^3) since high rotational rates were required.

The DLS procedure involved shearing a solution for a chosen duration of time, stopping shearing and taking DLS measurements. This process was repeated as required until the total time for which the solution was sheared for was as desired.

Table 6. 2
Shear rates and surface to volume ratio arrangements used for DLS experiments

Arrangement	Surface to Volume Ratio (cm^2/cm^3)	Shear Rate (s^{-1})
A	2.5	25
B	2.5	125
C	5	25
D	5	125

6.3.1 Glycine Solution Preparation

Glycine (CAS Number 56-40-6) of ≥99% purity was purchased from Sigma Aldrich (item G8898) and used without further purification. Solutions with a concentration (c) of 325 g glycine/kg water were prepared by dissolving glycine in deionised water. Solutions were cooled to 23°C and the solubility (c^*) of glycine was 232 g glycine/kg water at 23°C[15]. Cooling therefore resulted in a supersaturation (S) of 1.4, where

$$S = \frac{c}{c^*} \qquad \text{(6. 20)}$$

Solutions were prepared in sealed glass bottles and were stirred at 55°C for 24 hours to ensure that glycine was fully dissolved. When the solutions were at 55°C, they were undersaturated.

6.3.2 DLS Couette Experimental Procedure

15 ml undersaturated glycine solution (in incubator at 55°C) was filtered using 0.2 μm SFCA disposable syringe filters into a preheated Couette cell by syringe. The filters, syringe and Couette cell were preheated to 55°C in the incubator, and the filtration procedure took place inside the incubator to minimise the rate of heat loss.

The filled Couette cell was removed from the incubator and attached to the monitoring instrument. To minimise evaporation, a lid was secured to the Couette cell and parafilm was used to ensure it was well sealed. Solution was left to cool in the surrounding air for 30 minutes in order to reach ambient temperature (23°C) and the desired level of supersaturation. The temperature profile of the solution during cooling was measured to validate that the 30 minute cooling time was sufficient to ensure that the solutions had reached ambient temperature after this time. During cooling, a fan was used to speed up heat transfer. The ambient temperature remained constant throughout an experiment so the solution remained isothermal once it had cooled to ambient temperature.

Once the solution cooling period had finished, the fan was switched off and the motor was started for a desired duration of shear. Time=0 was taken as the end of the cooling period, when the motor was switched on. Rotational rates were measured using a digital tachometer and the voltage was adjusted to obtain the rotational rate necessary to give a desired shear rate for a particular cylinder arrangement.

After the solution in the Couette cell had undergone shear for the desired duration, the motor was switched off (gradually) to stop the outer cylinder rotating, and the solution was left to stabilise for 15 seconds. This time was significantly longer than the relaxation time of the solutions[16] and was sufficient to see that solutions were visibly stable. Dynamic light scattering measurements at 90° were then taken 5 times. Each measurement lasted for 5 seconds. Once the 5 measurements were taken, the motor was restarted and the procedure of shearing for a chosen duration,

stopping the motor, leaving the solution to stabilise and then taking 5 dynamic light scattering measurements was repeated. 5 repetitions were carried out, resulting in 25 DLS measurements for each duration of shear for each setup.

The total duration for which solutions were sheared depended on which Couette cylinder arrangement and shear rate were used. The maximum total length of time that solutions were sheared for was made similar to the shortest induction time measured during the induction time measurement experiments in Chapter 5, as shown in Table 6. 3. This was to avoid crystals/ turbidity affecting the measurements. In a small number of cases, crystals formed during the procedure so these results were discarded.

Table 6. 3
Comparison of the shortest induction times measured from Chapter 5 and the maximum duration for which solutions were sheared for in the DLS experiments.

Setup	Shear Rate (s-1)	Surface to Volume Ratio (cm^{-1})	Shortest Experimental Induction Time (s)	Maximum Shear Duration for DLS Expts. (s)
A	25	2.5	1200	1200
B	125	2.5	200	300
C	25	5	750	1200
D	125	5	100	120

6.4 Dynamic Light Scattering Measurement Results Based on a Cumulant Analysis

The autocorrelation functions obtained from DLS measurements were analysed to obtain values for the average size of nanodroplets (mesoscale clusters) in the solutions. Two methods were used- the cumulant method and CONTIN method. The basic theory on these was outlined in Section 6.1.4. It is noted that the data measured often had significant noise so the sizes found through both methods were sensitive to the data points used in the analyses. The CONTIN method was particularly sensitive to noise, so results from this method are given in the appendix and the main findings are summarised in Section 6.5.

Due to the noise in the data, several statistical evaluations were carried out to determine whether trends were statistically significant. This included analysing the individual autocorrelation functions measured, as well as analysing the averaged functions. Each cumulant fit of the autocorrelation function had an associated error, so this also had to be taken into consideration. Due to extreme noise at short delay times, data for delay times less than 0.01 ms were completely excluded from the following analyses.

6.4.1. Analysis of the Average of the 25 Measured Autocorrelation Functions

Since 25 measurements (5 measurements for each of 5 repetitions) were taken for each duration of applied shear for each experimental arrangement, the 25 autocorrelation functions were averaged and are shown in Figure 6. 11 to Figure 6. 14. The error bars represent 1 standard deviation. The individual autocorrelation functions are given in the appendix. The autocorrelation functions were normalised between the average value of the first 30 data points and the average value of the final data points from data point 70 onwards (46 points in total). Functions were normalised between these average values since the start and end of the functions were most strongly affected by noise.

6.4.1.1 Visual Inspection of the Average Functions

By visually inspecting the average autocorrelation functions, it could be seen that as the duration of applied shear was increased, the autocorrelation functions appeared to decay more slowly. This suggested that shearing caused the nanodroplets to increase in size on average. When the standard deviation of the average functions was taken into account, the trend, however, did not appear very significant, although the trend did remain consistent for each setup. The autocorrelation functions did not represent perfect exponential decays, which indicated that a degree of polydispersity occurred in the solutions.
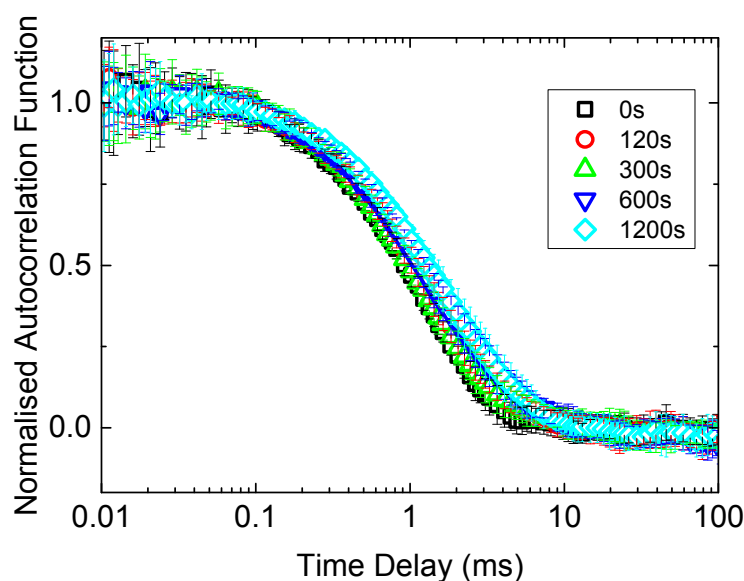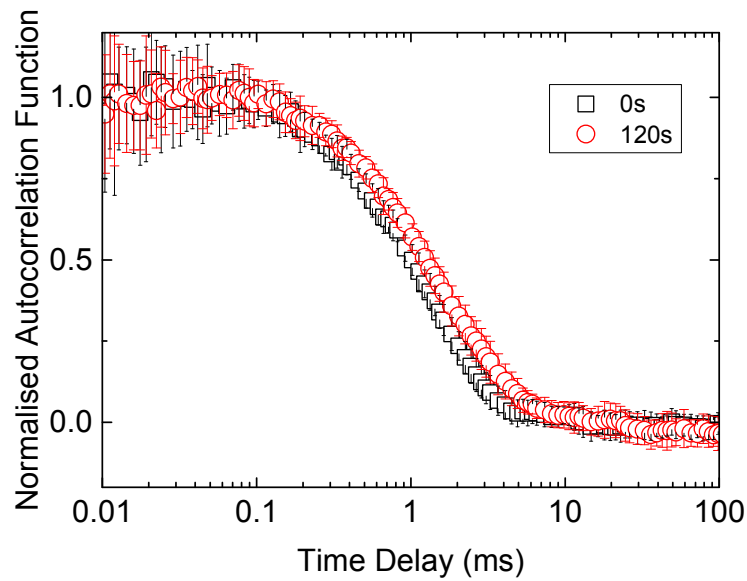

Figure 6. 11
Average of the 25 autocorrelation functions measured for each duration of shear for setup A. Error bars represent one standard deviation.
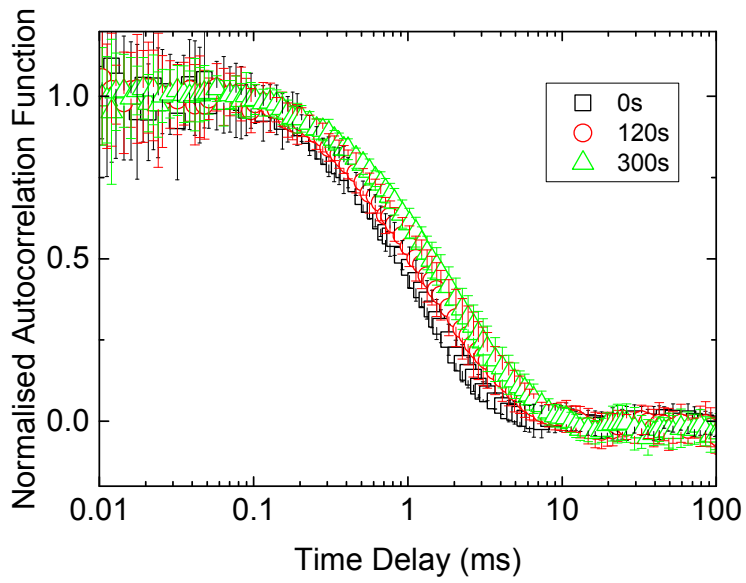
Figure 6. 12
Average of the 25 autocorrelation functions measured for each duration of shear for setup B. Error bars represent one standard deviation.
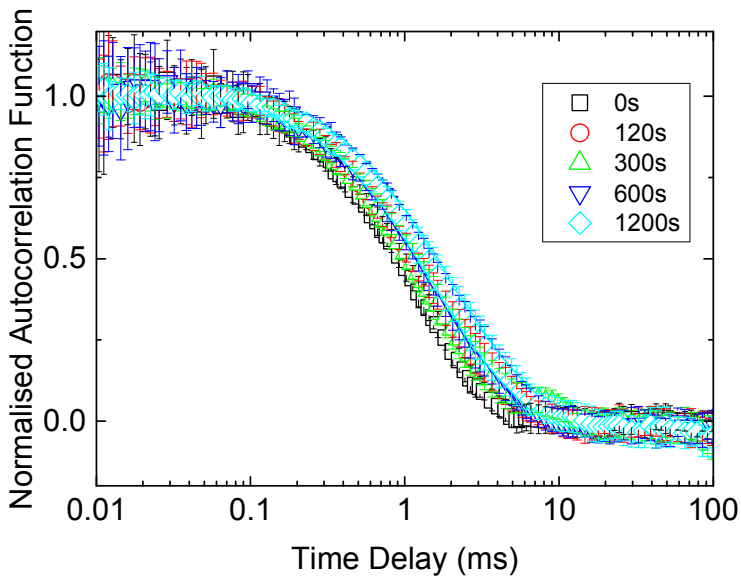
Figure 6. 13
Average of the 25 autocorrelation functions measured for each duration of shear for setup C. Error bars represent one standard deviation.

Figure 6. 14
Average of the 25 autocorrelation functions measured for each duration of shear for setup D. Error bars represent one standard deviation.

6.4.1.2 Cumulant Analysis of Average Functions

A cumulant analysis was carried out over the average autocorrelation functions and the average hydrodynamic radii found from this are given in Figure 6. 15. The error bars represent the 95% confidence interval of the fit performed during the non-linear regression aspect of the cumulant analysis. For consistency, fits were performed over the same data points (points corresponding to delay times of 0.1 ms to 2 ms) for each function. The sizes found suggested that the average hydrodynamic radius increased with increased shear duration, however, this analysis did not take the standard deviation of the averaged functions into account. As mentioned, visual inspections of the functions suggested that the spread of data was fairly large. A more robust analysis was therefore required.
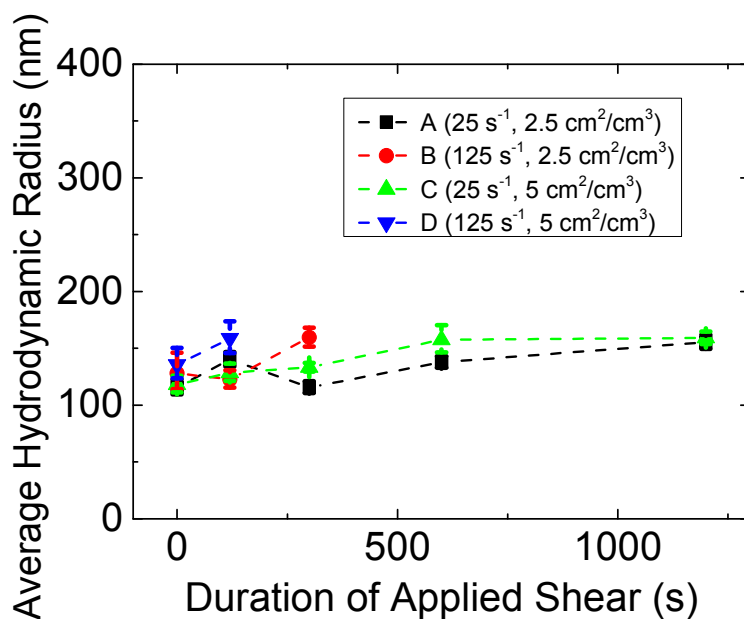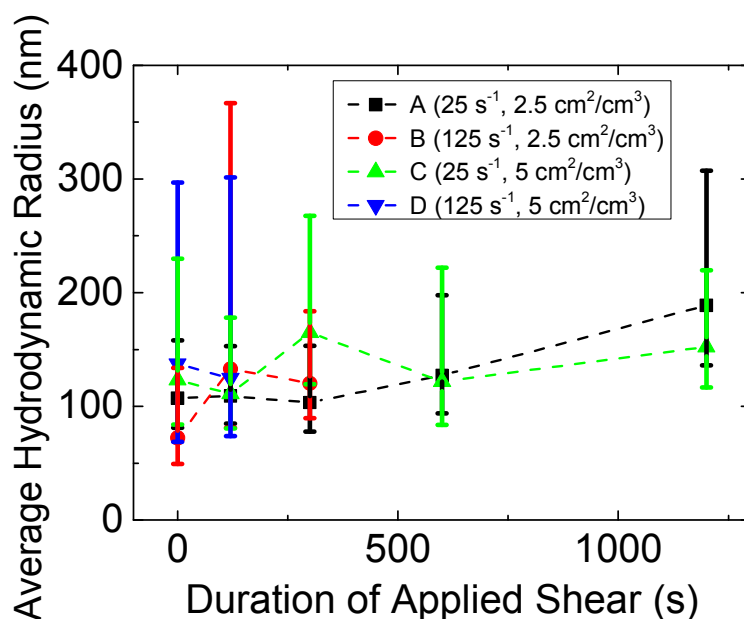
Figure 6. 15
Average hydrodynamic radius found by doing a cumulant analysis to the averaged autocorrelation functions using data points corresponding to delay times of 0.1 ms-2 ms.

It is worth noting, that the goodness of fits depended strongly on which data points were used in the analysis. For example, when data points corresponding to delay times of 0.09 ms to 0.8 ms were used, the errors were significantly larger (as shown in Figure 6. 16). The errors would have been even larger if the standard deviation of the averaged functions was taken into account.

Figure 6. 16
Average hydrodynamic radius found by doing a cumulant analysis to the averaged autocorrelation functions using data points corresponding to delay times of 0.09 ms to 0.8 ms).

6.4.2 Cumulant Analysis of Entire Data Set

In addition to analysing the average autocorrelation functions, all measured individual autocorrelation functions (given in the appendix) were analysed as well. By visually inspecting the autocorrelation functions, it could be seen that as the duration of applied shear was increased, the autocorrelation functions appeared to decay more slowly. This suggested that shearing caused the nanodroplets to increase in size. The autocorrelation functions generally did not represent perfect exponential decays, which indicated that a degree of polydispersity occurred in the solutions.

To analyse the autocorrelation functions quantitatively, firstly a cumulant analysis was performed across all autocorrelation functions obtained for a given set of conditions i.e. one function was fitted to the entire data set gathered for a set of conditions (25 autocorrelation functions). The average hydrodynamic radii and their associated errors are given in Figure 6. 17. The error bars represent the 95% confidence interval of the non-linear regression fit performed during the cumulant analysis. For consistency, fits were performed over the same data points (corresponding to delay times of 0.1 ms to 2 ms) for each set of conditions. The sizes found suggested that the average hydrodynamic radius increased with increased shear duration, however, the error bars were large since this analysis took into account the variability of autocorrelation functions measured for a given set of conditions. Therefore further analyses were required to ensure that trends were statistically significant. The further analyses were based on the slope of the average hydrodynamic radius plotted as a function of the duration of applied shear. The methods used were simple linear regression (6.4.2.1), Monte Carlo simulations (6.4.2.2) and weighted regression (6.4.2.3).
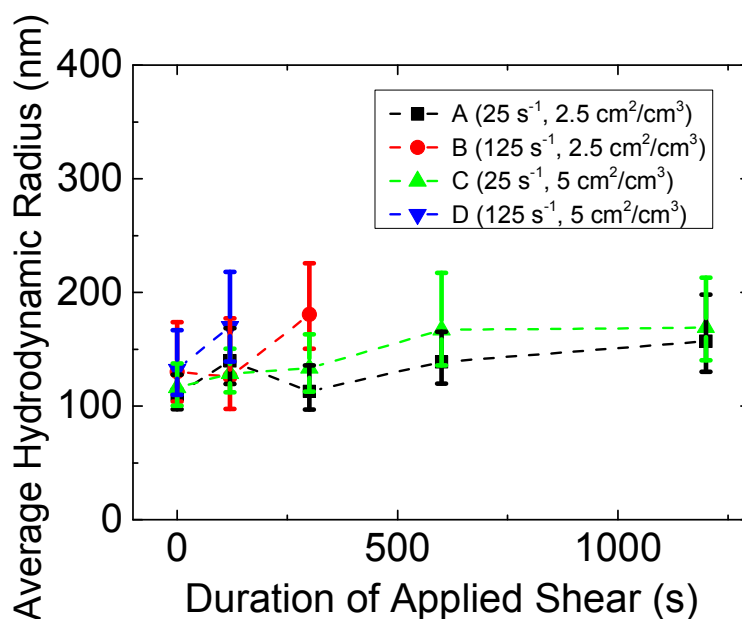
Figure 6. 17
Average hydrodynamic radius found by doing a cumulant analysis to all autocorrelation function data for a given set of conditions. The error bars represent the 95% confidence intervals from the fits.

6.4.2.1 Linear Regression of Cumulant Analysis Results

Simple linear regression was used to find the slope (and slope error) of the plots on Figure 6. 17. To try and ascertain whether the trend of increasing average hydrodynamic radius with shear duration held once the fitting error of each function (95% upper and lower confidence intervals) was taken into consideration, the slopes based on the upper and lower confidence limits were found in addition to the slope of the best fit values. The slopes are given in Figure 6. 18. The error bars represent the 95% confidence interval from the linear fit (setup B had no confidence interval as it had only 2 points).

The slopes generally appeared to remain positive within their confidence interval which suggested that shear resulted in an increase in the average hydrodynamic radius of nanodroplets in the solutions, but it was not possible to conclude this for certain. When the slopes were plotted as a function of shear rate multiplied by surface area, higher shear rates and surface areas resulted in a larger slope. Therefore, as with induction time measurements (Chapter 5), the choice of shear rate and Couette surface area appeared to be important. The shear rate appeared to have a stronger effect on the slopes than the surface area.
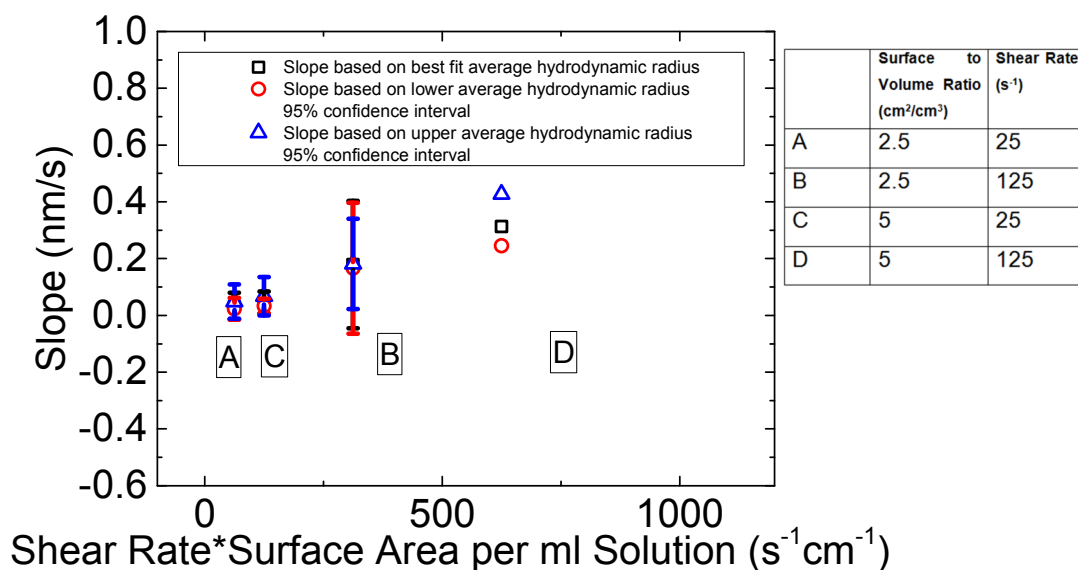
Figure 6. 18
Slopes found from the average hydrodynamic radius values (best fit and upper and lower 95% confidence limits) plotted as a function of shear duration i.e. Figure 6. 17 slopes. The error bars represent 95% confidence intervals from the linear fit.

This simple method of looking at trends was useful, but more advanced analyses (Monte Carlo simulations and weighted regression) were required to ensure that trends were significant.

6.4.2.2 Use of Monte Carlo Method to Analyse Cumulant Analysis Results

As mentioned, the cumulant fits done for the DLS analyses had associated errors (95% upper and lower confidence intervals (CI_{upper}, CI_{lower}) were obtained). Plots of average hydrodynamic radius as a function of duration of applied shear (e.g. Figure 6. 17) therefore had an error associated with each average hydrodynamic radius point. In order to calculate the slope of average hydrodynamic radius versus shear duration plots reliably, the error of each point had to be taken into consideration. A Monte Carlo method was used to achieve this, similar in principle to what was done in Chapter 4 Section 4.6. Two approaches were taken- the first was based on the asymmetric confidence intervals output from the non-linear regression fit from the cumulant analysis and the second involved transforming the asymmetric confidence intervals to symmetric confidence intervals.

Approach 1: Asymmetric Confidence Intervals

For this Monte Carlo approach, it was assumed that errors output from the non-linear regression cumulant fitting procedure were distributed normally around a mean value (μ). Each point's error bars were asymmetrical so the errors at either side of the mean value were assumed to follow normal distributions with different standard deviations at either side. The mean value was taken as the best fit value ($best$) given from the Matlab fit i.e. the data points plotted in the graphs in Figure 6. 17.

For the Monte Carlo method, 'new' average hydrodynamic radius data were drawn using a typical Monte Carlo procedure. The drawn average hydrodynamic radius values were plotted as a function of time (duration of applied shear) and the slope was found. The procedure of drawing average hydrodynamic radius values and finding their slope when plotted as a function of the shear duration was repeated 500 times and the mean slope and standard deviation were found.

Steps 1-5 were carried out for each data point in Figure 6. 17:

1. The standard deviations of the upper and lower distributions of the data point were calculated. The 95% confidence intervals output from Matlab (CI_{upper}, CI_{lower}) were taken as 1.96 standard deviations.

   The upper error bar's standard deviation (σ_{upper}) could be found from:

$$\sigma_{upper} = \frac{CI_{upper} - \mu}{1.96} \qquad \textbf{(6. 21)}$$

   The lower error bar's standard deviation (σ_{lower}) could be found from:

$$\sigma_{lower} = \frac{\mu - CI_{lower}}{1.96} \qquad \textbf{(6. 22)}$$

2. A random average hydrodynamic radius value (x) between $\mu - 5\sigma_{lower}$ and $\mu + 5\sigma_{upper}$ was generated. This represented an average hydrodynamic radius value within the errors associated with each data point.

3. The probability density function (p) of this average hydrodynamic radius value occurring was calculated. The calculation was based on x, μ and σ_{lower} or σ_{upper}. If x was less than μ, σ_{lower} was used. If x was greater than μ, σ_{upper} was used.

$$p = \frac{1}{\sigma\sqrt{2\pi}} \exp\left(\frac{(x-\mu)^2}{2\sigma^2}\right) \qquad \text{(6. 23)}$$

Here σ is σ_{lower} or σ_{upper}.

4. A random number between 0 and 1 (N_{rand}) was generated and this represented a probability. This value was compared to the calculated probability density function, p. If the random number (N_{rand}) was greater than the calculated probability density function (p) the random average hydrodynamic radius value (x) was rejected.

5. The procedure of generating a random average hydrodynamic radius value and checking probabilities (steps 2-4) was repeated until $N_{rand} \leq p$ i.e. it lay under the normal distribution curve. When this was the case, the random hydrodynamic radius value x was accepted.

6. Once steps 1-5 had been carried out for each data point in a plot of average hydrodynamic radius versus shear duration (and each data point now had a new accepted average hydrodynamic radius value, drawn from the Monte Carlo procedure), the drawn average hydrodynamic radius values were plotted as a function of shear duration and the linear slope of this was calculated.

7. Steps 1-6 were repeated 500 times to obtain 500 slope values. The mean and standard deviation of these slopes were then found.

The results from the Monte Carlo analysis of the data in Figure 6. 17 is given in Figure 6. 19. It shows that when the errors in the average hydrodynamic radius values were taken into consideration, the slope generally remained positive across its confidence interval (2 standard deviations). This suggested that the average hydrodynamic radius increased with the duration of applied shear. When the slopes

were plotted as a function of shear rate multiplied by surface area, higher shear rates and surface areas resulted in larger slopes.
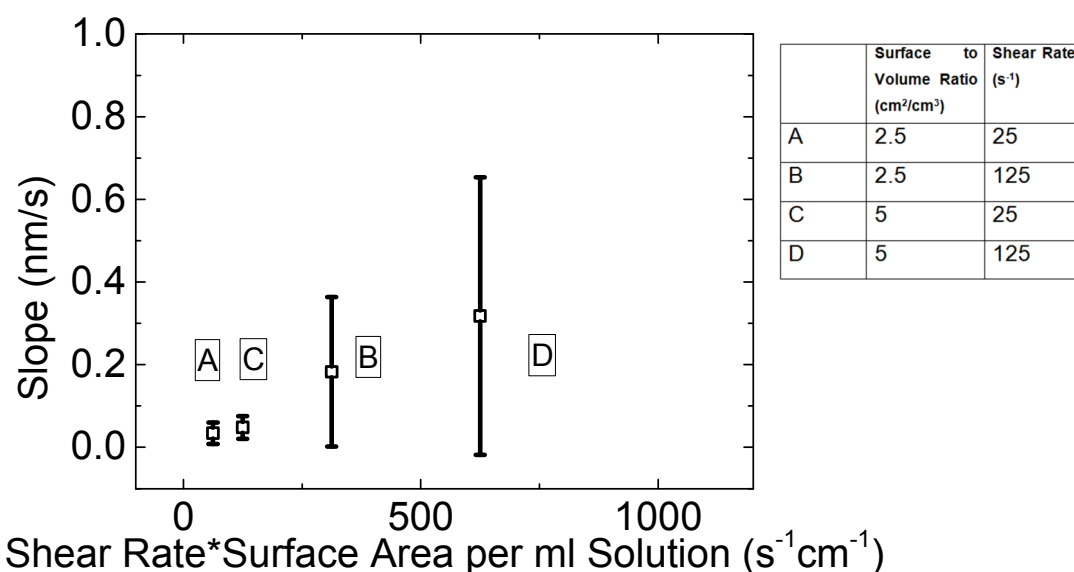

Figure 6. 19
Slopes found from the Monte Carlo analysis of average hydrodynamic radius values plotted as a function of shear duration. The error bars represent 2 standard deviations. The error was particularly large for setup D since it was based on the fewest data points.

Approach 2: Symmetric Confidence Intervals

In order to simplify the procedure, efforts were taken to make the confidence intervals symmetrical. This was achieved by transforming the average hydrodynamic radius data through the use of a power (z). If the confidence intervals were symmetrical, for every measurement:

$$\frac{CI_{upper}^{\,z} - best^z}{best^z - CI_{lower}^{\,z}} \approx 1$$

It was found that using a power of -1 resulted in perfectly symmetrical error bars. This meant that the confidence intervals output from Matlab were likely normally distributed around a mean value when based on the reciprocal of the average hydrodynamic radius values ($\frac{1}{R_h}$).

Since the confidence intervals from Matlab were based on 95% confidence, the standard deviation of the transformed data (σ_i) could be estimated for each measurement i from:

$$\sigma_i = \frac{CI_{upper}^{-1} - CI_{lower}^{-1}}{2 \times 1.96} \qquad \textbf{(6. 24)}$$

A Monte Carlo procedure similar to that outlined previously for data with asymmetric confidence intervals was carried to the transformed data, but rather than being based on the average hydrodynamic radius, it was based on the reciprocal i.e. plots of the reciprocal of the average hydrodynamic radius versus duration of applied shear. For this

$$\mu = best^p = \frac{1}{best} \text{ and } \mu - 5\sigma_i \leq x \leq \mu + 5\sigma_i$$

This Monte Carlo approach was used to find the slope of plots of the transformed data $\frac{1}{R_h}$ in Figure 6. 17 as a function of the duration of applied shear. The slopes and their errors (2 standard deviations) are shown in Figure 6. 20 and are plotted as a function of the product of shear rate and surface area. If the average hydrodynamic radius increased with the duration of applied shear, it would be expected that the slopes would remain negative within their confidence intervals. This could not be conclusively drawn from the analysis here. Therefore further analysis of the data was required.
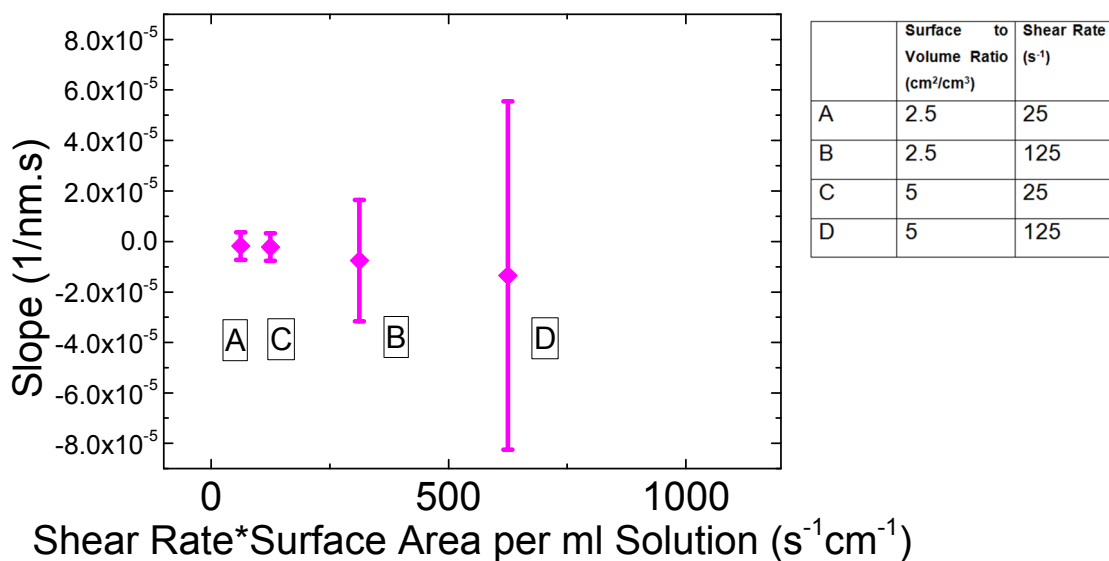
	Surface to Volume Ratio (cm²/cm³)	Shear Rate (s⁻¹)
A	2.5	25
B	2.5	125
C	5	25
D	5	125

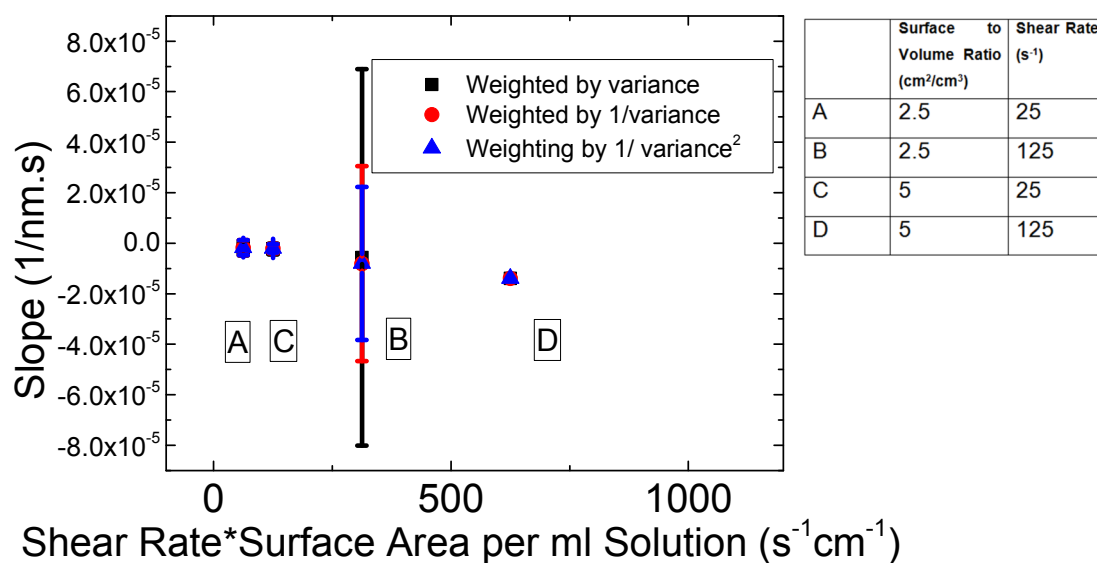**Figure 6. 20**
Slopes found from the Monte Carlo analysis of the reciprocal of the average hydrodynamic radius values plotted as a function of shear duration. The error bars represent 2 standard deviations.

6.4.2.3 Use of Weighted Least Squares Regression to Analyse Cumulant Analysis Results

Weighted least squares regression was carried out as a further analysis of trends. In order to simplify the procedure, efforts were taken to make the error bars symmetrical as detailed in Section 6.4.2.2.

For the weighted linear least squares regression, the following error term was minimised. Here y_i is based on experimental data point i (reciprocal of average hydrodynamic radius value, $best^p$), $y_{i,f}$ is the fitted value for point i and w_i is the weighting of point i. $i = 1, 2, ..., n$ where n is the total number of data points used in the weighted least squares procedure.

$$error = \sum_{i=1}^{n} w_i \left(y_i - y_{i,f} \right)^2 \qquad \text{(6. 25)}$$

Three different weightings were carried out. Either:

216

$$w_i = \sigma_i{}^2; \; w_i = \frac{1}{\sigma_i{}^2} \text{ or } w_i = \frac{1}{\sigma_i{}^{2\,2}}$$

Weighted linear regression in Matlab was used to find the slope of plots of the transformed data $\frac{1}{R_h}$ in Figure 6. 17 as a function of the duration of applied shear. The slopes and their errors (95% confidence limit) are shown in Figure 6. 21 and are plotted as a function of the product of shear rate and surface area.

If the average hydrodynamic radius increased with the duration of applied shear, it would be expected that the slopes would remain negative within their confidence intervals. This could not be conclusively drawn from the data shown in Figure 6. 21. It is noted that data corresponding to setup D would have had an associated error, but this could not be found using the weighted least squares procedure carried out here since point D only had two data points.

Figure 6. 21
Slopes found from the weighted least squares analysis of the reciprocal of the average hydrodynamic radius values plotted as a function of shear duration. The error bars represent 95% confidence.

6.4.2.4 Summary of Findings from Cumulant Analysis of Entire Data Set

The various methods of analysis outlined (basic linear regression, Monte Carlo simulations and weighted least squares regression) failed to conclusively show that increasing the duration of applied shear resulted in an increase in average cluster size. This was based on a single cumulant fit to the entire set of autocorrelation functions for a given set of conditions, so to gain a better understanding of the results, a cumulant analysis was done to each measured autocorrelation function.

6.4.3 Cumulant Analysis of Each Measured Function

The average hydrodynamic radius found through a cumulant analysis for each measurement for each setup is given in Figure 6. 22 to Figure 6. 25. The corresponding autocorrelation functions are given in the appendix. For consistency during all cumulant analyses, data points corresponding to delay times of 0.1 ms to 2 ms were used. Each average hydrodynamic radius value had a fitting error from the cumulant analysis, so the 95% confidence intervals were plotted.

In some instances, the fitting gave non-sensible outlier results so measurements that resulted in negative average hydrodynamic radii or radii values greater than 500nm were excluded from the following analysis. It should be noted that these outliers would have influenced the analyses performed in Section 6.4.2.
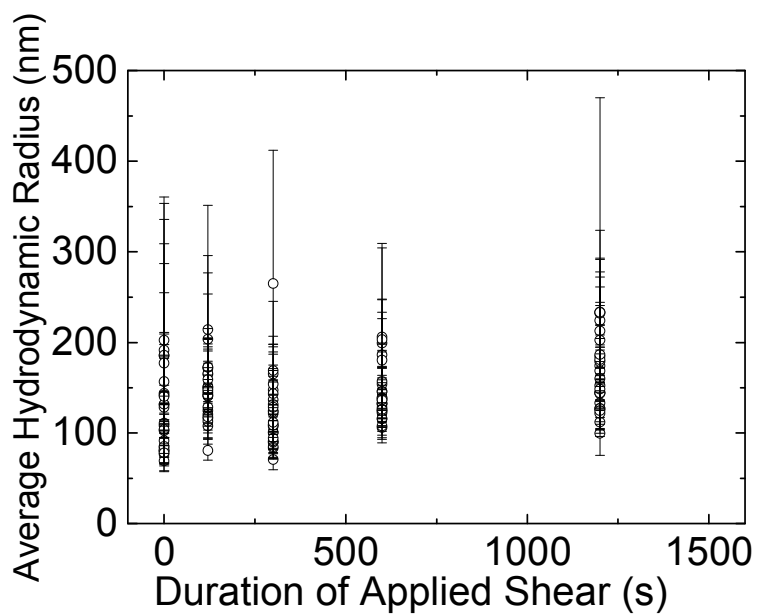
Figure 6. 22
Average hydrodynamic radii obtained from autocorrelation functions for setup A. Error bars represent the 95% confidence interval of the cumulant fit.
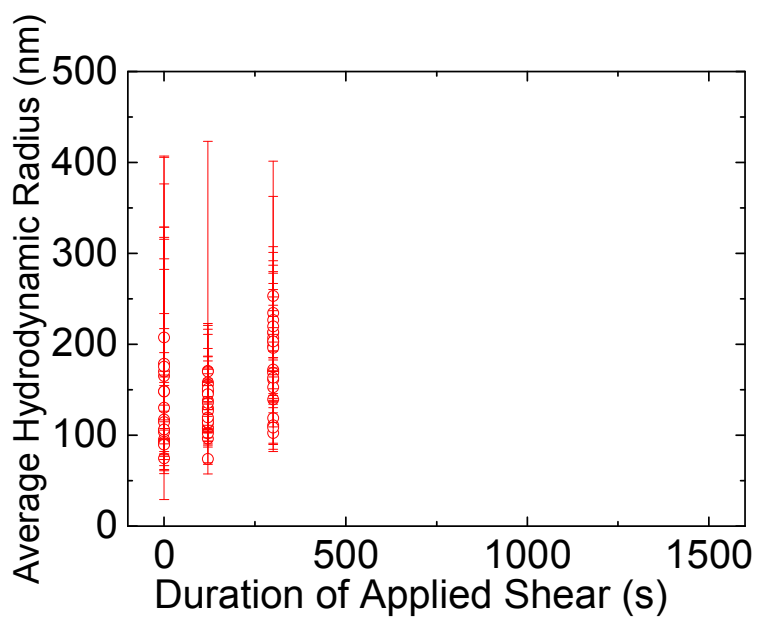

Figure 6. 23
Average hydrodynamic radii obtained from autocorrelation functions for setup B. Error bars represent the 95% confidence interval of the cumulant fit.
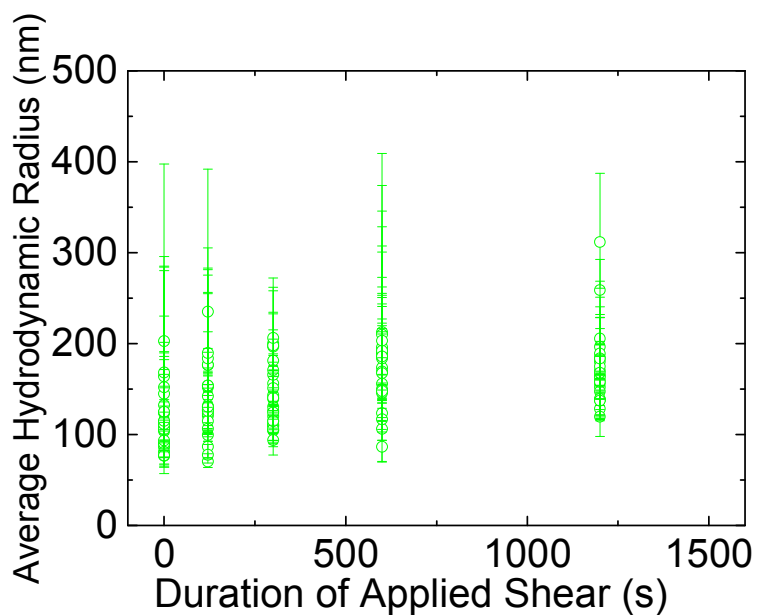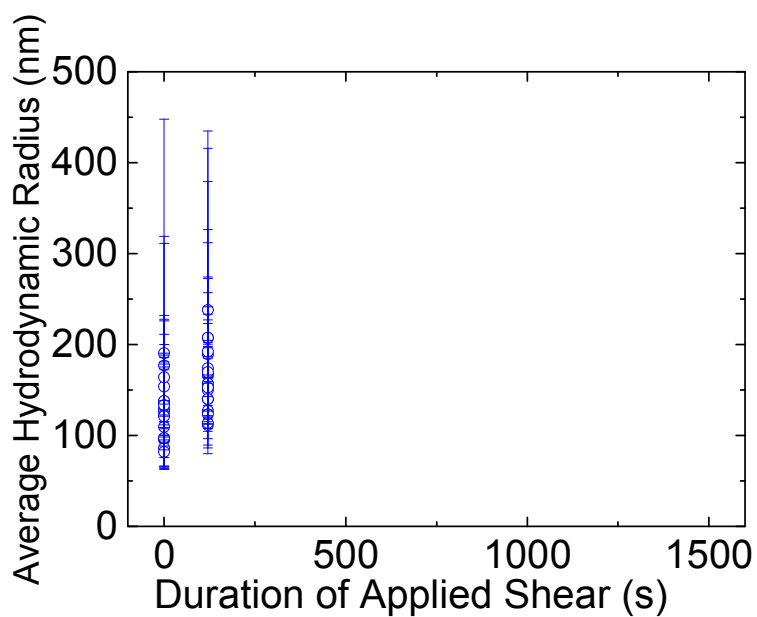
Figure 6. 24
Average hydrodynamic radii obtained from autocorrelation functions for setup C. Error bars represent the 95% confidence interval of the cumulant fit.

Figure 6. 25
Average hydrodynamic radii obtained from autocorrelation functions for setup D. Error bars represent the 95% confidence interval of the cumulant fit.

Several analyses of these data were carried out to see if trends were statistically significant, as had been done in Section 6.4.2. These included simple linear

regression (6.4.3.2), Monte Carlo simulations (6.4.3.3), weighted least squares regression (6.4.3.4), as well as a basic analysis based on mean values of the data (6.4.3.1).

6.4.3.1 Basic Analysis Using Mean Best Fit Values

The mean of the best fit average hydrodynamic radii for each set of conditions (Figure 6. 22 to Figure 6. 25) are shown in Figure 6. 26. The error bars represent 1 standard deviation. The graph shows that the mean average hydrodynamic radius value increases with the application of shear for each experimental setup. This analysis did not take the fitting errors for the points in Figure 6. 22 to Figure 6. 25 into consideration.
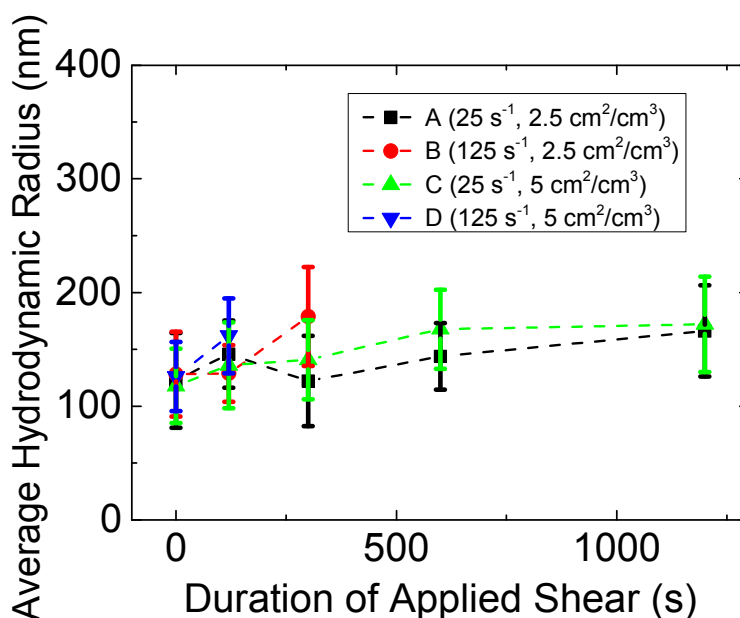
Figure 6. 26
Mean average hydrodynamic radius found from the DLS measurements. Error bars represent 1 standard deviation.

In Figure 6. 27, the mean of the best fit average hydrodynamic radii for each set of conditions are shown and the error bars represent the mean of the confidence intervals obtained from the fitting procedure for each set of conditions (see Figure 6. 22 to Figure 6. 25).

In Figure 6. 28, the mean of the average hydrodynamic radii for each set of conditions are shown and error propagation rules[17] were used to calculate the error in mean average hydrodynamic radius. The error propagation was based on each individual confidence interval from the fitting procedure for each function. The error was taken as equal to the square root of the sum of the square of the fitting errors from each repetition for a given set of conditions.

Although the mean values of hydrodynamic radius generally increased with the duration of applied shear for each cylinder arrangement, due to data noise and large errors, this could not be concluded to be statistically significant using these basic analyses of the data.
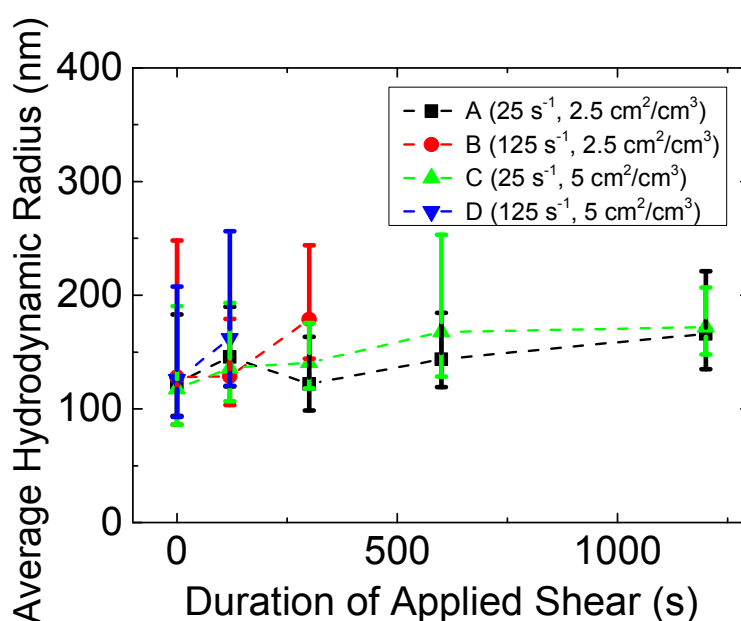

Figure 6. 27
Mean average hydrodynamic radius found from the DLS measurements. Error bars represent the mean of the 95% confidence limits for each autocorrelation function fit.
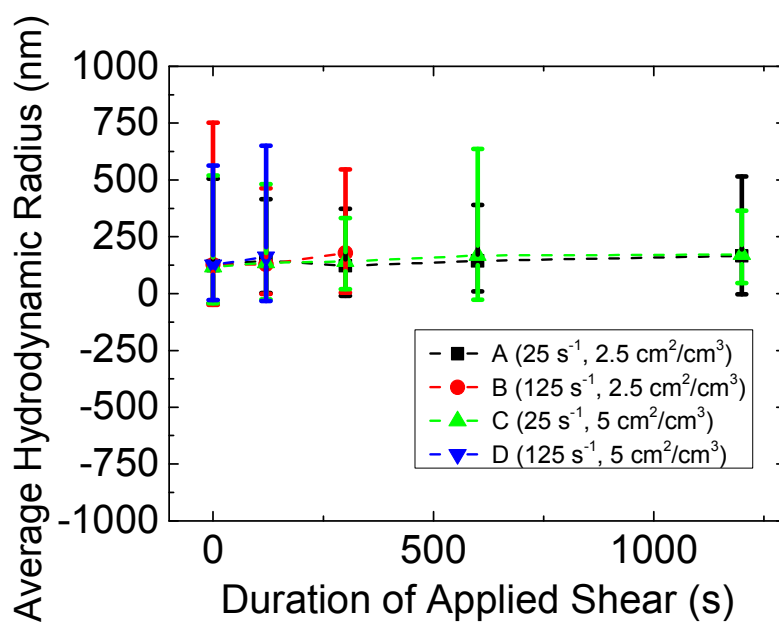
Figure 6. 28
Mean average hydrodynamic radius found from the DLS measurements. Error bars were found through error propagation of the error associated with each average hydrodynamic radius value.

6.4.3.2 Linear Regression of Cumulant Analysis Results

Linear regression was used to find the slope (and slope error) of the plots of Figure 6. 22 to Figure 6. 25. To try and ascertain whether the trend held once the fitting error of each function was taken into consideration, the slopes based on the upper and lower confidence limits were found, in addition to the slope of the best fit values. The slopes are given in Figure 6. 29. The error bars represent the 95% confidence interval from the linear fit.
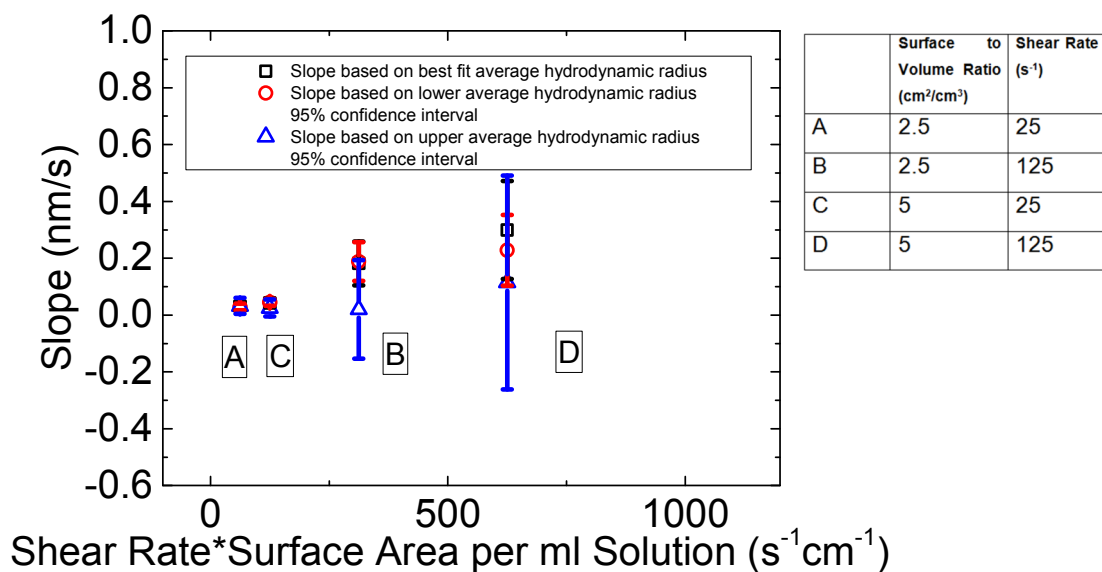
	Surface to Volume Ratio (cm²/cm³)	Shear Rate (s⁻¹)
A	2.5	25
B	2.5	125
C	5	25
D	5	125

Figure 6. 29
Slopes found from the average hydrodynamic radius values (best fit and upper and lower 95% confidence limits) plotted as a function of shear duration i.e. Figure 6. 22 to Figure 6. 25 slopes. The error bars represent the 95% confidence interval from the linear fit.

From Figure 6. 29, the linear regression slope of the best fit average hydrodynamic radius as a function of time remained positive for each setup and became steeper as the product of shear rate and surface area increased. The trend also held for the lower confidence limit, but not for the upper. Therefore, as with induction time measurements (Chapter 5), the choice of shear rate and Couette surface area appeared to be important. The shear rate appeared to have a stronger effect on the slopes than the surface area.

6.4.3.3 Use of Monte Carlo Method to Analyse Cumulant Analysis Results

In order to calculate the slope of average hydrodynamic radius as a function of shear duration (Figure 6. 22 to Figure 6. 25) reliably, the error bars of each point had to be taken into consideration. A Monte Carlo method identical to that outlined in Section 6.4.2.2 was used. Again, two approaches were taken: one for asymmetric confidence intervals (plots of average hydrodynamic radius versus duration of applied shear) and one where the data were transformed to results in symmetric confidence intervals (plots of the reciprocal of average hydrodynamic radius versus duration of applied shear).
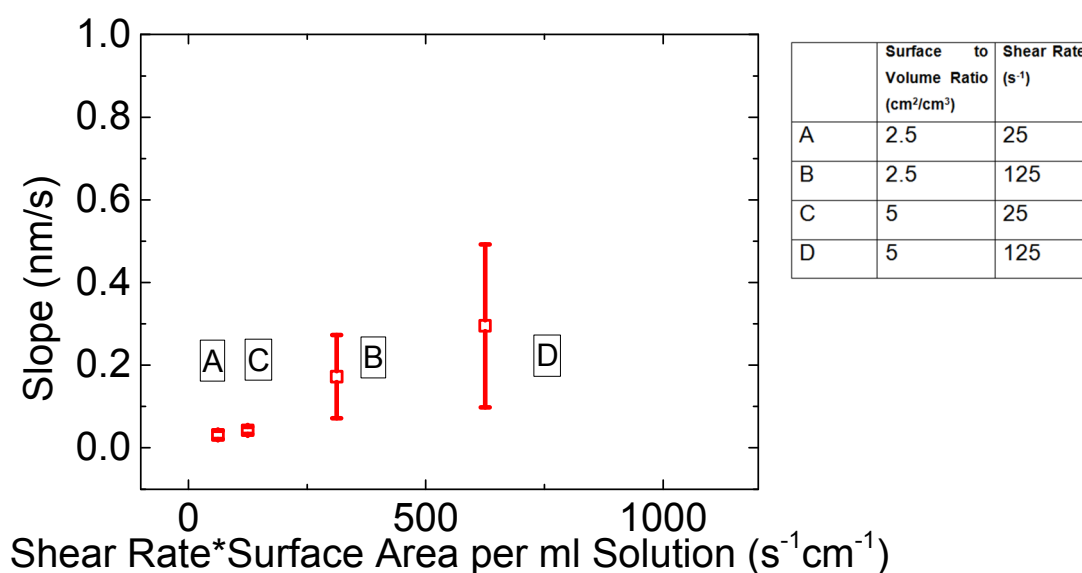

	Surface to Volume Ratio (cm²/cm³)	Shear Rate (s⁻¹)
A	2.5	25
B	2.5	125
C	5	25
D	5	125

Figure 6. 30
Slopes found from the Monte Carlo analysis of average hydrodynamic radius values plotted as a function of shear duration. The error bars represent 2 standard deviations.
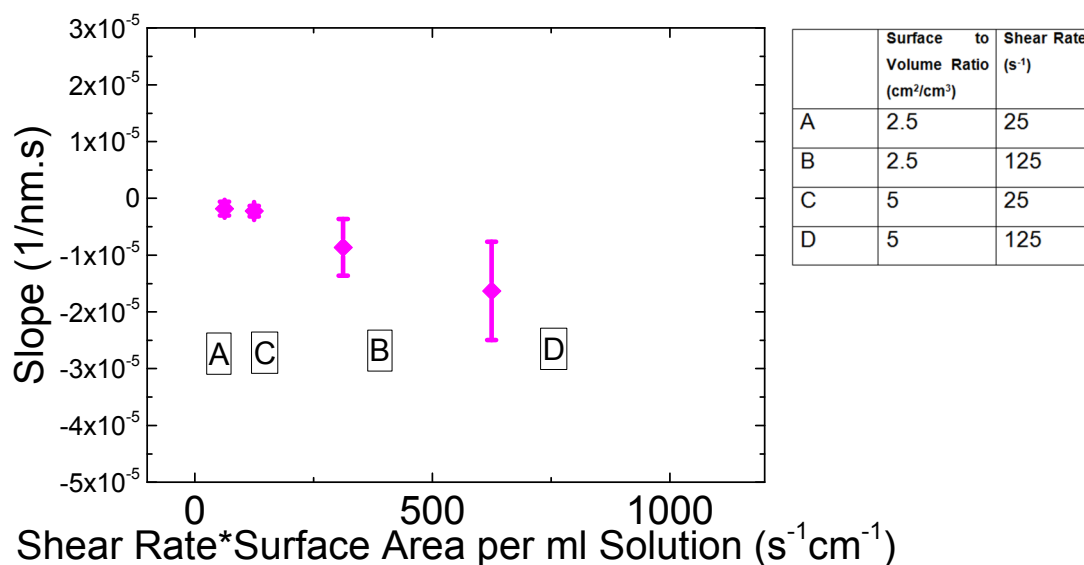
Figure 6. 31
Slopes found from the Monte Carlo analysis of the reciprocal of the average hydrodynamic radius values plotted as a function of shear duration. The error bars represent 2 standard deviations.

The results from the Monte Carlo analyses of the data in Figure 6. 22 to Figure 6. 25 are given in Figure 6. 30 (based on asymmetric confidence intervals) and Figure 6. 31 (based on symmetric confidence intervals). The plots show that when the errors in the average hydrodynamic radius values were taken into consideration, the slopes for each setup remained positive across their confidence interval when based on plots of average hydrodynamic radius versus duration of applied shear. The slopes for each setup remained negative across their confidence intervals when based on the reciprocal of average hydrodynamic radius versus duration of applied shear. These trends suggested that the average hydrodynamic radius increased with the duration of applied shear. When the slopes were plotted as a function of shear rate multiplied by surface area, higher shear rates and surface areas resulted in larger slopes.

The errors found through this method of analysing the fits from every autocorrelation function were lower than the method of performing a single cumulant fit to the entire data set for a given set of conditions (cf. Figure 6. 19 and Figure 6. 20). This would have been because for this method, outliers were removed- measurements that resulted in negative average hydrodynamic radii or radii greater than 500nm were

excluded from the analysis. Their corresponding functions would have been present during single cumulant fit analyses in Section 6.4.2, resulting in larger errors.

6.4.3.4 Use of Weighted Least Squares to Analyse Cumulant Analysis Results

A weighted least squares analysis was carried out to the data in Figure 6. 22 to Figure 6. 25 using a procedure identical to that detailed in Section 6.4.2.3.

Weighted linear regression in Matlab was used to find the slope of plots of the transformed data $\frac{1}{R_h}$ in Figure 6. 22 to Figure 6. 25 as a function of time (duration of applied shear). The slopes and their errors (95% confidence limit) are shown in Figure 6. 32 and are plotted as a function of the product of shear rate and surface area. If the average hydrodynamic radius increased with the duration of applied shear, it would be expected that the slopes here would remain negative within their confidence intervals. This could be reasonably confidently drawn from the data, though it was sensitive to which method of weighting was used. Weighting by 1/variance is the most conventional and results in the most convincing trend in Figure 6. 32. As before, higher shear rates and surface areas resulted in larger slopes.

The trends were clearer here in comparison to Figure 6. 21 (based on a single fit to all cumulant functions for a given set of conditions, see Section 6.4.2) since here, outlier measurements were removed.
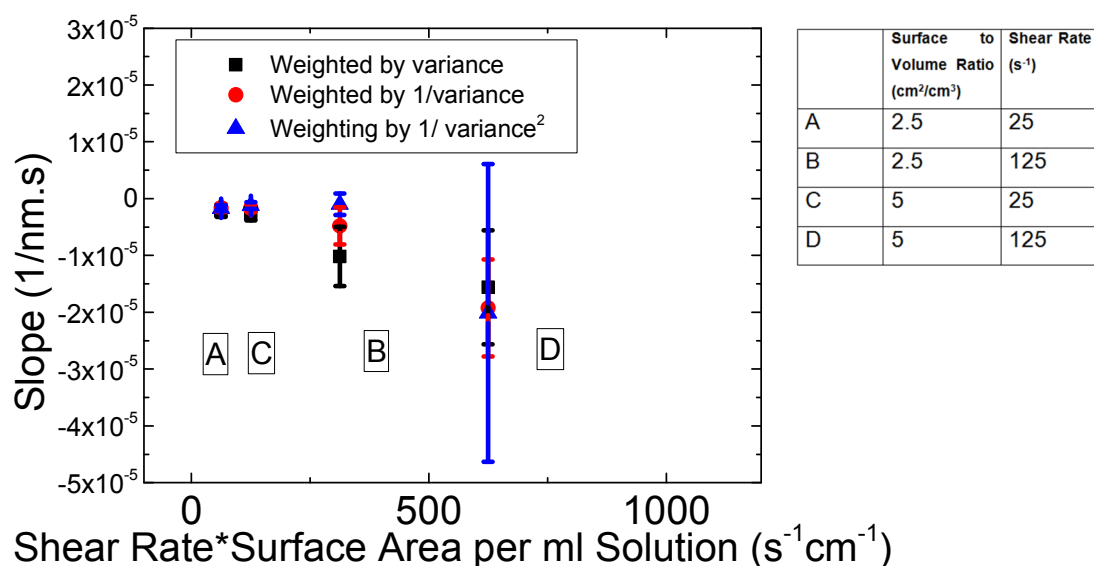
Figure 6. 32
Slopes found from the weighted least squares analysis of the reciprocal of the average hydrodynamic radius values plotted as a function of shear duration. The error bars represent 95% confidence.

6.4.3.5 Summary of Findings from Cumulant Analysis of Each Measured Autocorrelation Function

The various methods of analysis outlined (basic linear regression, Monte Carlo simulations and weighted least squares regression) suggested that increasing the duration of applied shear resulted in an increase in average cluster size. This method of doing cumulant fits to every measured autocorrelation function showed that the trend was significant, unlike the method of fitting a single function to the entire data set for a given set of conditions (see Section 6.4.2). This was because the method used here removed outlier data, which would have influenced the results in Section 6.4.2 making it difficult find reliable trends.

6.4.4 Summary of Statistical Evaluations of Cumulant Analysis Results

Due to data noise, various analyses were carried out to show that the trend of increasing average hydrodynamic radius with increasing duration of applied shear was statistically significant. Every average hydrodynamic radius value had an associated cumulant fitting error, so this had to be considered. The most convincing

analyses were done using a Monte Carlo method and weighted least squares fitting as these allowed the fitting errors to be taken into consideration. Cumulant fitting each measured correlation function proved to be notably more effective than fitting a single function to the entire set of correlation functions measured for a given set of conditions. This was because the former allowed outlier measurements to be identified, while the latter did not.

When outliers were removed, for the analyses based on plots of the average hydrodynamic radius as a function of the duration of applied shear, slopes remained positive within their entire 95% confidence interval. When these analyses were based on plots of the reciprocal of the average hydrodynamic radius as a function of the duration of applied shear, slopes remained negative within their entire 95% confidence interval. These findings indicated that the average size of nanodroplets in solution increased with the duration of applied shear. The trends also suggested that the product of shear rate and surface area that solution was exposed to was important for nucleation, in agreement with the induction time results in Chapter 5.

6.5 CONTIN Analysis Summary

As mentioned, the decays of the correlation functions did not represent entirely monodisperse samples and showed slight deviations from a single exponential decay. The deviation from a single exponential decay appeared to be greater for sheared solutions. To gain a better insight into the size distribution of particles in the solutions, the CONTIN method was used. The intensity-weighted size distributions were obtained and these were also converted to number weighted distributions (see Section 6.1.4.2).

Here a summary of the main findings from performing CONTIN analyses on the data are given. More details on the CONTIN analyses performed are given in the appendix. Due to noise in the measured data, the CONTIN fits were extremely sensitive to which points were used in the analyses. Also, the width of intensity distribution peaks tend to be overestimated by CONTIN analyses of DLS measurements and this can be magnified in the transformation to number based distributions[14]. Graphs and trends shown are therefore suggestive only.

From visually observing the particle size distributions obtained using CONTIN (intensity weighted and number weighted), shearing appeared to cause the particle size distributions to become broader, particularly in the case of intensity weighted distributions. The number weighted distributions were considerably narrower than the intensity weighted distributions. This would be expected since intensity weighted distributions are biased towards larger particles (scattering is roughly proportional to radius to the 6th power[13]); scattering from a small number of larger particles can mask scattering from a large number of smaller particles. Examples of intensity and number weighted distributions are given in Figure 6. 33 and Figure 6. 34 respectively. Since number weighted PSDs did not show the significant broadening that was observed with intensity weighted PSDs, the number of larger nanodropets that formed was potentially relatively low compared to the smaller nanodroplets.
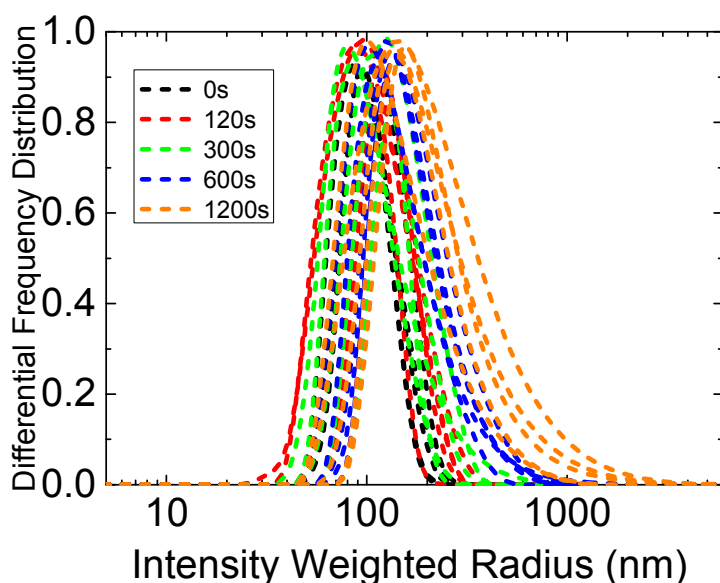

Figure 6. 33
Differential PSDs (intensity weighted) obtained using CONTIN analysis. Obtained from setup A (shear rate of 25 s^{-1} and surface area of 2.5 cm^2 per ml solution) DLS measurements. Normalised between 0 and 1.
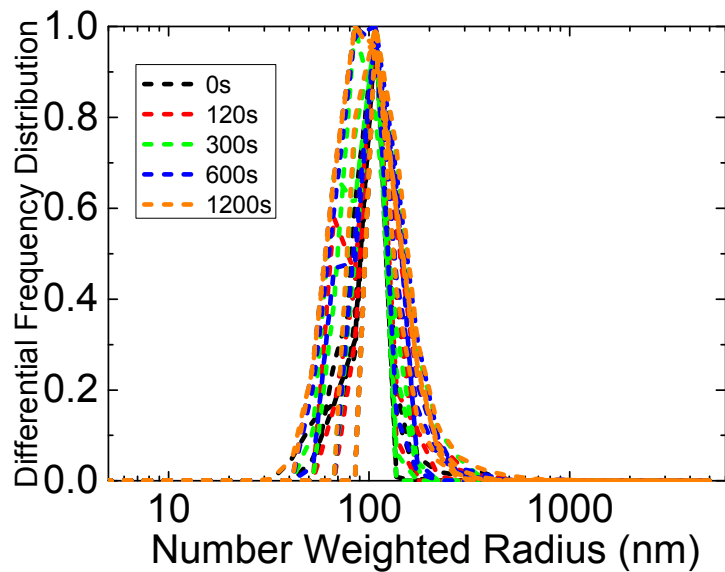
Figure 6. 34
Differential PSDs (number weighted) obtained using CONTIN analysis. Obtained from setup A (shear rate of 25 s^{-1} and surface area of 2.5 cm^2 per ml solution) DLS measurements. Normalised between 0 and 1.

To quantify the broadening of the peaks, the full width at half maximum (FWHM) was found for each distribution (see Appendix). This was chosen over the full width of the distributions since the extremes are more likely to be affected by noise. For intensity weighted distributions, the full width at half maximum consistently increased with the duration of applied shear for each arrangement, which was in agreement with the visual observation of PSDs becoming broader. The number weighted peaks generally increased over time, but by an amount significantly smaller than the intensity weighted PSDs. The choice of shear rate and Couette surface area appeared to be important in the rate of increase in FWHM, as shown in Figure 6. 35.
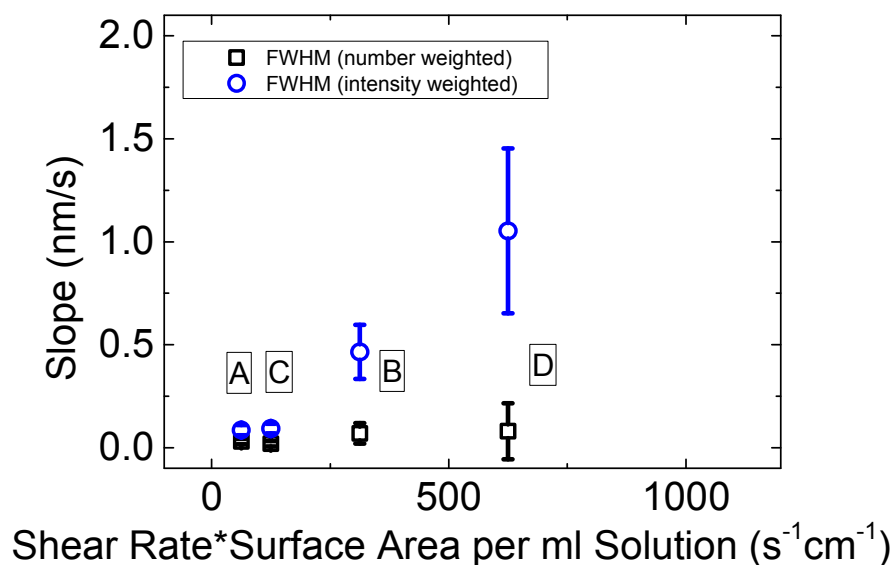
Figure 6. 35
Rate of increase in FWHM as a function of the product of shear rate and surface area (found through bootstrapping). Error bars represent 2 standard deviations.

6.6 Evaluation of Results

The trend of increasing average hydrodynamic radius with increased duration of shear was generally seen through multiple analyses of the measured data here, although it was not the most convincing of trends. Since increased shear rates (and surface areas) led to shorter induction times and hence higher rates of nucleation (Chapter 5), patterns seen in the increase in average hydrodynamic radius with exposure to shear (and surface) from DLS measurements here suggested that there was a link between increased cluster sizes and the onset of nucleation.

6.6.1 Shear Enhanced Coalescence of Clusters

A previous study on glycine nucleation by Jawor-Baczynska et al.[1] (see Chapter 1) proposed that glycine mesoscale clusters (nanodroplets) could be coalesced to give access to a more rapid nucleation pathway. For the more rapid nucleation pathway, it was proposed that productive nucleation of glycine occurred in large glycine-rich nanodroplets above a critical size (nucleation proceeded faster when diameters greater than 750 nm were measured in solution using Brownian microscopy). The presence of these larger nanodroplets was associated with accelerated rates of

crystal formation. The larger droplets were only observed in stirred solutions and they were not observed under quiescent conditions. The larger droplets were thought to form due to the coalescence of the smaller nanodroplets (~250 nm diameter); fluid shear was therefore thought to enhance the aggregation of clusters.

The increase in average hydrodynamic radius observed by shearing the glycine solutions in a Couette cell therefore suggests that the coalescence of nanodroplets may have been occurring in the experiments, and the coalesced nanodroplets may have led to a more rapid nucleation pathway.

As mentioned in Chapter 5 Section 5.7, the aggregation/ coalescence of clusters has been proposed in other recent studies on nucleation. For example, supersaturated solutions of calcium carbonate were found to contain distinct cluster sizes and this was interpreted as nucleation taking place by cluster aggregation[19-21]. The study of butyl paraben undergoing flow in a Couette cell concluded that enhanced cluster aggregation was a plausible outcome for the enhanced nucleation rates seen under flow[22], and a further study on the influence of flow on m-hydroxybenzoic acid was also supportive of the theory of enhanced cluster aggregation[23]. A study on the effect of mixing on mesoscale clusters in DL-valine solutions suggested that mixing resulted in the presence of larger mesoscale clusters than in quiescent solutions, and the presence of larger clusters corresponded to faster nucleation. The larger clusters were thought to form through shear-induced coalescence or surface-assisted coalescence[24].

Exactly why the larger clusters result in enhanced nucleation is unclear. The volume of a larger cluster formed through the coalescence of smaller clusters would be expected to be the sum of the volumes of the smaller clusters from which it was formed. The overall total volume of clusters in solution would therefore not change, so generally, this would not be expected to impact nucleation since JVt_n (see Chapters 4 and 5) would remain unchanged.

The clusters formed through coalescence would have a larger mass than the smaller clusters[1]. The smaller clusters may not contain a sufficient mass of glycine to be able to form stable nuclei which are able to survive and grow in the surrounding bulk solution. The critical cluster size that gives access to the more

rapid nucleation pathway would correspond to the cluster volume that contains enough glycine to form a viable growing crystal in bulk solution. It may be that mesoscale, glycine-rich clusters of all sizes intermittently sample the crystalline phase but smaller ones are not viable in the bulk solution so return to being a cluster or bulk solution[1, 24]. Therefore, the probability of a productive nucleation event occurring in a small cluster would be low, but once a critical cluster volume is reached, the probability of a productive nucleation event occurring would be much higher[24].

6.6.1.1 Film Drainage Description of Coalescence

The film drainage model is a popular description of coalescence[25]. In order for two droplets to coalesce, they must first collide and this traps a thin film of liquid between them. The film of liquid trapped between them must drain away to a critical thickness. The film then ruptures, leading to the formation of a single droplet[25, 26]. Fluid dynamics can have a strong influence on the collision step. In the case of uniform, laminar shear flow, the collision frequency (φ) is proportional to the average shear rate($\dot{\gamma}_{avg}$)[25, 27].

$$\varphi = \frac{4}{3}(r_1 + r_2)^3 \dot{\gamma}_{avg} \qquad \text{(6. 26)}$$

Here r_1 and r_2 are the radii of the droplets to be coalesced.

This direct proportionality between collision frequency and shear rate is interesting as the induction time data in Chapters 4 and 5 indicated that the induction times were inversely proportional to the shear rate applied. The induction times, and hence rate of primary nucleation, may therefore have been a function of the collision frequency of nanodroplets[22].

6.6.1.2 Péclet Number

The Péclet number ($P\acute{e}$) can be defined as:

$$P\acute{e} = \frac{advective\ transport\ rate}{diffusive\ transport\ rate}$$

For the case of mass diffusion by Brownian motion and shear flow, the Péclet number can be written in a form that relates the shear rate of a flow to the particle's diffusion coefficient[28]:

$$Pé = \frac{\dot{\gamma}_{avg}R_h{}^2}{D} = \frac{\dot{\gamma}_{avg}R_h{}^2}{\frac{k_BT}{6\pi\eta R_h}} = \frac{6\pi\eta\dot{\gamma}_{avg}R_h{}^3}{k_BT}$$

<div align="right">(6. 27)</div>

For coalescence to be a possibility, it would be expected that the shear flow would influence the particles i.e. shear flow transport would be of at least a similar magnitude to the Brownian transport i.e. $Pé \geq 1$. To obtain a Péclet number of 1, the length scale required (R_h) to achieve this for the shear rates used in the experiments was calculated. The length scales calculated (Table 6. 4) were similar in size to the clusters found through DLS measurements (~100 nm radius), which verified that the coalescence mechanism proposed was plausible. Shear flow would not be expected to have a significant influence on small molecules or molecular clusters of a few nanometres.

Table 6. 4
Length scales required for $Pé$ close to 1.

Average Shear Rate (s⁻¹)	Length Scale (R_h) for $Pé \approx 1$ (nm)
25	180
250	80

6.6.2 Role of Surface

Since the DLS results suggested that higher shear rates and surface areas resulted in a more rapid rate of increase in average hydrodynamic radius over time, coalescence may have been enhanced by both shear and surface i.e. surface and shear-enhanced coalescence may have been occurring. If surface-enhanced coalescence was occurring, this may account for the patterns seen in the decreasing growth time and increased nucleation rates with increased surface area. With larger surface areas, coalescence occurred more readily and sufficiently large clusters would have formed more readily.

6.6.3 Applicability of Jiang and ter Horst's Model

Jiang and ter Horst's model[29] was based on the assumption of a constant nucleation rate throughout. This may not have been valid for the results here since the presence of larger clusters was associated with the onset of nucleation via a more rapid nucleation pathway[1, 24]. The larger nanodroplets may therefore have resulted in higher primary nucleation rates i.e. the nucleation rate may have actually been a function of cluster size.

Further evidence that the nucleation rate may have been increasing with time came from using the induction time probabilities estimated for each shear rate and surface area geometry (see Chapter 5). The probability of solutions not having nucleated after a particular time $(1 - O(t_i))$ were plotted on log-linear axes and showed that the distributions eventually began to curve downwards, away from ~1. The distributions generally began dropping off more steeply as time increased. This behaviour would be expected if the nucleation rate increased with time[30]. More information of the applicability of Jiang and ter Horst's model to the system studied here is given in Chapter 5 Section 5.7.
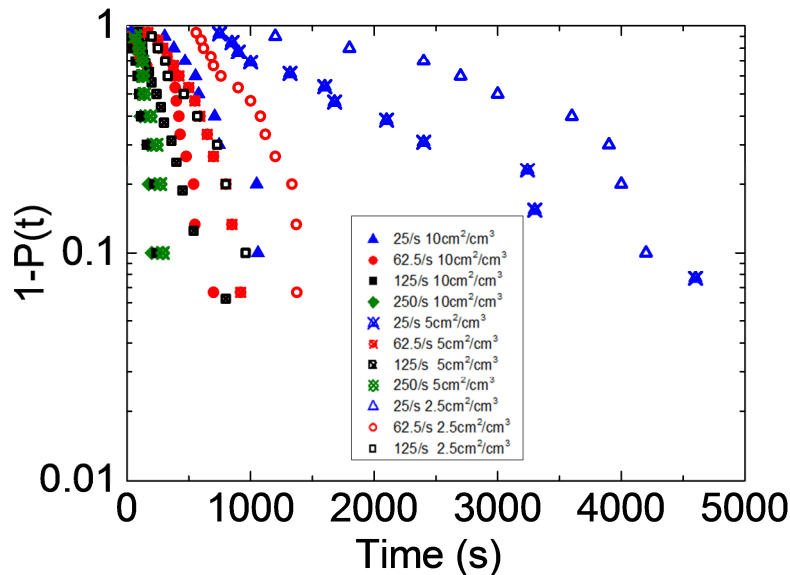

Figure 6. 36
Probability of no nucleation occurring as a function of time for each of the flow conditions studied in Chapter 5.

6.6.4 Further Consideration of Other Studies

For unsheared solutions, measurements made here consistently showed a decay in the autocorrelation function at delay times that indicated the presence of particles with a mean hydrodynamic radius in the region of 100 nm (found using a cumulant analysis). This was similar to sizes reported by Jawor-Baczynska et al[1]. The work by Jawor-Baczynska et al. found that there was a second decay at times less than 0.01 ms, corresponding to sizes in the region of 1 nm. Due to noise in data measured here at shorter delay times, this could not be interpreted from the data measured here.

The studies by Jawor-Baczynska et al. also used nanoparticle tracking analysis (Brownian microscopy) to obtain number concentrations of nanodroplets in solution. Nanoparticle tracking analysis results showed that agitating solutions resulted in a considerably higher concentration of nanodroplets (~10 fold increase). The size distribution of nanodroplets broadened and had a large tail corresponding to the presence of nanodroplets with sizes greater than 150nm radius; these were thought to have formed through the coalescence of smaller nanodroplets.

Since light scattering is sensitive to the presence of particles with larger sizes[2], the presence of coalesced nanodroplets would likely lead to an increase in the average hydrodynamic radius measured. The solutions would also have likely been largely ergodic as the number concentration of nanodroplets (and suspected coalesced ones) was sufficiently high that they would have been spread throughout the solutions[1]. These considerations help to validate the DLS results found here.

6.7 Conclusions

DLS studies were carried out on aqueous glycine solutions that had been sheared in a Couette cell. The trends suggested that shearing resulted in the average size of mesoscale clusters in the solutions to increase with increasing durations of applied shear. A detailed analysis of data was carried out to ensure that the trends were valid.

The rate of increase in cluster size appeared to be a function of the shear rate and surface area that solutions were exposed to. Since increased shear rates and

surface areas also led to shorter induction times and hence higher rates of nucleation (Chapter 5), patterns seen in the increase in cluster size with exposure to shear and surface suggested that there was a link between increased average cluster size and the onset of nucleation.

The findings showed agreement with work by Jawor-Baczynska et al[1]. which found that the onset of nucleation was accompanied with the presence of larger clusters, thought to have formed through the coalescence of smaller ones. Clusters of a critical size were thought to provide a productive nucleation pathway.

Péclet numbers were calculated and suggested that the shear flow would have influenced the mesoscale clusters in the solutions, but not small molecules or small clusters of a few nanometres. The shear and surface enhanced coalescence of clusters was therefore a plausible explanation for the increase in average cluster size observed.

6.8 Summary

- Controlled fluid shear was obtained using a Couette cell.
- Dynamic light scattering hardware was setup to allow measurements to be taken (in-situ) from aqueous glycine solution that had been sheared in the Couette cell.
- Cumulant and CONTIN analyses were performed to the measured data.
- Analyses suggested that the average size of mesoscale clusters in the solutions increased with the application of shear.
- The rate of increase of cluster size increased with increasing shear rates and surface areas. This suggested a link between larger cluster sizes and the onset of nucleation, as increased shear rates and surface areas also led to shorter induction times.
- The clusters may have increased in size due to the coalescence of the smaller clusters.

6.9 References and Nomenclature

6.9.1 References

(1)   Jawor-Baczynska, A.; Sefcik, J.; Moore, B. D., 250 nm Glycine-Rich Nanodroplets Are Formed on Dissolution of Glycine Crystals But Are Too Small To Provide Productive Nucleation Sites. *Crystal Growth & Design* **2013,** 13, (2), 470-478.

(2)   van de Hulst, H. C., *Light Scattering by Small Particles*. 2nd ed.; Dover Publications: New York, 1957.

(3)   Finsy, R., Particle Sizing By Quasi-Elastic Light-Scattering. *Advances in Colloid and Interface Science* **1994,** 52, 79-143.

(4)   Hahn, D. W. *Light Scattering Theory*; Department of Mechanical and Aerospace Engineering: University of Florida, 2009.

(5)   Liou, K., *An Introduction to Atmospheric Radiation*. ed.; Academic Press: 2002.

(6)   Pusey, P., Dynamic Light Scattering. In *Neutron, X-rays and Light. Scattering Methods Applied to Soft Condensed Matter*, P Lindner, T. Z., Ed. Elsevier: 2002.

(7)   Johnson, C; Gabriel, D., *Laser Light Scattering*. ed.; Dover Publications Inc: 1995.

(8)   Atkins, P., *Atkin's Physical Chemistry*. ed.; Oxford University Press: 2002.

(9)   Sorensen, C. M., Light scattering by fractal aggregates: A review. *Aerosol Science and Technology* **2001,** 35, (2), 648-687.

(10)   Pusey, P., Introduction to Scattering Experiments. In *Neutron, X-rays and Light. Scattering Methods Applied to Soft Condensed Matter*, P Lindner, T. Z., Ed. Elsevier: 2002.

(11)   Wyn, B., *Dynamic Light Scattering- The Method and Some Applications*. ed.; Oxford University Press: 1993.

(12)   Provencher, S. W., CONTIN - A General-Purpose Constrained Regularization Program For Inverting Noisy Linear Algebraic And Integral-Equations. *Computer Physics Communications* **1982,** 27, (3), 229-242.

(13)   Chu, B., *Laser Light Scattering- Basic Principles and Practice*. 2nd ed.; Dover Publications: New York, 2007.

(14)   ALV-GmbH, ALV Correlator Software Manual. In ed.; Germany, 2005.

(15)   JelinskaKazimierczuk, M.; Szydlowski, J., Isotope effect on the solubility of amino acids in water. *Journal of Solution Chemistry* **1996,** 25, (12), 1175-1184.

(16)   Mullin, J. W., *Crystallization*. 4th ed.; Heineman: 2002.

(17)   Ku, H. H., Notes On Use Of Propagation Of Error Formulas. *Journal of Research of the National Bureau of Standards Section C-Engineering and Instrumentation* **1966,** C 70, (4), 263-+.

(18)   Jawor-Baczynska, A.; Moore, B. D.; Lee, H. S.; McCormick, A. V.; Sefcik, J., Population and size distribution of solute-rich mesospecies within mesostructured aqueous amino acid solutions. *Faraday Discussions* **2013,** 167, 425-440.

(19)   Gebauer, D.; Voelkel, A.; Coelfen, H., Stable Prenucleation Calcium Carbonate Clusters. *Science* **2008,** 322, (5909), 1819-1822.

(20)   Meldrum, F. C.; Sear, R. P., Materials Science Now You See Them. *Science* **2008,** 322, (5909), 1802-1803.

(21)   Gebauer, D.; Kellermeier, M.; Gale, J. D.; Bergstrom, L.; Colfen, H., Pre-nucleation clusters as solute precursors in crystallisation. *Chemical Society Reviews* **2014,** 43, (7), 2348-2371.

(22)   Liu, J.; Rasmuson, A. C., Influence of Agitation and Fluid Shear on Primary Nucleation in Solution. *Crystal Growth & Design* **2013,** 13, (10), 4385-4394.

(23)   Liu, J.; Svard, M.; Rasmuson, A. C., Influence of Agitation and Fluid Shear on Nucleation of m-Hydroxybenzoic Acid Polymorphs. *Crystal Growth & Design* **2014,** 14, (11), 5521-5531.

(24)   Jawor-Baczynska, A.; Moore, B.; Sefcik, J., Effect of mixing, concentration and temperature on the formation of mesostructured solutions and their role in the nucleation of dl-valine crystals. *Faraday Discussions* **2015**.

(25)   Liao, Y.; Lucas, D., A literature review on mechanisms and models for the coalescence process of fluid particles. *Chemical Engineering Science* **2010,** 65, (10), 2851-2864.

(26)   Al-Mulla, A.; Gupta, R. K., Droplet coalescence in the shear flow of model emulsions. *Rheologica Acta* **2000,** 39, (1), 20-25.

(27)   Friedlander, S. K., *Smoke, dust and haze : fundamentals of aerosol behavior*. ed.; Wiley: Wiley, 1977.

(28)   Wagner, N. J.; Brady, J. F., Shear thickening in colloidal dispersions. *Physics Today* **2009,** 62, (10), 27-32.

(29)   Jiang, S. F.; ter Horst, J. H., Crystal Nucleation Rates from Probability Distributions of Induction Times. *Crystal Growth & Design* **2011,** 11, (1), 256-261.

(30)   Sear, R. P., Quantitative studies of crystal nucleation at constant supersaturation: experimental data and models. *Crystengcomm* **2014,** 16, (29), 6506-6522.

6.9.2 Main Nomenclature

a, b, c, d = coefficients of the polynomial fit

$best$ = best fit value from Matlab

c = concentration

c^* = solubility concentration

c_i = intensity weighted particle size distribution

$c_{i,n}$ = number weighted particle size distribution

CI_{upper} = 95% upper confidence intervals

CI_{lower} = 95% lower confidence intervals

D = diffusion coefficient of particles in solution

D_{lens} = diameter of incident laser beam on lens

d_{spot} = diameter of focussed spot (waist)

E = electric field

f = focal length of lens

$G(\Gamma)$ = decay rate distribution function

G_2 = intensity autocorrelation function

g_1 = normalised electric field autocorrelation function

g_2 = normalised intensity autocorrelation function

g_i^{expt} = experimental data point

g_i^{model} = value predicted by model

I = intensity of scattered light

k_B = Boltzmann constant = 1.38×10^{-23} J/K

L = length scale

M = magnification

n = refractive index of the dispersion medium or number of data points used in the least squares procedure

N_{rand} = random number between 0 and 1

P = form factor

p = probability density function

q = scattering vector

R_h = average hydrodynamic radius

R_i = particle radius

r_1, r_2 = radii of the droplets to be coalesced

S = supersaturation

S_i = distance from lens to image

S_o = distance from object to lens

T = temperature (absolute)

T_{obs} = total observation time

t= time

w_i = weighting of point i

x = randomly generated average hydrodynamic radius value

y_i= size of image or experimental data point i (reciprocal of average hydrodynamic radius value)

$y_{i,f}$= fitted value for point i

y_o= size of object

z= power used to make error bars symmetrical

β= coherence/ experimental factor

Γ= decay rate of $g_1(\tau)$

λ= wavelength of incident/ scattered beam in a vacuum

μ= mean value (taken as best fit from non-linear regression)

$\dot{\gamma}_{avg}$= average shear rate

θ= scattering angle

σ = standard deviation

σ_i= standard deviation of the transformed data

τ = delay time

φ= collision frequency

7. Effect of pH and Addition of Sodium Chloride on Mesoscale Clusters in Glycine Solution

Chapter Outline and Contents

In Chapter 6 (and in agreement with previous studies[1, 2]), it was shown that liquid like, glycine rich, mesoscale clusters (nanodroplets) exist in aqueous glycine solutions and these are thought to play a role in the nucleation mechanism. It is known that altering the pH of glycine solutions[3, 4] has a strong effect on glycine speciation and polymorphic outcome, so to improve our understanding of glycine nanodroplets, the effect of pH on nanodroplets in glycine solutions was investigated using dynamic light scattering measurements. The effect of the addition of sodium chloride on glycine nanodroplets was similarly investigated, since sodium chloride is known to influence polymorph formation[5] and clustering in solution[6].

The results suggested that the use of pH values away from neutral conditions (close to the isoelectric point) resulted in a decrease in the concentration of the nanodroplets in glycine solutions. The decrease of nanodroplet concentration appeared to correlate with the presence of more significant fractions of anions or cations, according to speciation models. It is therefore possible that the charged glycine ions reduced the formation of the glycine nanodroplets. Since γ-glycine formation is also associated with pH conditions where the nanodroplet population was lower, the nanodroplets may potentially be linked to the nucleation of α-glycine or γ-glycine.

The addition of sodium chloride to aqueous glycine solutions resulted in a decrease in the concentration of the glycine nanodroplets. The reduction could potentially have been a result of sodium chloride contributing to an ionic atmosphere, resulting in the charging of glycine molecules and reducing the likelihood of clusters forming. The addition of sodium chloride is well known to affect the polymorphic outcome, and there were strong similarities between the sodium chloride concentration that

was found to result in immeasurable levels of nanodroplets, and the sodium chloride concentrations found to result in the nucleation of γ-glycine (rather than α- glycine) from literature[5].

The results obtained by investigating the effect of pH and addition of sodium chloride on mesoscale clusters therefore indicated that pH and the presence of sodium chloride may influence the arrangement of molecules in solution, and the concentration of mesoscale clusters in the solutions may be linked to glycine polymorphism. The results also suggested that clusters did not form through standard Coulomb interactions.

This chapter covers:

- The experimental procedures carried out to investigate the effect of pH and the addition of sodium chloride on glycine solution behaviour.
- Experimental results on the effect of pH on glycine solution behaviour.
- Experimental results on the effect of the addition of sodium chloride on glycine solution behaviour.
- Possible explanations for the results obtained.

7.1 Influence of pH on Mesoscale Clustering in Aqueous Glycine Solutions

pH has a strong effect on glycine speciation and polymorph formation, so to try and gain an improved understanding of the mesoscale clusters (nanodroplets) that were found to exist in aqueous glycine solutions, a wide range of experiments were carried out to investigate the effect that pH had on glycine nanodroplets.

7.1.1 Experimental Methodology and Procedures

For the experiments carried out, two glycine concentrations were used- 110 g of glycine per litre of solvent or 220 g of glycine per litre of solvent. Each experiment was done on a basis of 2.2 g glycine being dissolved in either 20 ml or 10 ml solvent. (1 ml $\approx$ 1 g for the solvents over the conditions studied). Calculations were carried out to ascertain the composition of the solvent required to produce a glycine solution of a desired pH value i.e. the volume of 1M HCl, 1M NaOH, 2M NaOH or deionised water required. The solvent compositions used are given in Table 7. 1 and Table 7. 2. The calculations are described in Section 7.1.2.

Each solution was prepared in plastic containers and sealed. They were well shaken and incubated at 55°C for 3 hours to ensure that the glycine was fully dissolved. At least 5 solutions of each outlined in Table 7. 1 and Table 7. 2 were prepared and 2 samples were taken from each solution. Samples of solution were filtered using preheated 0.2 µm SFCA disposable syringe filters into preheated disposable glass tubes, which were then left to cool in surrounding air (23°C) for 15 minutes. Samples were then placed in a commercial DLS instrument (ALV/LSE-5004) and were left for 5 minutes to equilibrate to 25°C. A thermocouple was used to ensure the cooling times were valid as temperature fluctuations can cause drift in the scattering intensities measured using dynamic light scattering. Dynamic light scattering measurements at 90° were then taken from each sample. At least 10 measurements, each lasting 10 seconds, were taken from each sample.

The pH of the solutions was checked (at the start and the end of an experiment) using a Jenway 3510 pH meter and glass electrode (924 050) and the actual values measured were used in subsequent plots.

Table 7. 1
Compositions of the 20 ml solvent that was used in experiments to investigate the effect of pH on mesoscale clustering in glycine solutions.

pH	Volume of Water (ml)	Volume of 1M HCl (ml)	Volume of 1M NaOH (ml)	Volume Fraction of Water
~2	0	20.00	0	0
3	14.76	5.24	0	0.738
4	19.38	0.62	0	0.969
4.5	19.80	0.20	0	0.990
5	19.94	0.06	0	0.997
~6	20	0	0	1
7	19.93	0	0.07	0.997
8	19.29	0	0.71	0.965
9	14.14	0	5.86	0.707
~10	0	0	20.00	0
>12	0	20ml 2M NaOH		0

Table 7. 2
Compositions of the 10 ml solvent that was used in experiments to investigate the effect of pH on mesoscale clustering in glycine solutions.

pH	Volume of Water (ml)	Volume of 1M HCl (ml)	Volume of 1M NaOH (ml)	Volume Fraction of Water
~2.6	0	10.00	0	0
3	4.76	5.24	0	0.476
4	9.38	0.62	0	0.938
4.5	9.80	0.20	0	0.98
5	9.94	0.06	0	0.94
~6	10.00	0	0	1
7	9.93	0	0.07	0.993
8	9.29	0	0.71	0.929
9	4.14	0	5.86	0.414
~9.6	0	0	10.00	0
10	0	10ml 2M NaOH		0

7.1.2 Calculation of Solvent Composition

From the mass of glycine added to the solvent and the molecular weight of glycine, the total moles of glycine in the solutions ($moles_{glycine}$) could be calculated. For a particular pH value, the mole fraction of glycine that would exist in anion/ cation/ zwitterion form (see Chapter 1 Section 1.5) could be calculated using the Henderson Hasselbalch equation and pKa values[7].

The Henderson Hasselbalch equation is given in Eqn. (7. 1).

$$\text{pH} = \text{pK}_a + \log\left(\frac{[\text{conjugate base (proton acceptor} = \text{ unprotonated form)}]}{[\text{conjugate acid (proton donator} = \text{protonated form)}]}\right) \quad \textbf{(7. 1)}$$

The isoelectric point (pH at which a molecule carries no net electrical charge), could be found from:

$$\text{pI} = \frac{\text{pK}_{a1} + \text{pK}_{a2}}{2} \qquad \textbf{(7. 2)}$$

With glycine, for pH less than pI:

$$\text{pH} = \text{pK}_{a1} + \log\left(\frac{[\text{zwitterion}]}{[\text{cation}]}\right) \qquad \textbf{(7. 3)}$$

The mole fraction of glycine cations (x_{cation}) could be calculated by rearranging Eqn. (7. 3):

$$x_{cation} = \frac{1}{1 + 10^{(\text{pH} - \text{pK}_{a1})}} \qquad \textbf{(7. 4)}$$

With glycine, for pH greater than pI:

$$\text{pH} = \text{pK}_{a2} + \log\left(\frac{[\text{anion}]}{[\text{zwitterion}]}\right) \qquad \textbf{(7. 5)}$$

The mole fraction of glycine anions (x_{anion}) could be calculated by rearranging Eqn. (7. 5):

$$x_{anion} = \frac{10^{(\text{pH} - \text{pK}_{a2})}}{1 + 10^{(\text{pH} - \text{pK}_{a2})}} \qquad \textbf{(7. 6)}$$

The number of moles of ionised species (anion/ cation) ($moles_{ions}$) could be calculated using the total moles of glycine in the solution ($moles_{glycine}$) and the mole fraction that would be ionised at a particular pH value (x_{ion}):

$$moles_{ions} = x_{ion} \times moles_{glycine} \qquad \textbf{(7. 7)}$$

Here x_{ion} is the mole fraction of glycine that would form anions or cations, depending on pH i.e. x_{anion} or x_{cation}.

The moles of glycine ions ($moles_{ions}$) would be equal to the moles of hydrogen/ hydroxide ions to be added to the samples to obtain solutions of a desired pH.

1M HCl and 1M NaOH or 2M NaOH (strong acid and strong base) were used to provide hydrogen/ hydroxide ions respectively. The volume of acid/ alkali ($V_{acid\ or\ alkali}$) required to provide sufficient hydrogen/ hydroxide ions was calculated from:

$$V_{acid\ or\ alkali} = \frac{moles_{ions}}{M} \qquad \textbf{(7. 8)}$$

Here M is the molarity of acid/ alkali.

The volume of water (V_{water}) required could be calculated using the calculated volume of acid or alkali and the total solution volume (V_{total}):

$$V_{water} = V_{total} - V_{acid\ or\ alkali} \qquad \textbf{(7. 9)}$$

7.1.3 Experimental Results

When glycine nanodroplets were present in the solutions, the overall autocorrelation function decays appeared to be bimodal with an initial decay at shorter delay times which corresponded to small molecular clusters, smaller than one nanometre and a second decay at longer delay times due to the presence of glycine nanodroplets[1].

Three main analyses of the results were carried out for each glycine concentration: visual inspection of the autocorrelation functions (Figure 7. 1 and Figure 7. 2); a cumulant analysis of the nanodroplet decay in the autocorrelation functions to obtain average hydrodynamic radii (Figure 7. 3 and Figure 7. 4); and calculating the average intensity of light that was scattered during each measurement (Figure 7. 6 and Figure 7. 7).
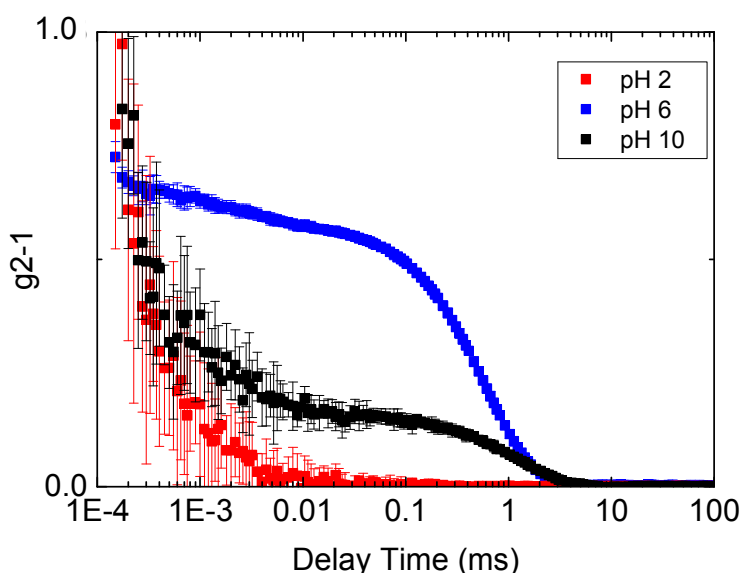
Figure 7. 1
Examples of autocorrelation functions obtained for different pH values for a glycine concentration of 110 g glycine per kg solvent. The functions are the average of the 10+ measurements taken of a sample and the error bars represent the standard deviation of the measurements taken of the sample.
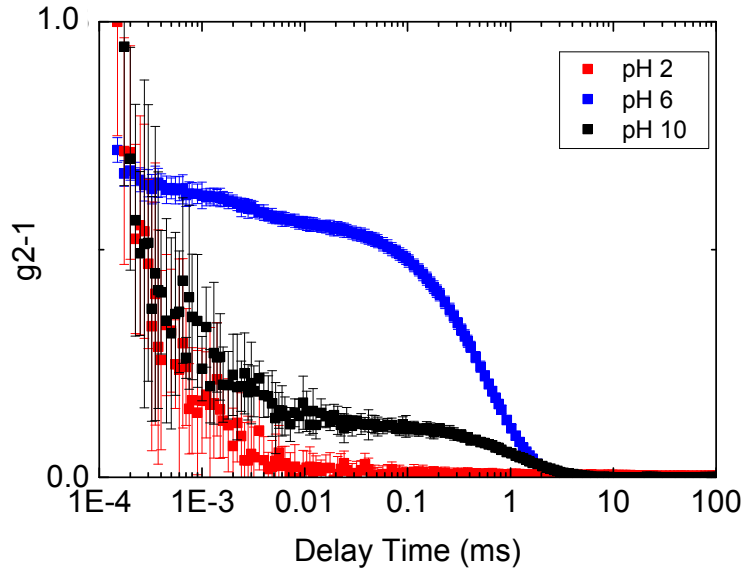
Figure 7. 2
Examples of autocorrelation functions obtained for different pH values for a glycine concentration of 220 g glycine per kg solvent. The functions are the average of the 10+ measurements taken of a sample and the error bars represent the standard deviation of the measurements taken of the sample.
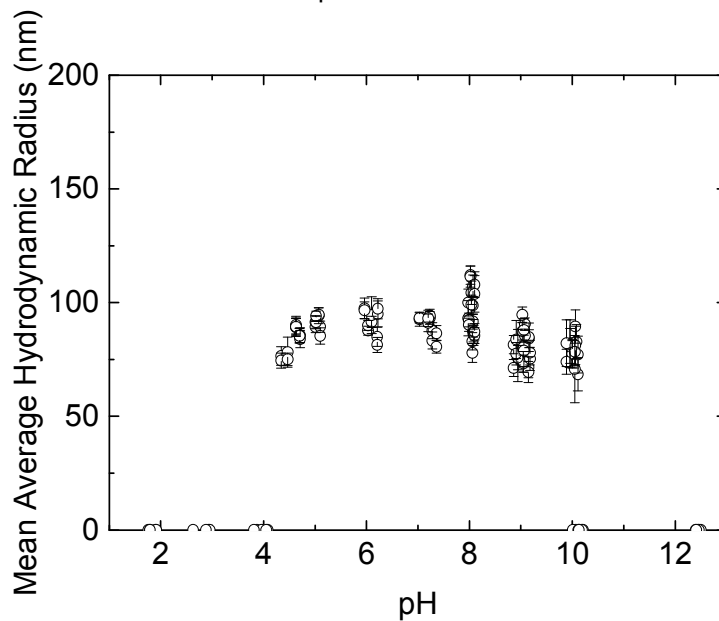
Figure 7. 3
Mean average hydrodynamic radii calculated for the various pH values for a glycine concentration of 110 g glycine per kg solvent. The values represent the average of the 10+ measurements that were taken from each sample and the error bars represent the standard deviation. When the function could not be fitted, a mean hydrodynamic radius of zero was plotted for reference.
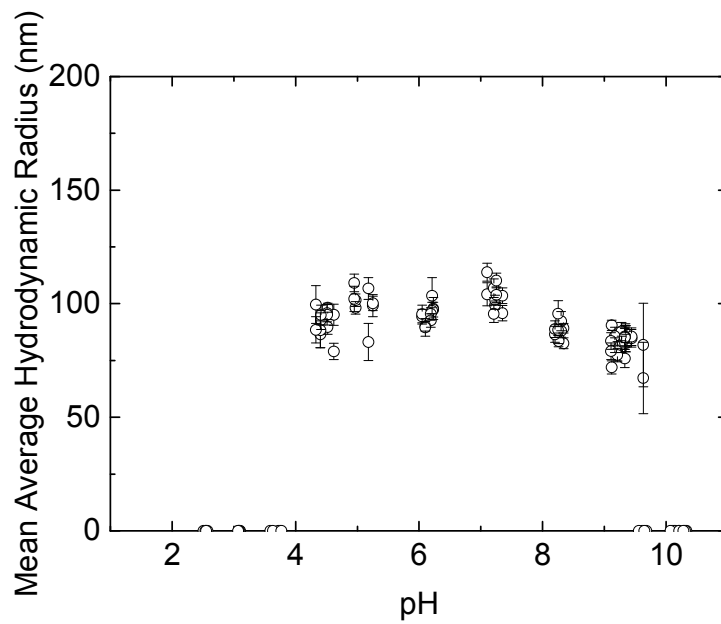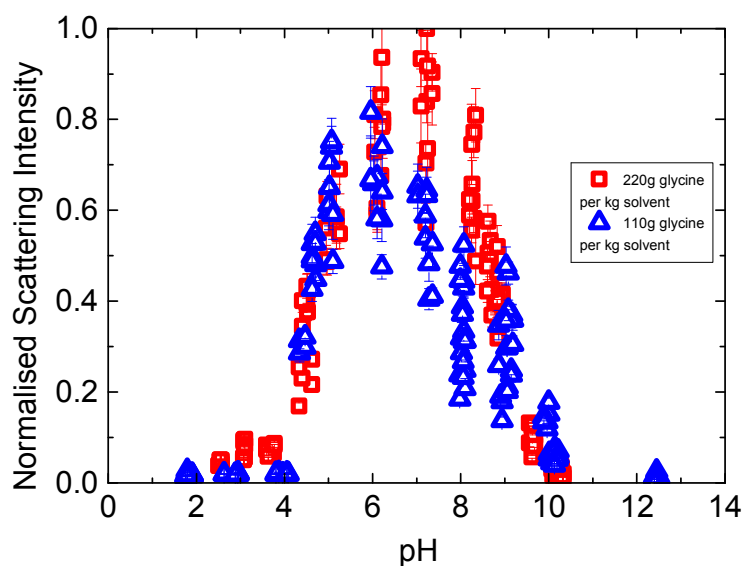
Figure 7. 4
Mean average hydrodynamic radii calculated for the various pH values for a glycine concentration of 220 g glycine per kg solvent. The values represent the average of the 10+ measurements that were taken from each sample and the error bars represent the standard deviation. When the function could not be fitted, a mean hydrodynamic radius of zero was plotted for reference.
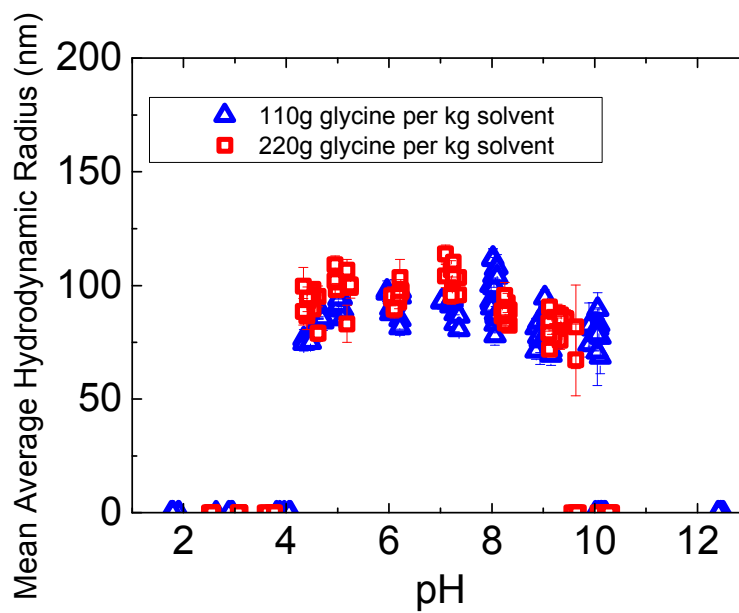
Figure 7. 5
Comparison of the mean average hydrodynamic radii calculated for the various pH values for each glycine concentration studied.
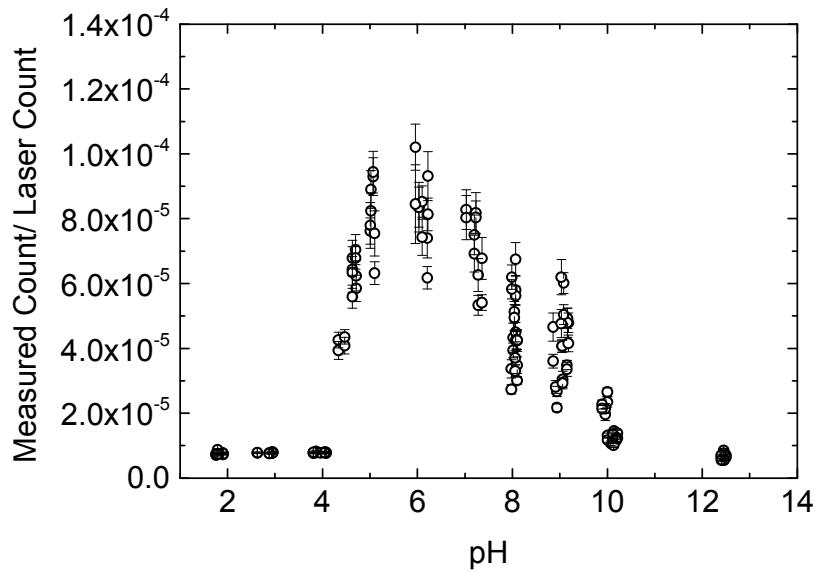
Figure 7. 6
Mean intensity of scattered light measured for the various pH values used values for a glycine concentration of 110 g glycine per kg solvent. The values represent the mean of the mean intensity measured for each of the 10+ measurements that were taken from each sample. The error bars represent the standard deviation.
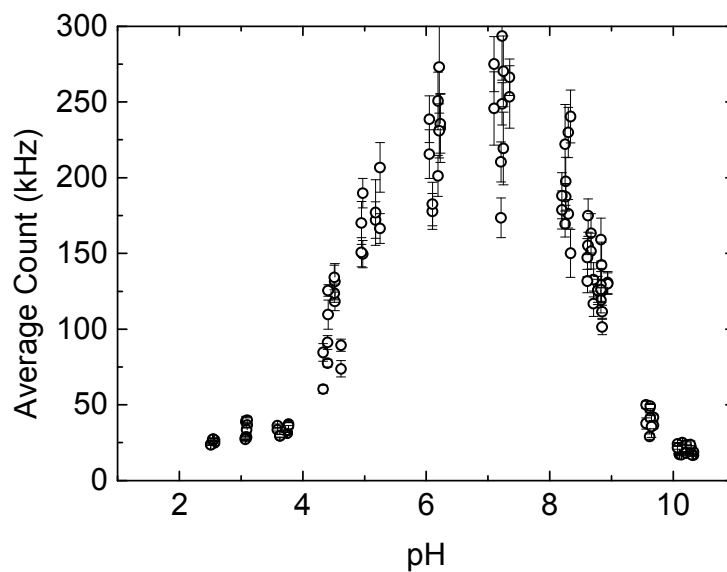
Figure 7. 7
Mean intensity of scattered light measured for the various pH values used values for a glycine concentration of 220 g glycine per kg solvent. The values represent the mean of the mean intensity measured for each of the 10+ measurements that were taken from each sample. The error bars represent the standard deviation.

Figure 7. 8
Comparison of the mean intensity of scattered light measured for the various pH values used
values for each glycine concentration.

Altering the pH of glycine solutions had a strong impact on the DLS measurements. pH had an influence on the prominence (y-intercept) of the decays of the autocorrelation functions due to glycine nanodroplets. For example, in aqueous solutions, strong decays with large y-intercepts were measured (corresponding to radii in the region of 100 nm) however, when more extreme pH values were used, the decays became significantly less prominent with lower intercepts. This is shown in Figure 7. 1 and Figure 7. 2. For both of these glycine concentrations, pH values less than 4 resulted in very weak or immeasurable nanodroplet decays. pH values greater than 9 also resulted in less prominent decays.

These observations are reflected in the measurements of the mean intensity of light scattered by the solutions (Figure 7. 6 and Figure 7. 7). The measurements showed that when the pH of the solutions was between ~5 and ~8, high intensities of scattered light were measured, while the use of more extreme pH values resulted in lower intensities of scattered light, particularly for pH less than 4 and greater than 9. The mean average hydrodynamic radii found by doing a cumulant analysis of the main decays (fitted across delay times between 0.03 ms and 0.7 ms for all) are given in Figure 7. 3 and Figure 7. 4 and show that the average hydrodynamic radius appeared to remain relatively constant across all pH values where autocorrelation

functions could be fitted (see Figure 7. 5). Since the sizes of the nanodroplets appeared to remain relatively constant, the average intensities of scattered light were indicative of the number concentration of glycine nanodroplets. This therefore suggested that pH had a strong influence on the number concentration of glycine nanodroplets in the solutions. When functions could not be fitted using the cumulant method employed (negative values or error was greater than 33% of the mean average hydrodynamic radius), a mean average hydrodynamic radius of zero was plotted; the mean hydrodynamic was immeasurable and would not actually have been zero but this was just for reference.

It should be noted that the average hydrodynamic radii will have a degree of uncertainty due to the values used for the viscosities of the glycine solutions at a particular pH value (η_{pH}). These were approximated by scaling the viscosity of glycine dissolved in water ($\eta_{aqueous\ glycine\ solution}$), which was found from rheology measurements or literature[8] (see Table 7.3), by the viscosity of the solvent used to obtain a particular pH value ($\eta_{solvent}$) relative to the viscosity of pure water (η_{water}).

$$\eta_{pH} = \eta_{aqueous\ glycine\ solution} \frac{\eta_{solvent}}{\eta_{water}} \qquad \textbf{(7. 10)}$$

The viscosity of the solvent was approximated from the viscosity of pure water (η_{water}) and the viscosity of the acid/ alkali solution used ($\eta_{\text{HCl or NaOH}}$).

$$\eta_{solvent} = x_{water}\eta_{water} + (1 - x_{water})\eta_{\text{HCl or NaOH}} \qquad \textbf{(7. 11)}$$

Here x_{water} is the water volume fraction of solvent.

Table 7. 3
Viscosities of aqueous glycine solutions, measured by PhD students Claire Forsyth and Alexander Hope using a parallel plate rotational rheometer (TA Discovery HR-2), or obtained from literature[8].

Glycine Concentrations (g glycine per kg water)	Viscosity of Solution at 25°C (Pa.s)
110	0.0011 (rheology)
220	0.0013 (literature)

To check whether the behaviour seen was dependent on the concentration of glycine in the solutions (and level of saturation since pH has an effect on solubility[4]), two glycine concentrations were studied. The patterns in behaviour were seen across both concentrations (Figure 7. 8). The concentration of glycine is thought to affect the formation of nanodroplets e.g. at low supersaturation (<0.2) fewer nanodroplets were observed using Brownian microscopy[2]. The range of glycine concentrations studied here meant that lower and higher levels of supersaturation were covered for each solvent (as low as 0.3 when glycine was dissolved in 1M HCl). Since trends were consistent for both concentrations used, this showed that when measurements suggested that no (or very few) nanodroplets formed, this was not due to a low concentration of glycine and was instead due to the effect of pH.

7.1.4 Consideration of Results
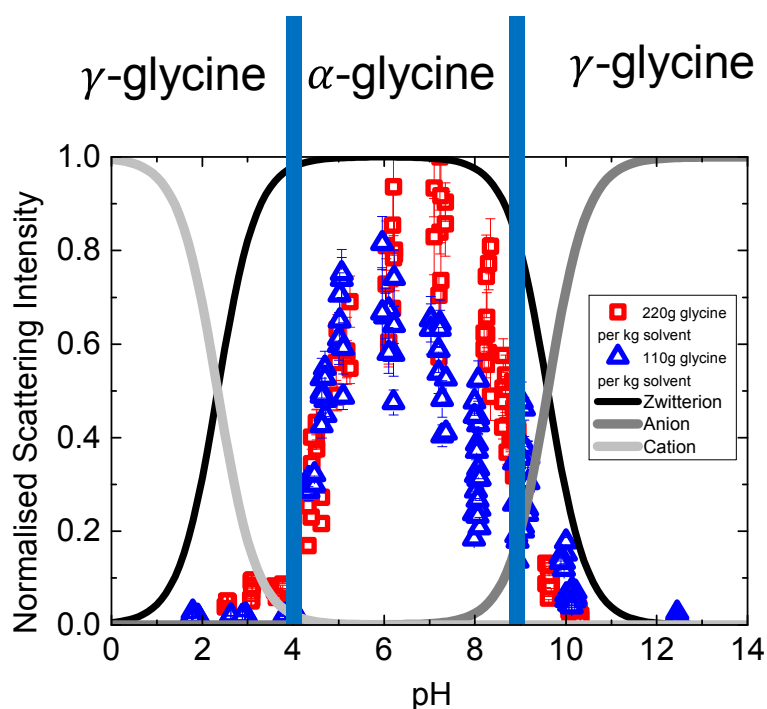
Figure 7. 9
Mean intensity of scattered light measured for the various pH values for each glycine concentration, normalised between 0 and 1. The lines divide the graph into regions where the α and γ polymorphs would be expected to form. Speciation (see Chapter 1 Section 1.5) is also shown.

It is well known that glycine speciation is strongly influenced by the pH of solutions. A plot of the mean scattering intensity measured as a function of pH (with intensities normalised between 0 and 1) and glycine speciation is given in Figure 7. 9. It showed that scattered light intensities generally started to decrease when anions and cations started forming in more significant quantities. This suggested that the number concentration of nanodroplets decreased when the fraction of glycine forming anions and cations increased.

As mentioned in Chapter 1 Section 1.5.2, glycine speciation is thought to have a profound effect on the arrangement of glycine molecules in the solutions, for example, in more neutral conditions, glycine is thought to form a large number of cyclic dimers[9] (α- glycine growth units), while at more extreme pH values, the glycine cations or anions were speculated to induce glycine to form head-to-tail open chains (γ- glycine growth units) and undermine the formation of cyclic dimers[4]. The previous study of glycine nanodroplets suggested that nucleation occurred in glycine nanodroplets[1]. Since literature generally indicates that cyclic dimers are the building blocks for α-glycine, nanodroplets could potentially be largely self-associations of cyclic dimers.

Han et al. speculate that the presence of glycine anions and cations can help explain the presence of liquid-like glycine clusters in solution (see Chapter 1 Section 1.5). The glycine ions were thought to interact strongly with glycine zwitterions to form charged dimers, and a charged dimer may then interact with several other zwitterions through strong ion-dipole interactions, leading to the formation of a higher n-mer. Han et al. postulated that this would be particularly likely when the concentration of anions or cations was low, since one ion would be surrounded by many zwitterions and would interact with them readily. When the concentration of anions/ cations was higher, there would be fewer zwitterions so the interaction would be less likely. This would weaken the effectiveness of the formation of liquid-like glycine clusters[4]. Han et al.'s concept of the presence of liquid-like glycine clusters being less prominent at more extreme pH values matched the results found here, which showed that lower number concentrations of glycine rich liquid-like nanodroplets occurred at pH values where the speciation suggested that the fraction of anions or cations became more significant.

For the pH values where scattering intensities were measured to be high in the experiments, only a very small fraction of glycine would have formed ions; therefore it was unclear whether there would have been a sufficient number of ions to result in the production of enough nanodroplets to result in the scattering observed. A previous study of glycine nanodroplets[1] estimated that they only contained a mole fraction of around 10^{-6} of the total glycine solute. A higher mole fraction than this would have formed ions according to the speciation for the pH values measured in the experiments, suggesting that there would have been plentiful ions to initiate the formation of clusters. Therefore, it remained possible that the presence of low quantities of anions and cations had a role in the formation of the glycine nanodroplets. The mechanism proposed by Han et al., however, may not explain the sizes of the clusters seen here.

Glycine speciation is thought to play a role in the formation of polymorphs[3, 4], which is detailed in Chapter 1 Section 1.5. As mentioned in Chapter 1 Section 1.5, at low and high pH values (pH < 3.8 and pH > 8.9), the γ polymorph of glycine forms in solution[3], while at intermediate pH values, α-glycine would be expected to form. The experiments here suggested that the nanodroplet population was notably lower (as evidenced by lower scattering intensities) under conditions where γ- glycine would form from solutions, had the solutions been supersaturated, compared to conditions where α-glycine would be expected to form. This is illustrated in Figure 7. 9, which shows the mean scattering intensities measured as a function of pH for each glycine concentration (normalised between 0 and 1), and also shows the regions where the α and γ polymorphs would be expected to form. The trends observed in the undersaturated solutions are expected to be similarly observed in supersaturated solutions[2], with preliminary data (unpublished) confirming this. These findings therefore suggest that there may be a link between the concentration of nanodroplets in the solutions and the formation of α- glycine and γ- glycine.

7.2 Influence of the Presence of Sodium Chloride on Mesoscale Clustering in Aqueous Glycine Solutions

In order to gain further understanding on the glycine nanodroplets, the effect of the addition of sodium chloride (NaCl) to aqueous glycine solutions was studied. NaCl was chosen since it is well known that sufficiently high concentrations of NaCl can be used to induce γ-glycine formation[5, 10] and it can affect clustering behaviour[6].

7.2.1 Experimental Methodology and Procedure

To ascertain the effect of the addition of sodium chloride on mesoscale clustering in glycine solutions, a set of experiments was carried out whereby various masses of NaCl were added to fixed volumes of aqueous glycine solution. Aqueous glycine solutions were prepared with 3 different concentrations (55 g glycine per kg water, 110 g glycine per kg water and 220 g glycine per kg water). Details of the solutions prepared are given in Table 7. 4.

Each solution was well shaken and left incubated at 55°C for 3 hours to ensure that the sodium chloride was fully dissolved. At least 5 solutions of each outlined in Table 7. 4 were prepared and 2 samples were taken from each solution. Samples of solution were then filtered using preheated 0.2 μm SFCA disposable syringe filters into preheated disposable glass tubes, which were then left to cool in surrounding air (23°C) for 15 minutes. Samples were then placed in a commercial DLS instrument (ALV/LSE-5004) and were left for 5 minutes to equilibrate to 25°C. A thermocouple was used to check that the cooling times were valid. Dynamic light scattering measurements at 90° were then taken from each sample. At least 10 measurements were taken for each sample and each measurement lasted for 10 seconds.

The pH of the solutions was checked (at the start and the end of an experiment) using a Jenway 3510 pH meter and glass electrode (924 050) and the values were not found to be influenced by the addition of NaCl i.e. pH values remained similar to aqueous glycine solution.

Table 7. 4

Details of the solutions that were used in experiments to investigate the effect of the addition of NaCl on glycine nanodroplets.

Concentrations of aqueous glycine solutions used (g glycine per kg water)	Mass of NaCl added to 10ml aqueous glycine solution (g)	Concentration of NaCl (g NaCl/l aqueous glycine solution)
55, 110, 220	0	0
55, 110, 220	0.1	10
55, 110, 220	0.3	30
55, 110, 220	0.6	60
55, 110, 220	1.0	100
55, 110, 220	1.5	150
55, 110, 220	2.0	200
55, 110, 220	3.0	300

7.2.2 Experimental Results

As with pH measurements, 3 main analyses of the results were carried out: visual inspection of the autocorrelation functions (Figure 7. 10 to Figure 7. 12); a cumulant analysis of the decay in the autocorrelation functions due to nanodroplets to obtain average hydrodynamic radii (Figure 7. 13 to Figure 7. 15); and calculating the average intensity of light that was scattered during each measurement (Figure 7. 17 to Figure 7. 19).
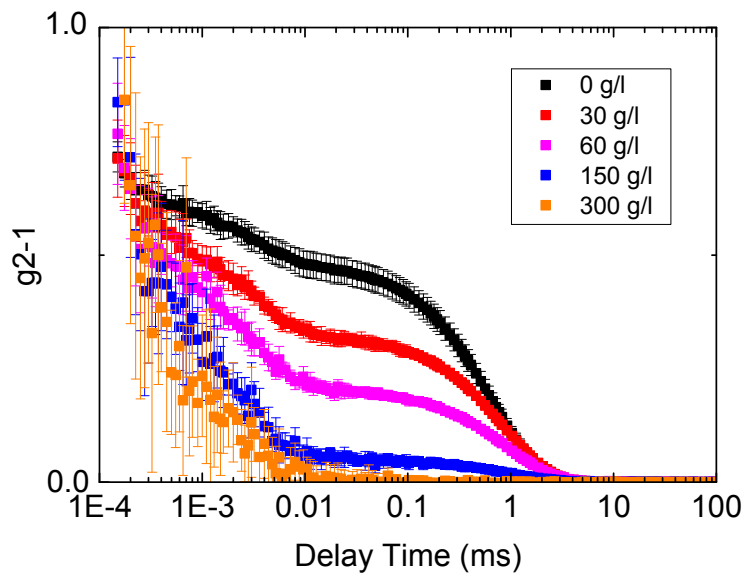
Figure 7. 10
Examples of autocorrelation functions obtained from experiments where known masses of NaCl were added to aqueous glycine solution with a concentration of 220 g glycine per kg water. The functions represent the average of the 10+ measurements that were taken from a sample and the error bars represent the standard deviation.
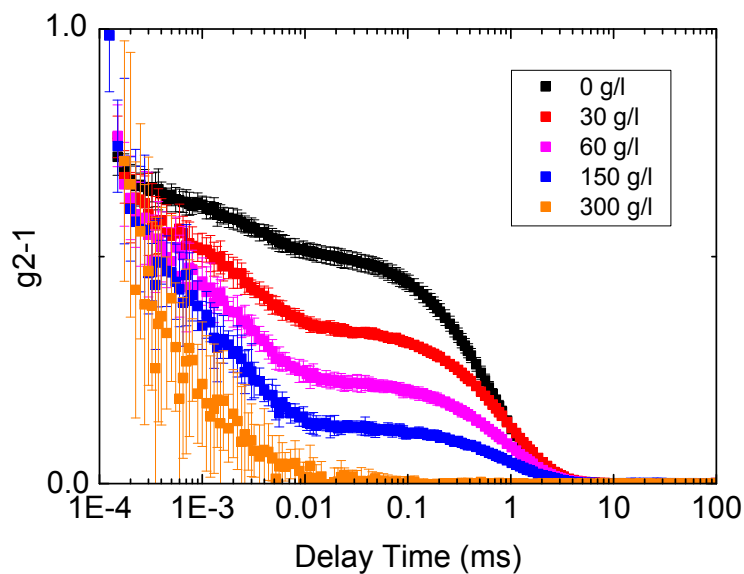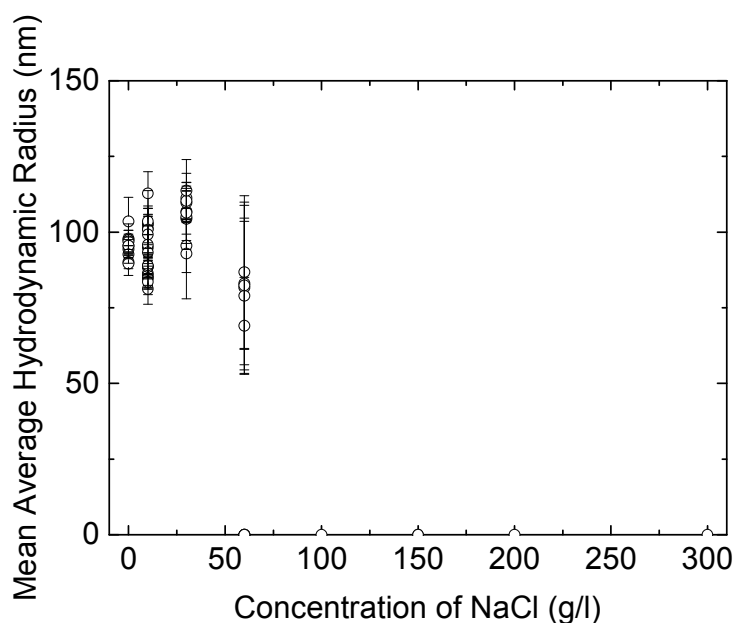

Figure 7. 11
Examples of autocorrelation functions obtained from experiments where known masses of NaCl were added to aqueous glycine solution with a concentration of 110 g glycine per kg water. The functions represent the average of the 10+ measurements that were taken from a sample and the error bars represent the standard deviation.
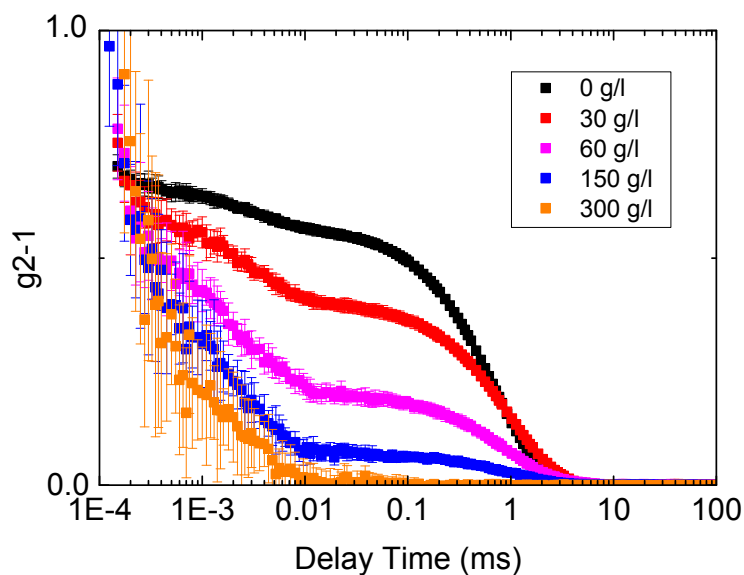
Figure 7. 12
Examples of autocorrelation functions obtained from experiments where known masses of NaCl were added to aqueous glycine solution with a concentration of 55 g glycine per kg water. The functions represent the average of the 10+ measurements that were taken from a sample and the error bars represent the standard deviation.
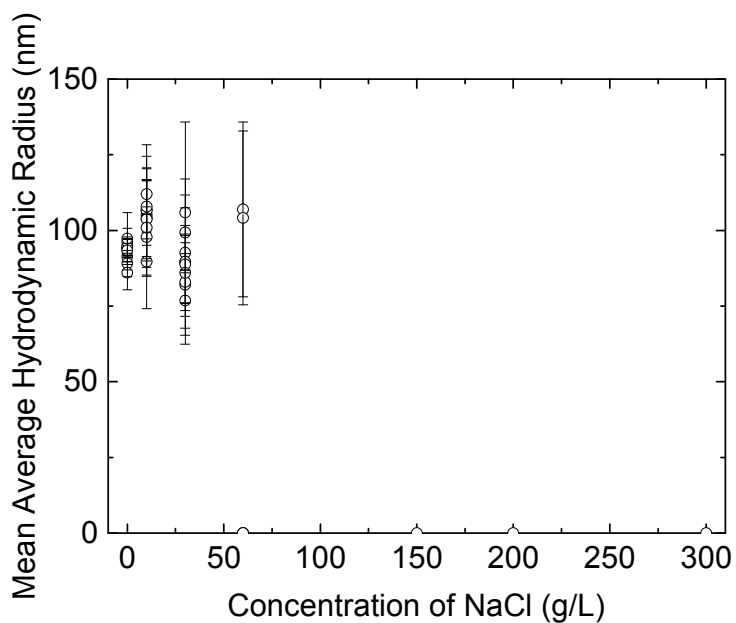

Figure 7. 13
Mean average hydrodynamic radii calculated for the various NaCl concentrations used with a glycine concentration of 220 g glycine per kg solvent. The values represent the average of the 10+ measurements that were taken from each sample and the error bars represent the standard deviation. When the function could not be fitted, a mean hydrodynamic radius of zero was plotted for reference.
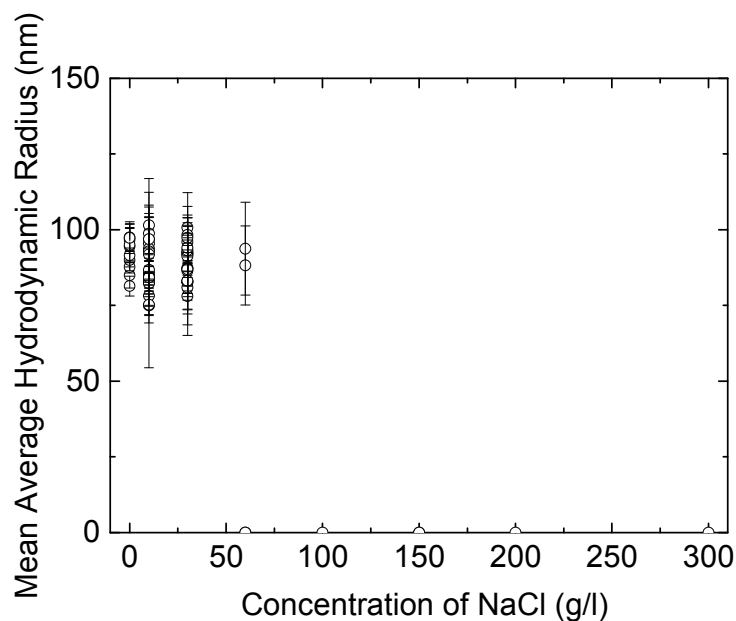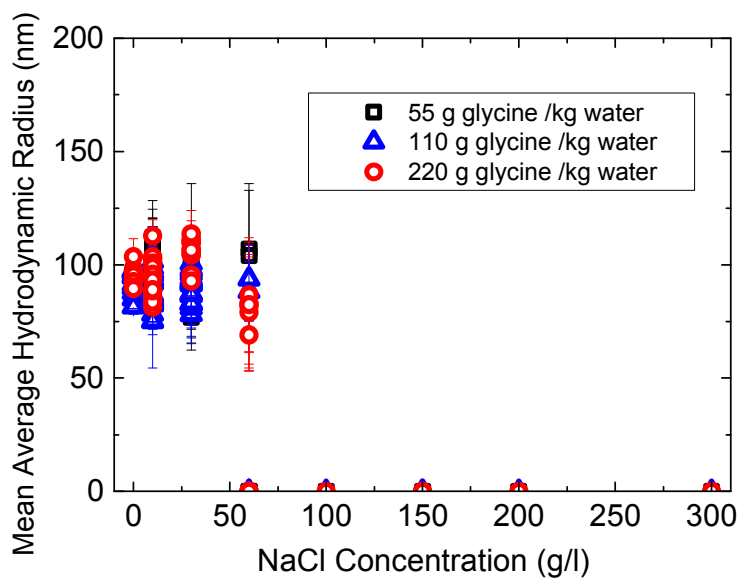
Figure 7. 14
Mean average hydrodynamic radii calculated for the various NaCl concentrations used with a glycine concentration of 110 g glycine per kg solvent. The values represent the average of the 10+ measurements that were taken from each sample and the error bars represent the standard deviation. When the function could not be fitted, a mean hydrodynamic radius of zero was plotted for reference.

Figure 7. 15
Mean average hydrodynamic radii calculated for the various NaCl concentrations used with a glycine concentration of 55 g glycine per kg solvent. The values represent the average of the 10+ measurements that were taken from each sample and the error bars represent the standard deviation. When the function could not be fitted, a mean hydrodynamic radius of zero was plotted for reference.

Figure 7. 16
Comparison of the mean average hydrodynamic radii calculated for each glycine solution concentration.
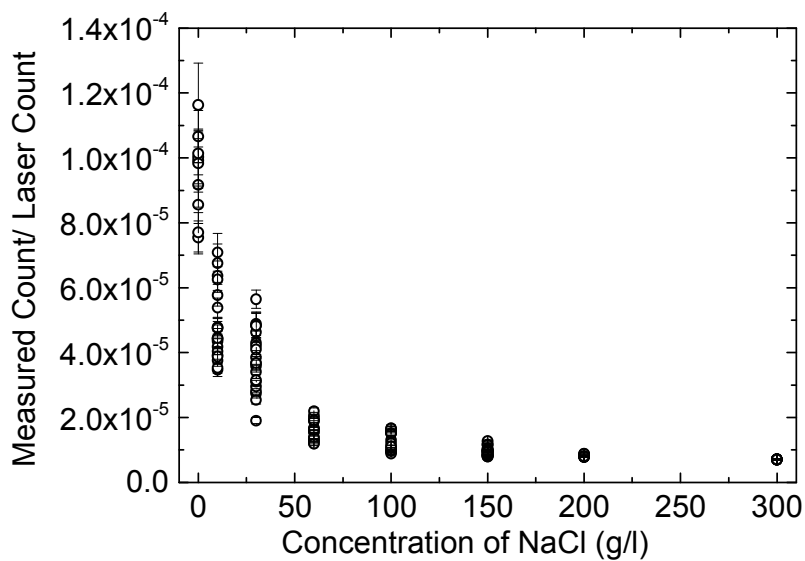
Figure 7. 17
Mean intensity of scattered light measured for the various NaCl concentrations used with a glycine concentration of 220g glycine per kg solvent. The values represent the mean of the mean intensity measured for each of the 10+ measurements that were taken from each sample. The error bars represent the standard deviation.
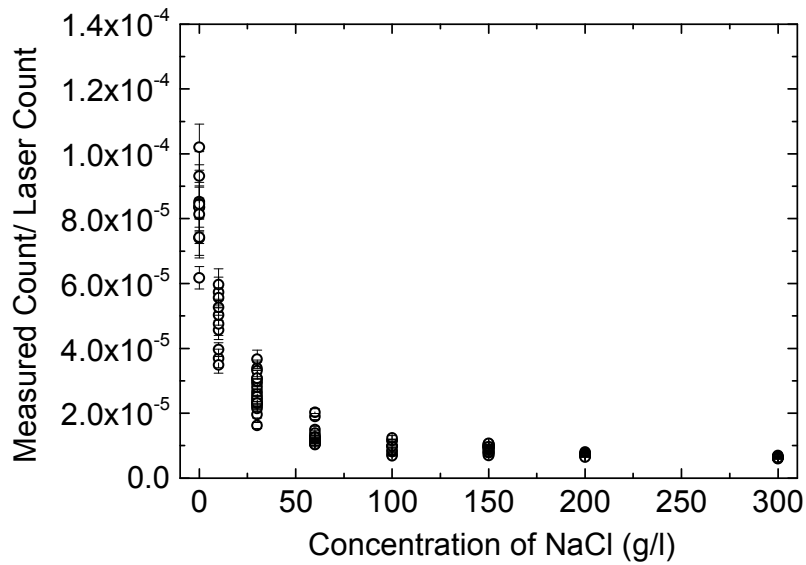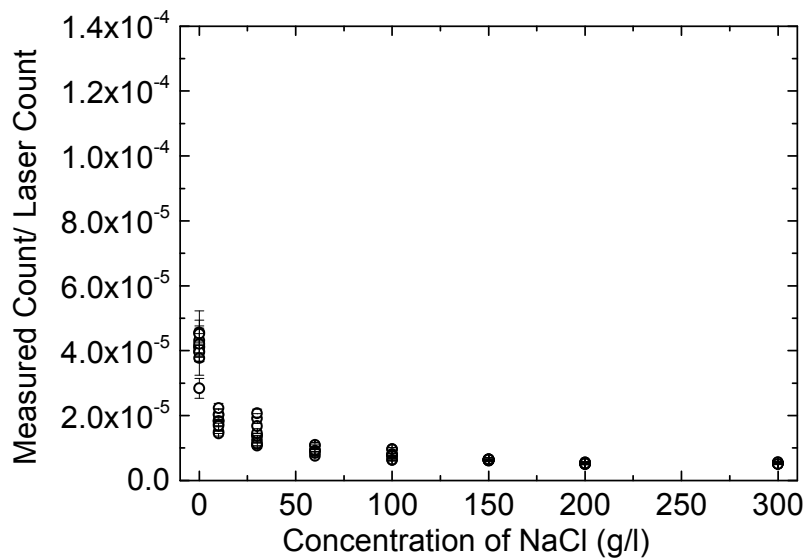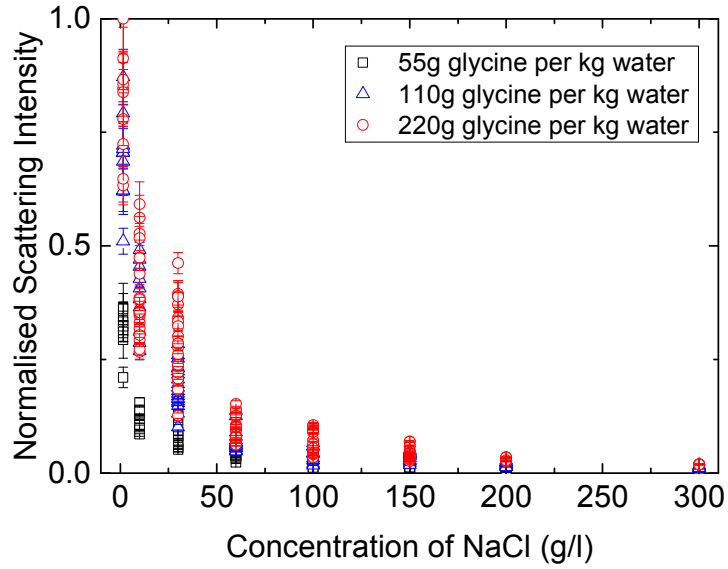
Figure 7. 18
Mean intensity of scattered light measured for the various NaCl concentrations used with a glycine concentration of 110g glycine per kg solvent. The values represent the mean of the mean intensity measured for each of the 10+ measurements that were taken from each sample. The error bars represent the standard deviation.

Figure 7. 19
Mean intensity of scattered light measured for the various NaCl concentrations used with a glycine concentration of 55g glycine per kg solvent. The values represent the mean of the mean intensity measured for each of the 10+ measurements that were taken from each sample. The error bars represent the standard deviation.

Figure 7. 20
Comparison of mean intensity of scattered light measured for the various NaCl concentrations used with each glycine concentration. The values represent the mean of the mean intensity measured for each of the 10+ measurements that were taken from each sample. The error bars represent the standard deviation. (linear-linear)
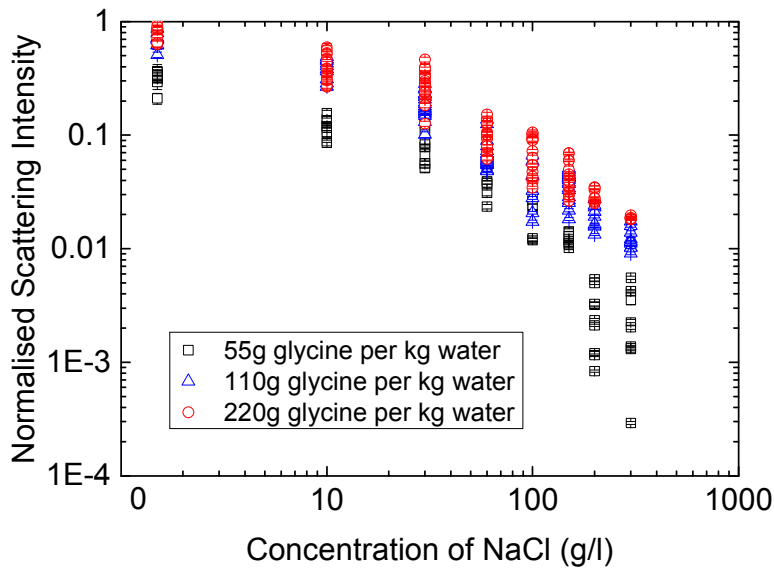

Figure 7. 21
Comparison of mean intensity of scattered light measured for the various NaCl concentrations used with each glycine concentration. The values represent the mean of the mean intensity measured for each of the 10+ measurements that were taken from each sample. The error bars represent the standard deviation. (log-log)

The addition of NaCl resulted in the decay of the autocorrelation functions due to glycine nanodroplets becoming less prominent (lower y-intercepts), as shown in Figure 7. 10 to Figure 7. 12. Eventually with the addition of a sufficient mass of sodium chloride, the decay could not be clearly detected. This trend occurred for each of the glycine concentrations studied and generally, the decays due to nanodroplets could not be detected once salt concentrations had exceeded 100 g/l.

These findings are reflected in the mean intensity of light scattered by the solutions (given in Figure 7. 17 to Figure 7. 19). They show that when no salt was present in the solutions, high intensities of scattered light were measured, while the addition of salt resulted in the lowering of the intensities of scattered light measured. The mean average hydrodynamic radii found by doing a cumulant analysis of the nanodroplet decays (fitted across delay times between 0.03 ms and 0.7 ms for all) are given in Figure 7. 13 to Figure 7. 15. The mean average hydrodynamic radius appeared to remain relatively constant across all salt concentrations where autocorrelation functions could be fitted by the cumulant method described. Since average hydrodynamic radii were calculated to remain relatively constant across all concentrations of NaCl and glycine, the intensity of scattered light was indicative of the number concentration of nanodroplets in the solutions. This therefore suggested that the presence of NaCl had a strong influence on the number concentration of glycine nanodroplets in the solutions. The intensities measured for each glycine concentration are compared in Figure 7. 20 and Figure 7. 21. The relationship between scattered intensity (and therefore nanodroplet concentration) and salt concentration appeared close to linear when plotted log-log (Figure 7. 21), which suggested there may have been a power law relationship between scattered intensity (therefore number concentration) and salt concentrations.

When the autocorrelation functions could not be fitted using the cumulant method employed here (negative values or error was greater than 33% of the mean average hydrodynamic radius), a mean average hydrodynamic radius of zero was plotted for reference. It was found that above a certain critical NaCl concentration, decays could not be fitted using the method employed here. This occurred once the NaCl concentration was greater than 60 g/l for each glycine concentration studied.

It should be noted that the average hydrodynamic radii will have a degree of uncertainty due to the values used for the viscosities of the solutions here since these were approximated from literature and rheology measurements. Rheology measurements were taken of NaCl solutions with glycine concentrations of 110 g glycine/kg water and 264 g glycine/kg water (by PhD students Claire Forsyth and Alexander Hope using a parallel plate rotational rheometer (TA Discovery HR-2). For NaCl solutions with glycine solution concentrations of 55 g glycine/kg water and 220 g glycine/kg water, the viscosities measured for NaCl solutions with glycine concentrations of 110 g glycine/kg water and 264 g glycine/kg water were scaled, respectively. For scaling the data, literature obtained values of viscosity for aqueous glycine values i.e. 0 g/l NaCl were obtained and used as the basis for scaling[8]. The values of viscosity used in calculating average hydrodynamic radii are given in Table 7. 5.

$$\eta_{[glycine],[NaCl]} = \frac{\eta_{[rheology\ glycine],[NaCl]}}{\eta_{[rheology\ glycine],[0\ g\ NaCl]}} \eta_{[glycine],[0\ g\ NaCl]}$$

(7. 12)

Here $\eta_{[glycine],[NaCl]}$ is the estimated viscosity of a solution with certain glycine and sodium chloride concentrations, $\eta_{[rheology\ glycine],[NaCl]}$ is the viscosity measured using a rheometer for solutions of certain glycine (110 g glycine/kg water or 264 g glycine/kg water) and sodium chloride concentrations, $\eta_{[rheology\ glycine],[0\ g\ NaCl]}$ is the viscosity measured using a rheometer for aqueous glycine solutions (110 g glycine/kg water or 264 g glycine/kg water) and $\eta_{[glycine],[0\ g\ NaCl]}$ is literature obtained viscosity values for aqueous glycine solution of a particular glycine concentration. When estimating viscosities, the measured rheology data used corresponded to the glycine concentration (110 g glycine/kg water or 264 g glycine/kg) closest to the concentrations of solution to be estimated (55 g glycine/kg water and 220 g glycine/kg water).

Table 7. 5
Viscosity values used for calculating the average hydrodynamic radius.

Concentration of NaCl (g NaCl/l aqueous glycine solution)	Viscosity of Solution at 25°C (Pa.s) (NaCl added to 55 g/kg aqueous glycine solution)	Viscosity of Solution at 25°C (Pa.s) (NaCl added to 110 g/kg aqueous glycine solution)	Viscosity of Solution at 25°C (Pa.s) (NaCl added to 220 g/kg aqueous glycine solution)
0	0.00090	0.0011	0.0013
10	0.00094	0.0012	0.0025
30	0.0010	0.0013	0.0013
60	0.0012	0.0014	0.0016
150	0.0014	0.0017	0.0018
200	0.0016	0.0020	0.0020
300	0.0019	0.0023	0.0027

7.2.3 Consideration of Results

The decreased formation of glycine nanodroplets with increased salt concentrations suggest that the nanodropets do not form due to Coulomb interactions. For a colloid aggregation mechanism, sodium chloride would screen electrostatic repulsion and allow short range attractive van der Waals attraction to dominate[6]. If nanodroplet formation followed such a mechanism, their size would be expected to increase with the addition of NaCl.

The effect of the addition of NaCl on glycine in solution is not well understood[5, 10]. As mentioned in Chapter 1 Section 1.5, the presence of electrolytes is thought to potentially modify the packing arrangement of glycine molecules[5]. For example, cyclic dimers (α- glycine growth units) may be disrupted by the presence of NaCl, while the formation of head-to-tail open chains (γ- glycine growth units) may be promoted[5]. The NaCl may contribute to an ionic atmosphere which results in the charging of glycine molecules. From the analysis of the pH results (Section 7.2.3), a large number of charged molecules were thought to reduce the likelihood of glycine forming liquid like clusters[4]. This could help explain why larger salt concentrations resulted in a lower concentration of nanodroplets being measured.

From literature, a salt concentration of 80 g/l was found to result in the γ- glycine polymorph of glycine forming[5] and computational studies showed that when a NaCl concentration of 80 g/l was used, γ- glycine nuclei were made more stable while α- glycine nuclei became less stable[10]. From the results obtained here, when a salt concentration of generally above 60 g/l NaCl was used, the decays of the autocorrelation functions due to nanodroplets were not prominent and scattering was low, which suggested that the population of nanodroplets was low. Although undersaturated solutions were studied here, due to the similarities of salt concentrations which resulted in the nucleation of γ- glycine in literature[5] and the salt concentrations which resulted in low levels of scattering from nanodroplets here, the findings suggest that there may be a link between the concentration of glycine nanodroplets and the formation of γ- glycine, which was also found with the pH studies detailed in Section 7.1. The trends observed in the undersaturated solutions are expected to be similarly observed in supersaturated solutions[2], with preliminary data (unpublished) confirming this.

It is worth noting that the presence of NaCl did not appear to influence the pH of the solutions. The range of glycine concentrations covered also showed that the effects seen could not be attributed to the effect of NaCl on the solubility of glycine in the solutions[5].The behaviour seen for the different pH results can also not be due to the presence of sodium or chlorine ions as the quantities of Na^+ or Cl^- present in pH experiments that resulted in nanodroplets being immeasurable were different than the quantities present in NaCl experiments[3, 4].

7.3 Conclusions

The results found here suggested that the use of pH values away from neutral conditions (close to the isoelectric point) resulted in a decrease in the concentration of liquid-like mesoscale clusters (nanodroplets) in glycine solutions. Evidence for this came from the measurement of lower intensities of scattered light when the pH was made higher or lower. The average size of nanodroplets remained constant across all conditions studied. The decrease of nanodroplet concentration appeared to correlate with the presence of more significant fractions of anions or cations, according to speciation models. It is therefore possible that the charged glycine ions reduced the formation of the glycine nanodroplets. Since γ-glycine formation is also

associated with pH conditions where the nanodroplet population was found to be lower, the nanodroplets may potentially be linked to the nucleation of α-glycine or γ-glycine.

The addition of sodium chloride to aqueous glycine solutions resulted in a decrease in the concentration of the glycine nanodroplets. Evidence for this came from the measurement of lower intensities of scattered light when sodium chloride was added to aqueous glycine solutions. The average size of nanodroplets remained constant across all conditions studied, which suggested that clusters did not form through standard Coulomb interactions. The reduction in scattering measured could potentially have been a result of sodium chloride contributing to an ionic atmosphere, resulting in the charging of glycine molecules and reducing cluster formation. The addition of sodium chloride is well known to affect the polymorphic outcome, and there were strong similarities between the sodium chloride concentrations that were found to result in immeasurable levels of nanodroplets, and the sodium chloride concentrations found to result in the nucleation of γ-glycine (rather than α- glycine) from literature[5].

The results obtained by investigating the effect of pH and the addition of sodium chloride on mesoscale clusters in glycine solutions therefore indicated that pH and the presence of sodium chloride may influence the arrangement of molecules in solution, and the concentration of mesoscale clusters in the solutions may be linked to glycine polymorphism.

7.4 Summary

- When the pH of glycine solutions was moved away from neutral conditions (close to the isoelectric point), a decrease in the concentration of nanodroplets in glycine solutions occurred.
- The addition of sodium chloride to aqueous glycine solutions resulted in a decrease in the concentration of the glycine nanodroplets.
- The presence of charged glycine species appeared to reduce the likelihood of clusters forming.

- The average size of nanodroplets remained constant across all conditions studied. This suggested that clusters did not form through standard Coulomb interactions.
- Conditions where the concentration of nanodroplets was low/ immeasurable correlated with conditions where γ-glycine would be expected to nucleate from supersaturated solutions.

7.5 References and Nomenclature

7.5.1 References

(1)   Jawor-Baczynska, A.; Sefcik, J.; Moore, B. D., 250 nm Glycine-Rich Nanodroplets Are Formed on Dissolution of Glycine Crystals But Are Too Small To Provide Productive Nucleation Sites. *Crystal Growth & Design* **2013,** 13, (2), 470-478.

(2)   Jawor-Baczynska, A.; Moore, B. D.; Lee, H. S.; McCormick, A. V.; Sefcik, J., Population and size distribution of solute-rich mesospecies within mesostructured aqueous amino acid solutions. *Faraday Discussions* **2013,** 167, 425-440.

(3)   Towler, C. S.; Davey, R. J.; Lancaster, R. W.; Price, C. J., Impact of molecular speciation on crystal nucleation in polymorphic systems: The conundrum of gamma glycine and molecular 'self poisoning'. *Journal of the American Chemical Society* **2004,** 126, (41), 13347-13353.

(4)   Han, G.; Thirunahari, S.; Chow, P. S.; Tan, R. B. H., Resolving the longstanding riddle of pH-dependent outcome of glycine polymorphic nucleation. *Crystengcomm* **2013,** 15, (6), 1218-1224.

(5)   Yang, X.; Lu, J.; Wang, X.-J.; Ching, C.-B., Effect of sodium chloride on the nucleation and polymorphic transformation of glycine. *Journal of Crystal Growth* **2008,** 310, (3), 604-611.

(6)   Rhodes, M., *Introduction to Particle Technology*. 2nd ed.; 2008.

(7)   Darvey, I. G., What Fraction Of Glycine Molecules Are Nonionic In A Solution Of Glycine At A Ph Value Equal To The Isoelectric Point Of Glycine. *Biochemical Education* **1995,** 23, (3), 141-143.

(8)   Myerson, A., *Handbook of Industrial Crystallization*. 2nd ed.; Butterworth-Heinemann: 2001.

(9)   Erdemir, D.; Chattopadhyay, S.; Guo, L.; Ilavsky, J.; Amenitsch, H.; Segre, C. U.; Myerson, A. S., Relationship between self-association of glycine molecules in supersaturated solutions and solid state outcome. *Physical Review Letters* **2007,** 99, (11).

(10)   Duff, N.; Dahal, Y. R.; Schmit, J. D.; Peters, B., Salting out the polar polymorph: Analysis by alchemical solvent transformation. *Journal of Chemical Physics* **2014,** 140, (1), 11.

7.5.2 Main Nomenclature

M = molarity of acid/ alkali

$moles_{glycine}$ = total moles of glycine

$moles_{ions}$ = total moles of glycine ions

$V_{acid\ or\ alkali}$ = volume of acid/ alkali

V_{water} = volume of water

V_{total} = total solution volume

x_{anion} = mole fraction of glycine anions

x_{cation} = mole fraction of glycine cations

x_{ion} = mole fraction of glycine that would be ionised

x_{water} = water mass fraction of solvent

$\eta_{aqueous\ glycine\ solution}$ = viscosity of aqueous glycine solution

$\eta_{HCl\ or\ NaOH}$ = viscosity of the acid/ alkali solution used

η_{pH} = viscosity of glycine solution at a particular pH value

$\eta_{solvent}$ = viscosity of solvent

η_{water} = viscosity of water

$\eta_{[glycine],[NaCl]}$ = estimated viscosity of a solution with certain glycine and sodium chloride concentrations

$\eta_{[rheology\ glycine],[NaCl]}$ = viscosity measured using rheometer for solutions of certain glycine and sodium chloride concentrations

$\eta_{[rheology\ glycine],[0\ g\ NaCl]}$ = viscosity measured using rheometer for aqueous glycine solutions

$\eta_{[glycine],[0\ g\ NaCl]}$ = literature obtained viscosity values for aqueous glycine solution of a particular glycine concentration.

8. Model to Estimate Nucleation Rates from Transmission Measurements

Chapter Outline and Contents

In Chapter 3, it was shown that transmission measurements could be used to gain information on the attenuation of incident light. In this chapter, the attenuation of light incident on a sample was further examined and a model was produced which ultimately allowed crystal nucleation rates to be obtained from transmission measurements of a crystallising solution.

The model was based on analysing the extinction of light incident on a sample. The extinction was a result of scattering by a constant number concentration of growing particles, much larger than the wavelength of incident light. A theoretical expression for the transmission of light through the sample was obtained, and this was fitted to experimental data and solved for the number concentration of particles, particle growth rates and initial particle sizes. It was ensured that the theoretical sedimentation time of the particles was matched to experimentally observed sedimentation times to narrow the range of possible solutions. A material balance was used to confirm the reliability of the model's solutions. The analysis carried out was based on cuboids but could easily be applied to other particle shapes.

This chapter covers:

- Basic theory on the transmission of light through monodisperse solutions of cuboids.
- Theory on the sedimentation of cuboids.
- Details of the model and how it was fitted to experimental data.
- The use of a material balance to assess the validity of the model.

8.1 Introduction

Nucleation rates are difficult to measure. Methods outlined in literature, as detailed in Chapter 1, often involve difficult and cumbersome techniques, such as counting the number of crystals formed in a given volume of solution and metastable zone width measurements[1-9]. Induction times can be measured easily experimentally and can be related to the nucleation rate using models (see Chapters 4 and 5), however, several repetitions are often required to obtain statistically valid results[10]. In addition, an experimentally deduced induction time cannot be considered a fundamental characteristic of a system due to the significant variability that arises depending on the sensitivity of detection equipment and procedures carried out[11]. Finding a simpler way of quantifying nucleation rates is therefore of value. The transmission measurement method outlined here provides a straightforward way of estimating the number concentration of growing crystals in a solution, which can easily be related to the nucleation rate.

The model here applies to a solution where all nuclei had already formed by time zero i.e. no further nucleation took place during the transmission measurements. The solution was quiescent during measurements so crystals were free to grow and settle. In such a system, the transmission of light would decrease initially due to the growth of crystals. The transmission data corresponding to this decrease in transmission due to crystal growth were used in the model and examples are given in Figure 8. 1. After a particular time, known here as the sedimentation time, the transmission increased back towards unity as particles had sedimented below the light's path through the solution. This sedimentation time was used in the model to limit the range of possible solutions.

The data analysed here to check the model were based on results obtained by previous PhD students Ulrich Schacht and Andrew Brown[12, 13]. The data used were transmission measurements of a valine solution that was undergoing anti-solvent crystallisation (aqueous valine solution plus isopropanol). Valine aqueous solution was mixed with isopropanol (1:1 v/v) using a static mixer setup (confined impinging jet mixer). The flow rate of solution through each entrance to the mixer was varied from 300 ml/ min to 700 ml/min. All nucleation was assumed to have taken place by the time a sample was transferred to a cuvette for transmission measurements[12, 13].

While in the cuvette, crystals grew until supersaturation was depleted. Solutions were quiescent so crystals were free to settle.
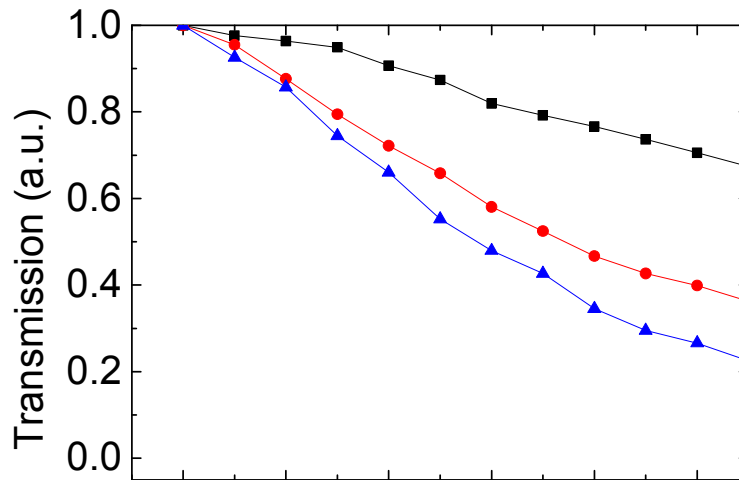

Figure 8. 1
Examples of the transmission data that were analysed. The data correspond to the intial decrease in transmission due to the growth of crystals.

8.2 Transmission of Light through Monodisperse Solutions

8.2.1 Light Scattering Introduction

In Chapter 3, the basic theory of how measurements of the transmission of light (T) through a sample across an optical path length (L) could be related to an attenuation coefficient (τ) was described.

$$\tau = \frac{-ln(T)}{L} \qquad \textbf{(8. 1)}$$

It was shown that the attenuation coefficient could be written in terms of the number of particles i per unit volume (N_i) and the extinction cross section of particle i, (C_i^{ext}). $i = 1, 2, ..., n$ where n is the total number of types of particle.

$$\tau = \sum_{i}^{n} C_i^{ext} N_i \qquad \textbf{(8. 2)}$$

The extinction cross section of particle i could be written in terms of the scattering cross section of particle i (C_i^{sca}) and the absorption cross section of particle i, (C_i^{abs}).

$$\tau = \sum_{i}^{n} C_i^{sca} N_i + C_i^{abs} N_i \qquad \textbf{(8. 3)}$$

For the system studied here, it was assumed that extinction due to molecular absorption was negligible and all extinction was therefore due to scattering. This was valid for the wavelength of light used. It was assumed that samples were monodisperse and homogenous so the term for the attenuation coefficient could be simplified to:

$$\tau = C^{sca} N \qquad \textbf{(8. 4)}$$

Here N is the total number of particles per unit volume and C^{sca} is the average scattering cross section of the particles.

The particles studied here (valine crystals) were approximated to be cuboids (plates), so for the model, a term for C^{sca} was devised that was applicable to growing cuboids. The dimension ratio of the cuboids was 1:10:30 (thickness (H): width (W): length (L)) and this ratio was assumed to stay constant throughout the transmission measurements[12, 13].

8.2.2 Transmission of Light through a Monodisperse Solution of Cuboids

For particles whose dimensions are much larger than the wavelength of incident light, scattering will be in the diffraction limit and their scattering cross section can be taken as their geometric cross section.

8.2.2.1 Geometric Scattering Cross Section at Angle θ

It is known that a cuboid settling in the Stoke's law region will align vertically (longest surface aligns almost parallel to direction of motion) to minimise drag[14]. The geometric scattering cross section of the cuboid would depend on the angle of the vertically aligned cuboid (θ) relative to incident light. For example, when angled at zero degrees, i.e. perpendicular to the direction of incident light, light would be blocked by the total cross section of the cuboid, however, if the cuboid was angled at 90° to the incoming beam, only the thickness of the cuboid (which was taken as negligible) would block incident light. This is shown diagrammatically in Figure 8. 2.
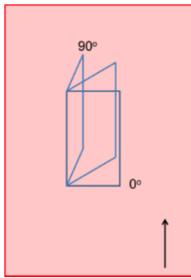
Figure 8. 2
Diagram showing how cuboids may align relative to the incoming light beam.

Since the geometric scattering cross section varied with cuboid angle, the average geometric scattering cross section of the cuboids had to be calculated over the angular range of zero to 90°. It was assumed that the cuboids had no particular angular preference and that the effect of cuboid thickness on the scattering of incident light was negligible (the thickness was small compared to cuboid height and width so this was reasonable).

The geometric scattering cross section at a particular angle was calculated using trigonometry. The 'scattering width' (see Figure 8. 3) at a particular angle was effectively the adjacent side of a right angled triangle whose hypotenuse was the actual width of the crystal.

The geometric cross section at angle θ ($XSA(\theta)$) could therefore be calculated from:

$$XSA(\theta) = LW\cos(\theta)$$

(8. 5)
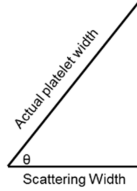
Figure 8. 3
Diagram showing how scattering width is related to the actual cuboid width and the angle at which the cuboid is aligned.

8.2.2.2 Average Geometric Scattering Cross Section

Using Eqn. (8. 5), the average geometric scattering cross section C^{sca} was calculated over the angular range of zero to 90°:

$$C^{sca} = LW \frac{\int_0^{\frac{\pi}{2}} \cos(\theta)d\theta}{\frac{\pi}{2} - 0} \tag{8. 6}$$

Since the area under a cosine curve between 0° and 90° is 1, this could be simplified to:

$$C^{sca} = \frac{2LW}{\pi} \tag{8. 7}$$

For simplicity, the dimension ratio of the cuboids was used so that the geometric scattering cross section C^{sca} was written in terms of length only.

$$L = \alpha H = \beta W \tag{8. 8}$$

Here α and β are dimension ratios.

C^{sca} could therefore be written as:

$$C^{sca} = \frac{2}{\beta} \frac{L^2}{\pi} \tag{8. 9}$$

From Eqn. (8. 4) and Eqn. (8. 9), the attenuation coefficient could be written in terms of the average geometric scattering cross section and the number concentration of particles. Assuming all particles were the same size and had the same dimension

ratio:

$$\tau = N\left(\frac{2}{\beta}\frac{L^2}{\pi}\right)$$

(8. 10)

8.2.2.3 Average Geometric Scattering Cross Section Accounting for Cuboid Growth

Due to the growth of cuboids, the average scattering cross section will vary with time, so this had to be taken into account for the model. The growth of cuboids was responsible for the initial decrease in transmission measured by experiment.

Since cuboid faces had different dimensions, the faces of the cuboids must grow at different rates. Assuming the dimension ratio (Eqn. (8. 8)) remains constant:

$$G_L = \alpha G_H = \beta G_W$$

(8. 11)

Here G_L is the length growth rate, G_H is the thickness growth rate and G_W is the width growth rate.

At time zero, it was assumed that all particles formed were of size L_0, W_0 and H_0. It was assumed that the growth rates and dimension ratio remained constant so equations could be written in terms of the length growth rate only. The change in length of the particles with time was written as:

$$dL = G_L dt$$

(8. 12)

Assuming a constant length growth rate and that at time zero, all particles were of an initial size L_0, Eqn. (8. 12) could be integrated over boundary conditions:

$$\int_{L_0}^{L} dL = G_L \int_0^t dt$$

(8. 13)

$$L = L_0 + G_L t$$

(8. 14)

This could similarly be done for the changes of cuboid width and thickness:

$$W = W_0 + G_w t$$

(8. 15)

$$H = H_0 + G_H t$$

(8. 16)

The term for length growth (Eqn. (8. 14)) could be substituted into Eqn. (8. 9), meaning that the scattering cross section could be written in terms of an initial length, the length growth rate and time:

$$C^{sca}(t) = \frac{2}{\beta} \frac{(L_0 + G_L t)^2}{\pi}$$

(8. 17)

This term for the scattering cross section could be used to write an expression for the change in transmission due to cuboid growth over time:

$$T(t) = e^{-N\left(\frac{2}{\beta}\frac{(L_0 + G_L t)^2}{\pi}\right)L}$$

(8. 18)

Since this expression for transmission took the number concentration of cuboids to be constant, it was assumed that additional nucleation of the sample did not occur during transmission measurements and cuboids did not agglomerate.

8.2.3 Settling of Cuboids

The transmission equation (Eqn. (8. 18)) was fitted to experimental transmission data corresponding to the initial decrease in transmission due to particle growth, and it was solved for N, L_0 and G_L. There were many possible solutions.

To obtain the best solutions of N, L_0 and G_L, the time taken for particles to sediment below the light source's path t_{sed} was taken into consideration. Only limited combinations of L_0 and G_L gave theoretical sedimentation times matched to experimentally measured sedimentation times. To quantify the settling of particles, the drag force on cuboids had to be calculated and this was used to find the settling velocity of the cuboids.

8.2.3.1 Drag Force for Cuboids

The total drag force for cuboids experiencing creeping flow (F_D) was estimated using Stoke's law with the inclusion of a dynamic shape factor (K_n) that accounted for the drag forces experienced by non-spherical objects[15]. The dynamic shape factor was

calculated from the form drag and friction drag experienced by a non-spherical object.

Form drag, which accounts for 1/3 of the total drag, is due to the integration of fluid pressure over the object's surface[15]. It should therefore be associated with the area of the object (cuboid) projected normal to its direction of motion. For non-spherical objects, it can be expressed through the Stoke's law form drag on a sphere with the same projected area as the projected area of the object, normal to its direction of flow[15]. The diameter of this sphere is D_n.

D_n can be calculated as follows. For a cuboid falling with its longest edge parallel to the direction of flow, the projected area normal to its direction of flow will be the width of the cuboid, multiplied by its thickness. The projected area of the sphere will be equal to its cross-sectional area.

$$WH = \frac{\pi D_n{}^2}{4} \hspace{2cm} \textbf{(8. 19)}$$

Writing in terms of length, α and β:

$$D_n = \frac{2L}{\sqrt{\pi \alpha \beta}} \hspace{2cm} \textbf{(8. 20)}$$

Friction drag, which accounts for 2/3 of total drag, is due to the integration of friction forces over the object's surface[15]. It should therefore be associated with the total effective surface area of the object. For non-spherical objects, it could be expressed through the Stoke's law friction drag on a sphere with the same total surface area as the object. The diameter of this sphere is D_s, which can be calculated as follows for cuboids:

$$2(LH + LW + WH) = \pi D_s{}^2 \hspace{2cm} \textbf{(8. 21)}$$

$$D_s = L\sqrt{\frac{2}{\pi}\left(\frac{1}{\alpha} + \frac{1}{\beta} + \frac{1}{\alpha\beta}\right)} \hspace{2cm} \textbf{(8. 22)}$$

The total drag force experienced by the non-spherical object was therefore written in terms of the diameters of spheres with equal projected and effective areas as the non-spherical object, rather than through directly measured dimensions of the non-spherical object.

$$F_D = 3\pi\eta v \left(\frac{1}{3}D_n + \frac{2}{3}D_S\right)$$ **(8. 23)**

Here η is the fluid's dynamic viscosity and v is the settling velocity of the non-spherical objects.

This is commonly written as:

$$F_D = 3\pi\eta v D_n K_n$$ **(8. 24)**

Where

$$K_n = \frac{1}{3} + \frac{2}{3}\left(\frac{D_S}{D_n}\right)$$ **(8. 25)**

Terms for D_n and D_s (Eqn. (8. 20) and Eqn. (8. 22)) were substituted into Eqn. (8. 25), so the dynamic shape factor for cuboids became:

$$K_n = \frac{1}{3} + \frac{2}{3}\sqrt{\frac{\alpha + \beta + 1}{2}}$$ **(8. 26)**

A term for the total drag force in terms of cuboid length and dimension constants α and β was written by substituting Eqn. (8. 20) for D_n into Eqn. (8. 24):

$$F_D = 6\sqrt{\frac{\pi}{\alpha\beta}}\eta v L K_n$$ **(8. 27)**

8.2.3.2 Use of Drag Force to Obtain Settling Velocity for Cuboids

The total drag force (F_D) was used in a force balance and the force balance was used to calculate the settling velocity of the cuboids. The force balance used the term for the total drag force applied to the cuboids (Eqn. (8. 27)), as well as expressions for the weight and buoyancy (gravitational forces) experienced by the cuboids. It was assumed that Reynolds numbers were low (Re<<1) i.e. creeping flow.

The force balance was written as:

$$Weight = Buoyancy + Drag\ Force$$ **(8. 28)**

Expressions for weight, buoyancy and the total drag force (Eqn. (8. 27) were substituted in:

$$LWH\rho_p g = LWH\rho_f g + 6\sqrt{\frac{\pi}{\alpha\beta}}\eta v L K_n$$ **(8. 29)**

Here ρ_p is the density of the cuboids and ρ_f is the density of the surrounding fluid.

The force balance was solved for the settling velocity, and the dimension ratio of the cuboids (Eqn. (8. 8)) was used so that the expression was written in terms of cuboid length.

(8. 30)

$$v = \frac{L^2(\rho_p - \rho_f)g}{6\sqrt{\alpha\beta\pi}\ \eta K_n}$$

Taking particle growth into account (Eqn. (8. 14)), a term for settling velocity as a function of time was obtained.

$$v(t) = \frac{(L_0 + G_L t)^2(\rho_p - \rho_f)g}{6\sqrt{\alpha\beta\pi}\ \eta K_n}$$ **(8. 31)**

8.2.3.3 Use of Settling Velocity to obtain Settling Time

When cuboids had settled below the light source's path, the transmission increased. The theoretical time taken for cuboids to settle below the light beam's path t_{sed_theo} was estimated by using the settling velocity of cuboids to calculate the displacement of cuboids as a function of time. Assuming that particles settled at their terminal velocity, the total displacement of particles (S) after a given time could be calculated by integrating the term for settling velocity (Eqn, (8. 31)) over time.

$$\int_0^S ds = \int_0^t v(t)\, dt \qquad \text{(8. 32)}$$

$$S(t) = Z_p \left(L_0{}^2 t + L_0 G_L t^2 + \frac{G_L{}^2 t^3}{3} \right) \qquad \text{(8. 33)}$$

Where

$$Z_p = \frac{(\rho_p - \rho_f) g}{6\sqrt{\alpha \beta \pi}\, \eta K_n} \qquad \text{(8. 34)}$$

The theoretical sedimentation time was found by finding the roots of the displacement expression (Eqn. (8. 33)) when S was made equal to the distance between the top of the solution and the light source beam, D (see Figure 8. 4) i.e.

$$Z_p \left(L_0{}^2 t + L_0 G_L t^2 + \frac{G_L{}^2 t^3}{3} \right) - D = 0 \qquad \text{(8. 35)}$$
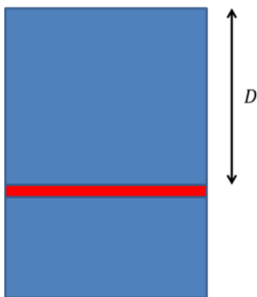
Figure 8. 4
Distance between top of solution and light beam.

8.2.4 Application to Different Shapes

This theory outlined for cuboids can easily be applied to other particle shapes, for example, when applied to monodisperse growing spheres, the transmission of light can be shown to be described by:

$$T(t) = e^{-N\left(\pi(r_0 + G_R t)^2\right)L} \qquad\qquad \textbf{(8. 36)}$$

Where r_0 is the initial radius of the sphere and G_R is the radial growth rate.

For the settling of growing spheres, the settling velocity and displacement can be shown to be:

$$v(t) = \frac{2}{9}\frac{(\rho_p - \rho_f)}{\eta} g(r_0 + G_R t)^2 \qquad\qquad \textbf{(8. 37)}$$

$$S(t) = Z_s\left(r_0{}^2 t + r_0 G_R t^2 + \frac{G_R{}^2 t^3}{3}\right) \qquad\qquad \textbf{(8. 38)}$$

Where

$$Z_s = \frac{2}{9}\frac{(\rho_p - \rho_f)}{\eta} g \qquad\qquad \textbf{(8. 39)}$$

As with cuboids, the theoretical sedimentation time for spheres can be found by finding the roots of the displacement expression, when S equalled the distance between the top of the solution and the top of the light beam, D.

8.3 Matlab Model

The theory outlined was used to analyse experimentally obtained transmission data[12, 13]. Code was written using Matlab and it used 10^6 combinations of N, L_0 and G_L values (from a user specified range of values) in Eqn. (8. 18) to obtain theoretical transmission values $(T_{theo}(t))$. These theoretical transmission values were

compared to the experimental transmission data ($T_{expt}(t)$) and the sum of squares of the residuals (SSR) was found.

$$SSR = \sum_{t=0}^{t=n} \left(T_{expt}(t) - T_{theo}(t)\right)^2 \qquad \textbf{(8. 40)}$$

n is the last transmission point used in the analysis.

The L_0 and G_L values were used in Eqn. (8. 35) to find the theoretical sedimentation times. These were compared to the experimental sedimentation time. If the times were within a 2% tolerance, the corresponding solution values (N, L_0, G_L and $\log(SSR)$) were plotted.

Solutions where $\log(SSR) \leq i$ (where i is the largest value of $\log(SSR)$ that generally gave good fits to the experimental data) were extracted and the mean values of N, L_0 and G_L were found, along with standard deviations.

If desired, the dimension ratio of cuboids (Eqn. (8. 8)) could be used along with solutions of the model (L_0 and G_L) to calculate initial cuboid heights and widths, as well as the growth rate for each plane. The number concentration of particles (N) could be used to obtain nucleation rates, J.

$$J = \frac{N}{t_n} \qquad \textbf{(8. 41)}$$

Where t_n is the time over which nucleation occurred.

8.4 Material Balance

As an additional check on the validity of the model's solutions, a material balance was carried out to estimate the mass of crystals that would have formed. This calculated mass was then compared to experimentally determined crystal masses.

The mass of crystals (M) formed per unit volume at time t could be estimated using

$$M(t) = N\rho_c \frac{L(t)^3}{\alpha\beta}$$

(8. 42)

Where (from Eqn. (8. 14)): $L(t) = L_0 + G_L t$

The values used for N and L_0 corresponded to the mean values of N and L_0 solutions where $\log(SSR) \leq i$ in the model. For the material balance, unlike the model which assumed G_L was constant, G_L was treated as a linear function of supersaturation (Eqn. (8. 43)). The maximum growth rate used was made equal to the mean growth rate predicted by the model for solutions where $\log(SSR) \leq i$. This was used as the growth rate at time zero when the supersaturation would be highest. The minimum growth rate used was zero (when the solution became saturated i.e. supersaturation was equal to 1).

$$G_L(t) = mS(t) + c$$

(8. 43)

Here S is the supersaturation, c is the y intercept of $G_L(t)$ versus $S(t)$, m is the gradient of $G_L(t)$ versus $S(t)$.

The supersaturation could be written as:

$$S(t) = \frac{C_0 - M(t)}{C^*}$$

(8. 44)

Where C_0 is the initial solute concentration and C^* is the solute's solubility.

The model had assumed that the growth rate was constant, unlike the material balances. The times for which theoretical (model) and experimental masses were compared here corresponded to short time scales. This meant that the mass of crystals formed was low so the supersaturation, and therefore growth rate, was relatively constant for the times at which masses were compared.

Due to the range of solutions that gave reasonable fits to the experimental data, errors in the theoretical mass concentrations δM were calculated using the general error propagation equation[16]. Assuming that errors in aspect ratio and crystal density were negligible and that other errors were uncorrelated and random:

$$\delta M = \sqrt{\left(\left|\frac{\partial M}{\partial N}\right| \delta N\right)^2 + \left(\left|\frac{\partial M}{\partial L}\right| \delta L\right)^2} \qquad \text{(8. 45)}$$

$$\delta M = \sqrt{\left(\left|\rho_c \frac{L(t)^3}{\alpha\beta}\right| \delta N\right)^2 + \left(\left|3N\rho_c \frac{L(t)^2}{\alpha\beta}\right| \delta L\right)^2} \qquad \text{(8. 46)}$$

δN was taken as the standard deviation of N values for model solutions where $\log(SSR) \leq i$.

The error in length δL could be found by using Eqn. (8. 14) for L:

$$\delta L = \sqrt{\left(\left|\frac{\partial L}{\partial L_0}\right| \delta L_0\right)^2 + \left(\left|\frac{\partial L}{\partial G_L}\right| \delta G_L\right)^2} \qquad \text{(8. 47)}$$

$$\text{(8. 48)}$$
$$\delta L = \sqrt{(|1|\delta L_0)^2 + (|t|\delta G_L)^2}$$

δL_0 was taken as the standard deviation of L_0 values for model solutions where $\log(SSR) \leq i$. Since the growth rate changed with time for the material balances $(G_L(t))$, its error $\delta G_L(t)$ was taken as the growth rate value at a particular time multiplied by the standard deviation of G_L values found for model solutions where $\log(SSR) \leq i$ $(\delta G_L(0))$, divided by the mean G_L value found for model solutions where $\log(SSR) \leq i$ $(G_L(0))$ (see Eqn. (8. 49)). As mentioned previously, the model solutions for G_L were used for time zero in the material balance.

$$\delta G_L(t) = \frac{\delta G_L(0)}{G_L(0)} G_L(t) \qquad \text{(8. 49)}$$

The error in time was assumed to have been accounted for in the 2% tolerance that was used in the model for accepting solutions that gave similar experimental and theoretical sedimentation times.

8.5 Results and Discussion

The results obtained from analysing the data from the thesis of a previous PhD student[12] (Andrew Brown) are shown in Figure 8. 5 to Figure 8. 8. The value of $\log(SSR)$ is represented by a colour and it can be seen there was a narrow region with lowest residuals. Solutions where $\log(SSR) \leq -3$ generally gave good fits to the experimental data. These better solutions are plotted in Figure 8. 9. The solutions to the model showed that increasing the flow rate of solution resulted in an increase in the number concentration of crystals. The mass evolution of crystals predicted is shown in Figure 8. 10.

A second set of data obtained by another past PhD student[13] (Ulrich Schacht) were also analysed. The results for these are shown in Figure 8. 13 to Figure 8. 11 and there was a narrow region with lowest residuals. Solutions where $\log(SSR) \leq -2$ generally gave good fits to the experimental data. These better solutions are plotted in Figure 8. 14. The mass evolution of crystals predicted is shown in Figure 8. 15.

The axes on the graphs were as follows: Number Concentration (cm^{-3}), Initial Length (μm), Growth Rate ($\mu m/min$). The flow rates are the flow rate of solution through each entrance to the mixer.

Results from Data Set 1
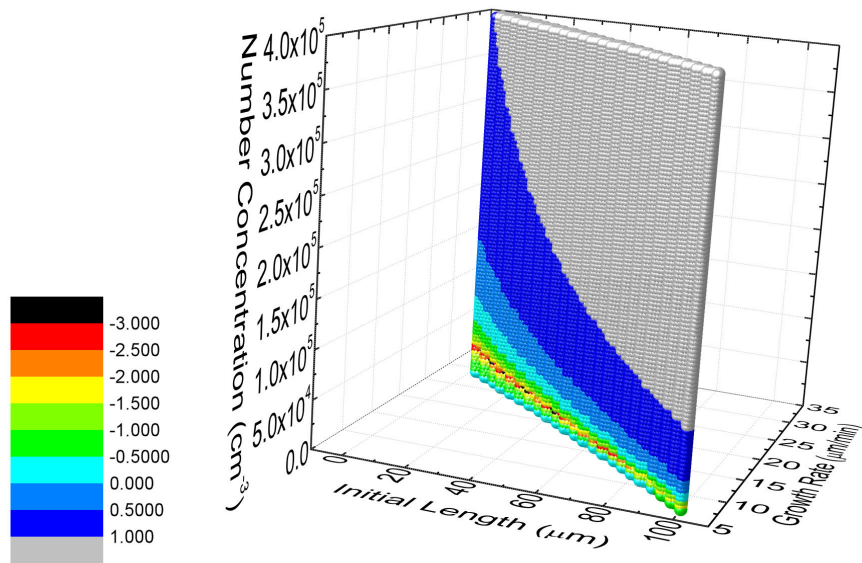
Figure 8. 5
Model solutions for 300 ml/min flow rates into mixer transmission data.
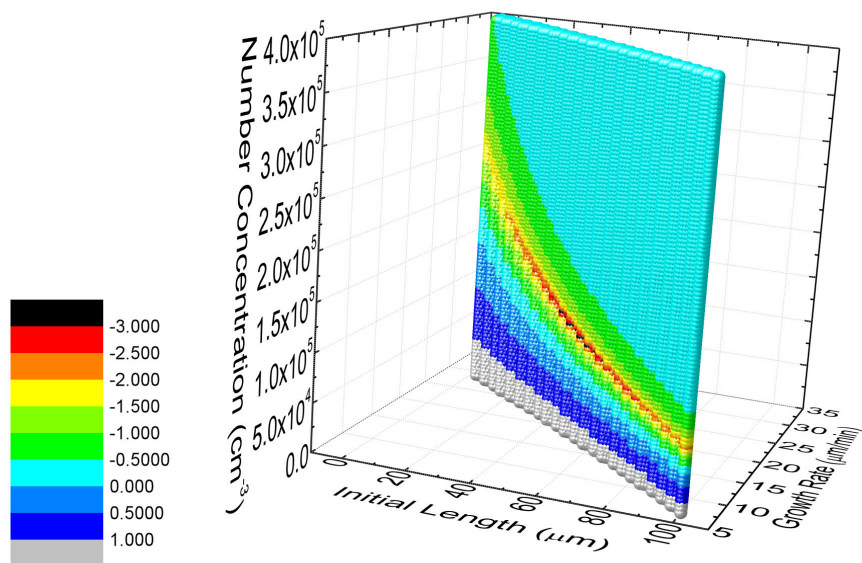
Figure 8. 6
Model solutions for 400 ml/min flow rates into mixer transmission data.
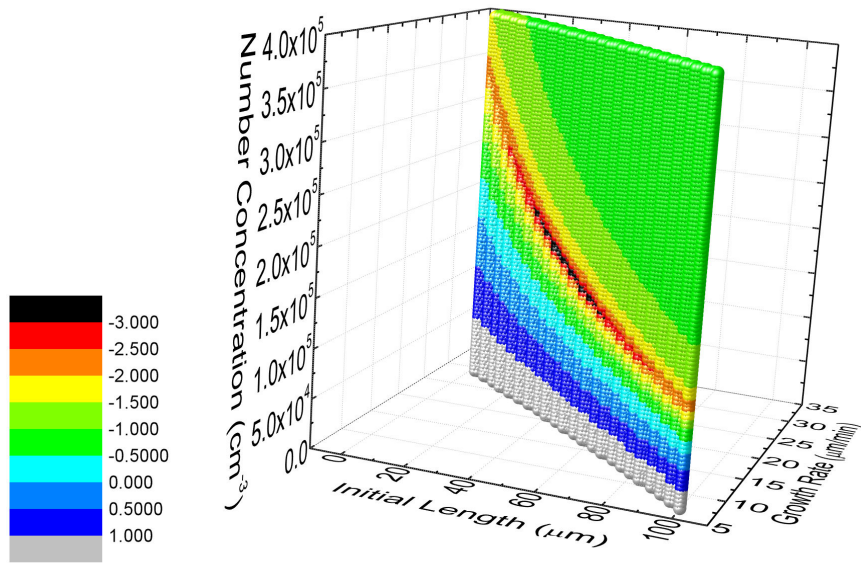
Figure 8. 7
Model solutions for 600 ml/min flow rates into mixer transmission data.
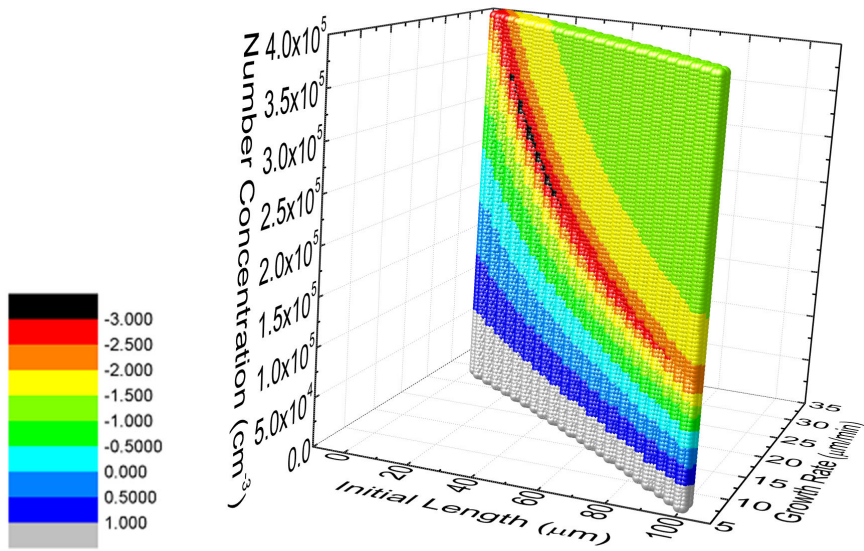
Figure 8. 8
Model solutions for 700 ml/min flow rates into mixer transmission data.
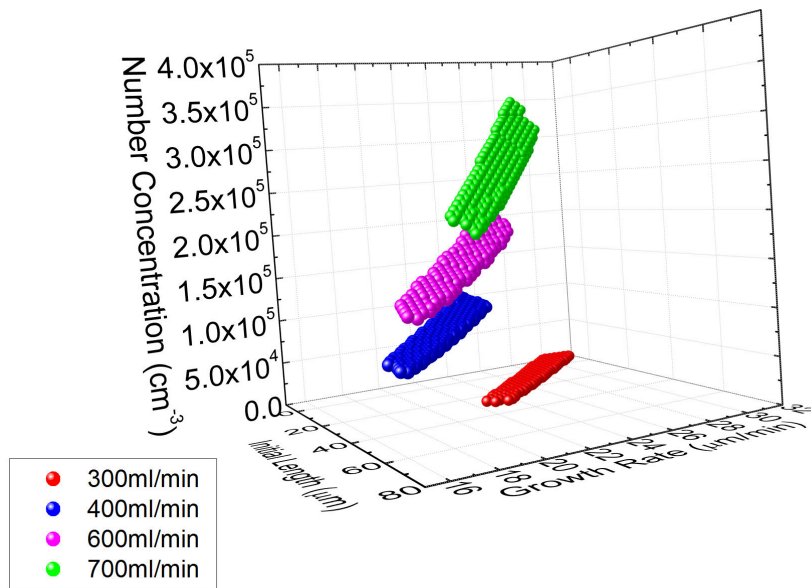
Figure 8. 9
Model solutions which corresponded to $\log(SSR) \leq -3$.
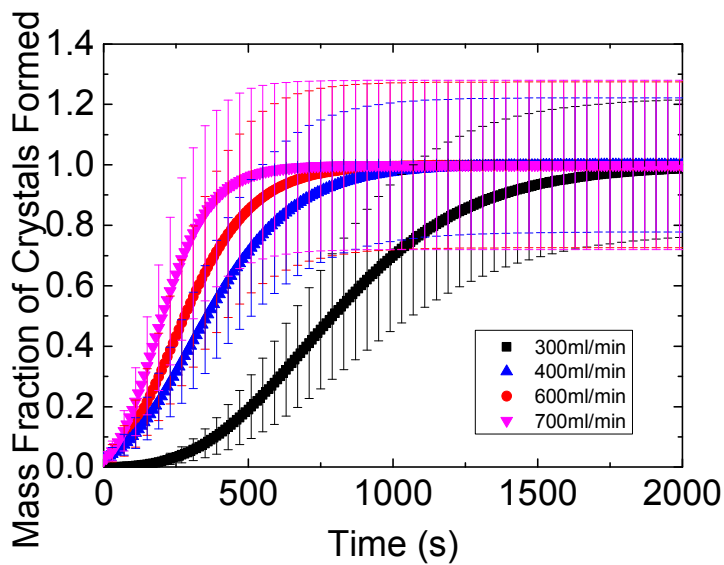
Figure 8. 10
Mass fraction of crystals formed using theoretical mass balance.

Results from Data Set 2
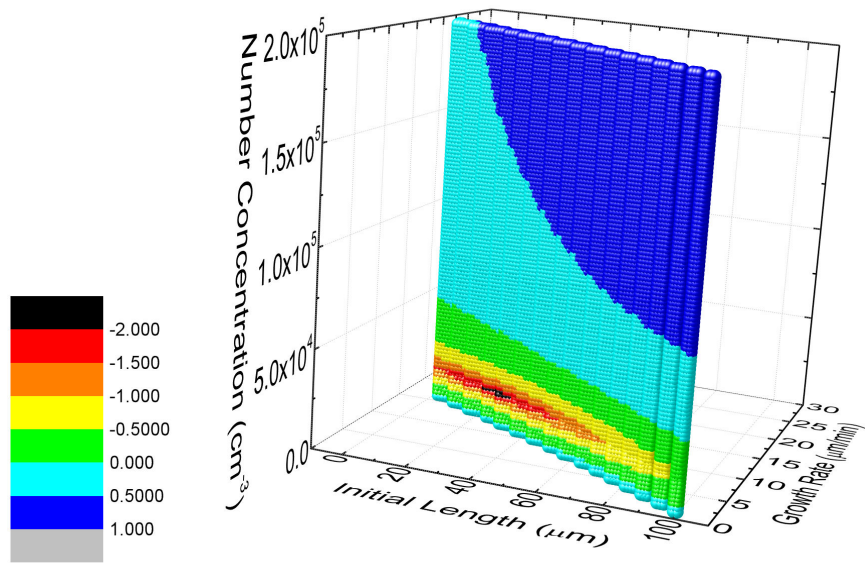
Figure 8. 11
Model solutions for 400 ml/min flow rates into mixer transmission data.
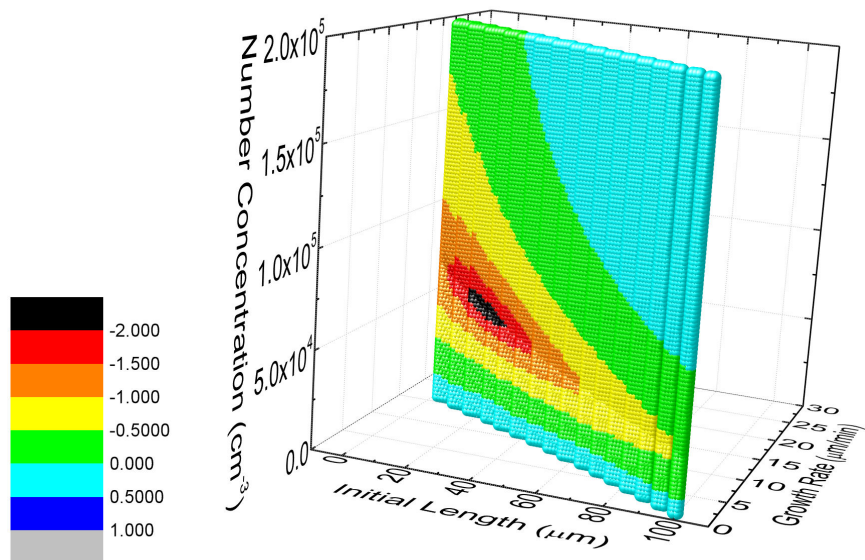
Figure 8. 12
Model solutions for 600 ml/min flow rates into mixer transmission data.
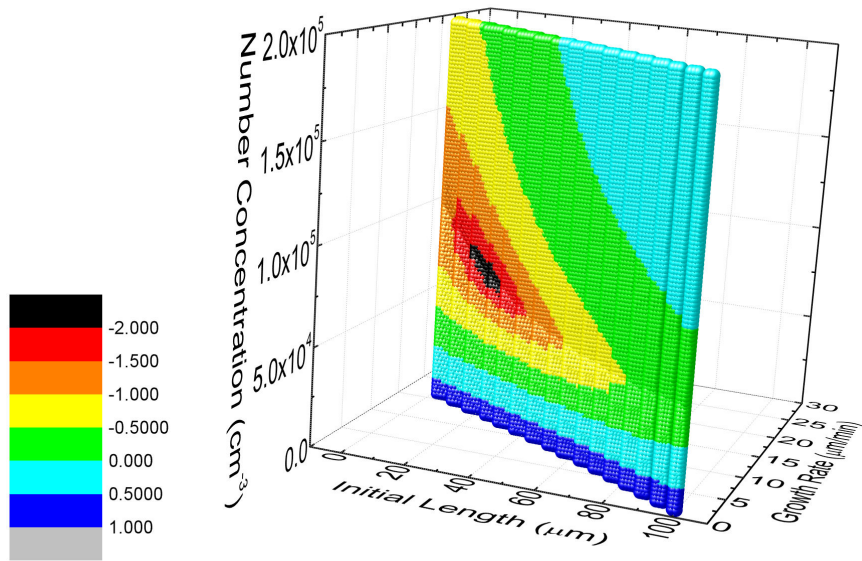
Figure 8. 13
Model solutions for 700 ml/min flow rates into mixer transmission data.
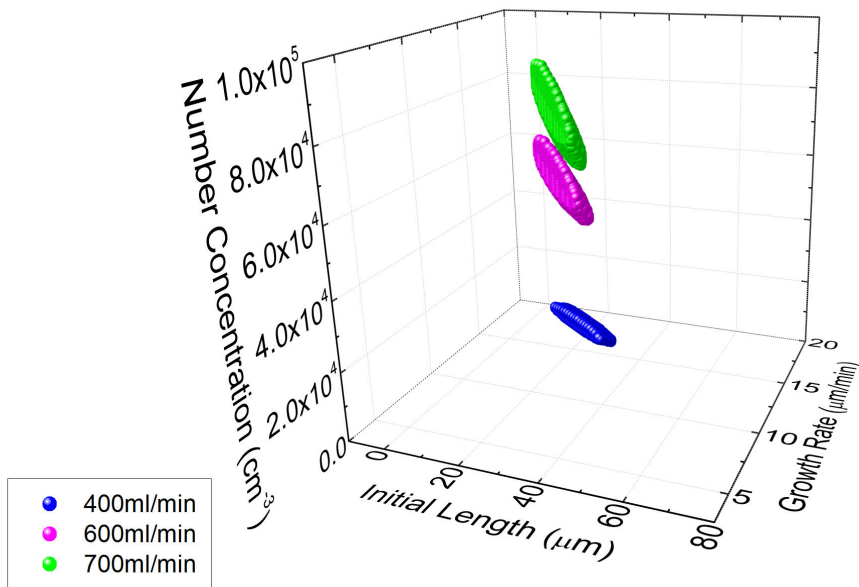
Figure 8. 14
Model solutions which corresponded to $\log(SSR) \leq -2$.
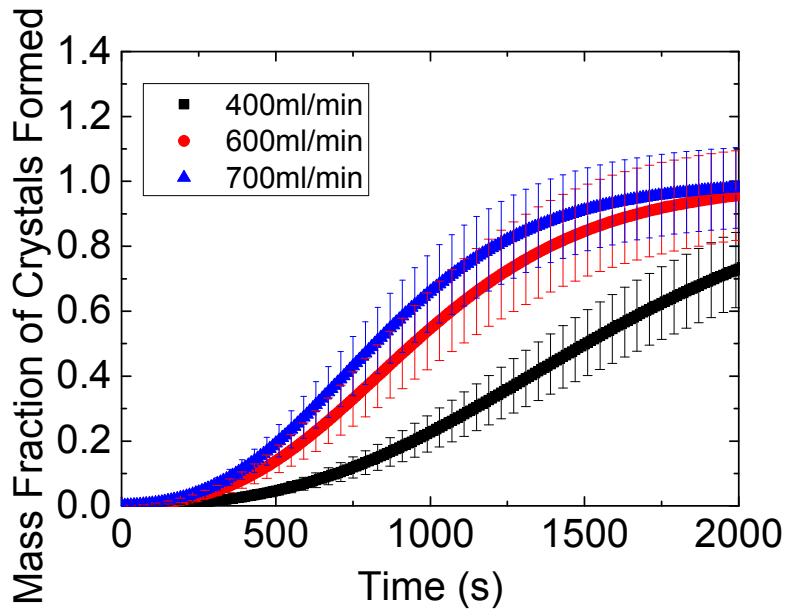
Figure 8. 15
Mass fraction of crystals formed using theoretical mass balance.

The solutions to the model that had the lowest residuals were of a relatively narrow range for each condition studied. The material balances showed that the theoretical total mass of crystals formed with time compared fairly well to the experimental measurements of the mass evolution of crystals[12, 13]. This served as a further check that solutions to the model were sensible. The several simplifying assumptions made for the model, such as monodisperse, homogenous cuboids, may account for the differences and the model could be modified to be more applicable to the system studied if needed.

Non-linear least squares fitting of Eqn. (8. 18) to the experimental data resulted in a wide range of solutions (extremely large confidence intervals) as it did not take the sedimentation time of the cuboids into consideration. Including the comparison of the experimental and theoretical sedimentation time was therefore important to limit the range of possible solutions. Another possibility to limit solutions would have been to obtain reliable growth rate data to eliminate it as a variable. Some of the assumptions made in the model may not be justified for more complex systems, such as those that are highly polydisperse, have highly variable growth rates and where nucleation is on-going. The simple principles behind this model, however, can be adapted to suit such a system.

8.6 Conclusions

A simple model to estimate nucleation rates from transmission measurements was produced. It was based on analysing the extinction of light incident on a sample of growing crystals under quiescent conditions. The extinction of light was assumed to be a result of the scattering of light by a constant number concentration of growing cuboids, much larger than the wavelength of incident light. A theoretical expression for the transmission of light through the sample was obtained, and this was fitted to experimental data and solved for the number concentration of cuboids, cuboid growth rates and initial cuboid sizes. It was ensured that the theoretical sedimentation time of the cuboids matched experimentally observed sedimentation times to narrow the possible solutions. A material balance was used to check the reliability of the model's solutions. Although the analysis carried out was based on cuboids, it could easily be applied to other particle shapes.

8.7 Summary

- A simple model to estimate nucleation rates from transmission measurements was produced.

- It was based on analysing the extinction of light incident on a sample of growing crystals under quiescent conditions.

- A theoretical expression for the transmission of light through the sample was obtained, and this was fitted to experimental data and solved for the number concentration of cuboids.

- The theoretical sedimentation time of the cuboids was matched to experimentally observed sedimentation times to limit the possible solutions.

- A material balance was used to check the reliability of the model's solutions.

- The model was based on cuboids but could easily be adapted to suit other particle shapes.

8.8 References and Nomenclature

8.8.1 References

(1)   Kadam, S. S.; Kramer, H. J. M.; ter Horst, J. H., Combination of a Single Primary Nucleation Event and Secondary Nucleation in Crystallization Processes. *Crystal Growth & Design* **2011,** 11, (4), 1271-1277.

(2)   Kulkarni, S. A.; Kadam, S. S.; Meekes, H.; Stankiewicz, A. I.; ter Horst, J. H., Crystal Nucleation Kinetics from Induction Times and Metastable Zone Widths. *Crystal Growth & Design* **2013,** 13, (6), 2435-2440.

(3)   Vekilov, P. G.; Galkin, O., On the methods of determination of homogeneous nucleation rates of protein crystals. *Colloids and Surfaces a-Physicochemical and Engineering Aspects* **2003,** 215, (1-3), 125-130.

(4)   Galkin, O.; Vekilov, P. G., Direct determination of the nucleation rates of protein crystals. *Journal of Physical Chemistry B* **1999,** 103, (49).

(5)   Ildefonso, M.; Candoni, N.; Veesler, S., Using Microfluidics for Fast, Accurate Measurement of Lysozyme Nucleation Kinetics. *Crystal Growth & Design* **2011,** 11, (5).

(6)   Kadam, S. S.; Kulkarni, S. A.; Ribera, R. C.; Stankiewicz, A. I.; ter Horst, J. H.; Kramer, H. J. M., A new view on the metastable zone width during cooling crystallization. *Chemical Engineering Science* **2012,** 72, 10-19.

(7)   Kubota, N., Effect of sample volume on metastable zone width and induction time. *Journal of Crystal Growth* **2012,** 345, (1), 27-33.

(8)   Wantha, L.; Flood, A. E., Nucleation Kinetics of the gamma-Polymorph of DL-Methionine. *Chemical Engineering & Technology* **2012,** 35, (6), 1024-1030.

(9)   Selimovic, S.; Jia, Y. W.; Fraden, S., Measuring the Nucleation Rate of Lysozyme using Microfluidics. *Crystal Growth & Design* **2009,** 9, (4), 1806-1810.

(10)   Jiang, S. F.; ter Horst, J. H., Crystal Nucleation Rates from Probability Distributions of Induction Times. *Crystal Growth & Design* **2011,** 11, (1), 256-261.

(11)   Mullin, J. W., *Crystallization*. 4th ed.; Heineman: 2002.

(12)   Brown, A. Characterisation of Turbulent Mixing and its Influence on Antisolvent Crystallisation (PhD thesis). University of Strathclyde, 2012.

(13)   Schacht, U. Control of nucleation in continuous crystallisation processes (PhD thesis). University of Strathclyde, 2014.

(14)   Rhodes, M., *Introduction to Particle Technology*. 2nd ed.; 2008.

(15)   Leith, D., Drag On Nonspherical Objects. *Aerosol Science and Technology* **1987,** 6, (2), 153-161.

(16)   Ku, H. H., Notes On Use Of Propagation Of Error Formulas. *Journal of Research of the National Bureau of Standards Section C-Engineering and Instrumentation* **1966,** C 70, (4), 263-265.

8.8.2 Main Nomenclature

A = absorbance

C^* = solute's solubility

C_0 = initial solute concentration and is the solute's solubility

C^{sca} = average scattering cross section of the particles

C_i^{abs} = absorption cross section of particle i

C_i^{ext} = extinction cross section of particle i

C_i^{sca} = scattering cross section of particle i

c = y intercept of $G_L(t)$ versus $S(t)$

D = vertical distance between top of solution and light beam

D_n = diameter of sphere whose projected area is the same as the projected area of the cuboid, normal to the direction of flow

D_s = diameter of sphere with same effective surface area as the cuboid

D_v = diameter of sphere with same volume as cuboid

F_D = total drag force experienced in creeping flow

G_L = length growth rate

δG_L = error in the crystal growth rate calculated

G_H = thickness growth rate

G_R = radial growth rate.

G_W = width growth rate

H = cuboid thickness (height)

H_0 = initial cuboid thickness (height)

i = largest value of $\log(SSR)$ that generally gave good fits to the experimental data

K_n = dynamic shape factor

L = optical path length or cuboid length

δL = error in the crystal length calculated

L_0 = initial cuboid length

δL_0 = standard deviation of L_0 values for model solutions where $\log(SSR) \leq i$

M = mass of crystals per unit volume

δM = error in the theoretical mass concentration calculated

m = gradient of $G(t)$ versus $S(t)$.

N = total number of particles per unit volume

δN = standard deviation of N values for model solutions where $\log(SSR) \leq i$

N_i= number of particles i per unit volume

n= number of types of particle or last transmission data point used in analysis

r_0 = initial radius of the sphere

S = supersaturation

SSR= sum of squares of the residuals

T = transmission of light through a sample

$T_{expt}(t)$= experimental transmission

$T_{theo}(t)$= theoretical transmission

t= time

t_n = time over which nucleation was occurring

v= settling velocity

W = cuboid width

W_0 = initial cuboid width

$XSA(\theta)$= geometric cross section at angle θ

α = cuboid thickness dimension ratio (length/ thickness (height))

β= cuboid width dimension ratio (length/ width)

η= fluid viscosity (dynamic)

ρ_p = density of the cuboids

ρ_f= density of the surrounding fluid

θ= angle of vertically aligned cuboid

τ= attenuation coefficient

9. Conclusions and Future Work

9.1 Conclusions

The main conclusions from this work are summarised below.

Equipment was designed and used for experiments.

Bespoke flow setups (Couette and capillary) were designed and constructed to allow the influence of controlled fluid shear on crystal nucleation to be studied. Using these devices was advantageous since fluid shear could be quantified and controlled.

To monitor solutions while they underwent controlled fluid shear in the flow devices, a custom made setup which measured the transmission of light through a sample while it was being sheared was designed and constructed. Light scattered by the sample at 90° could also be measured simultaneously. Induction times were obtained from these measurements as the onset of crystallisation caused solutions to rapidly become turbid, resulting in a sharp decrease in transmission and increase in scattering. Imaging was also used as a tool to obtain induction times as crystallisation resulted in a sharp increase in the mean pixel intensity.

To improve understanding of what was happening in solutions at small length scales (in the order of a few hundred nanometres), dynamic light scattering hardware was setup to allow in-situ measurements to be taken from solution contained within the Couette cell.

Controlled fluid shear was found to increase the rate of primary nucleation in aqueous glycine solutions.

The Couette and capillary flow devices were used to expose supersaturated, aqueous glycine solutions to well-controlled fluid shear under isothermal conditions. Average shear rates between 25 s^{-1} and 1000 s^{-1} were studied and induction times were measured. Great care was taken to eliminate any seeding in order to avoid secondary nucleation preceding the formation of the first crystals through primary nucleation.

Induction times obtained under shearing in the Couette and capillary setups were found to be considerably lower than those in unsheared solutions. The probability distributions of the induction times appeared to closely follow a distribution based on a previously published model by Jiang and ter Horst[1]. Using their model, where the induction time is related to the rate of formation of primary nuclei and the time it takes them to grow to the size where the secondary nucleation becomes significant, it was found that both the primary nucleation rate and the growth time were strongly dependent on the shear rate imposed. Moreover, increasing the average shear rate reduced the mean induction time in a power law relationship: $t_{ind} \propto \dot{\gamma}_{avg}^{-0.61 \pm 0.16}$. Due to the stochastic nature of nucleation, experiments were repeated multiple times and a detailed statistical analysis, which involved bootstrapping and Monte Carlo simulations, was carried out to ensure that the number of repetitions was sufficient for trends to be statistically valid.

<u>Exposing aqueous glycine solutions to increased surface areas was found to increase the rate of primary nucleation.</u>

Further Couette flow induction time experiments were carried out to investigate the influence of the surface area that supersaturated glycine solutions were exposed to, as well as the effect of fluid shear. A wide range of average shear rates (25 s^{-1} to 250 s^{-1}) were used and the surface area that solution was exposed to was varied (2.5 cm^2 per ml solution to 10 cm^2 per ml solution). Care was taken to ensure that the first crystals formed through primary nucleation, and due to the stochastic nature of nucleation, experiments were repeated multiple times.

Induction times obtained under shearing were found to be considerably lower than those in unsheared solutions for each of the surface to volume ratios used, with higher surface to volume ratios resulting in shorter induction times. The model proposed by Jiang and ter Horst showed that as the shear rate and surface area increased, the primary nucleation rate increased and growth time decreased. The induction times were found to decrease with increased shear rates and increased surface areas in a power law relationship: $t_i \propto (\dot{\gamma}_{avg} A)^{-0.83 \pm 0.2}$. The probability distributions of induction times were found to scale with shear rate and surface area. This suggested that all processes that took place during nucleation were measured on one key timescale, which was proportional to $\frac{1}{\dot{\gamma}_{avg} A}$. These findings therefore

suggested that the total deformation of solutions and the surface area that solutions were exposed to were important in determining induction times and hence rates of primary nucleation. Reasons behind the role that fluid shear and surface had on the nucleation of glycine is unclear but surface and shear enhanced cluster aggregation was the most likely mechanism.

<u>Exposing aqueous glycine solutions to controlled fluid shear may have resulted in the coalescence of mesoscale clusters, which led to a more rapid nucleation pathway.</u>

Dynamic light scattering studies of aqueous glycine solutions that had been sheared in the Couette cell suggested that shearing resulted in the average hydrodynamic radius of mesoscale clusters (nanodroplets) that exist in aqueous glycine solutions increasing with increasing durations of applied shear. A detailed analysis of data was carried out to ensure that the trends seen were valid.

The rate of increase in average hydrodynamic radius appeared to be a function of the shear rate and surface area that solutions were exposed to, with larger shear rates and surface areas resulting in higher rates of increase. Since increased shear rates and surface areas also led to shorter induction times and hence higher rates of primary nucleation, patterns seen in the increase in average hydrodynamic radius with increased exposure to fluid shear and surface suggested that there was a link between cluster size and the onset of nucleation. The shear and surface enhanced coalescence of clusters is a possible explanation for the increases in cluster size observed.

<u>Altering the pH away from the isoelectric point and adding sodium chloride was found to reduce the concentration of mesoscale clusters in glycine solutions.</u>

Dynamic light scattering studies suggested that when the pH of glycine solutions was moved away from neutral conditions (close to the isoelectric point), a decrease in the concentration of mesoscale clusters occurred. The decrease in mesoscale cluster concentration appeared to correlate with the presence of more significant fractions of anions or cations. Since γ-glycine formation is also associated with the pH conditions where the cluster population was found to be lower, the mesoscale clusters may potentially be linked to the nucleation of α-glycine or γ-glycine.

The addition of sodium chloride to aqueous glycine solutions resulted in the concentration of the mesoscale clusters decreasing. The reduction in clustering could potentially be a result of sodium chloride contributing to an ionic environment, resulting in the charging of glycine molecules and ultimately reducing the likelihood of liquid-like clusters forming. The addition of sodium chloride is well known to affect the polymorphic outcome, and there were strong similarities between the sodium chloride concentrations that were found to result in immeasurable concentrations of clusters, and the sodium chloride concentrations found to result in the nucleation of γ-glycine (rather than α- glycine) from literature[2].

The results obtained by investigating the effect of pH and addition of sodium chloride on mesoscale clustering therefore indicated that pH and the presence of sodium chloride may influence the arrangement of molecules in solution, and the concentration of mesoscale clusters in the solutions may be linked to glycine polymorphism.

<u>A basic model was produced to estimate nucleation rates from transmission measurements.</u>

A simple model to estimate nucleation rates from transmission measurements was produced. It was based on analysing the extinction of light incident on a sample of growing crystals under quiescent conditions. The extinction of light was assumed to be a result of the scattering of light by a constant number concentration of growing cuboids, much larger than the wavelength of incident light. A theoretical expression for the transmission of light through the sample was obtained, and this was fitted to experimental data and solved for the number concentration of cuboids. It was ensured that the theoretical sedimentation time of the cuboids matched experimentally observed sedimentation times to narrow the possible solutions. A material balance was used to check the reliability of the model's solutions.

<u>General Conclusions</u>
The research carried out for this thesis showed that the primary nucleation of glycine in aqueous solutions can be strongly influenced by fluid shear, with increased shear rates leading to higher rates of primary nucleation. Exposing solutions to increased surface areas also resulted in increased rates of primary nucleation. By subjecting

solutions to flow conditions where shear rates could be well quantified, experiments could be done in a controlled manner and allow quality data to be obtained.

The increased rates of primary nucleation seen with exposure to increased shear rates and surface areas were thought to be due to the coalescence of liquid-like, mesoscale clusters, with the larger coalesced clusters leading to a more rapid nucleation pathway. Coalescence was enhanced by exposing solutions to increased shear rates and surface areas.

The mesoscale clusters were found to be strongly influenced by the pH of the solutions and the addition of sodium chloride. The use of pH values away from the isoelectric point and the addition of sodium chloride were found to reduce the concentration of clusters.

Due to the suspected role of mesoscale clusters in the nucleation of glycine from aqueous solution, classical nucleation theory does not apply well to the glycine system studied, and some form of non-classical mechanism that involves the role of mesoscale clusters is more likely.

9.2 Future Work

This work has produced some useful conclusions and ideas but there are various areas of future work that would be useful to strengthen and broaden the work carried out here and advance the research done in this area.

Couette flow cells that allow for easier alignment could be worth designing. The current design required re-aligning each time they were used which was fairly time consuming. The use of x, y, z stages, etc. could make alignment easier and more robust.

Only one Couette flow experiment could be carried out at a time, which meant that it took a long time to obtain experimental data. It would therefore be useful to have multiple Couette cells setup and monitored simultaneously to allow large data sets to be obtained more quickly. Using imaging, rather than transmission measurements would be a cheaper and easier way to monitor multiple experiments simultaneously.

The development of other controlled flow geometries would be interesting e.g. cone and plate or parallel plate geometries. Refining the quantitative means of measuring induction times for use with the capillary setup would help reduce uncertainty in capillary based experiments.

The use of improved temperature control would be beneficial to ensure that supersaturations were known more accurately. A way to monitor the temperature of the solutions while they were being sheared would also be useful. A way to do this non-intrusively would be through the use of an infrared thermometer.

The use of magnetic stirrers is a quick and easy way to obtain induction time data for solutions that are being sheared since multiple experiments can be carried out simultaneously by using a multi-vial stirrer plate. Experiments can also be carried out in sealed bottles, so samples can be redissolved and reused, making experiments less cumbersome and tedious that the Couette cell experiments. Drawbacks, however, are that the shear is uncontrolled and unquantifiable, particularly due to the interaction of the stirrer bar and the bottom of the vial.

The model by Jiang and ter Horst used to obtain nucleation rates from induction times was fairly basic and involved many simplifying assumptions, such as a

constant nucleation rate. It was based on forming at least one crystal through primary nucleation during a nucleation time but it did not specify how many crystals. Since the growth times calculated appeared to be influenced by the surface area that solutions were exposed to, this suggested that a single nucleus mechanism may not have been occurring (discussed in Chapter 5). It could therefore be worthwhile further developing the model to deal with a polynuclear mechanism, which may have occurred and also varying nucleation rates.

The current understanding of crystal nucleation from solution is still lacking so perhaps carrying out more fundamental experiments would be advantageous before focussing on factors such as the influence of fluid shear. Further dynamic light scattering measurements could be a good way to do this and could also help to understand the composition and role of clusters and the mechanism of cluster formation. The effect of pH and addition of sodium chloride on the mesoscale clusters in glycine solutions were interesting findings, particularly since it suggested that the presence of clusters may be linked to polymorphism. It would be useful to carry out a wide range of light scattering experiments with supersaturated solutions and eventually check the polymorph of the crystals that form. It would also be interesting to monitor the glycine clusters over time, for example, one could initially begin with an aqueous solution (which would have a measurable population of clusters) and take measurements from it. Then salt could be added to the sample or the pH could be adjusted and the decrease in concentration of clusters over time could be monitored. The influence of filtration on cluster populations would also be worth investigating, particularly due to the unsteady state at which the syringe filters operate. The use of computer modelling work would also be helpful to gain an improved understanding of the role, composition and structure of glycine clusters.

Since coalesced clusters, thought to have formed due to fluid shear, were associated with increased nucleation rates, it would be interesting to investigate the influence of fluid shear on nucleation rates in solutions where the cluster population was lower e.g. under acidic conditions.

Studying the crystallisation of compounds other than glycine would be very useful to see whether the behaviour displayed by glycine could be generalised. The use of compounds with high solubilities and temperature dependence on solubility would be good since detectable quantities of crystals would form more easily than if

compounds with lower solubilities and temperature dependence were used. Using compounds with high growth rates, such as urea, ammonium chloride and citric acid (see Section 9.3), are also worth studying as these would close to eliminate the growth time required for crystallisation to reach a detectable level. This would reduce the uncertainty of the growth time aspect of the Jiang and ter Horst model. Studying other amino acids would be useful, as well as other solutions which show mesoscale clustering. The influence of pH and the addition of sodium chloride on these would be interesting. DLS studies of urea would be particularly interesting, particularly monitoring the clusters over time and after shearing (see Section 9.3).

The model that was produced to estimate nucleation rates from transmission measurements could be further adapted, for example, for particles with geometries other than cuboids or spheres. Literature obtained growth rates could be used instead of estimating them in the model. This would eliminate growth rates as a variable. The model also assumed that no nucleation took place during the transmission measurements, so terms for continuing nucleation could be added in if this was thought to occur in the system under investigation. If more information was known about secondary nucleation kinetics, terms for secondary nucleation could be included and the model could then be applied to systems where solutions were agitated and secondary nucleation was occurring.

9.3 Influence of Fluid Shear on the Nucleation of Urea from Aqueous Solution

Preliminary experiments to investigate the influence of fluid shear on the nucleation of urea from aqueous solutions were carried out in the Couette cell and showed that urea crystallisation from aqueous solution was strongly influenced by fluid shear, but it was affected differently than glycine. The procedures carried out were similar to those outlined for glycine experiments in the thesis (see Chapter 4). It was found that, for the supersaturations used $(1.40)^3$, urea solutions crystallised within the first 10 seconds of cylinder rotation (agitation). This happened for all shear rates tested. An example of how transmission through the sample varied with time when the motor was switched on is given in Figure 9. 1.

The growth rate of urea is very high[4] and when solutions were seeded, they rapidly became clouded by crystals, even when not agitated (widespread crystallisation became visible within 5 seconds). This meant that it was unlikely that small crystals which could not be seen by eye were present in the solutions when agitation was commenced, as these would rapidly have grown to visible levels. This, in conjunction with the strict procedures that were carried out in order to eliminate seeding of solutions, indicated that something which could not have been a crystal, was present in urea solutions and triggered nucleation when agitated.
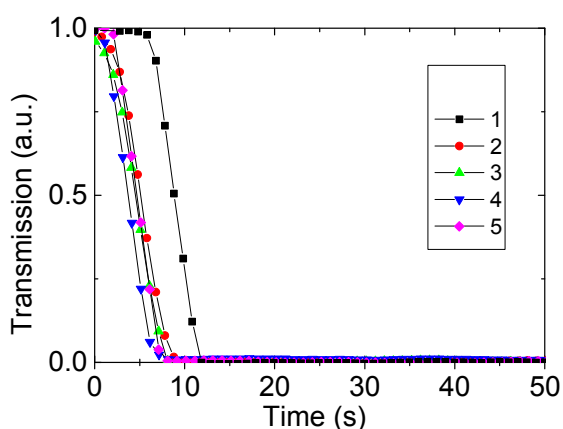
Figure 9. 1
Urea transmission measurement data (25 s^{-1} average shear rate). 1-5 are experimental repetitions.

These findings were further investigated by international project students (Danielle Trap, France and Leticia Maria Sampaio Barros, Brazil), where it was found that Couette cell experiments either resulted in the crystallisation of solution within the first few seconds of agitation, or solutions would not crystallise over an extended period of agitation. The experiments where the solution did not nucleate were thought to be due to the solution's temperature increasing while the fluid was sheared (solutions were fairly viscous), or due to heat from the motor causing the overall temperature inside the incubator to increase. This would have lowered the supersaturation and therefore driving force for nucleation.

Experiments were also carried out where urea solutions were agitated using a magnetic stirrer using a wide range of rotational rates (150 rpm to 900 rpm). Results for this showed some similarities with the Couette flow results for example, during the first few seconds of agitation by magnetic stirrer, many samples (up to 80%) would crystallise. Several samples, however, would take longer to nucleate (minutes to hours, rather than seconds). Further investigation of the first few seconds of agitation were studied by waiting for fixed periods of time after the vials had cooled to ambient temperature before commencing agitation. It was found that the longer the vials were left isothermally unstirred, the greater the fraction of vials that crystallised during the first few seconds of agitation.

The findings with urea therefore strongly suggested that something which could not have been a crystal was present in aqueous urea solutions and when agitated, could induce nucleation. It would be interesting to do dynamic light scattering studies on urea solutions (before and after shearing, as well as for quiescent solutions left to age for different times) to see whether mesoscale clusters[5] were likely to have been affected by the fluid shear and/ or the time that they were left isothermally unstirred.

9.4 References

(1)   Jiang, S. F.; ter Horst, J. H., Crystal Nucleation Rates from Probability Distributions of Induction Times. *Crystal Growth & Design* **2011,** 11, (1), 256-261.

(2)   Yang, X.; Lu, J.; Wang, X.-J.; Ching, C.-B., Effect of sodium chloride on the nucleation and polymorphic transformation of glycine. *Journal of Crystal Growth* **2008,** 310, (3), 604-611.

(3)   Lee, F. M.; Lahti, L. E., Solubility Of Urea In Water-Alcohol Mixtures. *Journal of Chemical and Engineering Data* **1972,** 17, (3), 304-&.

(4)   Piana, S.; Reyhani, M.; Gale, J. D., Simulating micrometre-scale crystal growth from solution. *Nature* **2005,** 438, (7064), 70-73.

(5)   Garetz, B. A.; Aber, J. E.; Goddard, N. L.; Young, R. G.; Myerson, A. S., Nonphotochemical, polarization-dependent, laser-induced nucleation in supersaturated aqueous urea solutions. *Physical Review Letters* **1996,** 77, (16), 3475-3476.

Appendix

Appendix 1 Design of Experiments (DoE) Minitab Statistical Analysis Theory (Chapter 5)

The main theory behind a 2 factor factorial experiment in given here. The theory summarises the calculations carried out by Minitab for DoE analyses. Full theory and explanations can be found in texts such as Montgomery's Applied Statistics and Probability for Engineers [1, 2].

A1.1 DoE Theory Introduction

For simplicity, factors will be referred to as A and B and their levels will be denoted i and j respectively. Each replicate is denoted k. The main table produced from a Minitab analysis includes the following headings: sum of squares; degrees of freedom; mean square, f_0 and P value. The steps required to calculate each value is addressed in this section, and the significance of what is calculated i.e. how one can deduce which factors/ interactions have an effect, is described.

An observation at a particular treatment (factor level combination) can be described by a linear statistical model[1, 2]. The theory given here is simplified to assume that each treatment is repeated n times. In practice, the number of repetitions of each treatment varied (see Chapter 5).

$$y_{ijk} = \mu + \tau_i + \beta_j + (\tau\beta)_{ij} + \epsilon_{ijk}$$

Here:

$i = 1, 2, \ldots, a$

$j = 1, 2, \ldots, b$

$k = 1, 2, \ldots, n$

i= level of factor A

a= number of levels of factor A

j= level of factor B

b= number of levels of factor B

k= replicate

n= number of replicates

y_{ijk}= observation made during the kth replicate for level i of factor A and level j of factor B.

μ= overall mean effect

τ_i= effect of the ith level of factor A

β_j= effect of the jth level of factor B

$(\tau\beta)_{ij}$= effect of the interaction between A and B

ϵ_{ijk}=random error component

For the experiments carried out, A and B are fixed factors as they are chosen by the experimenter. The effects (τ_i, β_j and $(\tau\beta)_{ij}$) are defined as deviations from the mean so that:

$$\sum_{i=1}^{a} \tau_i = 0$$

$$\sum_{j=1}^{b} \beta_j = 0$$

$$\sum_{i=1}^{a} (\tau\beta)_{ij} = 0$$

$$\sum_{j=1}^{b} (\tau\beta)_{ij} = 0$$

It is assumed that the errors are normally and independently distributed, with a mean of zero and variance σ^2. This means that for each treatment, the observations (and residuals) should be normally and independently distributed[1, 2].

A1.2 Hypothesis Testing and ANOVA

For the analysis, hypothesis testing is carried out using ANOVA (analysis of variance); since there are 2 factors, it can be called a two-way analysis of variance. The two-way analysis of variance procedure tests the equality of population means when there are two fixed factors[1].

The hypotheses tested are:

No main effect for factor A

$H_0: \tau_1 = \tau_2 = \cdots = \tau_a = 0$

$H_1: at\ least\ one\ \tau_i \neq 0$

No main effect for factor B

$H_0: \beta_1 = \beta_2 = \cdots = \beta_j = 0$

$H_1: at\ least\ one\ \tau_i \neq 0$

No interaction effect between A and B

$H_0: (\tau\beta)_{11} = (\tau\beta)_{12} = \cdots = (\tau\beta)_{ab} = 0$

$H_1: at\ least\ one\ (\tau\beta)_{ij} \neq 0$

ANOVA tests these hypotheses by breaking down the total variability (total sum of squares of the observations) into component parts, and the components are then compared and analysed[1, 2].

A1.3 Sum of Squares

The total sum of squares SS_T can symbolically be broken into:

$$SS_T = SS_A + SS_B + SS_{AB} + SS_E$$

SS_T= total sum of squares

SS_A= sum of squares for factor A

SS_B= sum of squares for factor B

SS_{AB}= sum of squares for the ineraction between A and B

SS_E= error sum of squares

The total sum of square SS_T and its decomposition can be written algebraicly as[1, 2]:

$$SS_T = \sum_{i=1}^{a} \sum_{j=1}^{b} \sum_{k=1}^{n} \left(y_{ijk} - \bar{y}_{...} \right)^2$$

$$= bn \sum_{i=1}^{a} \left(\bar{y}_{i..} - \bar{y}_{...} \right)^2 + an \sum_{j=1}^{b} \left(\bar{y}_{.j.} - \bar{y}_{...} \right)^2 + n \sum_{i=1}^{a} \sum_{j=1}^{b} \left(\bar{y}_{ij.} - \bar{y}_{i..} - \bar{y}_{.j.} - \bar{y}_{...} \right)^2$$

$$+ \sum_{i=1}^{a} \sum_{j=1}^{b} \sum_{k=1}^{n} \left(y_{ijk} - \bar{y}_{ij.} \right)^2$$

Where:

Dot subscripts imply summation over the subscript that it replaces.

$y_{i..}$ is the total of all observations taken at the ith level of factor A and $\bar{y}_{i..}$ is the mean value.

$$y_{i..} = \sum_{j=1}^{b} \sum_{k=1}^{n} y_{ijk}$$

$$\bar{y}_{i..} = \frac{y_{i..}}{bn}$$

$y_{.j.}$ is the total of all observations taken at the jth level of factor B and $\bar{y}_{.j.}$ is the mean value.

$$y_{.j.} = \sum_{i=1}^{a} \sum_{k=1}^{n} y_{ijk}$$

$$\bar{y}_{.j.} = \frac{y_{.j.}}{an}$$

$y_{ij.}$ is the total of all observations made at the treatment (factor level combination) of the ith level of factor A combined with the jth level of factor B and $\bar{y}_{ij.}$ is its mean value.

$$y_{ij.} = \sum_{k=1}^{n} y_{ijk}$$

$$\bar{y}_{ij.} = \frac{y_{ij.}}{n}$$

$y_{...}$ is the grand total of all observations and $\bar{y}_{...}$ is the mean value.

$$y_{...} = \sum_{i=1}^{a} \sum_{j=1}^{b} \sum_{k=1}^{n} y_{ijk}$$

$$\bar{y}_{...} = \frac{y_{...}}{abn}$$

A1.4 Degrees of Freedom

Degrees of freedom is the number of independent and fair comparisons that can be made from a set of data i.e. it is the number of values in the final calculation of a statistic that are free to vary. For DoE, the number of degrees of freedom for a main effect is equal to the number of levels for that factor minus one[1, 2].

Main Effect	Degrees of Freedom
Factor A	$a - 1$
Factor B	$b - 1$

The degrees of freedom for an interaction is equal to the product of the degrees of freedom associated with each factor involved in that particular interaction effect.

Interaction Effect	Degrees of Freedom
AB interaction	$(a - 1)(b - 1)$

The degrees of freedom for error is equal to the product of the number of levels for each factor and the number of replicates minus one. This arises since for each treatment, there are $(n - 1)$ degrees of freedom, and observations made for a particular treatment can only differ due to random error. There are ab treatments in total.

	Degrees of Freedom
Error	$ab(n - 1)$

The number of degrees of freedom for the entire experiment is equal to the total number of observations minus one.

	Degrees of Freedom
Total	$abn - 1$

A1.5 Mean Squares

Mean squares are obtained by dividing a sum of squares by its corresponding degrees of freedom[1, 2].

	Mean Square
Factor A	$MS_A = \dfrac{SS_A}{a - 1}$
Factor B	$MS_B = \dfrac{SS_B}{b - 1}$
AB Interaction	$MS_{AB} = \dfrac{SS_{AB}}{(a - 1)(b - 1)}$
Error	$MS_E = \dfrac{SS_E}{ab(n - 1)}$

MS_A = mean square for factor A

MS_B = mean square for factor B

MS_{AB} = mean square for AB interaction

MS_E = mean square for error

A1.6 F Test

To test the null hypothesis that that the factor/ interaction effects are equal to zero i.e. are insignificant, the ratio of the factor or interaction mean square and the error mean square is used to obtain a parameter f_0, the F statistic[1,2].

F test for factor A

To test the null hypothesis that factor A has no effect on the response ($H_0: \tau_1 = \tau_2 = \cdots = \tau_a = 0$), the following ratio is used to obtain the F statistic:

$$f_0 = \frac{MS_A}{MS_E}$$

This has an F-distribution with $a - 1$ and $ab(n - 1)$ degrees of freedom if the null hypothesis is true. The null hypothesis is rejected at the level of significance α if

$$f_0 > \alpha, a - 1, ab(n - 1)$$

F test for factor B

To test the null hypothesis that factor B has no effect on the response ($H_0: \beta_1 = \beta_2 = \cdots = \beta_j = 0$), the following ratio is used to obtain the F statistic:

$$f_0 = \frac{MS_B}{MS_E}$$

This has an F-distribution with $b - 1$ and $ab(n - 1)$ degrees of freedom if the null hypothesis is true. The null hypothesis is rejected at the level of significance α if

$$f_0 > \alpha, b - 1, ab(n - 1)$$

F test for AB interaction

To test the null hypothesis that the interaction between A and B has no effect on the response ($H_0: (\tau\beta)_{11} = (\tau\beta)_{12} = \cdots = (\tau\beta)_{ab} = 0$), the following ratio is used to obtain the F statistic:

$$f_0 = \frac{MS_{AB}}{MS_E}$$

This has an F-distribution with $(a-1)(b-1)$ and $ab(n-1)$ degrees of freedom if the null hypothesis is true. The null hypothesis is rejected at the level of significance α if

$$f_0 > \alpha, (a-1)(b-1), ab(n-1)$$

A1.7 P-Value

The p-value is the level of significance that would lead to rejection of the null hypothesis. If the p-value is less than or equal to α, it can be concluded that the effect is significant. If the p-value is greater than α, it can be concluded that the effect is not significant[1, 2].

A1.8 Residuals

Analysis of the residuals from the ANOVA procedure gives a good indication of model adequacy. The residuals from a 2 factor factorial are:

$$e_{ijk} = y_{ijk} - \bar{y}_{ij.}$$

i.e. an observation for a particular factor level combination minus the mean of all the replicates for the particular factor level combination. A normality plot of the residual gives a good indication that the normality assumption made for the analysis was valid.

A1.9 Normal plots

Normal plots of the residuals can be produced by plotting the residuals against their cumulative frequency on normal probability plotting paper. First the residuals are ordered from smallest to largest and numbered $(x_1, x_2, ..., x_n)$ with x_n being the largest[1, 2]. The ordered residuals x_j were then plotted against their observed cumulative frequency, which was calculated from

$$cumulative\ frequency = \frac{j - 0.5}{n}$$

n= total number of residuals

j= number associated with an ordered residual

If data followed the assumed normal distribution, the plots would form approximately a straight line. If they deviated strongly from a straight line, it could be concluded that the normality assumption was not appropriate.

A1.10 Summary Table

Source of Variation	Sum of Squares	Degrees of Freedom	Mean Square	f_0 (F Test)	Reject null hypothesis if	P Value
Factor A	SS_A	$a-1$	$MS_A = \dfrac{SS_A}{a-1}$	$\dfrac{MS_A}{MS_E}$	$f_0 > \alpha, a-1, ab(n-1)$	
Factor B	SS_B	$b-1$	$MS_B = \dfrac{SS_B}{b-1}$	$\dfrac{MS_B}{MS_E}$	$f_0 > \alpha, b-1, ab(n-1)$	
Interaction between A and B	SS_{AB}	$(a-1)(b-1)$	MS_{AB} $= \dfrac{SS_{AB}}{(a-1)(b-1)}$	$\dfrac{MS_{AB}}{MS_E}$	$f_0 > \alpha, (a-1)(b-1), ab(n-1)$	
Error	SS_E	$ab(n-1)$	$MS_E = \dfrac{SS_E}{ab(n-1)}$			
Total	SS_T	$abn-1$				

Appendix 2 Additional DLS Information (Chapter 6)

A2.1 Regularisation

The general structure of the regularisation function is[3]:

$$R\big(G(\Gamma)\big) = \int_{\Gamma_{min}}^{\Gamma_{max}} G^{(n)}(\Gamma)d\Gamma$$

Here R is the regulariser function and n is the nth differentiation of $G(\Gamma)$ with respect to Γ.

For the CONTIN analyses performed here, a zero order regulariser was used and it tried to keep the 'total mass' in the system as small as possible: the area under the function $G(\Gamma)$ was minimised. Another option was to use a second order regulariser which would have tried to minimise the 2nd derivative of the distribution function i.e. it tried to get a smoother function. These types of regulariser were very general. The choice of regulariser was not very important since due to the relatively low data quality and small number of extractable degrees of freedom, each type of regulariser would not be able to show its distinct features[3].

For fitting, the regularisation term along with a term for the sum of the square of the residuals of the fit to the data, were minimised[3, 4]:

$$Min = \sum_{i}^{M} w_i\big(g_i^{expt} - g_i^{model}\big)^2 + \alpha R^2$$

Here α is the strength of regulariser, $i = 1, 2, …, M$, M is the number of data points, g_i^{expt} is an experimental data point , g_i^{model} is a value predicted by the model, $w_i = \frac{1}{\sigma_i^2}$ is a weighting factor.

The strength of the regularisation is set by the factor α. This was optimised during the fitting process. If $\alpha = 0$, or is very small, the solution will be equivalent to a standard least squares fit to the data, whereas if α is larger, the regulariser becomes

more influential and solutions with many peaks will be penalised[4]. If α is very large, the solution is solely determined by the regulariser and the correlation data has negligible influence of the experimental results.

It is important that the value of α is selected properly. For CONTIN, Provencher[5] uses a Fisher F-test to calculate the probability of rejecting the regularised/penalised solution. This method is suitable when little is known about the solution or the errors. For the method, a 'reference solution' for which $\alpha = 0$ is obtained. The variance (sum of the weighted squared deviations of the fit to the data) of this 'unsmoothed' problem is compared to the variance of a 'smoothed' solution with a particular value of α. This is repeated for a range of α values. The regularised solutions will have higher variances than the solution without regularisation. For the unsmoothed solution, the variance is due only to experimental noise[4].

As mentioned, the F-test calculates the probability of rejecting the penalised/ regularised solutions; this probability of rejection indicates when α has reached such a value that the variance of the smoothed/ penalised solution exceeds the variance of the unsmoothed solution too much[4]. A probability of rejection value of 0.5 was chosen since it is generally considered to be the best compromise between too little regularisation and too strong biasing due to the regularisation[3]. The solution which corresponds best to this F-test is the chosen solution[4].

A2.2 Autocorrelation Functions

The following are plots of the 25 autocorrelation functions measured for each setup for every duration of applied shear. For all graphs given, data have been normalised based on the average of the first 30 data points and final data points from point 70 onwards. Times less than 0.01 ms have been excluded from analysis.

Setup A
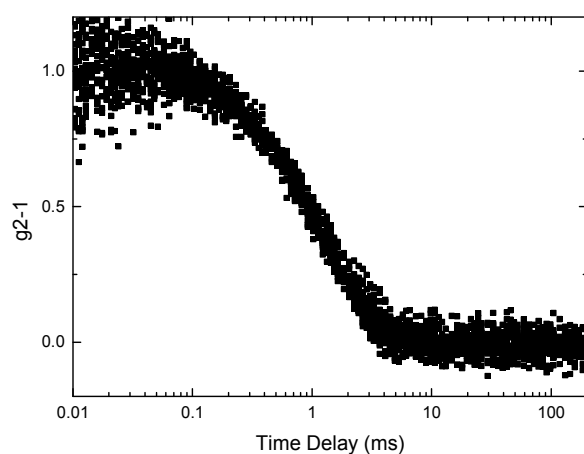
Figure 2. 1
Autocorrelation functions measured for setup A (25 s^{-1} and surface area of 2.5 cm^2 per ml solution) after 0 s applied shear.
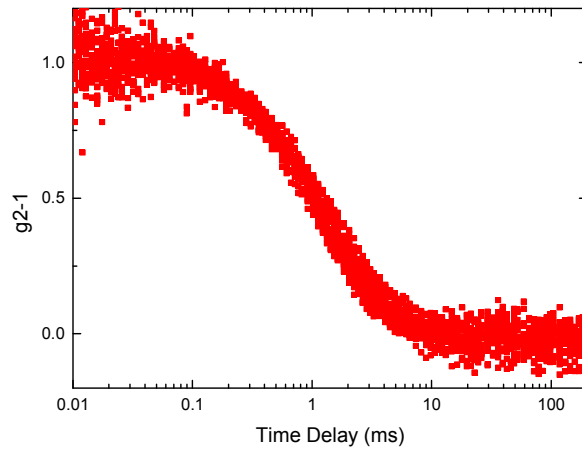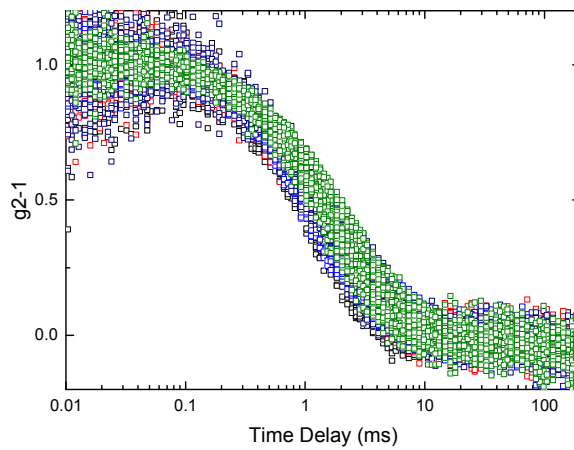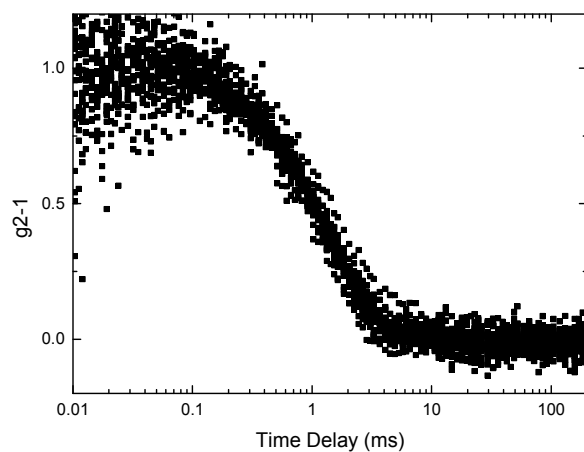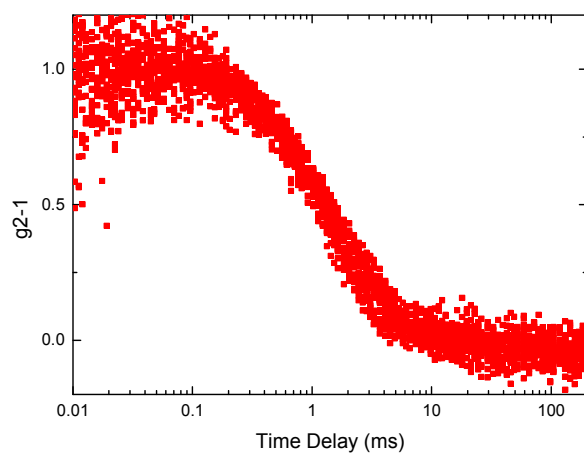
Figure 2. 2
Autocorrelation functions measured for setup A (25 s^{-1} and surface area of 2.5 cm^2 per ml solution) after 120 s applied shear.
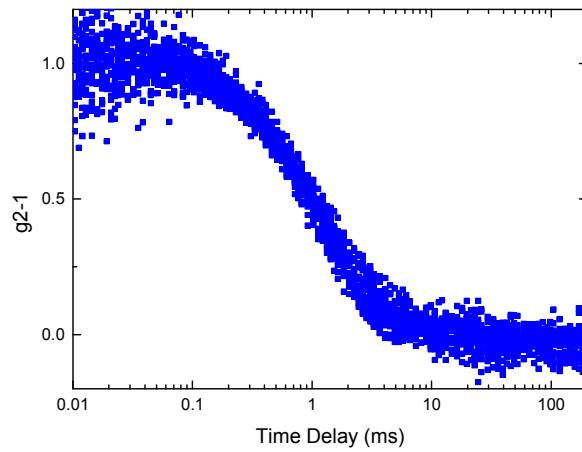
Figure 2. 3
Autocorrelation functions measured for setup A (25 s^{-1} and surface area of 2.5 cm^2 per ml solution) after 300 s applied shear.
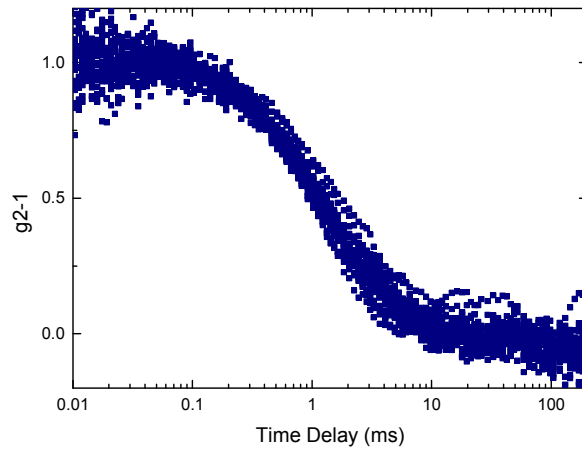
Figure 2. 4
Autocorrelation functions measured for setup A (25 s^{-1} and surface area of 2.5 cm^2 per ml solution) after 600 s applied shear.
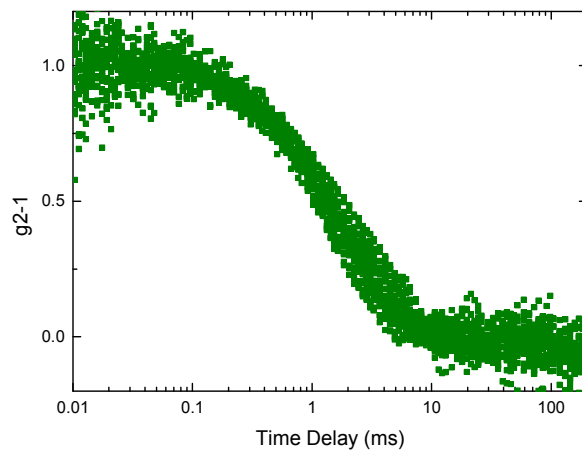
Figure 2. 5
Autocorrelation functions measured for setup A (25 s^{-1} and surface area of 2.5 cm^2 per ml solution) after 1200 s applied shear.
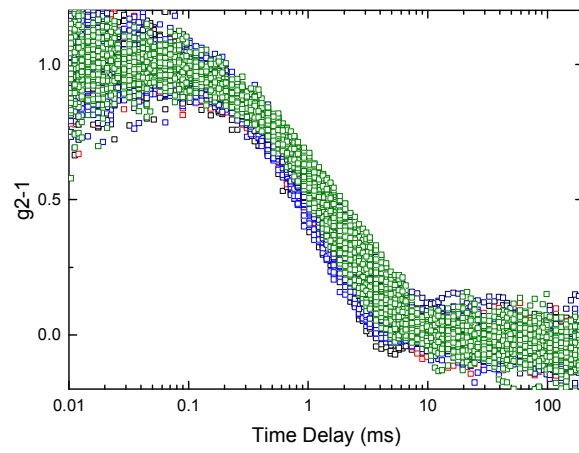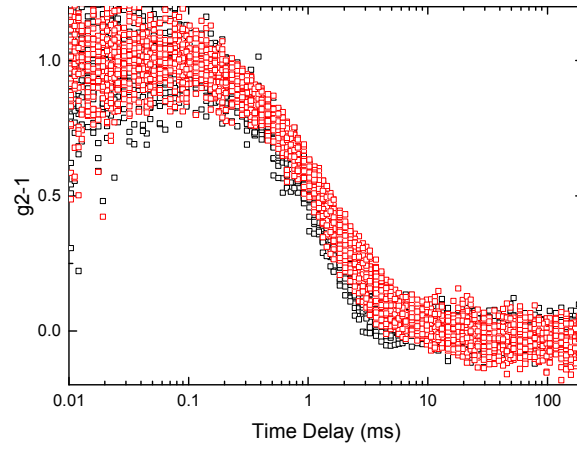
Figure 2. 6
Autocorrelation functions measured for setup A (25 s^{-1} and surface area of 2.5 cm^2 per ml solution) after each duration of applied shear. Colours represent the shear durations of the previous plots.

Setup B
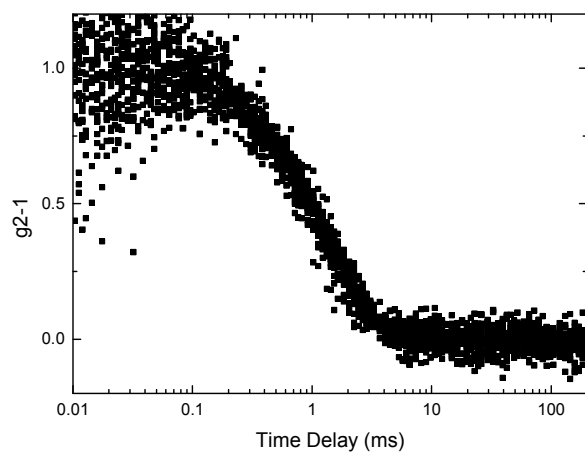
Figure 2. 7
Autocorrelation functions measured for setup B (125 s^{-1} and surface area of 2.5 cm^{2} per ml solution) after 0 s applied shear.
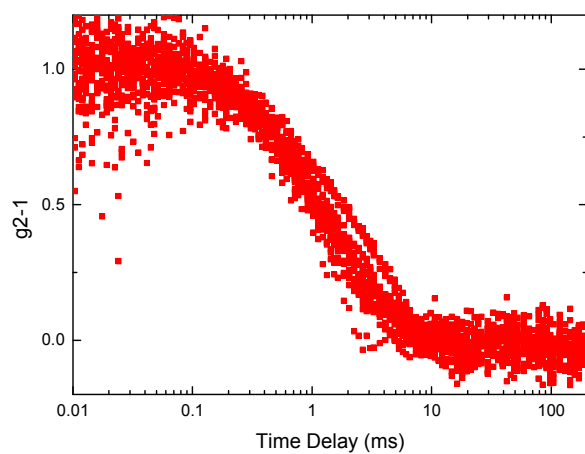
Figure 2. 8
Autocorrelation functions measured for setup B (125 s^{-1} and surface area of 2.5 cm^{2} per ml solution) after 120 s applied shear.

17
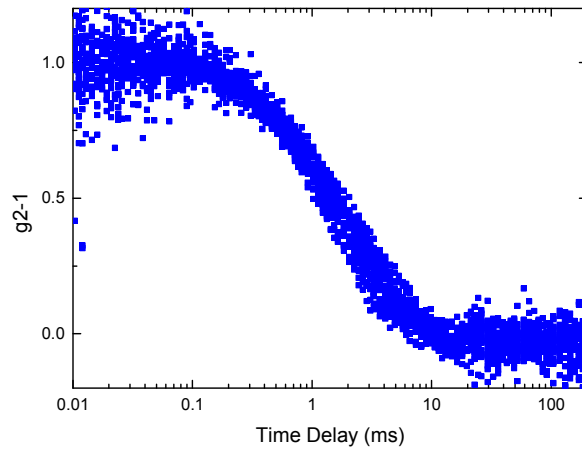
Figure 2. 9
Autocorrelation functions measured for setup B (125 s^{-1} and surface area of 2.5 cm^2 per ml solution) after 300 s applied shear.
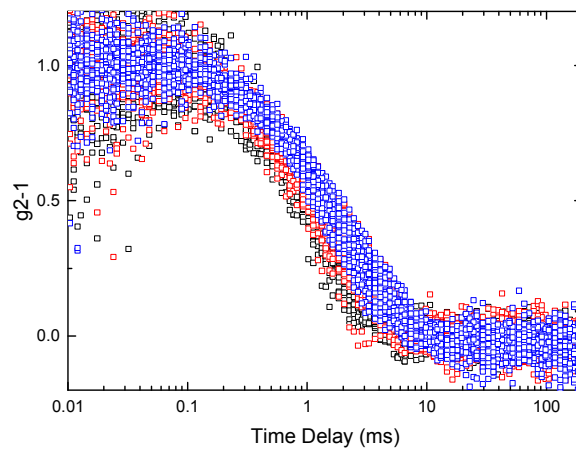
Figure 2. 10
Autocorrelation functions measured for setup B (125 s^{-1} and surface area of 2.5 cm^2 per ml solution) after each duration of applied shear. Colours represent the shear durations of the previous plots.

Setup C
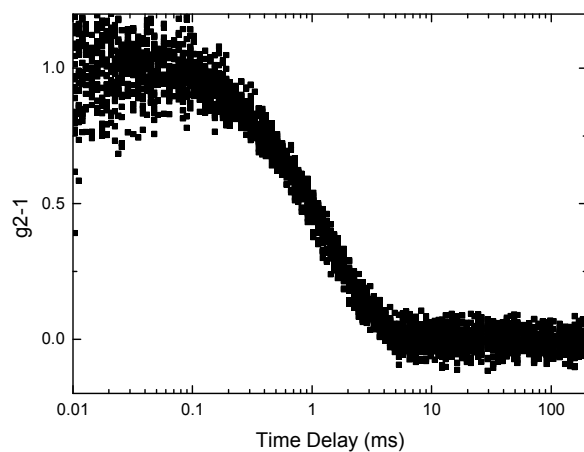
Figure 2. 11
Autocorrelation functions measured for setup C (25 s^{-1} and surface area of 5 cm^2 per ml solution) after 0 s applied shear.
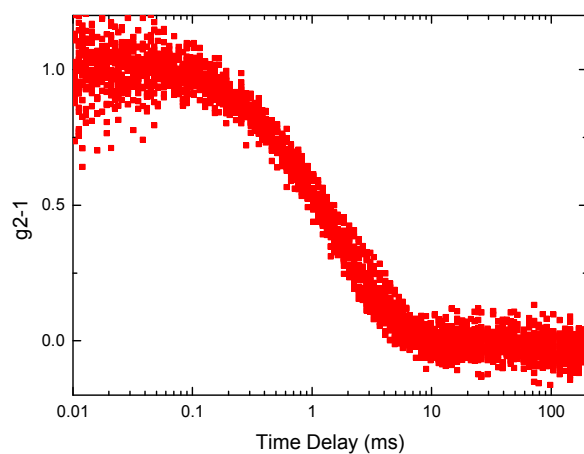
Figure 2. 12
Autocorrelation functions measured for setup C (25 s^{-1} and surface area of 5 cm^2 per ml solution) after 120 s applied shear.
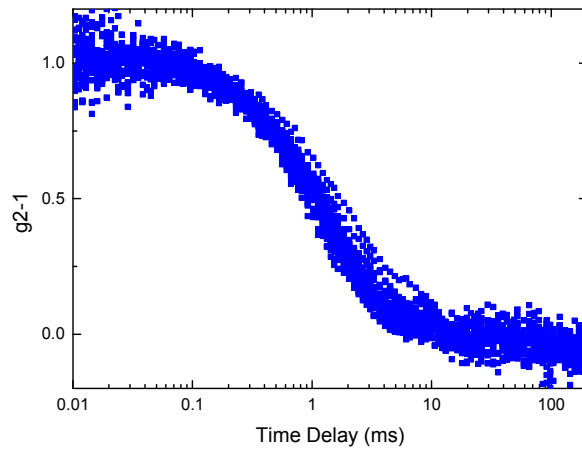
Figure 2. 13
Autocorrelation functions measured for setup C (25 s^{-1} and surface area of 5 cm^2 per ml solution) after 300 s applied shear.
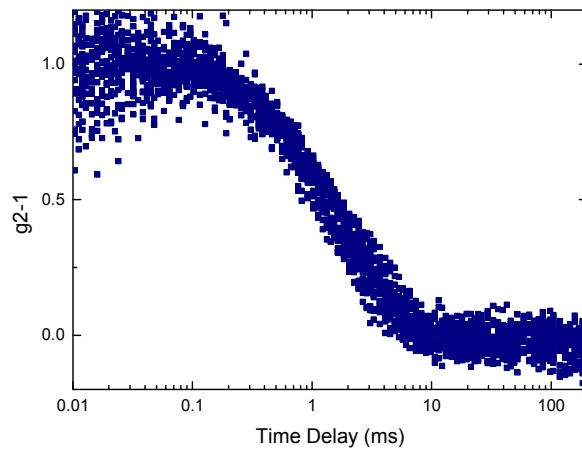
Figure 2. 14
Autocorrelation functions measured for setup C (25 s^{-1} and surface area of 5 cm^2 per ml solution) after 600 s applied shear.
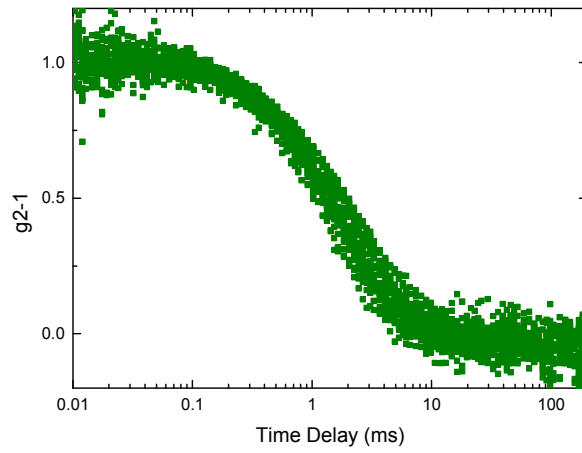
Figure 2. 15
Autocorrelation functions measured for setup C (25 s^{-1} and surface area of 5 cm^2 per ml solution) after 1200 s applied shear.

Figure 2. 16
Autocorrelation functions measured for setup C (25 s^{-1} and surface area of 5 cm^2 per ml solution) after each duration of applied shear. Colours represent the shear durations of the previous plots.

Setup D

Figure 2. 17
Autocorrelation functions measured for setup D (125 s^{-1} and surface area of 5 cm^2 per ml solution) after 0 s applied shear.

Figure 2. 18
Autocorrelation functions measured for setup D (125 s^{-1} and surface area of 5 cm^2 per ml solution) after 120 s applied shear.

Figure 2. 19
Autocorrelation functions measured for setup D (125 s^{-1} and surface area of 5 cm^{2} per ml solution) after each duration of applied shear. Colours represent the shear durations of the previous plots.

A2.3 CONTIN Analysis of DLS Results

The decays of the correlation functions did not represent entirely monodisperse samples and showed slight deviations from a single exponential decay. The deviation from a single exponential decay was greater for sheared solutions. To gain a better insight into the size distribution of particles in the solutions, the CONTIN method was used to obtain particle size distributions (PSDs). The intensity-weighted size distributions were obtained and these were also converted to number weighted distributions.

The fundamental size distribution data output by the ALV CONTIN software corresponded to the intensity weighted logarithmic differential distribution of decay rates, normalised between 0 and 1. The decay rates were converted to radii through the Stokes-Einstein relation, to give an idea of particle size[3]. Logarithmic differential number weighted distributions were obtained by assuming that scattering was in the Rayleigh-Debye regime. Cumulative distributions were easily obtained from the differential distribution data.

The logarithmic differential distribution, $q(\log(x_{i+1}))$, can be expressed as:

$$q(\log(x_{i+1})) = \frac{Q(x_{i+1}) - Q(x_i)}{\log(x_{i+1}) - \log(x_i)}$$

Here $Q(x_i)$ is the cumulative distribution function value at radius, x_i.

The logarithmic differential distribution shows the differential distribution of the logarithm of the characteristic parameter (particle size), and this can be difficult to interpret when distributions are monomodal. The maximum value corresponds to the most frequently occurring value of the logarithm of particle size, which is not very meaningful, rather than the mode of the particle size distribution[6]. Therefore, standard differential distributions, $q(x_i)$, were calculated, normalised between 0 and 1 and plotted.

$$q(x_{i+1}) = \frac{Q(x_{i+1}) - Q(x_i)}{x_{i+1} - x_i}$$

The intensity weighted PSDs obtained are given in Figure 2. 20 to Figure 2. 27 and the number weighted PSDs obtained are given in Figure 2. 28 to Figure 2. 35. Due to the amount of data collected, PSDs were only obtained for randomly selected measurements. 5 PSDs were obtained for each shear duration for each arrangement (A, B, C and D). A statistical analysis was then done to validate that this was sufficient for trends to be reliable. It is noted that due to data noise, the CONTIN fits were extremely sensitive to which points were used in the analyses. Graphs and trends shown are therefore suggestive only.

From visually observing the particle size distributions, shearing caused the particle size distributions to become broader, particularly in the case of intensity weighted distributions. The number weighted distributions were considerably narrower than the intensity weighted distributions. This would be expected since intensity weighted distributions are biased towards larger particles (scattering is roughly proportional to radius to the 6th power[7]); scattering from a small number of larger particles can mask scattering from a large number of smaller particles. The width of intensity distribution peaks tend to be overestimated in DLS measurements and this can be magnified in the transformation to number based distributions[3]. This was not the case here so strongly suggested that the number weighted peaks were indeed notably narrower than the intensity weighted peaks. Due to the assumptions made e.g. Rayleigh-Debye scattering, however, the number weighted distributions can be taken as approximate only[4].

To quantify the broadening of the peaks, the full width at half maximum (FWHM) was found for each distribution (Figure 2. 36 and Figure 2. 37). This was chosen over the full width of the distributions since the extremes are more likely to be affected by noise. For intensity weighted distributions, the full width at half maximum increased with the duration of applied shear for each arrangement, which was in agreement with the visual observation of PSDs becoming broader. The number weighted peaks generally increased over time, but by an amount significantly smaller than the hydrodynamic radius or intensity weighted PSDs.

Intensity Weighted Particle Size Distributions
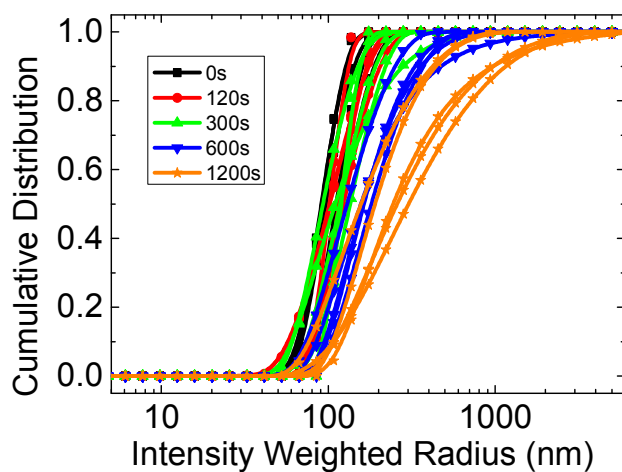
Figure 2. 20
Cumulative PSDs (intensity weighted) obtained using CONTIN analysis. Obtained from setup A (shear rate of 25 s^{-1} and surface area of 2.5 cm^2 per ml solution) DLS measurements.
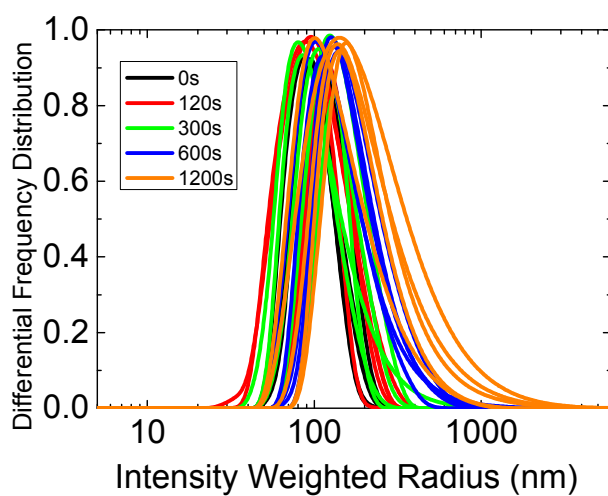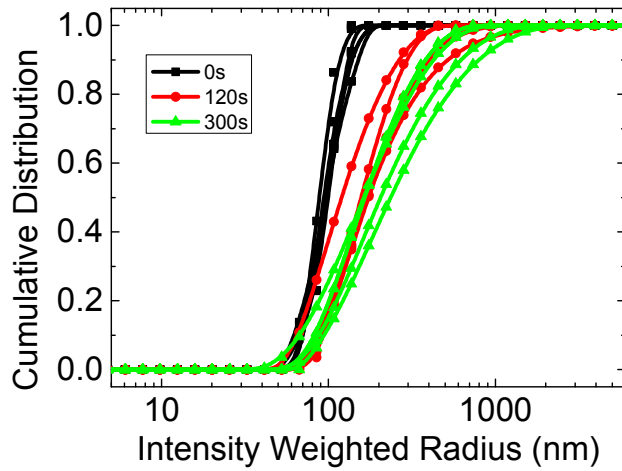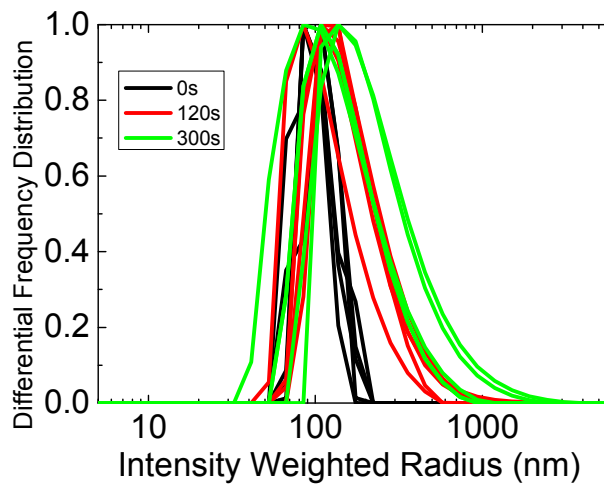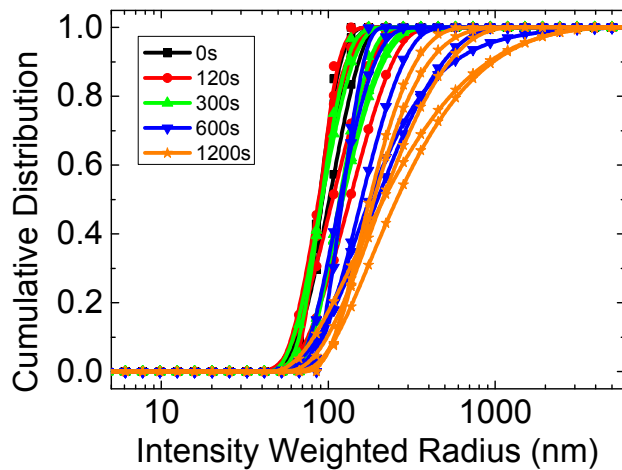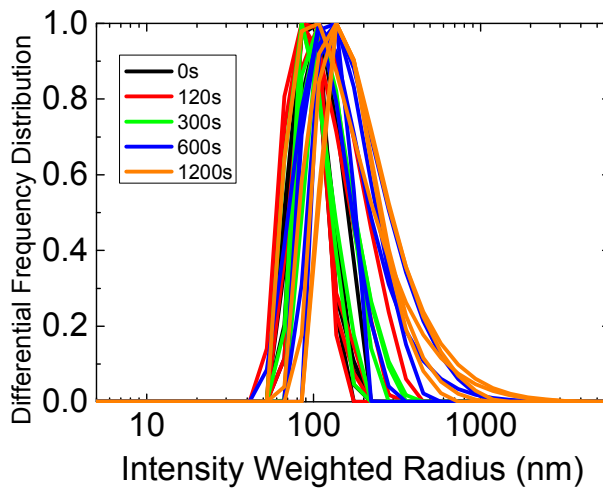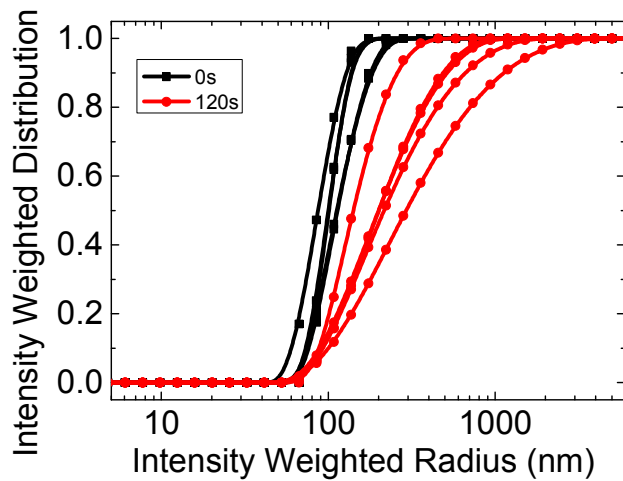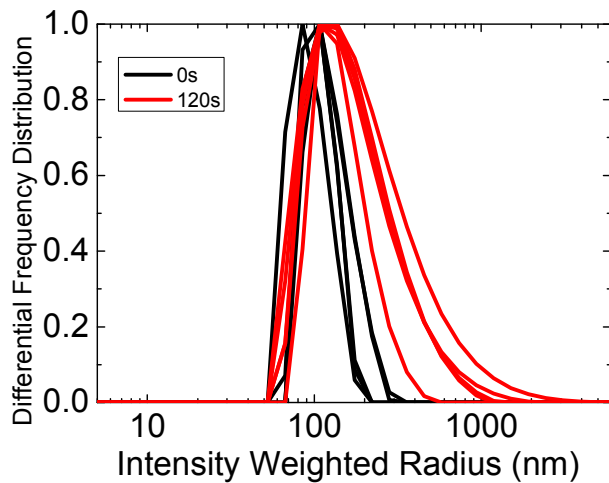

Figure 2. 21
Differential PSDs (intensity weighted) obtained using CONTIN analysis. Obtained from setup A (shear rate of 25 s^{-1} and surface area of 2.5 cm^2 per ml solution) DLS measurements. Normalised between 0 and 1.
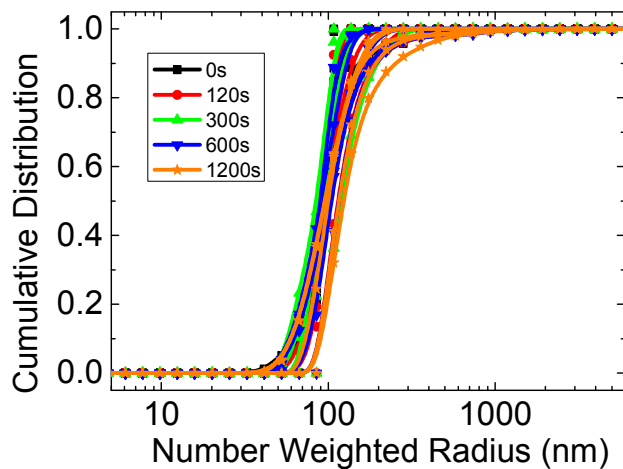
Figure 2. 22
Cumulative PSDs (intensity weighted) obtained using CONTIN analysis. Obtained from setup B (shear rate of 125 s^{-1} and surface area of 2.5 cm^2 per ml solution) DLS measurements.

Figure 2. 23
Differential PSDs (intensity weighted) obtained using CONTIN analysis. Obtained from setup B (shear rate of 125 s^{-1} and surface area of 2.5 cm^2 per ml solution) DLS measurements. Normalised between 0 and 1.
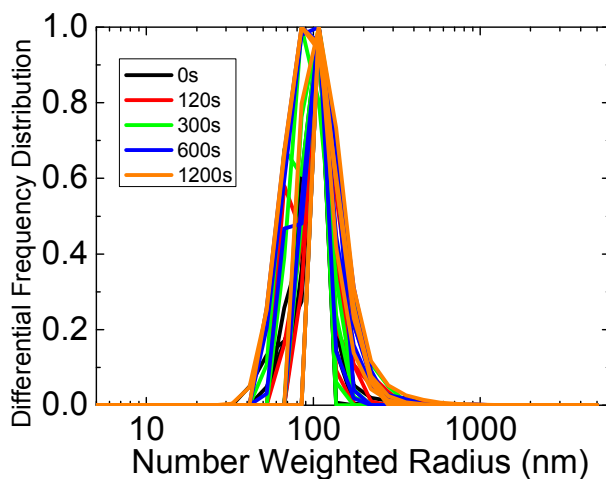
Figure 2. 24
Cumulative PSDs (intensity weighted) obtained using CONTIN analysis. Obtained from setup C (shear rate of 25 s^{-1} and surface area of 5 cm^2 per ml solution) DLS measurements.

Figure 2. 25
Differential PSDs (intensity weighted) obtained using CONTIN analysis. Obtained from setup C (shear rate of 25 s^{-1} and surface area of 5 cm^2 per ml solution) DLS measurements. Normalised between 0 and 1.
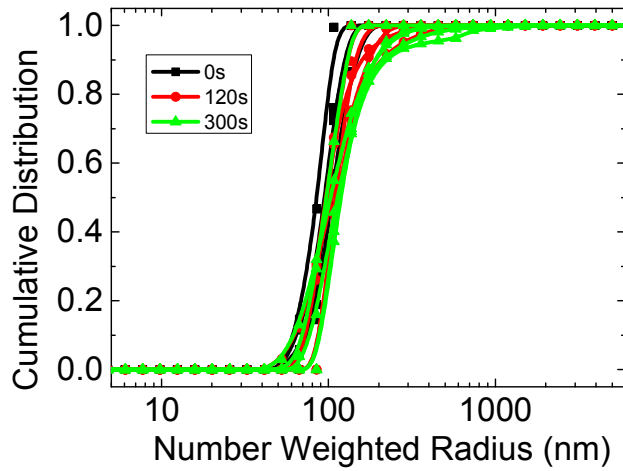
Figure 2. 26
Cumulative PSDs (intensity weighted) obtained using CONTIN analysis. Obtained from setup D (shear rate of 125 s^{-1} and surface area of 5 cm^{2} per ml solution) DLS measurements.

Figure 2. 27
Differential PSDs (intensity weighted) obtained using CONTIN analysis. Obtained from setup D (shear rate of 125 s^{-1} and surface area of 5 cm^{2} per ml solution) DLS measurements. Normalised between 0 and 1.

Number Weighted Particle Size Distributions

Figure 2. 28
Cumulative PSDs (number weighted) obtained using CONTIN analysis. Obtained from setup A (shear rate of 25 s^{-1} and surface area of 2.5 cm^2 per ml solution) DLS measurements.
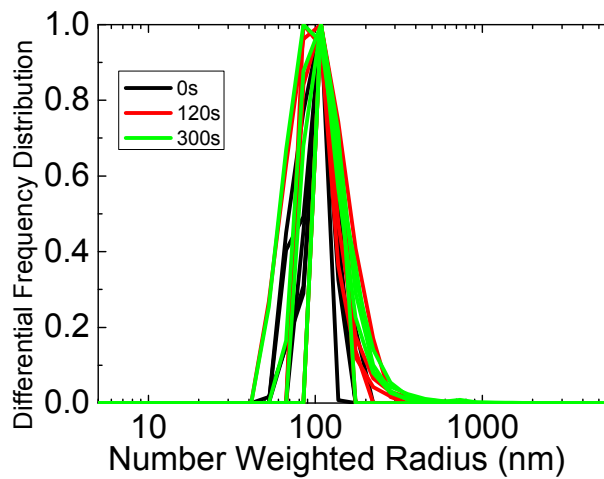

Figure 2. 29
Differential PSDs (number weighted) obtained using CONTIN analysis. Obtained from setup A (shear rate of 25 s^{-1} and surface area of 2.5 cm^2 per ml solution) DLS measurements. Normalised between 0 and 1.
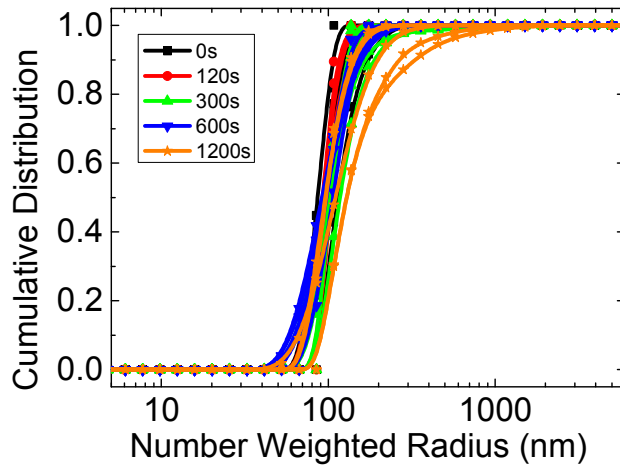
Figure 2. 30
Cumulative PSDs (number weighted) obtained using CONTIN analysis. Obtained from setup B (shear rate of 125 s^{-1} and surface area of 2.5 cm^2 per ml solution) DLS measurements.
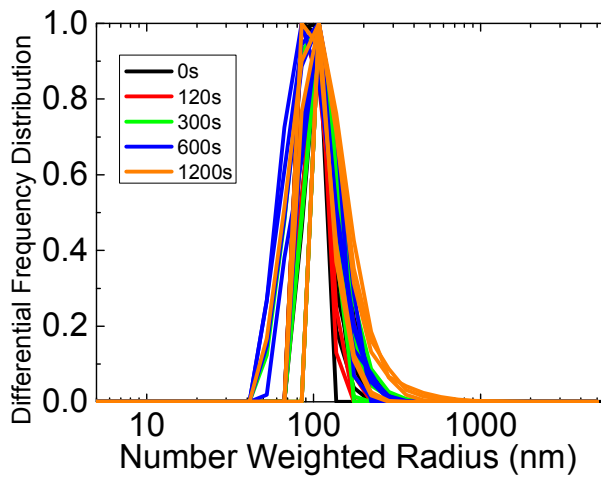

Figure 2. 31
Differential PSDs (number weighted) obtained using CONTIN analysis. Obtained from setup B (shear rate of 125 s^{-1} and surface area of 2.5 cm^2 per ml solution) DLS measurements. Normalised between 0 and 1.
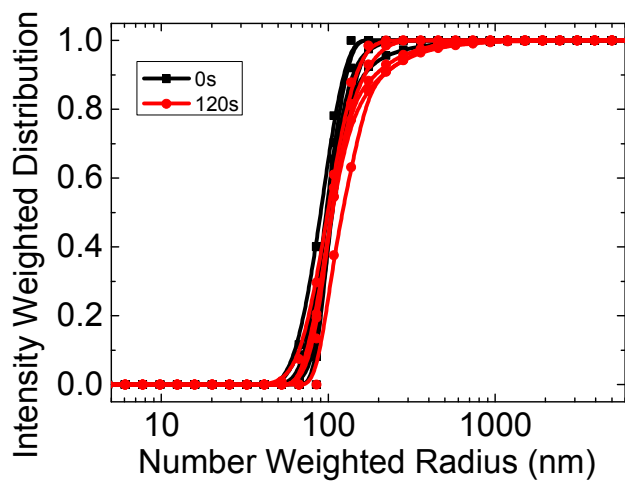
Figure 2. 32
Cumulative PSDs (number weighted) obtained using CONTIN analysis. Obtained from setup C (shear rate of 25 s^{-1} and surface area of 5 cm^2 per ml solution) DLS measurements.

Figure 2. 33
Differential PSDs (number weighted) obtained using CONTIN analysis. Obtained from setup C (shear rate of 25 s^{-1} and surface area of 5 cm^2 per ml solution) DLS measurements. Normalised between 0 and 1.
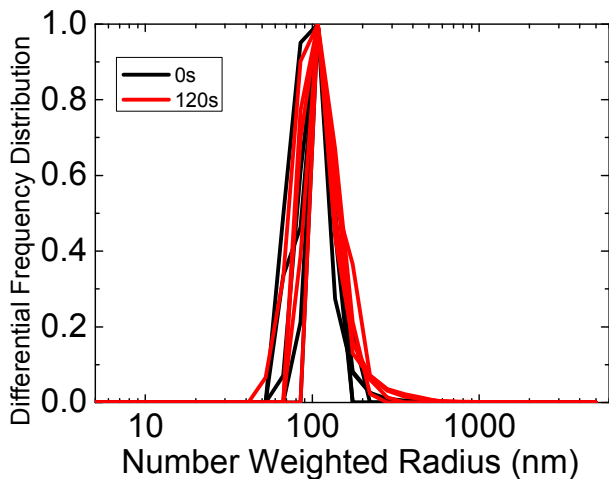
Figure 2. 34
Cumulative PSDs (number weighted) obtained using CONTIN analysis. Obtained from setup D (shear rate of 125 s^{-1} and surface area of 5 cm^2 per ml solution) DLS measurements.

Figure 2. 35
Differential PSDs (number weighted) obtained using CONTIN analysis. Obtained from setup D (shear rate of 125 s^{-1} and surface area of 5 cm^2 per ml solution) DLS measurements. Normalised between 0 and 1.

FWHM Data

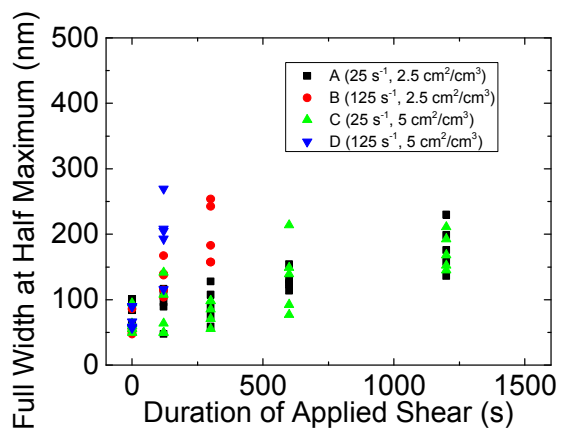The values of FWHM found from the PSDs given previously are given below.

Figure 2. 36
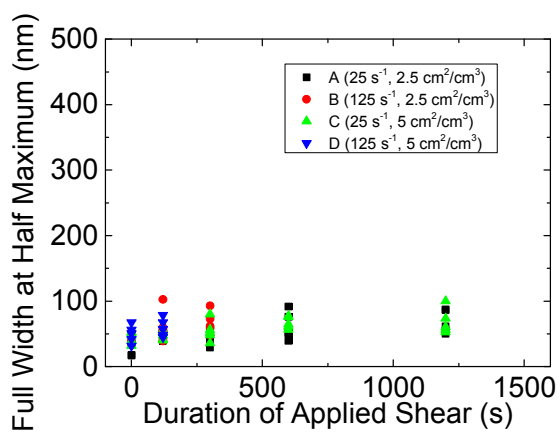Intensity weighted FWHM as a function of the duration of applied shear.

Figure 2. 37
Number weighted FWHM as a function of the duration of applied shear.

Statistical Validity of CONTIN Trends

To ensure that this trend of increasing FWHM with increasing duration of shear was statistically significant, a bootstrapping statistical analysis was carried out. Bootstrapping has been used to prove the reliability of trends in nucleating systems before (see Chapter 4).

For bootstrapping, the reliability of the regression slopes obtained from linear least squares fits to the FWHM data as a function of shear duration was found. If the slope remained positive within its whole confidence interval, it was valid to conclude that the FWHM increased with increasing durations of applied shear.

The experimental data were randomly resampled (with replacement so that a given data point could be re-selected) for each set of conditions and the slope from the least squares fit for the resampled data was calculated. This was repeated 400 times and the mean slope and standard deviation were found. Full bootstraps were done. For this, the number of resamples was equal to the number of measurements in each data-set taken at the various experimental conditions.

From the full bootstrap slope values and their confidence interval of 2 standard deviations (Figure 6. 1), for intensity weighted distributions, it is clear that the trend of increasing FWHM with increased durations of applied shear appears to be statistically significant for each of the arrangements studied here since the slopes remained positive within their whole confidence interval range. For number weighted distributions, this is less clear since arrangement D had very large confidence intervals.

As with the average hydrodynamic radius (Chapter 6) and induction times (Chapter 5), the choice of shear rate and Couette surface arrangement was found to affect the rate of change of FWHM. A plot of the rate of change in FWHM as a function of the product of shear rate and surface area, as given in Figure 6. 1, suggested that increased shear rates in conjunction with increased surface areas led to a faster increase in FWHM. The rate of change of FWHM of intensity weighted PSDs was a strong function of the product of shear rate and surface area, however, this was less obvious with the rate of change of FWHM of number weighted PSDs.

By comparing the number and intensity weighted PSDs, the results suggest that shear causes a small number of larger nanodroplets to form (in comparison to the larger number of smaller nanodroplets).
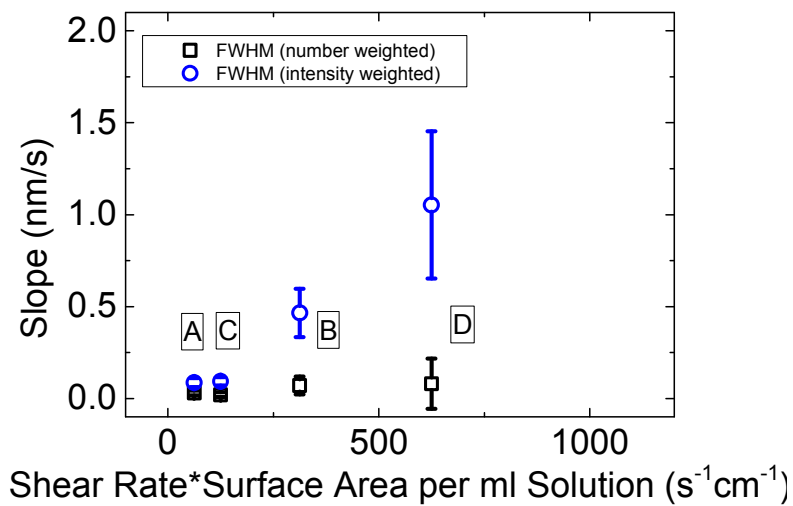

Figure 6. 1
Rate of increase in FWHM as a function of the product of shear rate and surface area.
Error bars represent 2 standard deviations.

References

(1)   Montgomery, D.; Runger, G., *Applied Statistics and Probability for Engineers*. 4th ed.; John Wiley & Sons: 2006.

(2)   Antony, J., *Design of Experiments for Engineers and Scientists*. ed.; Elsevier: 2004.

(3)   ALV-GmbH, ALV Correlator Software Manual. In ed.; Germany, 2005.

(4)   Wyn, B., *Dynamic Light Scattering- The Method and Some Applications*. ed.; Oxford University Press: 1993.

(5)   Provencher, S. W., CONTIN - A General-Purpose Constrained Regularization Program For Inverting Noisy Linear Algebraic And Integral-Equations. *Computer Physics Communications* **1982,** 27, (3), 229-242.

(6)   Sommer, K., 40 years of presentation particle size distributions - Yet still incorrect? *Particle & Particle Systems Characterization* **2001,** 18, (1), 22-25.

(7)   Chu, B., *Laser Light Scattering- Basic Principles and Practice*. 2nd ed.; Dover Publications: New York, 2007.